Global Earthquake Forecasting System

Funded by the SCOR foundation for Science 2015-June 2018
Final Report

Friedemann Freund - Yavor Kamer - Guy Ouillon - Anton Rau - Dorsa Sanadgol
John Scoville - Didier Sornette*

ETH Zurich and GeoCosmo

Table of contents

*contact person

1 – Executive summary: scope of the GEFS/SCOR initiative and main results

1.1 What is GEFS?

The overall objective of the **G**lobal **Ea**rthquake **Fo**recast **Sy**stem is to provide a reliable, rigorously tested platform to issue earthquake predictions within the few days or weeks before a large event strikes a vulnerable area. It thus requires to simultaneously process a wide range of physical data provided by different sensors embarked on satellites or located on the ground. Its general logic is thus based on:

(i) the multi-phenomena nature of earthquake precursors,

(ii) a unifying physical theory in terms of stress activation of mobile electric charges,

(iii) multi-observations, and multi-dimensional continuous monitoring,

(iv) multi-criteria and multi-dimensional analyses and synthesis of precursors into a decision function providing earthquake alarms and likelihoods of target events,

(v) a decision making process towards operational activation and use by authorities, industry and citizens.

While earthquake prediction, at least in the field of seismology, has been traditionally focusing on mechanical quantities (such as stress or strain) and has viewed large events mainly as a consequence of their variations, a totally different school has developed within the field of solid-state physics, dealing with quantities considered as observable tracers of the approach of a given spatial domain to global failure. Many of those phenomena (mainly of electromagnetic or chemical nature) appeared rather exotic, if not esoteric, to the mainstream community of seismologists; this ended up in a significant schism between the two communities, often deepened by pure sectarism, but also stemming from a lack of solid, quantified evidence: in the end, any prediction method should be qualified by its reliability and skill.

The underlying physical idea beneath GEFS is based on decades of research investment of the first PI, who has derived a credible, unifying theory for a solid-state mechanism that is capable of providing explanations for the multitude of reported pre-earthquake phenomena. A synthesis has emerged that all pre-earthquake phenomena trace back to **one** fundamental physical process: the activation of electronic charges (electrons and positive holes) in rocks subjected to ever-increasing tectonic stresses prior to any major seismic activity. The holes are unusual inasmuch as they are able to flow out of the stressed rock volume, into and through surrounding unstressed or less stressed rock, forming electric currents, traveling fast and far, and causing a wide range of physical and chemical follow-on processes along the way, which can be measured, ranging from electrical ground potentials, stimulated infrared emission, massive air ionization, to increased levels of ozone and toxic levels of carbon monoxide (CO). A detailed review of the theory and its unnumerable consequences is provided in Annex F of the present report. In this context, it must be emphasized that any precursory signal, whether measured at the Earth surface or from space, is 'only' an indicator of stresses building up within the Earth's crust. Since not every measureable level of tectonic stress will lead to a catastrophic rupture, 100% reliable prediction is impossible (reminding that prediction is commonly interpreted to mean the ability to pinpoint an exact time, place and magnitude of an impending seismic event).

We thus took on an unprecedented effort in order to rationalize, process, detect, and statistically characterize anomalies within a wealth of different planetary and solid physics signals, and potentially test for the evidence of their potential for predicting future large earthquakes. This effort has been organized around five fundamental pillars:

(i) building a database of various time and space variable physical signals;
(ii) define and test signal processing and statistical tools to detect anomalies within such signals;
(iii) apply those techniques to laboratory and field data at different scales;

(iv) build, improve and compare physical models allowing for a quantitative modeling of the underlying phenomena, using theoretical developments as well as numerical simulations;

(v) last but not least, build a worldwide community of researchers, who would share ideas, tools and data, with the goal of defining a rigorous protocol to tackle and solve the prediction problem.

1.2 People involved

The 3-years GEFS project was mainly funded by SCOR through the ETH Zurich foundation, hosted and with some additional support within the chair of Entrepreneurial Risks of Prof. D. Sornette (second PI), part of the deparment of Management, Technology and Economics, at ETH Zürich, Switzerland. The GEFS project also benefited from the collaboration with GeoCosmo (Mountain View, California, USA). The two PIs (Friedemann Freund and Didier Sornette) are funded by their own institutions, so that the budget is mainly spent to hire collaborators:

- 2 senior researchers (John Scoville and Guy Ouillon; recruited in November 2015), who are in charge of targeting and acquiring relevant datasets; their experience in signal processing and physical or geophysical modelling has also helped understanding and operating properly the transfer of the microscopic model to the particular scales encompassed by tectonic processes.
- 1 programmer (Anton Rau; recruited in January 2016), specialist of data management and analysis. His role has been to focus on the development of the collaborative and computation platforms.
- A post-doc (Yavor Kamer; recruited in January 2016) specialized in forecasting techniques, pattern recognition, data analysis and testing; he has handled the definition of appropriate high-dimensional data processing techniques.

Note that Hong-Jia Chen, a PhD student from the National Central University of Taiwan (main advisor: Pr. Chen-Chieh Chen), has joined us at ETH Zürich, while being funded from a Taiwanese grant. His knowledge of the Taiwanese geolectric dataset he is working on has been very precious to us and has led to novel results on empirical tests in Taiwan and to a new theoretical mesoscale model.

1.3 Organization of the report and main achievements

1.3.1 Organization of the report

In Sections 2 to 12, we present in more detail the various works that have been targeted by the GEFS team. When we could keep that section short (less than four pages), it is reported in its full size. When that section stems from a large amount of work, it is presented as a summary of a more extensive report. The latter is attached as an Annex to this report, whose number is mentioned in the header of the associated section (for instance, Section 4 is associated with Annex A). Most of the times, this Annex is a compressed draft of an upcoming manuscript that is about to be submitted, as we have simply removed most of the introduction as well as references for the sake of readability. The next section 1.3.2 provides an overview of the various achievements.

1.3.2 Achievements of the proposal funded by SCOR

As mentioned in the initial proposal, the GEFS is a long-term project that is in large part focusing on data analysis to test for the evidence of reliable precursors to earthquakes. These data concern very diverse physical quantities. Beyond gathering these datasets from various sources, an ambitious goal of GEFS is also to develop a global network of multi-parameters stations that would record and process in near real time the recorded signals. To initiate the ambitious machinery that GEFS should become, we sollicited support by the SCOR Science Fundation in order to:

(i) help create the infrastructure for the data center that will store the data from all precursory phenomena described above,

(ii) ensure the continuation and expansion of the collaboration and travel to promote exchanges with international data-centers,

(iii)   support the development of a standard testing process for earthquake predictability based on these precursors.

We shall summarize below our main achievements, emphasizing more on the challenges and consequences than on the scientific language, which is more abundantly used in the other sections. Those short summaries also feature references to the related sections or annexes of this report.

- ***Data center and collaborations with international teams (see Sections 2, 3 and 12; Annex F):***

  o The database has been growing ever since the beginning of the project, 2.5 years ago. Right now, the database has a size of about 100Tb, and should grow to a much larger size as new data will come in. We are now able to directly read or indirectly compute the values of 11 signals out of the 20 we initially targeted: Thermal Infrared anomalies, Total Electron Content anomalies, Ionospheric tomography, Ionospheric electric field turbulences, Atmospheric Gravity Waves, Magnetic field variations, ULF emission from within the Earth crust, Tree potentials and ground potentials, Soil conductivity changes, Air ionization at the ground surface. Most of the others would necessitate the installation of a dedicated network of recording stations, a longer-term goal of GEFS. Unfortunately, we initially had to face some problems independent of our will, as there has been a migration of computational and storage facilities at the scale of ETH Zurich, which delayed our schedule. Now, the database is progressively implemented into a common format for all signals and accessible for the GEFS members, a family that we hope to see growing soon. Part of this database now includes a more 'historical' set in the sense that we have been reassessing one important historical case, the 1976 Tangshan event precursors in China, directly from the sources, as this event is often advocated as an emblematic failure of earthquake prediction. We are now reassessing carefully this qualification, and we have found evidence that the often claimed Tangshan earthquake predition failure is much more multi-facetted than reported and teaches important lessons on the need for integrating scientific research, empirical recording of signals, involvement of the public at large and close collaboration with motivated and responsible decision makers and politicians. We are writing a book to summarise all our findings, with the goal that the book will be submitted to an editor by the end of 2018.

  o We developed a very active research program with the Department of Earth Science of the National Central University, Taoyuan City, in Taiwan. Hong-Jia Chen, a Taiwanese PhD student, spent a year in our group at ETH Zürich for a very fruitful (and still ongoing) collaboration giving birth to 3 articles (1 published, and 2 submitted). This scientific collaboration will be detailed below and allows us to access to continuous time monitoring of the geoelectric field in Taiwan measured at 16 ground stations. Luca Piroddi (Environmental Engineering and Architecture (DICAAR), University of Cagliari, Cagliari, Italy) also agreed to be part of GEFS and, as a specialist in Thermal Infrared anomalies, will bring his share of data and processing expertise.

  o The cowriters of the SCOR proposal are all associate editors of a forthcoming special volume about GEFS, which will be published by Springer, ensuring a very high visibility in the community. It has also been the opportunity to ask contributions to several well-known authors in the domain of earthquake prediction. This volume (to which our GEFS group expects to submit no less than seven papers) is also an opportunity to establish a common approach to process data and evaluate the results, given the high standards we defined in our proposal (such as defining training datasets to fit the models, and independent validation datasets to evaluate their performance; the latter being preferrably assessed using Molchan or error diagrams). We are now in the review process of the papers, as this volume should feature about 30 papers in all.

- ***Data processing and testing the predictability of earthquakes (Sections 4 to 6, 8 and 9; Annexes A to D and G):***

  o Our toolbox has also grown as we have been developping different non-parametric techniques to

analyze signals and/or find anomalies in a variety of physical quantities. Such non-parametric techniques are mandatory as the theory is still not advanced enough to predict the actual shape of anomalies potentially related to earthquakes. Those techniques are based on estimating different moments of the recorded signals in different time windows (mean, variance, skewness, kurtosis) or by estimating the full probability density function of the signal values. Corrections for the signal autocorrelation are also applied when necessary. Not mentioned further in the remaining of this report, we are developping a new set of techniques with our Taiwanese colleagues, which are based on the cross-correlation of wavelet transforms among different stations. The developed methodologies have been used to obtain the results indicated below.

o We reported important physical rock properties during laboratory experiments. which conclude that the peroxy defect theory, on which the GEFS project is based, is certainly the most pertinent candidate to explain a wealth of electro-magnetic anomalies, and particularly Thermal Infrared radiation (TIR) anomalies. Recording the emission spectrum of rock samples of different scales (from 4.10^{-3} to 2 m^3) loaded at increasing levels, we were able to observe frequency bands that are in perfect agreement with the theory. The time evolution of spectrum evolution as final rupture approaches is rather complex and deserves additional efforts, but these results are very encouraging and define the TIR signals as recorded by satellites to be the priority target for our next tests.

o We also considered a larger scale 'laboratory' experiment in a nearly natural setting, i.e. a tramway line in Zürich and its associated electromagnetic perturbations. The exercise consisted in recording continuously the magnetic field close to a tramway station, then to correlate it with the tram arrivals/departures. We used different methods in order to extract the anomalies and train the prediction model. The use of Molchan diagrams showed a very nice performance of the general detection methods we used, both in training and validation phases. These techniques, which look for anomalies in different frequency bands and issue a decision optimized through a machine-learning algorithm, will now be implemented on our platform to search for anomalies in a variety of other potential earthquake generated signals.

o Using natural ground geoelectric data and earthquakes, we obtained very promising results for earthquake predictability in Taiwan by extending a method previously defined by our Taiwanese collaborators to a set of multiple stations. We first significantly improved the single station method that allows to characterize for each station the maximum distance up to which it can associate an event with recorded anomalies, and the various optimal time windows that should be used to look for those anomalies and within which the future event might occur. A second significant step consisted in defining a method able to combine observations from different recording stations within a given network (here 16 stations). When correlating with local seismicity, the Molchan scores we obtain are improved and very high, suggesting to extend the methodology to many more datasets of various nature and continue this experiment in other areas. Preliminary results also show that such a joint station approach allows us to compute a spatial probability map for future events, which correlates nicely with the subsequent seismicity that we effectively observed.

o We obtained more contrasted results when looking at the elecric field measured by the French DEMETER satellite[1] (Detection of Electro-Magnetic Emissions Transmitted from Earthquake Regions) in the Very Low Frequency Range. Despite our best efforts to detrend the data according to latitude and time/season, comparison of the recorded amplitude in different frequency bands do not show any specific behavior before earthquakes. Those results clearly contradict what has been previously published by the DEMETER team. However, in a paper they submitted to the GEFS special volume

---

[1] DEMETER is a French micro-satellite operated by CNES devoted to the investigation of the ionospheric disturbances due to seismic and volcanic activity. It was launched on June 29, 2004 on a quasi Sun-synchronous circular orbit with an inclination of about 98.23° and an altitude of about 710 km. The altitude was changed to about 660 km in December, 2005. Scientific operations ended December 9, 2010.

described above that we are editing, the same team now reports detecting some changes of VLF amplitudes after the event and not before. This suggests that such VLF anomalies, if they exist, may be very difficult to detect and/or are the apparent result of the specific properties of the detection method used. More work will be needed to obtain a final conclusion about their prediction potential.

  o Looking at data sampled on the Kodiak Island (carbon monoxide, ozone, and air ion count), we have been able to show that their associated signals were closely correlated to each other as well as to seismicity. Together with our other laboratory experiments, this is in excellent agreement with the peroxy defects theory, showing that we are following the right track.

- *Theoretical approaches and numerical simulations (Sections 10 and 11; Annex E).*

  We developed a purely theoretical model of unipolar pulses, which are electromagnetic anomalies that are widely observed in the field. The model is based on volumetric instabilities due to a transition of the thermal expansion coefficient when peroxy defects are nucleated. In parallel, we also developed an alternate model based on the possible precursory micro-slips that may hold before large events: the progressive loading of the tectonic plates activates the peroxy defects, while micro-slips on faults perturb this stress field and induce transient signals. The latter mechanism has been implemented numerically (and studied analytically), by considering a standard spring-block model for a fault, where each block also features a set of RLC circuit elements. The simulations reveal that even slips that get unnoticed by seismographs could have a strong signature in the electromagnetic field, and that the simulated electric field fluctuations bear common statistical characteristics with those observed in the field (for instance in Taiwan). As these models provide descriptions at different levels of coarse-graining, we still need to dig into their dynamics to find out which one holds in the natural setting.

- *Coupling with statistical seismology (Section 7 and future works):*

  o In some of the reported works, we have been able to quantify the reliability of some methods that could be applied to anomaly detection or earthquake prediction. In the latter case, those scores should be compared with the output of other competing forecasting or prediction methods. As mentioned in our proposal, statistical seismology now offers tools to compare various forecasts. As our team is also one of the world leading ones in developing such forecasting techniques (taking into account the variation of its parameters with space, time, and size of the events), we are now implementing a tool which provides the Molchan diagram of the best statistical seismology forecasting method for a given area. Results of the GEFS will then be permanently translated into such Molchan diagrams and compared with the ones provided by statistical seismology. That way, we shall be able to demonstrate the added value of our approach more convincingly.

  o These statistical seismology models will also shed light on a very puzzling result we obtain, showing a daily time dependence of the seismicity rate in California, which we were unable to explain by any mechanism or bias. Our next step will be to use our latest and sophisticated earthquake catalog declustering tool to eliminate from the earthquake catalog all the remaining biases that may be due to subtle correlations of seismicity itself.

1.4 Conclusion

After 2.5 years of funding, scheduled for a total period of 3 years, we can thus state that GEFS reached most, if not all, of its objectives. After some initial problems, the database is now definitively on tracks and should be available on the collaborative platform by the end of the year 2018, in time with the special volume published by Springer Verlag and built around GEFS. Several new techniques of data processing have been defined and assessed. Works on synthetics and real datasets show very promising results, especially in the natural setting of Taiwan. These positive developments are further strengthened by our other results on the theoretical, experimental and numerical dimensions, which definitely help to

understand better the expected signatures and properties of the anomalies. This, in turn, should definitely boost upwards our next investigations.

2 - Building the GEFS database
(Anton Rau, John Scoville , Yaver Kamer, Guy Ouillon, Didier Sornette)

Non-seismic space and ground anomalies preceding and/or contemporaneous to earthquakes include:

Satellite Component	Ground Station Component
1. *Thermal Infrared (TIR) anomalies*	1. *Magnetic field variations*
2. *Total Electron Content (TEC) anomalies*	2. *ULF emission from within the Earth crust*
3. *Ionospheric tomography*	3. *Tree potentials and ground potentials*
4. *Ionospheric electric field turbulences*	4. *Soil conductivity changes*
5. *Atmospheric Gravity Waves (AGW)*	5. Groundwater chemistry changes
6. CO release from the ground	6. Trace gas release from the ground
7. Ozone formation at ground level	7. Radon emanation from the ground
8. VLF detection of air ionization	8. *Air ionization at the ground surface*
9. Mesospheric lightning	9. Sub-ionospheric VLF/ELF propagation
10. *Lineaments in the VIS-NIR*	10. Nightglow

In the above list, all quantities in italic can be read or derived from the various sets of data we have gathered.

Data list
The database we started to build now features (total size is indicated within brackets):
- GOES-13, GOES-14, and GOES-15 weather satellites – Infrared and Visual images (147.6 GB)
    This dataset consists of infrared and visual spectrum images from geostationary weather satellites over the western hemisphere from 2015 to the present. It consists primarily of image files, but also contains higher-precision HDF5 data.
- COMS weather satellite – Infrared and Visual images (28.6 GB)
    Like the GOES satellite data, this consists of infrared and visual spectrum images from geostationary weather satellites from 2015 to the present. It consists primarily of image files.
- MET-10 weather satellite - Infrared and Visual images (141.8 GB)
    This dataset consists of infrared and visual spectrum images from geostationary weather satellites from 2015 to the present. It consists primarily of image files.
- MTSAT weather satellite – Infrared and Visual images (7.9 GB)
    These data are infrared and visual spectrum images from the MTSAT satellite operated by the Japan Meteorological Agency, from 2015 to the present.
- AVHRR (Advanced Very High Resolution Radiometer) – Spectroscopic data (48.3 GB)
    This dataset consists of multi-channel spectroscopic image data from polar orbiting satellites from 2015 to the present. These are primarily image files but there are also higher-resolution HDF5 representations of the data.
- AMSU (Advanced Microwave Sounding Unit) – Radar reflectivity data (225.2 GB)
    This dataset consists of images from a multi-channel microwave radiometer. Laboratory experiments have suggested that stressed rocks exhibit changes in radar reflectivity and these data are useful in testing this in the field.
- GASP (GOES Aerosol/Smoke product) – Aerosol/Smoke data (7.9 GB)
    instrument on board GOES satellites tracks aerosol and smoke data from 2015 to the present.
- NASA CDDIS – GPS/GNSS data (5 TB)

- UNAVCO – GPS/GNSS data (partial, 3 TB)
- NOAA – GPS/GNSS data (partial, 3 TB)
    - We have aggregated compressed GPS RINEX files dating back to 1995 from NASA CDDIS, UNAVCO, and NOAA. This is currently our largest dataset and it has at least two potential uses - first, we can use it to compute total electron content and produce a tomography of the ionosphere. Secondly, it can be used to compute crustal deformation, which is an additional mechanical parameter to use in our models.
- ANSS composite EQ catalog – Consolidated records of seismicity since 1800 (1 GB)
    - This dataset consists of consolidated records of seismicity since 1800. It aggregates seismic records from many regional earthquake catalogs.
- Intelesense – magnetometer, air ionization, carbon monoxide data (manual download, 100 MB)
- MOPPIT satellite – Carbon monoxide levels
- OMI – Ozone monitoring instrument – ozone levels
- Comprehensive Test Ban Treaty Organization – infrasound data (pending approval)
- PISCO network – Air ionization data (276 MB)
    - This dataset consists of air ionization data from Japan. It differentiates positive and negative ions as well as large and small particles.
- QuakeFinder network – Magnetometer data (partial, 1 TB)
    - This dataset consists of magnetometer data sampled at a relatively high rate (~50Hz) and at very high precision (~10 picotesla). It was made available by Quakefinder for the 'Quest for Quakes' algorithm design competition.
- Taiwanese geolectric database (50GB) since 2012.
    - These data consist of recordings of electromagnetic signals taken in Taiwan around the time of the Chi-Chi earthquake (1999) as well as higher sampling rate data collected since 2012.
- DEMETER satellite – VLF, magnetometer, electrometer, ion count data, electron density and temperature (8Tb).
    - The DEMETER dataset is a very high quality collection of various signals recorded by this satellite initially launched in June 2004 until December 2010. The satellite was equipped to record different fields with different sampling rates, with two main modes of acquisition: a low sampling rate mode (called the 'survey mode'), and a high sampling rate mode ('burst mode') triggered only above some predefined seismically active zones. We have now collected the whole dataset, featuring electric and magnetic field, electron density and temperature, ionic density data, as well all the satellite trajectory characteristics. These data are nicely completed by the NASA dataset of TEC measured by GPS technology.
- Taiwanese magnetometer database.
- Kodiak Island multi-parameter ground station data
    - This dataset consists of time series of magnetic field, positive and negative air ion counts, carbon monoxide, and ozone measurements from five ground stations located on Kodiak Island, Alaska, 2014 to present. These ground stations also record environmental parameters such as temperature, humidity, etc. This dataset is unique in that it provides simultaneous ground measurements of several precursory signals.

The European Space Agency also allowed us to download the full set of archives of their SWARM mission, launched on November 22, 2013. The research objectives of the Swarm mission are to provide the best-ever survey of the geomagnetic field and its temporal evolution as well as the electric field in the atmosphere using a constellation of 3 identical satellites carrying sophisticated magnetometers and electric field instruments. The average size of this database amounts to about 1.6Gb per day.

Their entire RSS (Research and Service Support) data catalogue can be made available to us too, including the Meteosat Second Generation data from the end of 2007 onward (available in near real time as well), as well as the entire ERS ATSR-1/2 (centred at 11.0 and 12.0 µm) and ENVISAT AATSR (centred at 10.85µm and

12.0μm) missions to compute TIR signals. For instance, the MSG satellite has a geostationary position (0°, 0°), covering a full hemisphere. The resolution is about 3km at the zenith and 7km over Italy, with a time sampling rate of 15 minutes. It grows at a rate of about 290 GB/month, with a compression ratio close to 16. This dataset will be processed with the help of the team of the University of Cagliari, Cagliari, Italy (contact: Luca Piroddi; see Section 12).

All ESA data now represent about 50Tb.

We plan to acquire additional historical data in the near future:
- Geoelectric measurements from Kamchatka peninsula
- Chinese soil conductivity / geoelectric database
  These data consist of Schlumberger-style ground resistivity measurements taken in China at various points dating back as early as the 1970s.
- Airglow images
- VLF lightning detector data
- DE-2 data
  The DE-2 satellite (Dynamics explorer 2) was a 1980s-era satellite that carried instruments similar to the DEMETER satellite but with a lower sampling rate. It recorded various ionospheric parameters with a Langmuir probe, electrometers, and magnetometers.
- Multielectrode geoelectric data measurements
  EMF measurements from buried electrodes at ten locations worldwide, dating back as early as 2012. These consist of 12 channels of DC EMF measurements sampled at 1Hz, as well as the power in 10 AC EMF bands. Several of the stations were in the proximity of large earthquakes.

Data Framework and Cloud computing
We have transitioned from primarily using local storage to making full use of cloud storage. Google provided a prototype high-capacity transfer device (a 'fireball') to facilitate the bulk transfer of data from local machines to the cloud. Since the device was a prototype, Google provided engineers to assist with aspects of the transfer process that were still being developed.

The first attempt at transferring data via the fireball failed due to some issues with the transfer software. First, the unique identifier for transfers was truncated to only a date, and therefore only one folder could be transferred per day. This was corrected in the software, but later an IP address was dynamically reassigned, necessitating a reset of the fireball appliance. Once this took place, the data was successfully uploaded to the cloud ('rehydrated') and became available for access through Google Cloud Storage (GCS).

GCS is an object database that also has interfaces to mount cloud storage on standard filesystems and connect via services such as FTP. It can also be configured to acquire data in quasi real time using the same sort of automated downloads that until now we have performed on our local computers.

Depending on the schedule of resource availability, we had the option of either performing analytics and compute instances in the Google cloud or simply using GCS as a storage mechanism for analytics that are performed on other machines. As the new Leonhard computer cluster at ETH Zurich became available for general-purpose use, we chose the latter.

Usage of Leonhard cluster leads to some implications though. Originally ETH was planning to develop a new computing cluster for "big data" research called ETH OpenStack. It was anticipated to provide the hardware platform for our Hadoop/Spark implementation. ETH IT has provided us with access to a prototype OpenStack node. Unfortunately, the OpenStack platform never reached the production stage and later it had been decided to keep the Leonhard cluster architecture resembling existing architecture of ETH Euler (and previously Brutus) computing clusters. This solution has good distributed computing characteristics, but very strictly predefined software stack, so it means one can only use existing applications, which lacks such tools as Apache Cassandra, Apache Spark or Hadoop MapReduce. Mainly, the only difference it makes

in terms of big data is that it provides access to high-performant parallel file system with bigger storage sizes.

Database implementation

At the moment of writing, lots of datasets have been collected, and many of them are currently stored in a variety of compressed formats, both standard and proprietary. The data needs to be decompressed, which necessitates a significant amount of additional storage and a non-trivial amount of computation. The current data store consists of about 15Tb of data in approximately 20-30 million files, many of which are compressed. We estimate that the size of the full, uncompressed raw data set will be on the order of 100Tb.

For instance, around 20TB of data are acquired from satellites and ground observation stations. In order to deal with such amount of data, Prof. Sornette's group invested in the ETH Leonhard Open cluster designed for "big data" applications, becoming one of its shareholders. Specifically, we have bought 5 large-memory nodes (each with 36 cores, 512 GB RAM, 10 Gb/s Ethernet, 100 Gb/s InfiniBand) + one block of the Leonhard Open cluster Work storage (High-performance parallel file system, of 20 TB), valid until 2021-12-31. The high-performance parallel file system is used for distributed data processing and for establishing a shared access on the file level across members of the group.

To optimize the workflow and performance of the group, some data that are time-series by their nature were migrated to Timescale database, which is hosted on one of the group's private servers. Timescale DB is an extension for Postgres database to deal with time-series, which is also compatible with PostGIS extension for spatial datasets.

As an example, conversion of compressed binary DEMETER satellite dataset – VLF, magnetometer, electrometer, ion count data, electron density and temperature (6 Tb of measurements starting 2004) into Timescale database lead to the following conversion into tabular format:
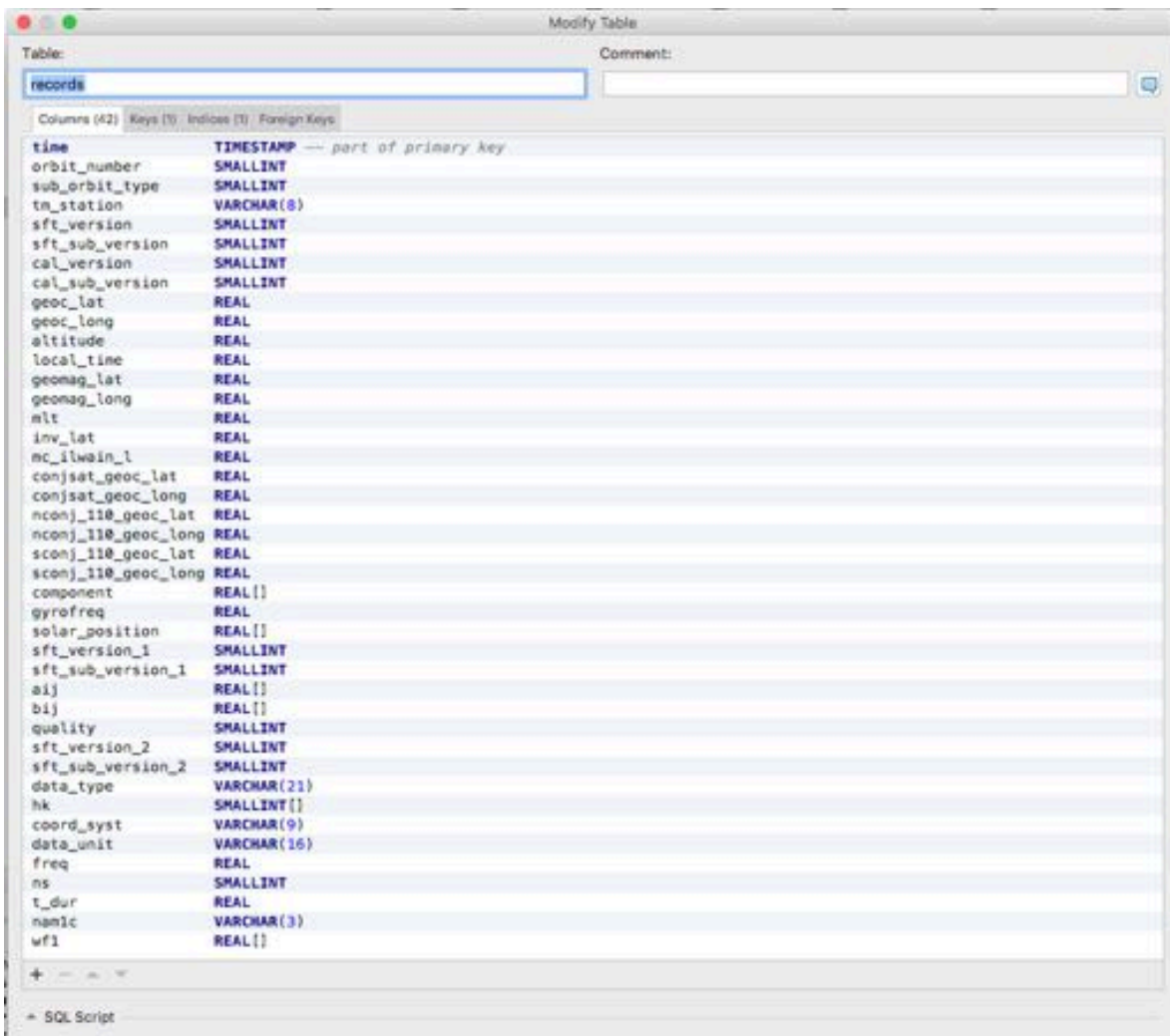
Next steps

The next major effort will be to connect all the raw data to analytics modules. To this end, we will first reorganize all the data. In order to facilitate analysis, the raw data - comprising a wide variety of data coming from many sources – will all be translated into a common data format. This format will provide a minimal time-series model that can be consumed by common analytics modules regardless of the data type or source.

xYotta platform

In order to facilitate communication among members of the project and to establish a foundation for public data exchange in the future, xYotta collaboration platform had been developed.

It is a novel collaboration platform to empower innovation with peers or any community. Collaboration is as easy as writing documents in real-time by multiple users (same way as Google Docs), uploading/downloading file resources, participating in discussions, etc. Users can work on, or suggest projects on topics that interest them the most and benefit from their own and complementary strengths. The platform facilitates quality assessment of various ideas/projects and takes advantage of the "wisdom of the crowd" phenomenon to reveal valuable information possessed by participants.

Over the last five years, xYotta has been funded by the Chair of Entrepreneurial Risks (Prof. D. Sornette), by the Rectorat of ETH Zurich via an education grant and by the Singapore-ETH center on Future Resilient Systems. xYotta is planned to interface synergetically with the GEFS, with the GEFS making full use of xYotta collaborative platform and its scientific toolboxes.

During the last year, xYotta has undergone significant development efforts, resulting in a

presentable prototype that has been demonstrated in a specific relevant environment supporting lectures given at ETH Zurich (Technology Readiness Level 6-7). Designed initially around exchange/prediction market to empower innovation with peers or any community, further developments are more focused on scientific tasks. We envision that xYotta will play an important role for the GEFS as an instrument for user friendly data management/analysis, research data rich visualization and integration of experimental results into collaborative environment. It features a toolbox allowing users to upload their own data, processing them and downloading the results.

Our goal is to use xYotta as a portal which integrates across multiple sources of data, bringing together disparate information into a unified data analysis and human collaboration environment. Scientific communities will be able to create research groups and collaborate on their research projects on xYotta by collecting, sharing and improving knowledge on particular subjects.

xYotta follows the principles of micro-service architecture, which facilitates accurate scaling according to project's needs. It is developed using state-of-the-art software tools and methods, such as Docker containerization, real-time WebSocket communication, Node.js backend and modern React frontend. The platform has the goal of simplifying user interaction with multiple heterogeneous databases and provide an interface for easy and productive discussions on research projects. Not being as powerful and complex as solutions like Palantir, xYotta allows fine tuning of scientific tools for specific projects, such as our Global Earthquake Forecast System.

3 - Reassessing the Great Tangshan earthquake precursors
## *(Didier Sornette, Euan Mearns, Niu Shangla, Wei-Xing Zhou)*

Complementing the build-up of a digital database, we also established a solid contact with the Chinese community and authorities in order to reconsider the case of the Great Tangshan earthquake that occurred in China in 1976. Contrarily to the Haicheng event in 1975, its scientific prediction has not been mediated by the authorities despite similar monitoring strategies prevailed. Discussing with some Chinese collaborators suggested that the Tangshan event indeed had been predicted by the scientific community, but that the ambient unstable political background (the death of Mao and the demise of the gang of four) didn't allow for an evacuation decision to be made, which led to a human disaster. This is why we also started to gather data and archives about this event in order to clarify the status of this case. As mentioned in our initial proposal, the goal of GEFS is not to provide a collection of well chosen case studies, but rather to rely on global statistics. In this respect, the Tangshan earthquake case is of specific importance because it has always been pushed forwards by the adversaries of the idea that earthquake prediction is possible. Then, possibly showing that this event had indeed been predicted may raise some new interest from the community as a whole. Moreover, the Haicheng earthquake of 1975 and Tangshan earthquake of 1976 illustrate that earthquake prediction is not just a scientific or technical issue: it requires participation of the public, as well as strong commitment of policy makers, with a rigorous communication process between scientists, public and authorities. We are thus continuing to study the Tangshan earthquake in order to learn the "Chinese way" initiated by prime minister Zhou Enlai. The lessons of these times may have been lost as a result of various political forces as well as hubris from the West, and we think that these lessons may be very useful in the present digital age to revive a comprehensive integrated prediction system involving scientists, the public and authorities.

We thus unearthed three reports about the Tangshan event in a Chinese antiquarian bookstore, and after getting them, began a translation process for each of them. The first one has already been fully translated in english ('Tangshan Earthquake - Animal Abnormal Behavior: 100 Incidents', translated by Niu Shanglan) and reports many weird animal behaviors recorded before the event together with indications about their time and spatial locations. The two other volumes (still under translation process) deal with more usual anomalies, some of which are shown below for a comparison between the Haicheng and Tangshan events.

Haicheng and Tangshan precursors: a comparison

Haicheng, M7.3   Tangshan, M7.8
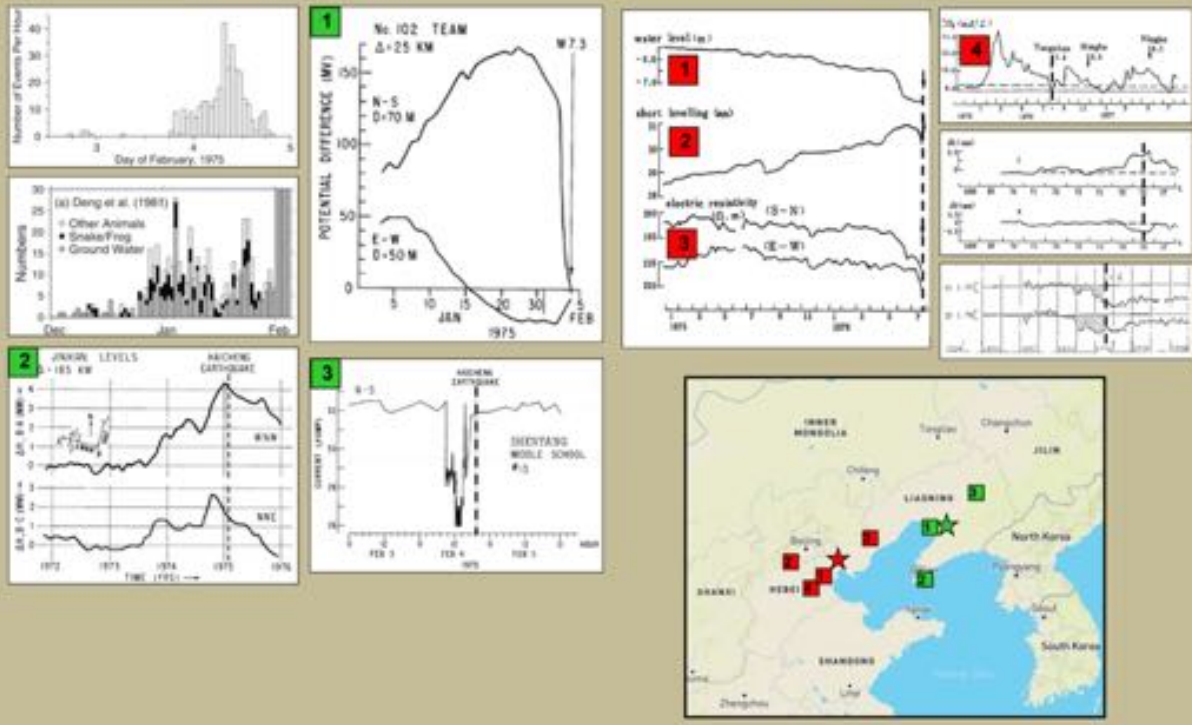
A few geophysical measurements performed before the Haicheng and Tangshan events at Chinese observation stations.

4 - Comparison of general transient signals detectors.

(Yaver Kamer, Guy Ouillon, Didier Sornette)

An extended version of the report is available in Annex A. All mentioned figures refer to that Annex.

The search for a precursory earthquake signal, whatever the underlying physical quantity, is a challenging task. The challenge manifests itself in two different ways: (i) reports of such signals are not ubiquitous, and they often are not consistent in their amplitude, direction and time-space proximity to future events; for instance, nearby stations may not both record an anomaly; (ii) due to the low frequency of large destructive events (i.e. our targets), testing and establishing the statistical significance of such signals becomes difficult. Any practical application aimed at establishing the existence (or lack thereof) of precursory earthquake phenomena requires addressing these two main challenges.

We thus tackled the general problem of anomaly detection within a given time-series in the case where the signal is 'unknown', i.e. we have a priori no information about its statistical or spectral characteristics. Thus the method relies on designating a portion of the time-series as noise. The signal is then extracted as time segments of the dataset that are significantly different from the noise. In a nutshell, the signal is first decomposed along different and non-overlapping frequency bands. The statistics of its amplitudes are then computed for each frequency band and time interval. By performing pair comparisons of segments featuring only noise, we can compute a maximum 'distance' among noise segments. Computing the same distance for all pairs of segments allows us to identify segments that have a very low probability to be noise.

The figure below (Figure 5 in the Annex) shows synthetic examples with a continuous background noise over which anomalies of different kinds (sinusoids, gaussian kernels) are superimposed:
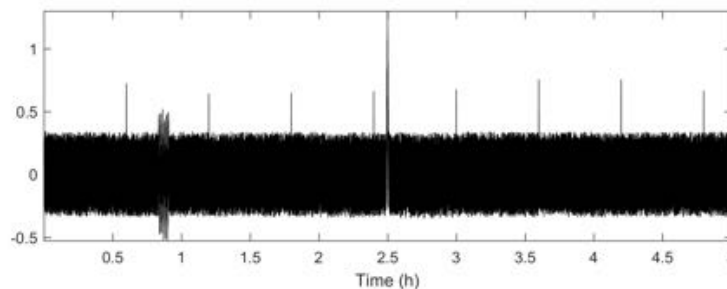
The resulting classification after applying our algorithm is the following (last plot of Figure 6 in the Annex):
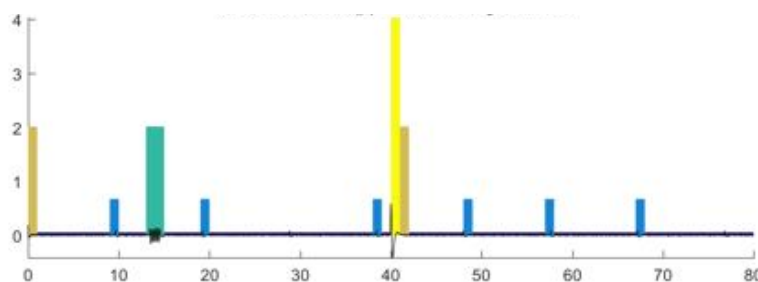
Each vertical bar is located at a detected anomaly, the height of the bar indicating the local 'signal-to-noise' ratio. The synthetic dataset test allows us to make the following observations:

(i) the method is able to classify the input trace into noise and various types of anomalies: the 5 minutes long sinusoidal signal at 0:50 is detected as a single anomaly. The 10 seconds long Gaussian at 2:30 is detected as two separate anomalies due to the band pass filter response that prolongs the signal duration. Six out of the eight 1 second long Gaussian signals are detected and correctly classified as being of the same type.

(ii) the method fails to identify some of the anomalies, such as the two missed signals at segments 28 and 77. These missed detections can be attributed to those signals being individually splitted into distinct

segments and hence failing to match the statistical properties of the rest of similar signals. To counter this effect, in the real dataset application, we perform several runs where we offset the input data with different time lengths so as to explore all possible segmentations.

(iii) the method makes a false detection at the beginning of the input signal. This is due to the band-pass filter response, which is initially at zero and outputs a transient signal whose duration is proportional to the band-pass filter period. To counter this effect in the tram application, we should thus ignore the initial segments that fall within this transient duration.

To address the second challenge of testing the detection method on a set of scarce target events, we conducted an analogous experiment that allows us to record data of multiple target events as well as a well-defined background noise. The experiment is based on recording electromagnetic field amplitudes in the vicinity of a tramway station in Zurich, using a small Arduino type magnetometer. The target events are defined as tram arrival/departures during which the current in the power lines is expected to induce detectable changes of the magnetic field. Coupling the magnetometer with a digital camera taking pictures at a short time interval, we are thus able to match the recorded electromagnetic signal with the set of times of departures and arrivals of trams. The nighttime, when trams do not circulate, is used to define the noise domain. The daytime is the period where we look for anomalies and is divided into two sets: a training set that allows us to optimize for all detection parameters by matching (or not) detected anomalies with observed trams, and a validation dataset that is used to quantify the skill of the method in real conditions (i.e. the data of the validation set are not used to constrain the optimal parameters). The detection parameters include a weight to each frequency band in computing a characteristic function, a 'characteristic function threshold' above which an alarm is effectively triggered, and a time window setting the duration of the alarm. The performance of the model on the training dataset is assessed using a Molchan diagram (see figure below; same as Figure 9 in the Annex). Once a couple (threshold, duration) has been defined to qualify alarms, we simply estimate the share of time covered by alarms (abscissa) and the corresponding share of trams that have not been detected. The corresponding point qualifies the performance of this set of parameters: the closer to the origin (the perfect detection), the better. The skill of the method itself is assessed by computing the area under the Molchan curve (obtained by varying the alarms' properties). The smaller it is, the more skilled if the method. In our case, the area is about 0.17, significantly smaller than 0.5 (the descending diagonal on the figure represents a random detection). We thus conclude that the proposed method is likely to have an interesting potential in detection applications. Due to its non-parametric, data-driven formulation, and only requiring the labeling of the noise portion of the data, it should provide added value in the search for earthquake precursors in various datasets. However, supplementary tests showed that a similar approach using a simple STA/LTA (for short term average over long term average) instead of a statistical distance between pairs of segments improves the detection skills (see Figure 11). We shall thus pursue our comparison efforts on synthetic datasets of different nature to definitively conclude on the strategy to adopt in the case of natural signals.
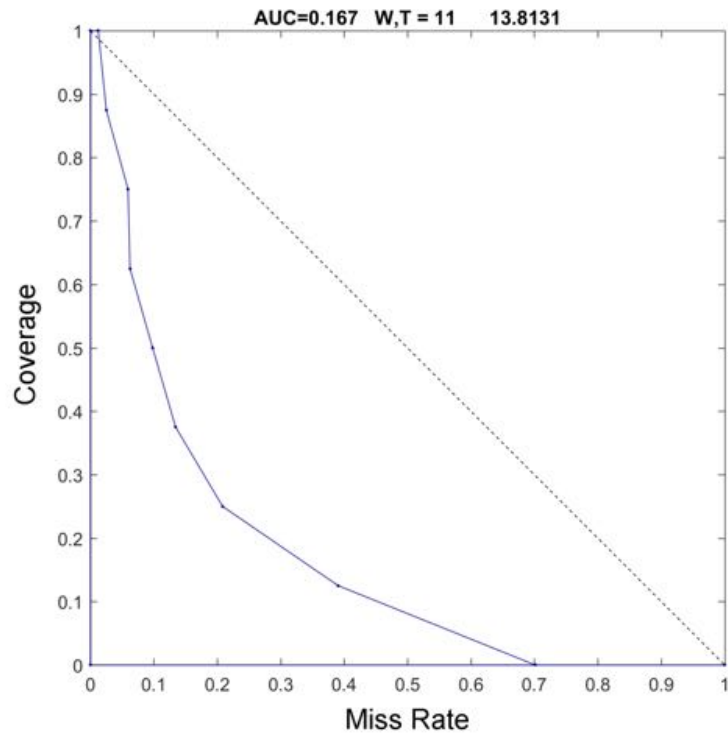
Molchan diagram of our proposed detection method when applied to a set of tram stops and departures in Zurich.

5 - Analysis of precursory signals on Demeter VLF data conditioned on M>5 earthquakes.

(Yaver Kamer, Guy Ouillon, Didier Sornette)
An extended version of the report is available in Annex B. All mentioned figures refer to that Annex.

The data used in this analysis is the VLF magnetic power amplitude spectrum data recorded by the DEMETER satellite. The spectrum frequency (0-10Khz) is divided and aggregated into 16 frequency bands plus one band for the total power amplitude and one band for the range 1.6-1.8Khz (which according to some authors is the most sensitive frequency band). The satellite takes continuous measurements as it flies along its orbit. These measurements are geocoded and time-stamped. For the purpose of the following analysis, the Earth is tessellated into equally sized triangular regions, each with an area of 250,000 km^2. The satellite makes a fly-over above each of these regions approximately every 24 hours. During each fly over, multiple measurements within the region are taken (yet the satellite doesn't fly exactly over the same locations during consecutive days as its orbit inclination is not exactly 90°). To decrease the noise level, we combine these multiple measurements into a single data point by averaging. This leads to approximately one data point per day for each triangle. This is what is presented on the following figure (Figure 1 in the Annex):
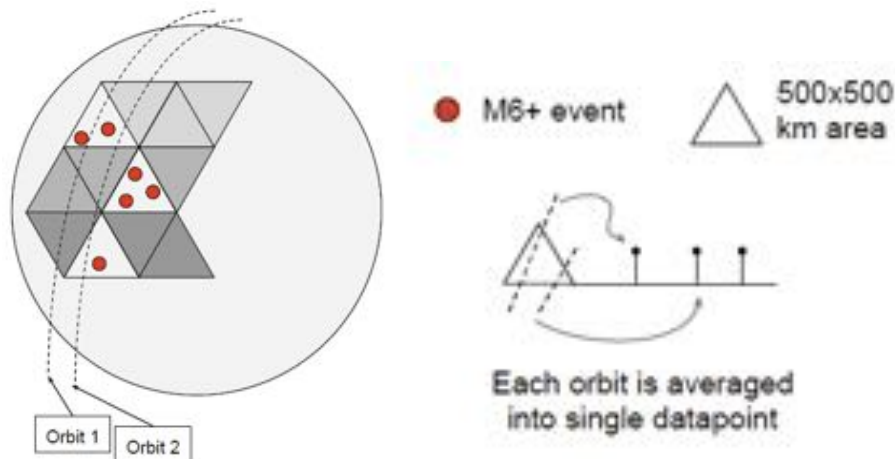

Triangular tessellation of the Earth's surface, with large occurring events (here, larger than M=6, red full circles) and two orbits corresponding to the trajectory of the satellite on the same day. The bottom right sketch shows that all measurement points on the same day over the same triangle are averaged out to get a daily measure.

The goal of the analysis is to establish if there is a significant decrease/increase in the measured VLF magnetic power amplitudes prior to major earthquakes. The analysis is based on stacking the VLF power amplitude time series conditioned on earthquake times. The general method is the following:
(1) We first model the seasonal variation within each triangle by considering only aseismic areas within the same latitude band. The correction for the seasonal variation is estimated as the median of the associated signal within successive time bins.
(2) For each latitude range, we subtract those medians from the signal observed over all corresponding triangles, aseismic or seismic.
(3) We condition all the season corrected aseismic time-series on the local time (0-24h). This allows to compute an hourly aseismic median. This detrending is necessary as the sun activity influences the recorded signal.
(4) The aseismic hourly medians defined above are subtracted to the corresponding values over all aseismic and seismic triangles.
(5) In a superposed epoch analysis, shifting the times of target events to *t*=0, we look at the distribution of the corrected signal amplitudes in time bins before and after the events.

This analysis is repeated for the signal filtered within different frequency bands, and for different target magnitudes (M>6 and M>5, respectively) in the time period 2005-2011. All the target events occur at a depth<50km, as the most superficial events would have the strongest signature. In order to avoid the influence of wild fluctuations during the day, only nighttime data are considered.

The figure below (Figure 19 in the Annex) shows an example of reults obtained for target events with M>6, using the 1.6-1.8Khz frequency band (the rest of the figures for different magnitudes and time windows can be found in the Annex), for times extending between 4 days before and 4 days after the events (which all 'occur' at *t*=0). The grey dashes and boxes indicate in each time bin the median corrected amplitude, as well as the associated 25%, 50% and 95% quantiles. There is no observable change in the distribution of the signal amplitudes before or after events, so that no correlation can be demonstrated between the VLF electromagnetic radiations and earthquake occurrence.
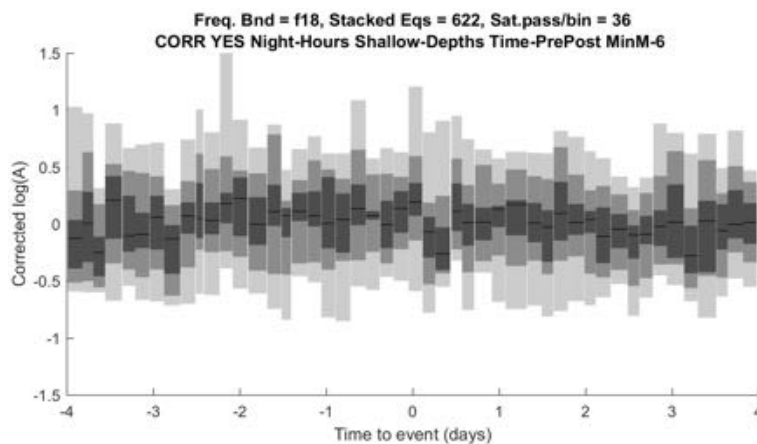
We extended this analysis by considering all events with magnitude M>5 within a similar depth range. Figures in Annex document the results and confirm the previous conclusions.

Those results, contradicting the claims of works previously published by the DEMETER team, indeed confirm more recent results by the same team after re-analyzing the same data in a different way.

6 - Earthquake prediction experiment in Taiwan using geoelectric data

(Hong-Jia Chen, Chien-Chih Chen, Guy Ouillon, Yaver Kamer, Didier Sornette)

An extended version of the report is available in Annex C. All mentioned figures refer to that Annex. A related published paper is available in Annex G.

This work is the fruit of the collaboration initiated with the National Central University of Taiwan (Pr. Chien-Chih Chen), which benefited from the presence of Hong-Jia Chen at ETH Zürich for one year (who will defend his PhD in Taiwan this Summer 2018). We focused on improving an earthquake alarm model previously defined by the Taiwanese team, based on the statistical analysis of the geoelectric field measured at ground stations. This technique, initially devised for a single station, has now been extended to a multi-station approach and shows very promising results.

Single station results

The Taiwanese dataset consists in 16 stations sampling the geolectric field along NS and EW directions at a frequency of 1Hz. The Taiwanese team defined an algorithm (GEMSTIP - Geoelectric Monitoring System Time of Increased Probability) to forecast large events based on anomalous values of the skewness and kurtosis (computed on a daily timescale) of the distribution of the observed geoelectric field amplitudes. As there are four different signals for a given station (skewness and kurtosis along NS and EW directions), one can detect an anomaly for each of them each day. The algorithm mainly consists in determining: (i) the optimal size of the time window within which anomalies should be counted; (ii) the minimum significant number of such anomalies during this time window; (iii) the size of the upcoming time window within which an event will occur; (iv) the radius from the station within which such an event will occur. This has been until now a pure fitting exercise. We helped the Taiwanese team to redefine slightly some of the parameters of the model as well as to develop more correct null hypotheses (in order to compare with random processes). The fitting parameters on the natural dataset are significantly different from the ones we get when destroying all correlations by randomization, which lead us to believe that the signature is genuine. Another interesting result is that, if the dataset is split into two subsets consisting of, respectively, high-pass and low-pass filtering of the original signal, the score of the forecast is increased for both subsets. It also appears that the learning period to forecast an immediate future should be short in comparison to the size of the whole dataset.

The electric data are first preprocessed by computing their skewness and kurtosis for each day. For each station, this provides 4 different time series (2 per component). Upper and lower anomaly thresholds are defined for each of them (and stand beyond 3 times the interquartile range from the median), and the number of such anomaly indices (from 0 to 4) are counted each day and constitute the final time series which we attempt to correlate with earthquake occurrence (The seismological data we use to train and validate the model consist in the earthquake catalog provided by the Central Weather Bureau of Taiwan, from which we extracted all M≥5 events). The GEMSTIP method consists in defining a threshold for the number of anomalous indices above which a day is declared anomalous or not. If, within a given time window, the number of anomalous days is larger than another predefined threshold, an alarm is declared, beginning right at the end of the previously defined window, with a finite duration. Concerning earthquakes, they are not considered as a pure point process anymore, but are coarse-grained in time to take into account the possible stochasticity of their nucleation process, which provides the time window within which they might have occurred with a more or less uniform probability. Optimizing the GEMSTIP model on training data consists in optimizing all the aforementioned parameters (thresholds and size of time windows) so that the alarm windows set from the geoelectric data are able to catch most of the earthquakes but also minimize the number of false alarms. A hidden fitting parameter is the maximum distance up to which we expect earthquakes to provoke a signature at a given station. Three indices are then defined to characterize the performance of True Positive associations, True Negative associations, and

an overall performance index combining the two. A second model (modified GEMSTIP) is also defined by allowing a time lag between the end of the observed anomalous time window and the beginning of the alarm window. This model is then also trained using the same datasets and performance indices.

We first find that the modified GEMSTIP model slightly improves on the original one during the training phase. It also shows that better results are obtained if the model is trained over a short time window of about a year, suggesting that the underlying process is non-stationary, so that only the most recent data should be used to calibrate the model and predict the future. Moreover, the duration of the optimal alarm window is smaller in the case of the modified model so that it allows one to point out more precisely the time when an earthquake will occur in the future. The best models defined by optimization on the training dataset are then applied to the validation dataset. We observe that the associated predictions are significantly improved when using the modified model. In particular, the Meinong M6.6 is then among the events successfully predicted.

Beyond the pure statistical aspects, the time lag between the decision to trigger an alarm and the beginning of the associated time window seems to depend on the local geology, and features a non-zero value only for stations located in the central mountain regions of Taiwan. This is interpreted as the consequence of mixed and complex processes of fresh fracturing and fluid diffusion in this area, which may affect the propagation of electromagnetic signals through the source zone. An additional observation is that the duration of observed anomalies also seems to be specific to each earthquake, and may also vary in space and time.

These first results have been published (Chen et al., 2017).

Molchan diagrams and multiple stations results

The next step has been to quantify the performance of the single station methodology using the concept of Molchan diagrams (see Section 4 of this report). For each station and possible model, we compute the quantity $d = 1 - \tau - n$, where τ is the fraction of time occupied by all alarms and n is the fraction of missed events. The larger d (which belongs to [-1;1]), the better. Thus, for each station, we have been able to select the best ten models, i.e. those corresponding to points which are the closest to the origin on a Molchan diagram.

We then consider joint models by first combining the top 1 model of each of the 16 stations; then by combining their top 2 models; then combining their top 3 models, etc., so that we get ten joint forecasts in all. This allows us to take into account the spatial variation of the best prediction parameters on the island, as well as to maximize the chances for a given event to have its precursor signal caught by at least one station. These resulting joint forecasts are then again scored on a Molchan diagram, using validation datasets of various lengths.

The results of this joint forecast (quantified by the parameter D, which is just the multiple stations equivalent to d described above) are impressive: D values reach up to 0.8 to 0.9 and improve on the skill of individual stations. We also find that the optimal length of the period to train the models is about 3 to 4 years, while the validation results show that the Molchan scores decrease slightly with the size of the predicting window: thus, predictions for the next 3 months are more accurate than those for the next year. This confirms our initial guess that electromagnetic precursors are short-term precursors. We anyway still need to inspect shorter time horizons to fully assess the performance of this method.

We also repeated these analyses using filtered versions of the original signal (initially sampled at 1Hz). This showed that the frequency band within $10^{-4.0} \leq f \leq 10^{-1.75}$ Hz may be less contaminated by non-earthquake-related signals as the Molchan scores keep at the same level within this band and seem less dependent on the size of the prediction window. This opens the door to considering different frequency bands for different time horizons, and this study thus lays the foundation of very promising earthquake forecasting techniques using non-seismic signals.

Our future work will then focus on applying this general algorithm to other types of recorded signals,

possibly optimizing the parameters during daytime and nighttime separately to eliminate solar influence. Of course, the model will be updated as new data are acquired.

One important step towards probabilistic prediction

Combining all the best individual models at each station, we can also estimate a probabilistic forecast at time t using the geoelectric data before time t. The figure below shows the spatio-temporal probability maps for the optimal parameter tensors obtained from the unfiltered data, using the training phase extending from the onset time of each station up to 2015/03/31. Two target earthquakes in 2013/06/02 are located in the middle part and southern part of Taiwan, respectively, which coincide with high probabilities for the forecast. Note that the probability increases from 2013/05/15 to 2013/06/01 before the two earthquakes, and decreases from 2013/06/03 to 2013/06/13. Similar results are obtained when using band-pass filtered data.
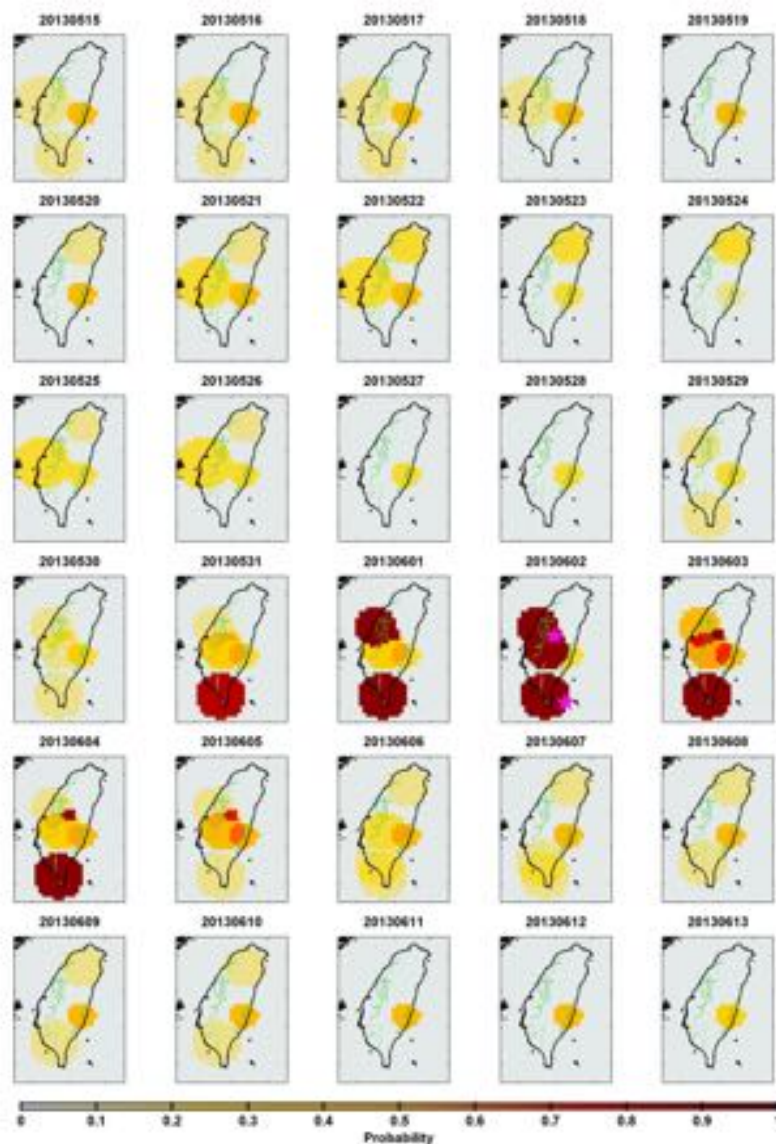

Temporal and spatial probability map of future events for the raw data.

7 - Diurnal patterns in Earthquake distribution
(John Scoville, Yaver Kamer, Guy Ouillon, Shyam Nandan)

One unresolved point in earthquake precursor research is the possibility of a solar influence on earthquakes. Some authors claim that the occurrence of earthquakes have a diurnal component, depend on the solar cycle, or are triggered by solar storms. Other studies claim that these effects are either not present or are purely coincidental.

In order to test this hypothesis, the Southern California earthquake catalog (which has the advantage of a single time zone) was analyzed first. The frequency of earthquakes having magnitudes 3+, 4+, and 5+ were evaluated for each hour of the day, and for older (1980-1995) and newer (1995-2016) parts of the catalog. Moreover, we declustered the catalog, i.e. provided for each event the probability to be independent and the probability to have been triggered by another previous one. We then also estimated the sum of independence probabilities for each hour of the day. This is to remove the potential effect of a single large event with many aftershocks, which would then cluster around the time of the former and distort the statistics. Both analyses are shown on Figure 1. Some of the older data seemed to indicate a diurnal cycle, but this was not evident in the newer catalogs.
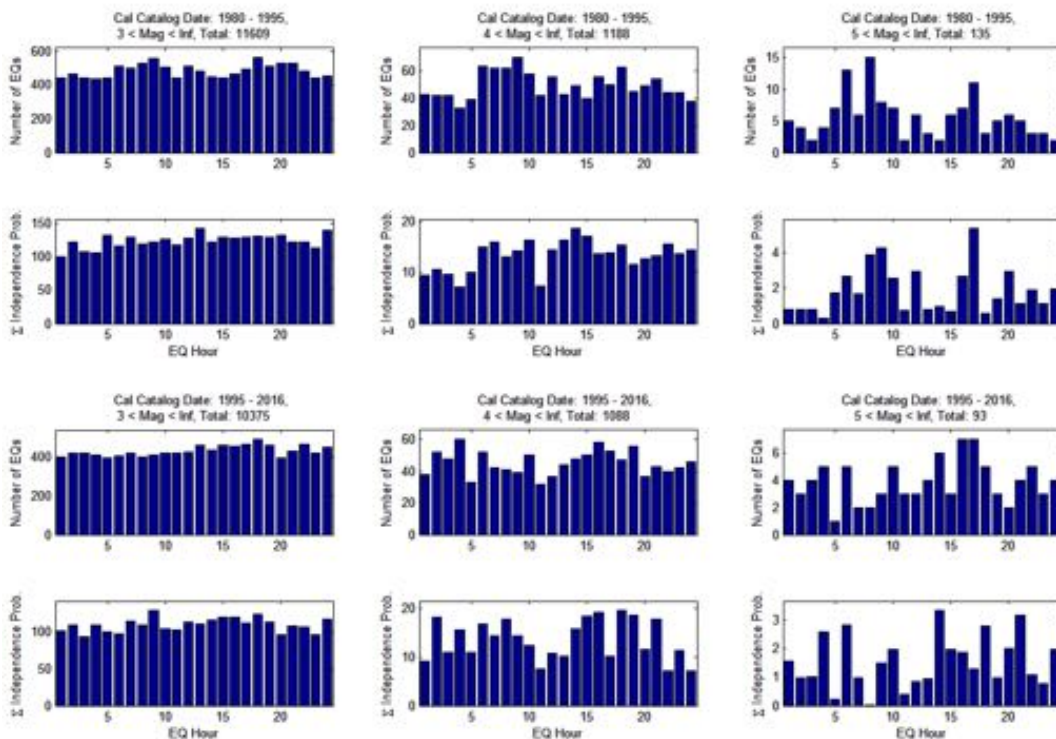
The ANSS composite catalog, containing all earthquakes in California from 1900 to 2016, was subsequently analyzed. Earthquakes were sorted by longitude into 15-degree bins, corresponding to the rotation of the Earth during one hour. Based on the longitude, the UTC time of the earthquakes were converted into a quasi-local time by adding or subtracting one hour per 15-degree bin. The result showed a strong 24-hour cycle, essentially sinusoidal with the exception of a spike at 4pm (see Figure 2). The total number of earthquakes before noon exceeded the number of events after noon, with a maximum during mid-morning and a minimum during mid-evening. Based on this, it does seem that the ANSS earthquake catalog contains a diurnal component. While this does not necessarily indicate a bona fide variation in the frequency of

24

earthquakes, neither does it refute such a hypothesis. One explanation that has been proposed for such diurnal effects is the increased incidence of seismic noise during the daytime due to anthropogenic activity, reducing the detection capability of small earthquakes. However, the observed diurnal cycle does not seem to match the times typically associated with human activity – if it did, the minimum should occur midday instead of in the morning.

While there is no generally accepted physical mechanism for this pattern, given that the 24-hour cycle has inflection points at noon and midnight in quasi-local time, it seems reasonable to consider the possibility that this could be related to the orientation of the Earth and Sun.
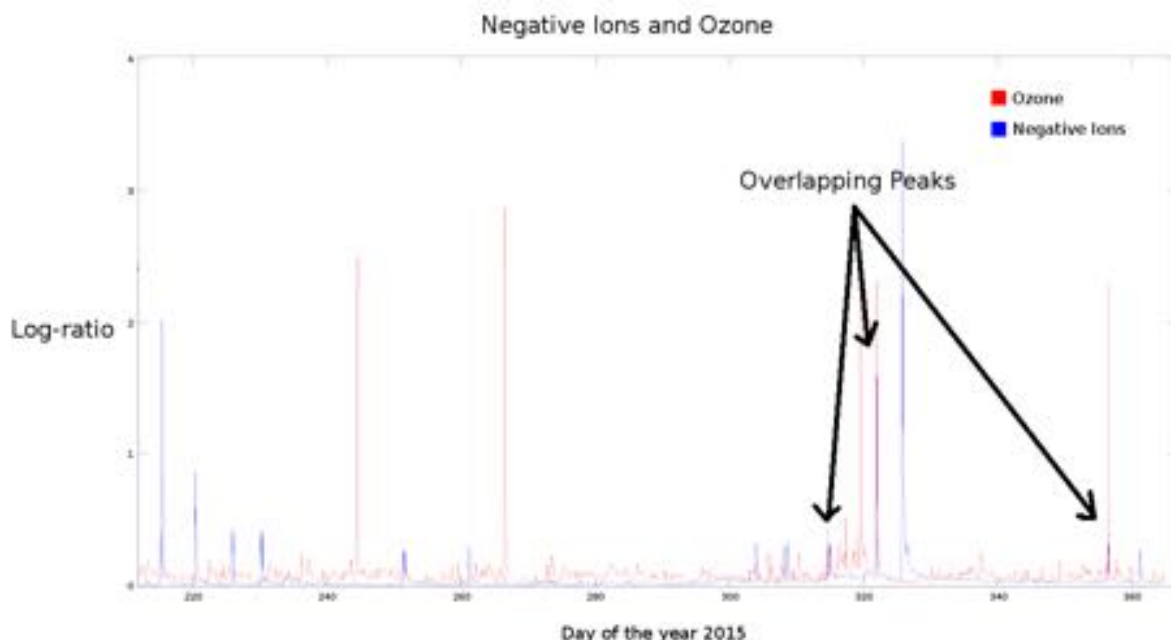
The same catalog will now be reprocessed by the declustering algorithm of our post-doc Shyam Nandan, who is also able to map very precisely changes of the completeness magnitude and of the clustering parameters in space and in time. This will ensure testing whether the observed effect is genuine. We will then need to generate synthetic catalogs on which the same analysis will be performed in order to definitely accept or reject the hypothesis of a diurnal effect.
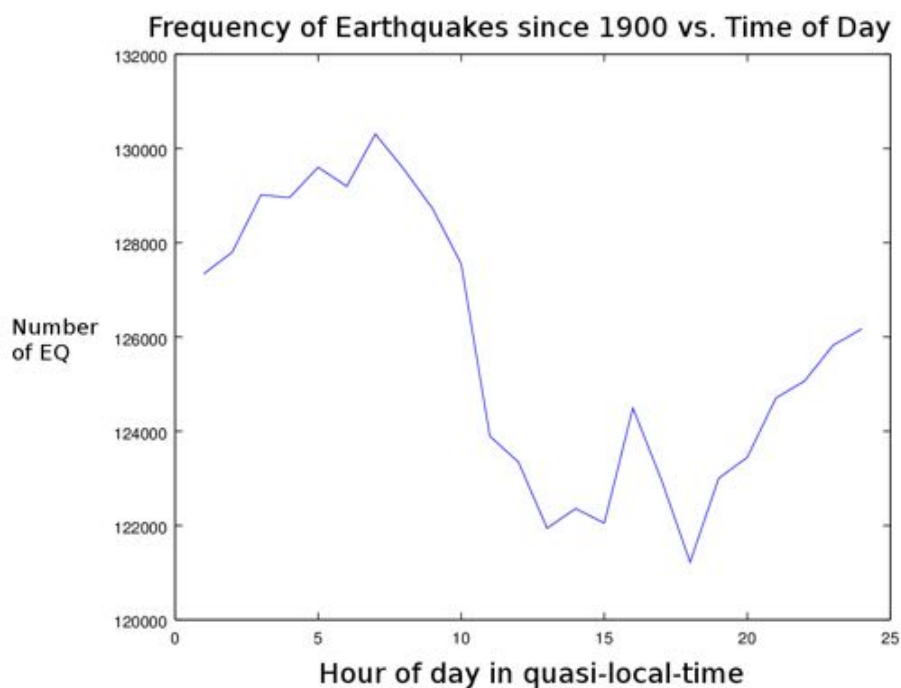
8 - Correlations between air ionization, ozone, and carbon monoxide
(John Scoville, Friedemann Freund)

A network of ground stations located on Kodiak Island in Alaska has been equipped with a number of sensors to target earthquake precursors. Among these are a carbon monoxide sensor, an ozone sensor, and an air ion counter capable of measuring both positive and negative ion species. The data produced by these sensors suggests a strong correlation between these airborne species, as previously predicted by Friedemann Freund's positive hole theory. Moreover, there is evidence that these signals occur in the predicted order: carbon monoxide is produced first, as positive holes travel through soil, and positive air ionization is subsequently produced when the holes reach the surface. Anomalous levels of negative air ionization are also observed at the same time as anomalous levels of ozone. This is consistent with laboratory experiments and is suggestive of an electrical breakdown phenomenon such as a corona discharge. This sort of electrical breakdown is also thought to be related to earthquake lights.

Preliminary analysis seems to indicate that anomalous levels of the maximal short-to-long averages of ozone and negative air ion count also tend to occur around the same times as seismic activity. Assuming self-similarity of the rupture process, if we roughly quantify the precursory effect before a seismic event at a given measurement station by the released energy of the event over the cube of distance-to-station (i.e. $10^{1.5M}/r^3$, where M is the magnitude of the event and r is the distance from the observation point to the earthquake hypocenter), the 30 largest seismic activities occur at times which correlate (ρ=0.82) to the times at which negative ions had the 30 largest STA/LTA (short-term average/long-term average) values. While this does not necessarily indicate a precursory relationship, it provides additional evidence that the phenomena are related. The following plot shows the logarithm of the maximum of the short-to-long term averages ratio. The short-to-long term ratio is calculated with many different values of the short and long time windows lengths, and the largest observed ratio for each point in time is shown in the figure.

Maximum of short-to-long term average ratios as a function of time for Ozone (red) and negative ions (blue) signals.

9 - Stress-Activated Infrared Emission from Rock Surfaces in the Thermal Infrared (TIR) Window.

(John Scoville, Friedemann Freund)
An extended version of the report is available in Annex D. All mentioned figures refer to that Annex.

We conducted experiments to test the hypothesis that the infrared emission coming off the surface of the unstressed portion of large rock samples is due to de-excitation of pairs of positive holes recombining to return to the peroxy state.

Throughout this study, conducted at room temperature, a large thermal background was present due to emission of ambient air, resulting in raw emission spectra that appear to a casual observer to be the ubiquitous graybody spectrum of air at room temperature. In order to overcome this obstacle, we analyzed time-series of spectra in order to separate rapidly changing non-equilibrium quantities from more slowly varying equilibria. Two analytical approaches were considered to accomplish this. The first is principal components analysis (PCA), a common analytical technique that finds routine application in remote sensing spectroscopy. The second is an application of fluctuation spectroscopy. We believe this to be a novel application of the principles of fluctuation spectroscopy to geophysics. In this approach, the random or nonlinear behavior associated with the non-equilibrium part of the spectrum is characterized by parameterizing the distribution of its associated random variables and observing the manner in which these parameters change over time.

Two sets of experiments were conducted: (1) with rectangular blocks of various rocks, typically 10x10x40-60cm^3, and (2) with large irregular gabbro-norite boulders, up to 7 tons, extracted from the Granite Rock quarry in Aromas, CA, located on the San Andreas Fault.

Rocks Stressed in a Hydraulic Press

Rectangular blocks of rocks were increasingly stressed at one end. The InfraRed emission was recorded from the unstressed end of the blocks. The experiments were carried out in the Engineering Evaluation Laboratory, EEL, at the NASA Ames Research Center.

For both sets of experiments (using granite and gabbro samples), a Bruker VERTEX 70 FT-IR spectrometer was used to collect the ambient temperature IR emission. The emission spectra were continuously recorded at 2cm^{-1} resolution over the 600 to 2500cm^{-1} range, or about 16μm to 4μm.

Figure 1 shows the loading force applied to a sample of red granite as a function of time. Fractures can be seen as discontinuous decreases in the applied load. The average infrared spectral variance versus time is shown in Figure 2. Figure 4 shows the average variance of each spectral band before and during loading. An increase in the amplitude of low frequency noise was a common feature of these experiments. Effectively, the infrared spectral noise became colored in response to stress.

Similar observations hold for the gabbro samples. A common spectral signature of stress found in these experiments is that the spectrum of noise changes from nearly white noise to colored noise. Lower frequencies generally exhibit wider ranges of fluctuation than higher frequencies, up to a characteristic 'cut-off' or 'corner' frequency that seems to coincide with the 1->0 radiative transition of the peroxy bond around 920-930cm^{-1}. Spectral analysis reveals that, under stress, infrared noise as measured by the VERTEX 70 spectrometer changes from nearly white to colored noise having a 'pink' to 'brown' spectrum. Pink noise is associated with electron and hole trapping in semiconductors, and the appearance of pink noise in the rock could indicate that the rock has undergone a transition from an insulating state to a semiconducting state in response to stress.

A series of sharp peaks was repeatedly noted in these experiments at wavenumbers of 760, 783, 807, 831, 854, 878, 902, and 926 cm^{-1} from which we derived a dissociation energy of 2.29eV, in very good agreement with the 2.2+/-0.2 eV dissociation energy previously obtained from electrical conductivity experiments. Additionally, the ground state transition of 926 cm^{-1} is in good agreement with the 920cm^{-1}

derived from computational chemistry calculations of peroxy defects, as well as the suspected ground state transition measured earlier by us at 930cm^{-1}. While a definitive characterization may be premature due to the relative novelty of the analysis presented here, these facts are consistent with the hypothesis of radiative de-excitation of peroxy bonds.

Gabbro-Norite Boulders Stressed with BUSTAR

Large boulders (up to 7 tons) were stressed from the inside using BUSTAR expanding cement poured into boreholes placed on one side of the boulders, while the IR emission was recorded from the opposite side, about 1m from the boreholes. We conducted 8 runs, each lasting for 8-12 hrs from filling the BUSTAR slurry into the boreholes to final rock failure. The experiments were carried out overnight in a large unheated machine shop hall at the NASA Ames Research Center.

Analyzing the frequency dependence of the time series of each band and averaging over all frequencies, we see that the spectrum of the time series approximately follows a power law, specifically, it exhibits the 'pink' noise profile associated with thermoelectric fluctuations in semiconductors rather than the 'white' noise associated with thermoelectric fluctuations in insulators (see Figure 7).

Applying fluctuation spectroscopy to the data collected from this experiment, we observe long periods of low-level thermal fluctuations punctuated by episodes of spectroscopically distinct TIR emission activity. The results of this process can be seen in Figures 8 to 11 (displaying emission spectral variance at various times) for a single TIR event. We also observe some complex shifting and broadening of some frequency bands as the system evolves towards final rupture.

Conclusions

By analyzing subtle fluctuations in the infrared emission spectrum of rocks, several previously unknown phenomena have been observed, offering confirmation of a number of earlier studies and hypotheses regarding the nature of positive hole charge carriers in stressed rock.

While at rest, in their normal insulating state, rocks exhibited TIR fluctuations similar to white noise. As rocks were loaded, however, it was found that lower frequencies had greater fluctuations during periods of stress, up to a cutoff (or 'corner') frequency around 1000cm^{-1}, beyond which white noise dominates. This suggests that some underlying physical process was producing colored noise. Pink noise is consistent with electron/hole trapping during direct current flow in semiconductors, a mechanism that has been proposed by us for thermal infrared emission and other electromagnetic phenomena in rocks. Observations of higher-order fluctuations (such as spectral kurtosis) also reveal activity in the 900-1000cm^{-1} range. All these observations are consistent with activity near the ground state transition of the peroxy bond, theoretically calculated to be 920cm^{-1}, as well as the experimentally measured dissociation energy of 2.2+/-0.2 eV.

Thus, more than 25 years after the first reports were published on TIR anomalies associated with active faults and earthquakes, a comprehensive picture of the underlying physical processes begins to emerge. The early ideas, that emanation of warm gases might be the cause of these remarkable TIR anomalies, can be put to rest in view of the wealth of data presented in this study. What has emerged instead is a story of a series of complex solid state and interfacial processes that start with the presence of peroxy defects in most, if not all rocks in the Earths crust down to about 35-45 km, including the depth range, 7-45 km, where a large majority of tectonic earthquakes originate. Available evidence suggests that many of these peroxy defects sit on grain boundaries or even straddle adjacent mineral grains. Therefore, when stresses are applied, those peroxy defects are particularly susceptible to activation, releasing positive hole charge carriers that can flow out of the stressed rock volume.

10 - Coupled electrokinetic Burridge-Knopoff model of fault sliding events and transient geoelectric signals.

(Hong-Jia Chen, Chien-Chih Chen, Guy Ouillon, Didier Sornette)
An extended version of the report is available in Annex E. All figures refer to that Annex.

This work is the continuation of the collaboration initiated with the National Central University of Taiwan (Pr. Chien-Chih Chen, PhD Hong-Jia Chen). The goal is to study the possible morphology of anomalous signals before large earthquakes.

We introduced the first fully self-consistent model combining the seismic micro-ruptures occurring within a generalized Burridge-Knopoff spring-block model with the nucleation and propagation of electric charge pulses within a coupled electrokinetic system. This model provides a general theoretical framework for modeling and analysing geoelectric precursors to earthquakes. In particular, it is able to reproduce the unipolar pulses that have often been reported before large seismic events, as well as various observed anomalies in the statistical moments of the ambient electric fields.

To begin with, we introduce a one-dimensional spring-block system. We consider a linear chain of N blocks of identical mass m pulled over an interface at a velocity v_L by a loading plate as shown in Fig. 1. Each block is connected to the loading plate by a spring with stiffness K_L, while adjacent blocks are connected to each other by a spring with stiffness K_C. In our study, geometrical boundary conditions are assumed to be periodic so that the Nth block is linked with the 1st one. Depending on the amount of slip of the plate, stress accumulates on the blocks and is counteracted by frictional contact of the blocks on their substrate. If one of the blocks starts slipping, it obeys the fundamental laws of dynamics and, by interaction with is neighbors, might trigger an 'avalanche', i.e. causes slip of its neighbor, which themselves trigger other blocks, etc. This family of models is often used to simulate slip organization over a fault plane.

Experiments on positive hole charge carriers in rocks provide evidence that the production of electric charges (hence voltage, the equivalent of an electrical pressure) is proportional to the applied stress, due to the constant resistance of the compressed material. Hence, we consider that the mechanical and electrical variables within the crust are linearly coupled through a stress-induced voltage (V_{in}) within each block. We also assume that each block plays the role of a resistor with resistance r and of a capacitor with capacitance c, as shown in Fig. 1. The block capacitor charges or discharges depending on the stress acting on the block. On the other hand, the block is embedded in the Earth's crust, i.e. is electrically grounded. The grounded current passes through a grounded resistor with resistance R and a grounded inductor with inductance L. Doing so, we now have a fully coupled model able to simulate both the mechanical and electrical behavior of stressed rock in a faulted medium, and their interplay.

This new model, which combines the mechanics of stick-slip in a spring-block system with the generation and propagation of electric charges within a coupled RLC circuit, has been coined the Chen-Ouillon-Sornette (COS) model. The mechanical component of the system is essentially a one-dimensional Burridge-Knopoff model, which is used to simulate stick-slip motions and earthquake ruptures. On the other hand, the electrokinetic component consists of a series of RLC-type circuits, while the peroxy-defect theory is used to motivate the description of the coupling between the stress acting on blocks with the amount of electric charges newly created. We studied this model both for the single-block case (analytically) and for the multi-blocks case (using numerical simulations).

In the single block case, it is easy to check that the phase space (resulting from the variation of all parameters) is divided into three domains (Figure 2): one underdamped domain, surrounded by two overdamped domains; the separations consist in critical damping surfaces. Studying the amplitude of stress fluctuations and their correlation with slip of the block, we find an overall linear relationship (see Figure 3). However, in the limit of small slips, we find that the voltage fluctuations are much larger than what the linear relationship predicts: this suggests that we might be able to record electric field fluctuations while the associated (and even precursor) micro-slips would remain too small to be recorded by seismographs.

This offers an interesting concept to reconcile partisans of different techniques of earthquake forecasting.

In the COS model, the multi-blocks problem is far more complicated than the single block one due to interactions among elements. Hence, we solve all the differential equations of the mechanical and electrokinetic systems numerically. The results confirm our analytical work, and predicts a possible variability of slip-induced voltage statistics depending on local constitutive parameters. This variability explains in turn why large earthquake slips are not systematically followed by large electric signals, as the crust is not in a damping state favorable to such dynamics. On the other hand, our results clearly suggest that precursory electromagnetic signals may be observed before large events if: (i) there are slip foreshocks, i.e. small earthquakes that would be too small to be detected seismically; (ii) the local damping conditions allow them to leave a measurable electromagnetic fingerprint. The COS model thus offers a nice opportunity to test for this feature, provided we modify its mechanical part in order to allow for such small precursory slips.

Field observations of electromagnetic signals suggest the existence of propagating unipolar pulses prior to earthquakes. The proposed COS model generates unipolar voltage changes due to local stress drops, which could be analogous to the real observations. Furthermore, the small-scale ruptures before a large event could generate unipolar signals with different properties, depending on the underground electrokinetic parameters, their amplitudes and shapes being controlled by the underground resistance, capacitance, and inductance. Besides, the background values of the spring-block voltage are not zero, suggesting that the measurement of mean values of natural occurring geoelectric fields in a certain period might be used to infer to the stress level of the region. Hence, it would be possible to use the geoelectric field in order to invert for the stress level.

Relationships between the geoelectric field skewness and kurtosis, in one hand, and earthquakes, in the other hand, have been recently reported by us (see above), suggesting that the statistical distribution of amplitudes of geoelectric signals is perturbed during the preparation stage of earthquakes. Figure 5 shows the time series of the event slips, as well as the skewness and kurtosis of the voltage series for the multi-blocks COS model described above. It seems that slips, and even micro-slips, perturb electric signals, as both skewness and kurtosis time series display quite ample fluctuations. The proposed COS model thus also provides an explanation for similar transients observed in real systems.

In our study, even a homogeneous system can also produce anomalous and complex voltages, depending on the state of the electrokinetic parameters. This suggests that the heterogeneity of a system is not necessary to produce the complicated fracture-induced electromagnetic emissions prior to large earthquakes. The stress changes indeed appear to be the key to produce geoelectric variations. However, future studies might also focus on stress-induced damage and fluid flow, which would make underground kinetic parameters dependent on space and time as well.

11 - Unipolar Pulses due to Volume Instabilities Deep in the Earth Crust
(Friedemann Freund, John Scoville)

Unipolar pulses have been identified in many data sets collected at seismically active sites. It was found that the USGS has known about these short EM pulses for many years, though most USGS data referring to ULF signals have been recorded at 1 Hz, insufficient to catch ULF pulsations that may last only about 150 msec. The USGS geophysicists in charge of archiving data from USGS stations worldwide decided that the short EM pulses, which showed up in their data, were noise. As a result, they removed the alleged noise from the raw data sets that the USGS makes available to the scientific community. It should not come as a surprise that there was no reference to the enigmatic short EM pulses in the published literature. However, north of Lima, Peru, Prof. Jorge Heraud (collaborating with Prof Freund's team) has been continuously recording unipolar pulses coming from a shallow submarine ridge that is being subducted along with the Nazca Plate underneath the South American continent. Many of these pulses also last for only 150msec, but others can last to up to a second and are followed by reverberations that can last for tens of seconds. Over a 2 year period, Prof Heraud recorded more than 2500 unipolar pulses and determined their points of origin within an accuracy of better than 5 km in the x-y-z directions. On the basis of this record (which, unfortunately, is still unpublished), it has been shown that the unipolar pulses come from the upper Benioff Zone of the downgoing Nazca Plate from the depth range of 25 to 65 km. While it is possible that unipolar pulses may be generated by singular mechanical fracture events in the hypocentral volume, there is another explanation, based on the peroxy defects theory.

Ubiquitous Peroxy Defects

Peroxy defects are characterized by two oxygen anions that have paired up, each with one electron less than the common 2–valence state: the peroxy bond is formed by two O^- substituting for O^{2-}. The left of Figure 1 depicts a regular $O_3Si-O-SiO_3$, representative of nearly all bonds in silicate minerals. The right of Figure 1 depicts an $O_3Si-OO-SiO_3$ peroxy bond. The presence of this seemingly innocuous atomic-scale defect has enormous consequences for processes that are of interest in the context of the GEFS.
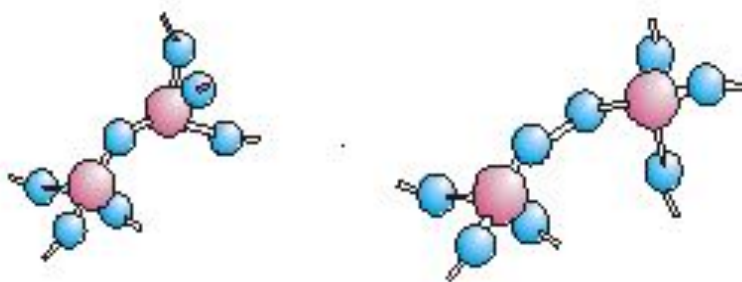
Figure 1: *Schematic representation of a common $O_3Si-O-SiO_3$ bond (left) and a peroxy bond, $O_3Si-OO-SiO_3$, where Si^{4+} may be replaced by Al^{3+} etc. The pink spheres represent the Si^{4+}, while the blue spheres (which are much larger) represent the oxygen positions.*

In peroxy defects, the two O^- are tightly coupled in a very short O^--O- bond, localized and electrically inactive. When peroxy bonds break, two types of electronic charge carriers become activated, electrons and holes, designated e' and h• respectively.
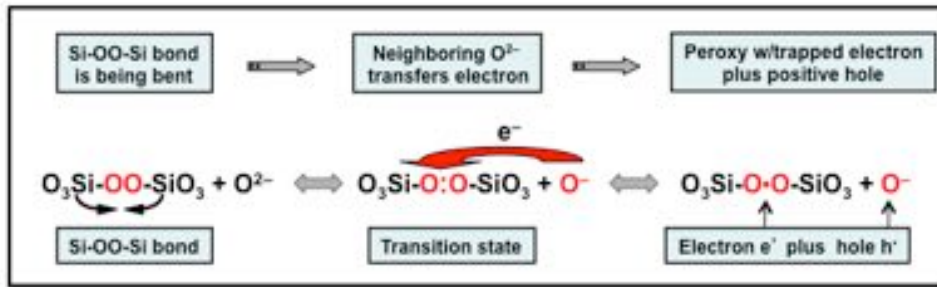
Figure 2: Activation of a peroxy bond in a silicate matrix leading to electron-hole pairs.

Peroxy anions, O_2^{2-}, thus consist of pairs of oxygen anions that have changed their valence from 2– to 1–. In semiconductor parlance, an O^- in a matrix of O^{2-} represents a defect electron or "hole". Thus, a peroxy defect represents a self-trapped hole pair in the oxygen anion sublattice. In its intact state, it is a point defect with a very short $O^- - O^-$ bond distance, less than 1.5 Å as compared to the regular $O^{2-} - O^{2-}$ bond distance in MgO of 3.0 Å. Thus, the volume occupied by the two O^- in the peroxy bond is roughly the same as the volume of a single O^{2-}. In other words, the partial molar volume of one O^- in the peroxy bond is about ½ the partial molar volume of O^{2-}. This very large difference in partial molar volumes is important in the discussion of the generation of unipolar pulses.

Break-up of Peroxy Defects

The basic processes linked to the thermal break-up of peroxy defects have been unraveled by studying a simpler system, MgO single crystals of the highest nominal purity grade, 99.99%, equivalent to <10 ppm total cationic impurities, but containing 500-1000 ppm peroxy defects. In MgO, the peroxy defects exist in the form of peroxy anions, O_2^{2-}. Even at such low concentration levels, the activation of the peroxy defects expresses itself in distinct changes in thermal expansion, magnetic susceptibility and dielectric polarization.

Figure 3 illustrates the 2-stage break-up of peroxy in MgO, accompanied by significant delocalization of the wave functions associated with the decoupling hole states. When hole states delocalize, all O^{2-} within the delocalization volume experience a slight decrease in their effective electron density. This decreases the Coulomb interaction between O^{2-} and Mg^{2+}. Since the Coulomb interaction contributes significantly to the lattice energy, an increase in the $Mg^{2+} - O^{2-}$ distances will cause a large increase in the thermal expansion coefficient.
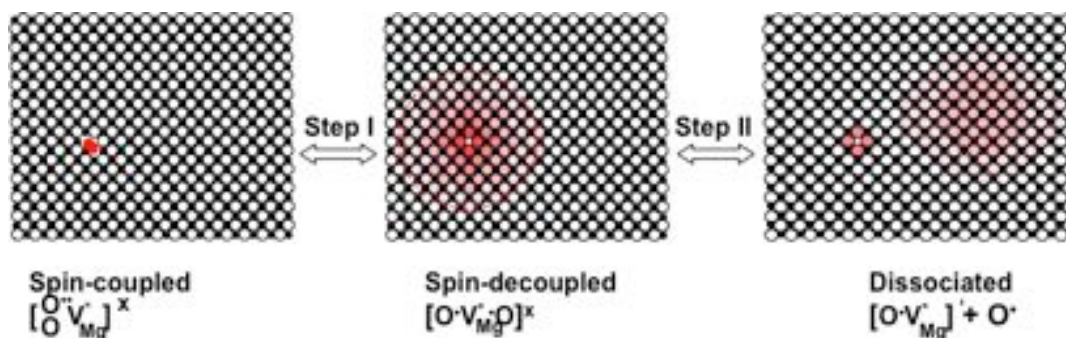

Figure 3: Break-up of peroxy defect in the (100) plane of MgO (left); partly broken peroxy bond by decoupling of the hole spins (center); dissociated state and generation of a trapped hole at the Mg^{2+} vacancy site plus a mobile positive hole charge carrier (right).

Figure 3 illustrates the 2-stage break-up. The left panel shows the tightly coupled holes in the peroxy defect. The middle panel shows the decoupled peroxy bond, characterized by the two hole states still bonded to the Mg^{2+} vacancy site. The right panel shows the transition to the fully dissociated state with one hole remaining at the Mg^{2+} cation site and the other hole turning into a mobile h• charge carrier. This latter step is accompanied by a decrease of the thermal expansion coefficient. The red lines are intended to aid

the eye.
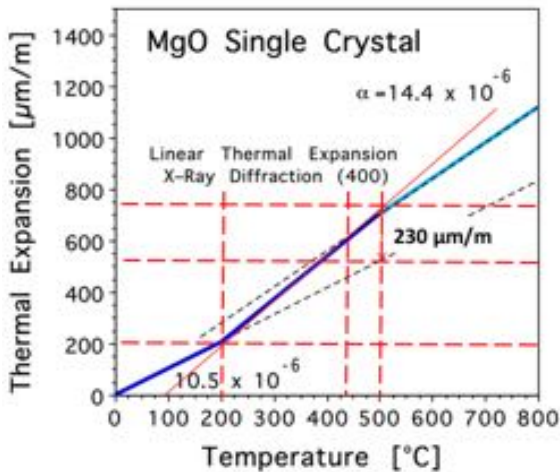
Figure 4a: Thermal expansion of nominally 99.99% pure single crystal MgO up to 800°C, using the fourth order of the (100) x-ray diffraction line.
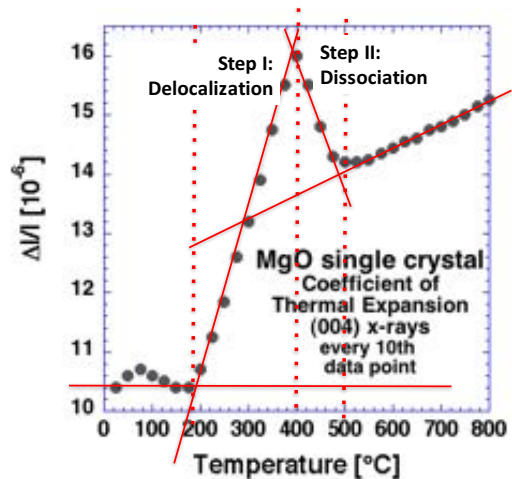
Figure 4b: Thermal expansion coefficient of nominally 99.99% pure single crystal MgO up to 800°C, plotting every 10th data point.

Figure 4a shows a precision thermal expansion measurement of single crystal MgO up to 800°C, using the fourth order of the (100) x-ray diffraction. The bold blue line marks the experimental data as obtained, plotting every data point, illustrating the accuracy of the experiment. Figure 4b shows the thermal expansion coefficient derived from the same data set, where l is the interplanar spacing derived from the 004 Bragg x-ray reflection. Every tenth data point was used to generate this plot. Except for an uneven response at low temperatures, due to chemisorbed water, the noteworthy features are:

(1) abrupt change in $\Delta l/l$ starting at 180°C, indicating a volume increase due to the delocalization of the wave functions associated with peroxy defects as they begin to decouple during Step I,

(2) decrease between 430°C and 500°C, indicating a relative contraction as the peroxy defects split off positive holes during Step II turning into the state depicted on the right of Figure 3, and

(3) resumption of a slightly increasing thermal expansion coefficient above 500°C.

Outburst of Positive Hole Charge Carriers

A key element of the situation depicted in Figures 4a,b is that the temperature-driven volume expansion reaches a critical point. In short, as long as the delocalization of the electronic wavefunctions associated with the decoupling of the peroxy defects increases, the volume will increase. However, in the moment the peroxy defects break-up and release h$^\bullet$ charge carriers, the volume ratchets back. This instability probably holds the key to understand unipolar pulses. All we need to do is to transform this reaction sequence from the Temperature–Pressure (P-T) plane into the Pressure–Volume (P-V) plane. The local temperature does not change. We can assume that, deep in the Earth, the peroxy break-up occurs isothermally at the high confining pressure due to the overload of many kilometers of rocks.
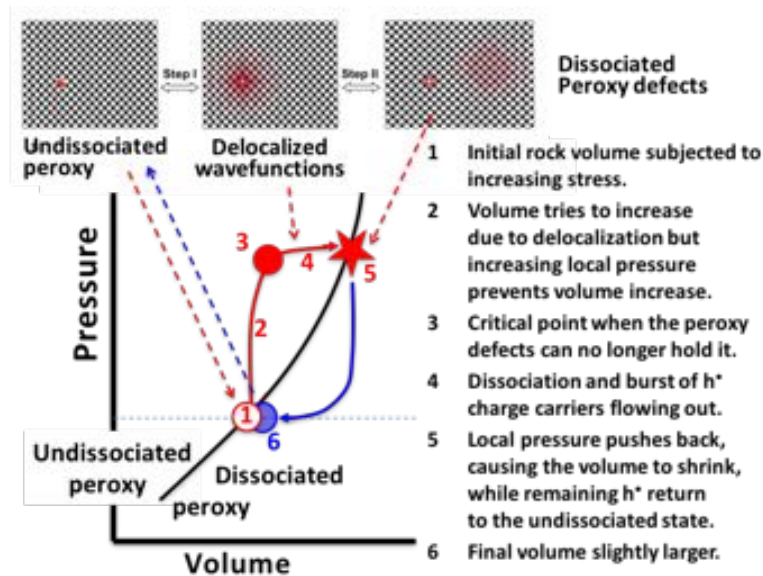
Figure 5: *Projection of the break-up of peroxy defects onto the P–V plane. The black solid line marks the phase boundary between the fully undissociated and the fully dissociated peroxy states. 1–3 mark the pressure change due to the volume increase during the delocalization of the peroxy wave functions; 4-6 mark the volume instability during the break up (ratchet) of peroxy bonds and outburst of positive holes.*

If the peroxy dissociation is driven by stresses that increase with time, the rock volume must increase as indicated in Figure 4a, due to the delocalization of the wave functions during Step I. Such a volume increase will be counteracted by an increase in the local confining pressure along the line 2 in Figure 5. Such a pressure increase will push the peroxy defects back towards the non-decoupled state. However, if the stresses continue to increase and peroxy defects continue to be challenged to break up, point 3 will eventually be reached. At that moment, the system becomes unstable. It ratchets through point 5, hence through Step II, causing a volume oscillation and a sudden outburst of positive holes. This positive hole outburst would be expected to cause a unipolar EM pulse. Thereafter, the system will return to point 6 near the phase boundary line.

Conclusion

In summary, we can say with a relatively high degree of confidence that we have made significant progress towards understanding the nature of the unipolar pulses. Since the unipolar pulses are one of the remaining major mysteries of pre-earthquake emissions, gaining insight into the mechanism by which they are generated will help to bring the GEFS forward.

12 - Building a community

One of the main goals of the GEFS is also to build a strong international community in order to quickly converge to a set of promising prediction techniques allowing efficient short-term earthquake prediction. As already pointed in other sections of this report, we already acquired some large size datasets and began to process them using a wealth of different techniques. For instance, we are tightly collaborating with the National Central University of Taiwan, but are also in close contact with people at CNES who provided us the DEMETER datasets. A new collaboration is also starting with the Department of Civil Engineering, Environmental Engineering and Architecture (DICAAR), University of Cagliari, Cagliari, Italy, who specialized in TIR anomalies measured by satellite (contact: Luca Piroddi). They agreed to provide their share of data and processing tools to our platform. A formal agreement procedure is on the way.

On another front, we have also convinced the editor board at the European Physics Journal (published by Springer Verlag) to release a special volume dealing with non-seismic precursors to earthquakes within their 'Discussion and debate' series. This volume will open with a review paper that we attach to this report (see Annex F), which presents in a pedagogical way the theory of peroxy defects and its potential to explain the various earthquake precursors signatures, as well as a critical analysis of previous statistical studies of data in this field. Indeed, if many of the works we are aware of have presented quite interesting results, they certainly lacked the needed rigor for hypothesis testing. We thus sent this review paper to all authors that we invited to contribute to this special issue (20 authors and groups in all), in order to define a common and proper way of testing their results. In return, this will help to strengthen significantly the overall quality of this volume which would both motivate new teams to join us with their tools, theories and data. The publication of this EPJ volume is planned for Winter 2018.

We also established a very encouraging contact with researchers of the Swiss Data Science Center in Zürich (https://datascience.ch/) with whom we have defined and written a preliminary research proposal draft. We expect that such a collaboration would allow us to benefit from more computing resources as well as from their strong expertise in pattern recognition techniques and large database management. In particular, our goal is to develop with them a generalized machine learning approach (mainly based on neural networks) in order to correlate the signals of our database with earthquake activity. Conditional of funding, our common next step is now to recruit at least two PostDoc level researchers to build an effective bridge between our institutions.

Also, in order to facilitate and simplify a collaborative workflow, we are continuing the development of a software platform called xYotta (https://xyotta.com). The main aim is to provide a unified service infrastructure that introduces a common modern authentication/authorization mechanisms via JSON Web Tokens/LDAP, simultaneous real-time content editing by multiple users and communication capabilities between members of different projects.

Future integration of available GEFS datasets with multiple modules of the xYotta scientific toolbox was taken into account since early stages of design and development of the platform. IW tools for online data analysis and visualization can be programmed in such popular languages for data processing as R and Python and later be deployed on multiple computing nodes. To guarantee an accessibility of the service during peak loads, all web services are designed with a horizontal scalability in mind, i.e. hosting of InnovWiki micro-services is Docker-based and can be easily expanded through simple increase of available containers when needs arise. Additional features as plagiarism detection functionality and notification subsystem are present as well.

ANNEXES A TO F

Annex A:
Comparison of general transient signals detectors.

*(Yaver Kamer, Guy Ouillon, Didier Sornette)*

Introduction

The search for a precursory earthquake signal is a challenging task. The challenge manifests itself in two different ways: (i) reports of such signals are not ubiquitous, and the reported signals are not consistent in their amplitude, direction and time-space proximity to future events; (ii) due to the infrequency of large events, testing and establishing the statistical significance of such signals becomes difficult. Any practical application aimed at establishing the existence (or lack thereof) of precursory earthquake phenomena requires addressing these two main challenges.

In this study, we propose a time-series detection method that addresses the problem of 'unknown' signal. The method relies on designating a portion of the time-series as noise, rather than formulating the signal properties, which can be elusive. The signal is then extracted as segments of the dataset that are significantly different from the noise. To address the second challenge of testing the detection method on a set of scarce target events, we conduct an analogous experiment that allows us to record data of multiple target events as well as a well-defined background noise. The experiment is based on recording electromagnetic field amplitudes in the vicinity of a tramway station. The target events are defined as tram arrival/departures during which the current in the power lines is expected to induce detectable changes of the magnetic field.

The paper is organized as follows. We fist present the electromagnetic tram data collection procedure and explain its technical implementation. We then introduce the non-parametric data driven signal detection method and demonstrate its performance on a synthetic dataset. We then apply the method to the tram dataset and evaluate the detection performance using the well-known Molchan diagram approach. Finally, we summarize our findings and discuss the presented methodology's applicability to detecting precursory electromagnetic phenomena in earthquake forecasting.

Magnetic field recording at a tram station

For this experiment, we recorded the daily magnetic field variations at a tram stop. The measurements are conducted using a Bosch BNO055 magnetometer sensor that has a range of ±1300µT with a resolution of ~0.3µT. The data acquisition is done by a Arduino Uno processor that continuously polls the sensor and records measured data onto an SD card at a sampling rate of 20Hz. The sensor's location and axes orientations with respect to the tram tracks and the overhanging power lines are indicated in Figure 1.
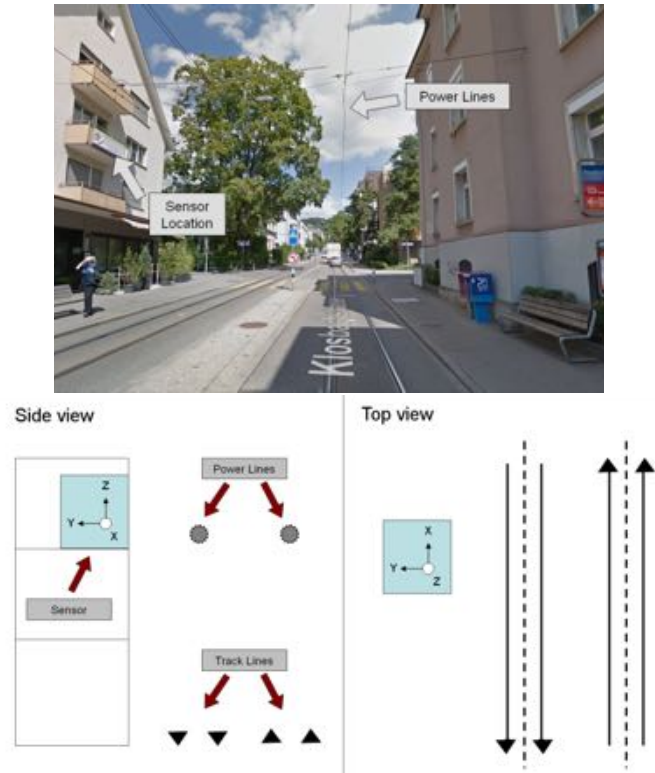
Figure 1. *Top: Google Street View of the tram stop and sensor location. Bottom: Side and top view schematics showing the power-lines and the tram tracks in relation to the sensor axes.*

The data record obtained from 04:50 AM 28.06.2016 to 04:50 AM 29.06.2016 is shown in Figure 2. Preliminary inspection of these records indicates that the tram traffic, which starts at 5 am and lasts till 1 am, seems to affect the measurements on *y* and *z* axis. This stems from the fact that the current flowing through the power lines induces an electromagnetic field that is perpendicular to the flowing direction.
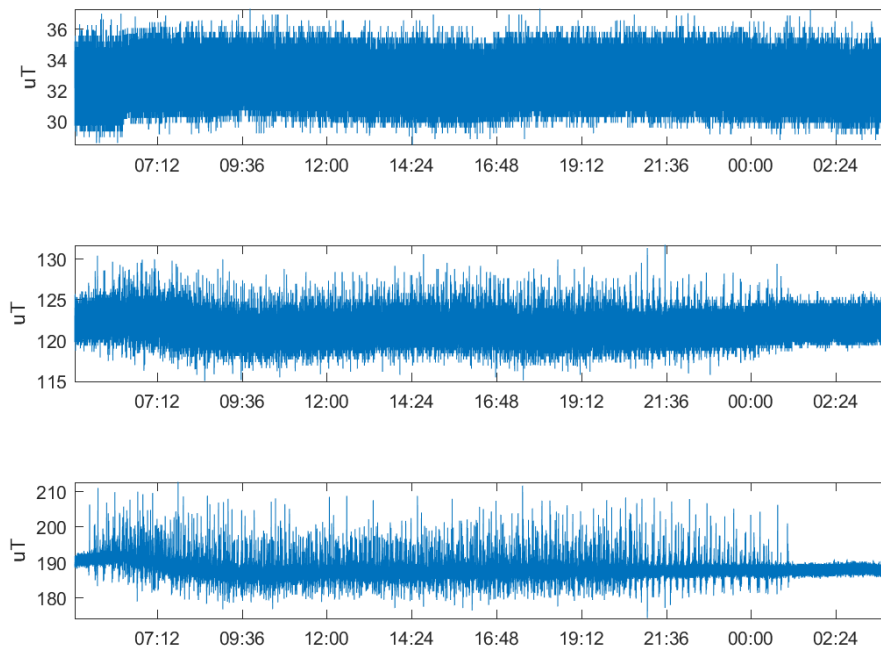
Figure 2. *Magnetic field amplitudes recorded 04:50 AM 28.06.2016 to 04:50 AM 29.06.2016. The panels show the x, y and z axis in the top-bottom order.*

In order to establish a useful benchmark dataset, the recorded electromagnetic data needs to be matched

38

with the actual tram traffic. One possible way is to use the published tram times for the given station, but to achieve the highest accuracy we opted for installing a camera that takes pictures at a 5 seconds interval. The camera footage was then synchronized with the sensor recordings. Figure 3 show a sample frame of the synchronized video.

Figure 3. Left: Footage of the actual tram traffic. Right: The recorded magnetic field amplitude at x, y and z axes for two moving average windows of 1 and 5 seconds.

By manually going through all the photos and labeling each tram arrival, we were able to extract accurate tram times to match the electromagnetic recordings. The tram direction affects the current flow direction which in turn affects the induced electromagnetic field. Thus it is important to classify the trams according to their direction as well. A sample of the obtained tram times dataset is given in Figure 4.
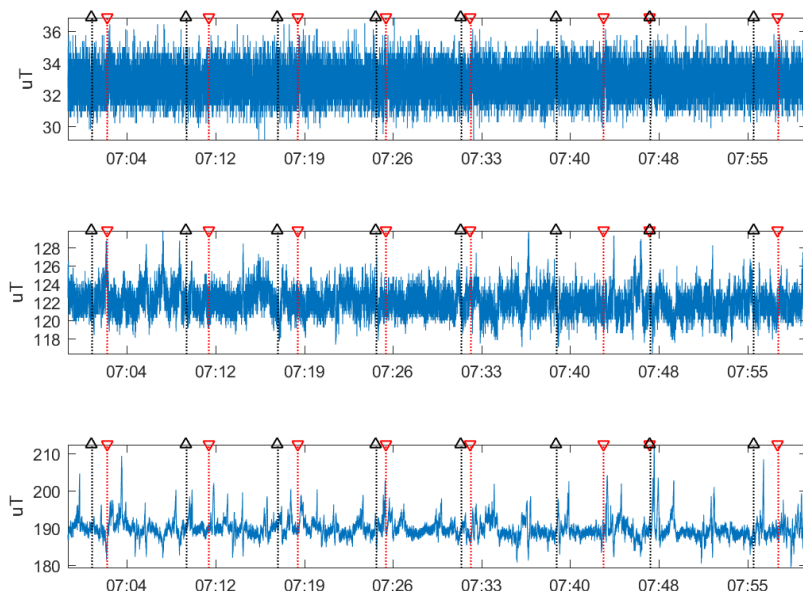
Figure 4. Magnetic field data on x, y and z axes for the time interval from 8AM to 9AM overlaid with tram arrival times shown as triangles. Black: positive x-axis direction, red: negative x-axis direction.

A generic signal/anomaly detection method

Having established the magnetic field recording database and the corresponding tram arrival times allows us to define the signal detection problem as follows: the goal is to detect a tram arrival event solely based on the measured magnetic field data. The signal detection algorithm should analyze this data and designate

a time interval in which a tram arrival is most likely to have occurred. This concept can be generalized not only to the detection of earthquake precursors, but also to any kind of process that requires analyzing continuous time-series data as input to evidence the time interval of occurrence of discrete events.

The method is based on splitting the time-series signal into multiple segments and performing pair-wise comparisons using non-parametric hypothesis tests. Rather than relying on the properties of the signal, which can be elusive, the method relies on designating a portion of the time-series data as noise. This noise dataset is then used to construct an expected distribution of the pair-wise similarity metrics that serves as a benchmark for detecting significantly different segments in the remaining part of the dataset. The segments that are the most dissimilar to noise are singled out as anomalies/signals.

The method algorithm is given below:

1) The whole dataset is divided into two classes: noise and signal. This distinction can be done on prior information about the signal generating process. For instance, for the tram application, the interval for noise can be selected as the night time during which trams are not operating. For earthquake precursors, data recorded in aseismic regions can similarly be labeled as noise. The signal label designates the portion of the dataset where signals might be present.

2) For a given time scale, we divide the noise amplitude time-series $a(t)$ into n segments $a_i(t)$, $a_j(t)$… $a_n(t)$, each containing equal numbers of samples.

3) For all (i,j) pairs, where $i>j$ and $i\neq j$, calculate and record the 'distance' S_{ij} between amplitude distributions of a_i and a_j. S_{ij} can be any symmetric measure that quantifies how similar the two amplitude distributions are (e.g Kolmogorov-Smirnoff, Cramer von Mises criteria, cross-correlation coefficient...). The distribution of all inter-pair distances $n(S)$ serves as a null-distribution that characterizes the statistical incoherence of the noise.

4) Repeat steps 2) and 3) for the signal dataset, which contains noise and anomalies to detect.

5) Assess the similarity between each (i,k) signal segment pair with respect to the null-distribution $n(S)$. The two segments are considered to come from the same distribution if $S_{ik}<max(n(S))$. In other words the two signal segments are considered to come from the same parent distribution if their similarity distance measure is smaller than the largest similarity distance measure observed in the noise segment pairs.

6) Segments satisfying the $S_{ik}<max(n(S))$ condition are iteratively joined (agglomerated) into bigger segments.

7) Each signal segment receives a signal-to-noise ratio (SNR) score which is estimated as $1/N$, where N is the number of units size segments contained in each agglomerated segment. Thus, large segments get a low SNR score and small segments that less merge with others get high a SNR score. The idea is that large clusters of segments define the noise part. Small clusters define anomalies.

Application to a synthetic dataset

To demonstrate the performance of the signal detection method, we apply it on a 5-hour long synthetic time-series dataset sampled at 10Hz. The dataset consists of the addition of noise and anomaly components given in Table 1. The resulting time-series is plotted in Figure 5.

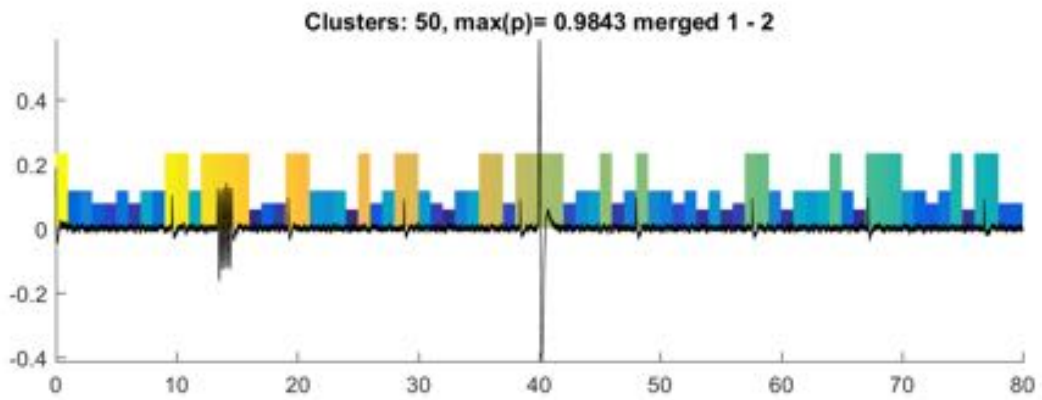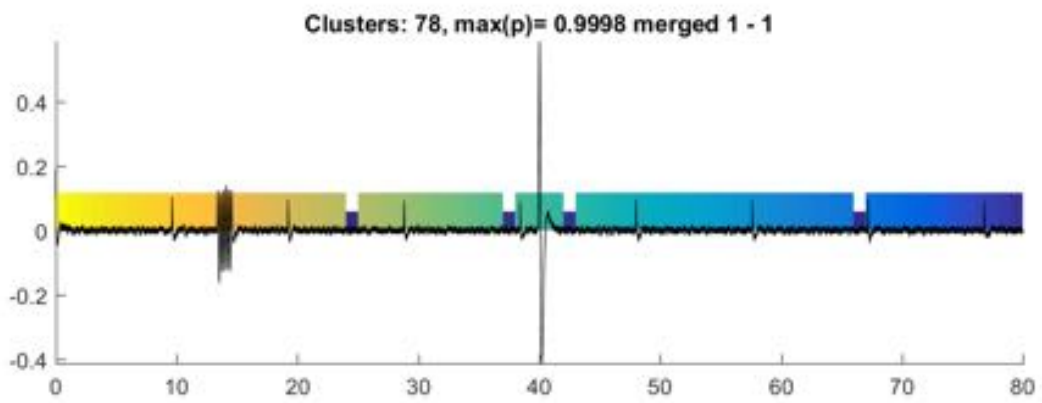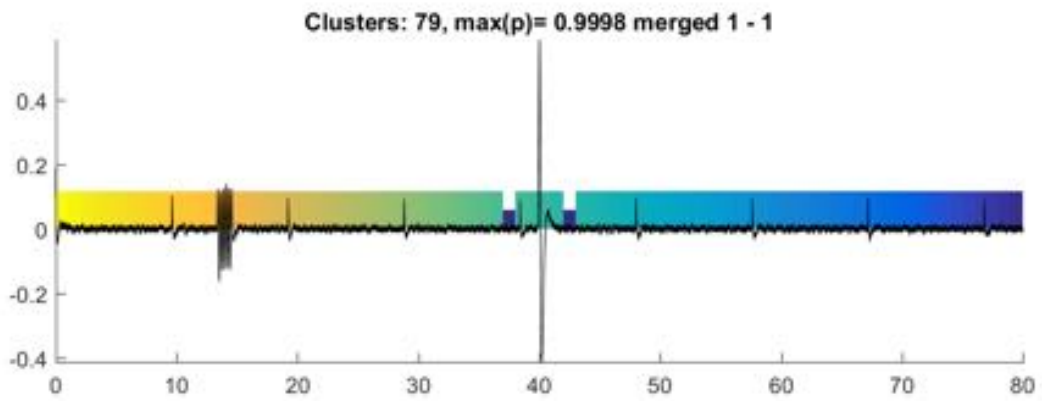| Noise			Anomalies			
Sinusoidal			Sinusoidal			
Period	*Amplitude*	*t-range*	*Period*	*Amplitude*	*t-range*	*Repeat*
0.5 s	0.1	5 hours	25 s	0.2	5 min	once @0:50
2.0 s	0.1	5 hours	Gaussian kernel			
Uniform White Noise				1.0	10 sec	once @2:30
	0.3	5 hours		0.5	1 sec	every 36 min

Table 1: *characteristics of the noise and signal anomalies for the synthetic example.*
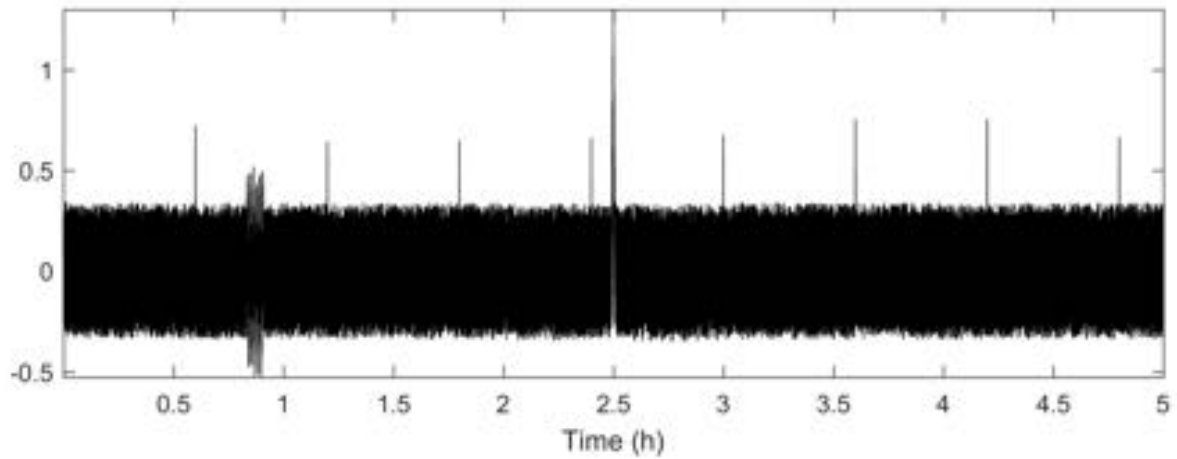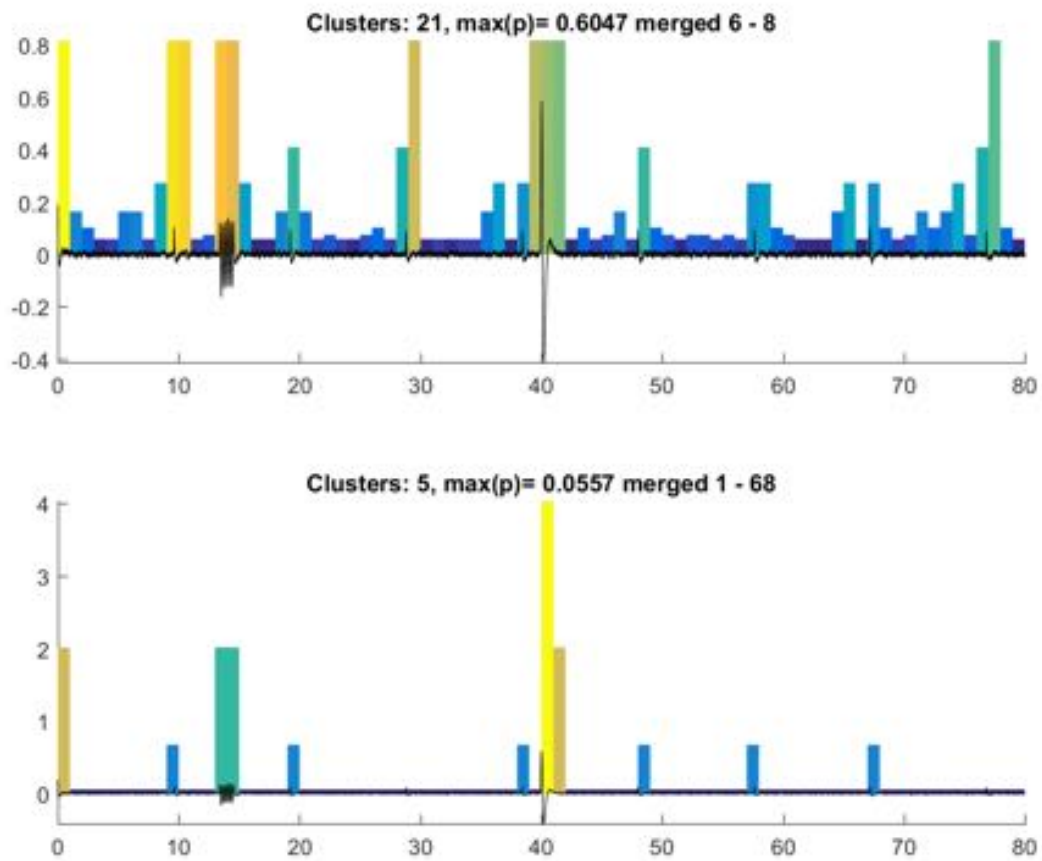
Figure 5. Synthetic amplitude time series created by adding the sinusoidal and Gaussian components given in Table 1.

The original time-series is band-pass filtered with filter periods varying from 0.1 to 0.8 seconds and each trace was divided into 80 segments of 225 seconds long each. For this test, we use the Kolmogorov-Smirnoff (KS) distance, which is the maximum difference in the cumulative probability functions of the two distributions, as a similarity measure. The results of the iterative merging steps for a band pass filter period of 0.2 second is given in Figure 6.

Clusters: 79, max(p)= 0.9998 merged 1 - 1

Clusters: 78, max(p)= 0.9998 merged 1 - 1

Clusters: 50, max(p)= 0.9843 merged 1 - 2

Figure 6*. Synthetic signal overlaid with colored regions depicting individual segments. The height of the segments is proportional to their SNR score. Segments are iteratively merged together depending on the similarity of their statistical similarity.*

The synthetic dataset test allows us to make the following observations:

(i) the method is able to classify the input trace into noise and various types of anomalies: the 5 minutes long sinusoidal signal at 0:50 is detected as a single anomaly. The 10 seconds long Gaussian at 2:30 is detected as two separate anomalies due to the band pass filter response that protracts the signal duration. Six out of the eight 1 second long Gaussian signals are detected and correctly classified as being of the same type.

(ii) the method fails to identify some of the anomalies, such as the two missed signals at segments 28 and 77. These missed detections can be attributed to those signals being individually splitted into distinct segments and hence failing to match the statistical properties of the rest of similar signals. To counter this effect, in the real dataset application we perform several runs where we offset the input data with different time lengths so as to explore all possible segmentations.

(iii) the method makes a false detection at the beginning of the input signal. This is due to the band-pass filter response, which is initially at zero and outputs a transient signal which duration is proportional to the band-pass filter period. To counter this effect in the tram application, we ignore the initial segments that fall within this transient duration.

Application to the tram dataset

Before applying the proposed method to the tram dataset, we made preliminary analyses to determine which of the 3 axes had the greatest potential for the application. Contrarily to our expectations, the data recorded on y and z axes, which are perpendicular to the current flow, perform very poorly. This is likely the result of currents in the power lines not being exclusively associated with the tram we aim to detect, i.e. currents drawn by other nearby trams are also flowing through the same wires. Our initial investigation suggested that the data recorded on the x-axis is the most promising one, possibly being insensitive to the main current flows increases its sensitivity to secondary effects caused by the trams' electrical engines. We also realized that the coherence between the electromagnetic field signal and the tram arrivals was limited only to trams traveling in the positive x direction. This is likely due to the uphill slope in this direction, causing the tram to pull more current and hence producing larger electromagnetic interferences. As a result, we have decided to limit our target events only to the arrival times of the trams going in the positive x direction and consider only the x-axis recordings of the magnetometer. The noise portion of the dataset is chosen as the time interval between 2:00-4:00 AM and the signal portion between 6:00-8:00 AM. The method is applied on equally sized segments of 60 seconds, using the KS distance as a similarity measure. The SNR scores are calculated for a total of n_f=10 traces consisting in distinct band-pass filtered signal at periods of 0.05, 0.1, ..., 6.4, 12.8s. The resulting SNR scores are aggregated by weighted averaging where each frequency band's weight is optimized on a training dataset. The averaged so-called characteristic function can then be thresholded to raise constant duration alarms regarding the target events. Figure 7 shows the thresholded characteristic function together with the tram arrival events from 6:00 to 8:00 AM.
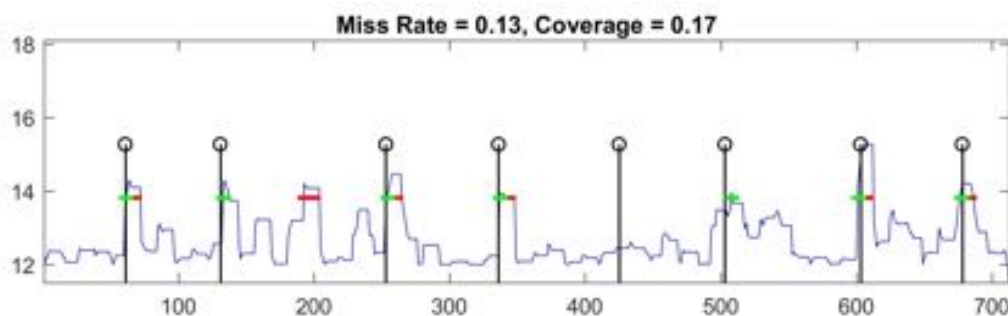
Figure 7. *Characteristic function (blue curve) together with the tram arrival (vertical lines). The horizontal lines represent used the successful (green) and false (red) alarms obtained by thresholding at 13.8.*

Considering that the detection algorithm has a total of n_f -1=9 free parameters, which are the band-pass weights, and only 8 target events, it is difficult to assess the performance of the proposed method. Therefore we consider an independent portion of the dataset from 8:00-9:00 AM, which has not been used neither in the derivation of the null-distribution $n(S)$ nor in the optimization of the band-pass weights. The results obtained for this independent validation set are shown in Figure 8. As expected, we see an increase in the miss rates from 13% in the training dataset to a 25% in the validation set.
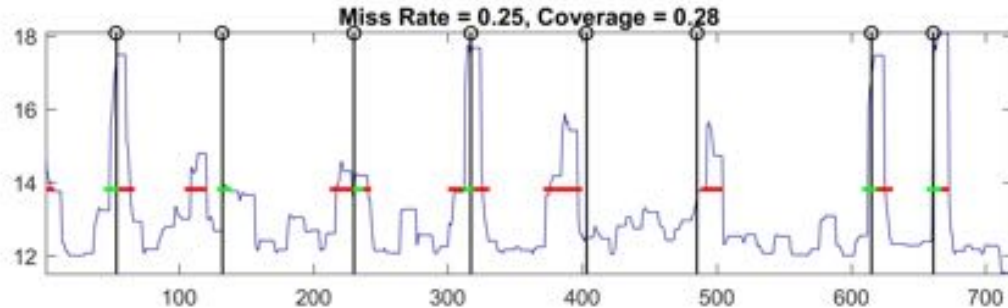
*Figure 8. Same as Figure 7 for the independent validation dataset.*

To objectively asses the detection capabilities of the algorithm, we need to investigate the 'specificity' of the obtained characteristic function. For this purpose, we employ the commonly used technique of Molchan diagrams. By plotting the resulting miss rate versus the ratio of the time domain covered by alarms estimated for different thresholds, as well as individual alarm duration, one is able to visualize the performance of a given detection algorithm. The Molchan diagram for the validation dataset is given in Figure 9.

The origin point of the diagram (zero coverage and zero miss rate) represents the perfect prediction while the diagonal line represents the random guess performance. Thus, given that the area under the Molchan curve (0.167) is significantly smaller than 0.5, we are able to safely conclude that the proposed method is likely to have potential in detection applications. Due to its non-parametric, data-driven formulation, and only requiring the labeling of the noise portion of the data, we are hopeful that the method will provide added value in the search for earthquake precursors in various datasets.
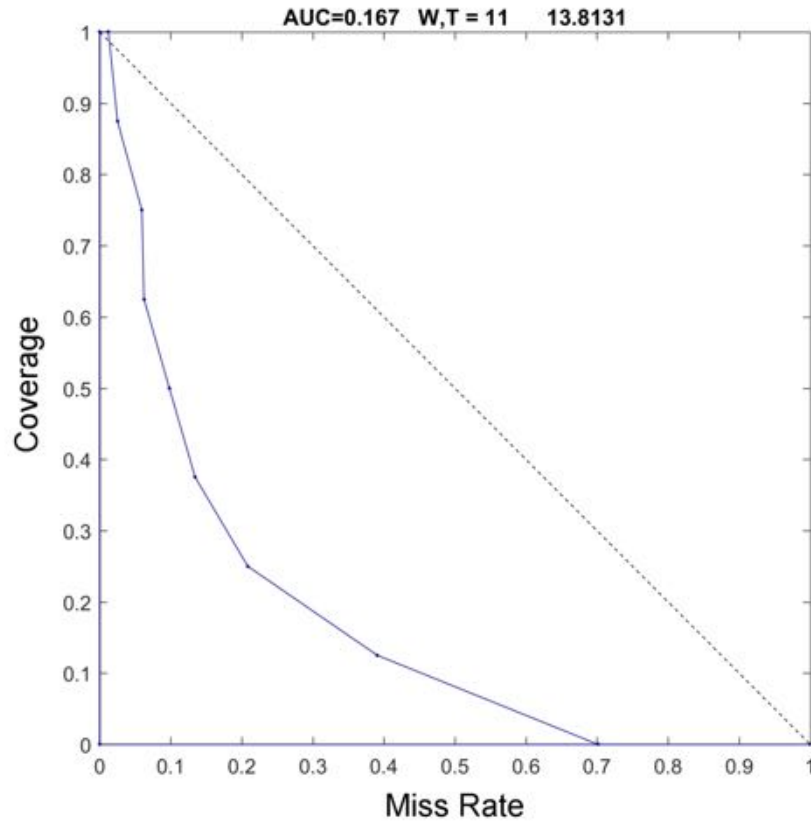
Figure 9.Molchan diagram for the validation dataset obtained by varying the alarm threshold and duration parameters.

In order to perform a more insightful test, we considered the training signal dataset to be within 6:00-8:00 AM and the validation set to be within 8:00 AM - 8:00 PM. Figure 10 shows the autocorrelation of the signal over the 3 axes.
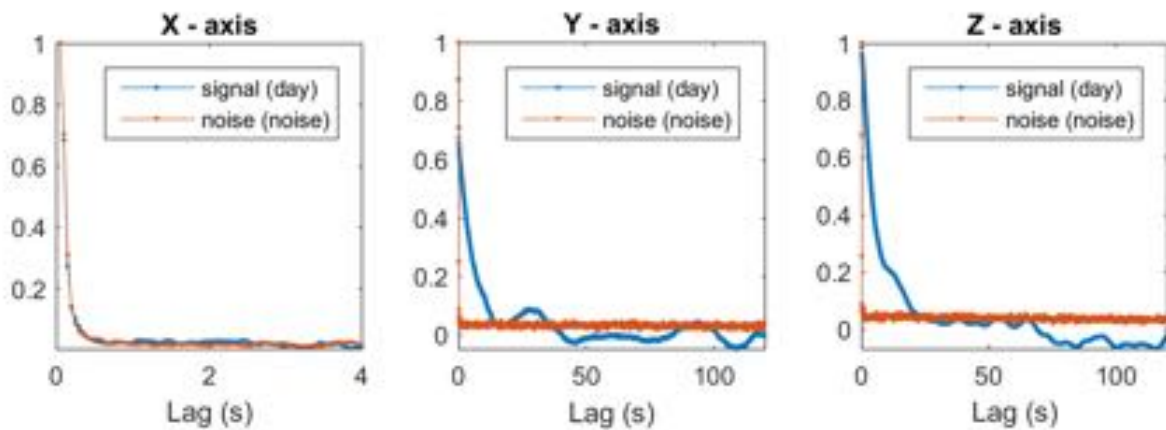
Figure 10: *autocorrelation of the signal and noise on the 3 axes.*

The signals being obviously correlated, we compute Molchan diagrams by repeating our analyses using the original signals, as well as decimated versions of it (one of two samples, one out of four samples). The results are presented on Figure 11. Each plot represents the Molchan diagram obtained on a different axis (x, y or z) using a different similarity metrics (Kolmogorov-Smirnoff, Cramer von Mises criteria, cross-correlation coefficient). The last columns stands for a similar analysis using an optimized STA/LTA algorithm (Lomax et al., 2012). The latter consists in filtering the original signal into different frequency bands, performing an STA/LTA ratio on each band and weighting optimally the responses to define a characteristic

46

function which defines the alarms. Each curve color on Figure 11 corresponds to a specific decimation of the original signal. The Molchan diagrams are drawn by varying two parameters. The first one is the threshold at which the detection is triggered, the second one is the duration of the detection window. So, for the same threshold you can have different window lengths and this causes the coverage to vary. The horizontal arrows represent the IQR range of this spread. All curves are computed using the training dataset. On each plot, a single full circle (green, red or black) indicates the performance on the validation dataset.
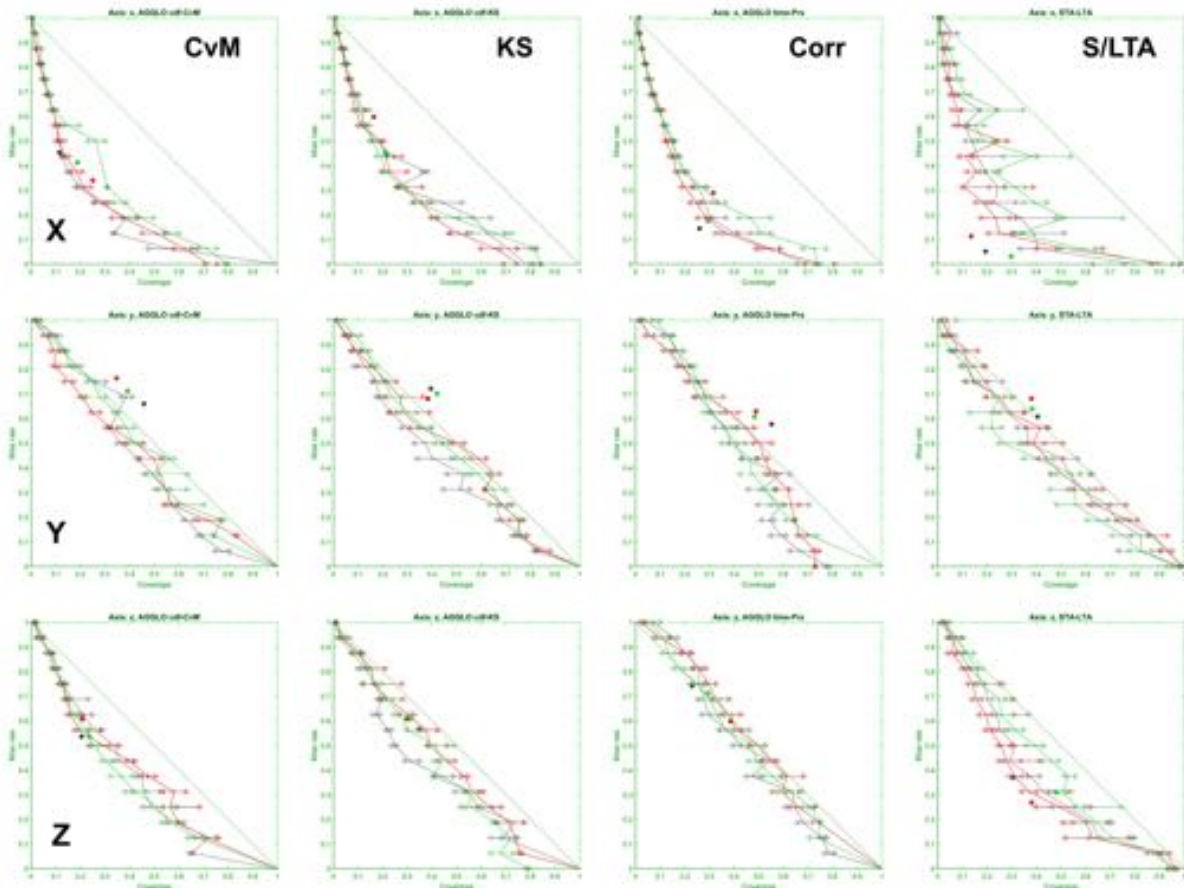
Figure 11: *Molchan diagrams obtained on different axes for different metrics and different decimations of the original signal (green: no decimation; black: 1 sample out of 2; red: 1 sample out of 4).*

The results confirm that the x axis contains more information about trams arrivals/departures than the z (second best) and y (worst) axes. Subsampling the signal also improves the performance as we get rid of correlations, suggesting that we subsample the signals at a rate equal to the correlation length. Anyway, it seems that our general method does not improve on an optimized STA/LTA technique, especially when considering the results obtained on the validation dataset. This suggests the use of the latter when analyzing natural datasets.

Lomax, A., C. Satriano and M. Vassallo (2012), Automatic picker developments and optimization: FilterPicker - a robust, broadband picker for real-time seismic monitoring and earthquake early-warning, Seism. Res. Lett. , 83, 531-540, doi: 10.1785/gssrl.83.3.531.

Analysis of precursory signals on Demeter VLF data conditioned on M>5 earthquakes.

(Yaver Kamer, Guy Ouillon, Didier Sornette)

The data used in this analysis is the VLF magnetic power amplitude spectrum data recorded by the DEMETER satellite. The spectrum frequency (0-10Khz) is divided and aggregated into 16 frequency bands plus one band for the total power amplitude and one band for the range 1.6-1.8Khz (which according to some authors is the most sensitive frequency band). The satellite takes continuous measurements as it flies along its orbit. These measurements are geocoded and time-stamped. For the purpose of the following analysis, the Earth is tessellated into equally sized triangular regions with an area of 250,000 km^2. The satellite makes a fly-over above each of these regions approximately every 24 hours. During each fly over, multiple measurements within the region are taken. To decrease the noise, we combine these multiple measurements into a single data point by averaging. This leads to approximately one data point per day for each triangle. This is what is presented on Figure 1.
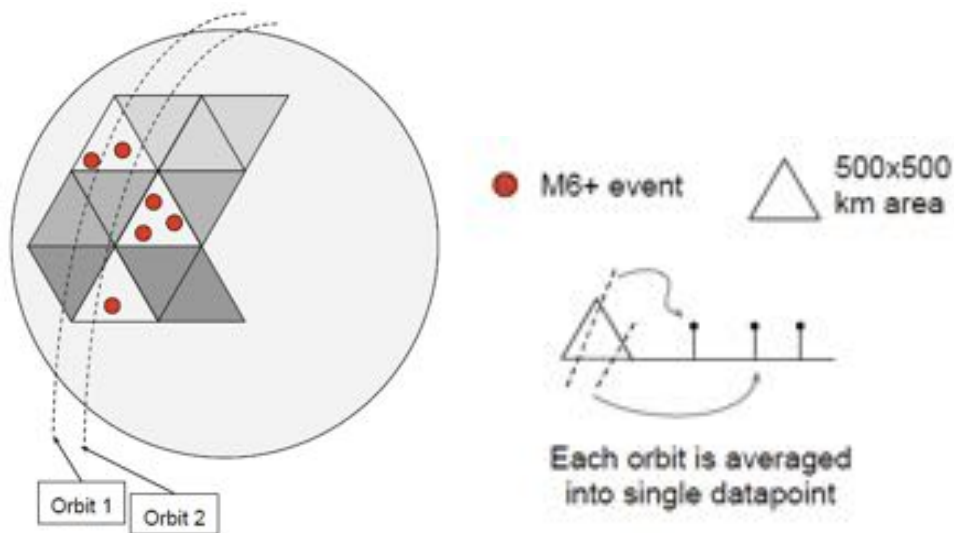
Figure 1: Triangular tessellation of the Earth's surface, with occurring large events (here, larger than M=6, red full circles) and two orbits corresponding to the trajectory of the satellite on the same day. The bottom right sketch shows that all measurement points on the same day over the same triangle are averaged out to get a daily measure.

The goal of the analysis is to establish if there is a significant decrease/increase in the measured VLF magnetic power amplitudes prior to major earthquakes. The analysis is based on stacking the VLF power amplitude time series conditioned on earthquake times. The general method is the following:

(1) We first model the seasonal variation within each triangle by considering only aseismic areas within the same latitude band. The correction for the seasonal variation is estimated as the median of the associated signal within successive time bins.

(2) For each latitude range, we subtract those medians from the signal observed over all corresponding triangles, aseismic or seismic.

(3) We condition all the season corrected aseismic time-series on the local time (0-24h). This allows to compute an hourly aseismic median. This detrending is necessary as the sun activity influences the recorded signal.

(4) The aseismic hourly medians defined above are subtracted to the corresponding values over all aseismic

and seismic triangles.

(5) In a superposed epoch analysis, shifting the times of target events to t=0, we look at the distribution of the corrected signal amplitudes in time bins before and after the events.

This analysis is repeated for the signal filtered in different frequency bands, and for different target magnitudes in the time period 2005-2011: M>6 and M>5, respectively. All the target events occur at a depth<50km. In order to avoid the influence of wild fluctuations during the day, only nighttime data are considered.

Figures 2 to 19 compile the results in the various frequency bands for M>6 events within a time window extending between 4 days before and 4 days after the events (which all occur at t=0). The grey dashes and boxes indicate in each time bin the median corrected amplitude, as well as the associated 25%, 50% and 95% quantiles. We clearly see that there is no observable change in the distribution of the signal amplitudes before or after events, so that no correlation can be evidenced between the VLF electromagnetic radiations and earthquake occurrence.

We extended this analysis by considering all events with magnitude M>5 within a similar depth range. Figures 20 to 37 document the results and confirm the previous conclusions.

Those results, contradicting the claims of previous works previously published by the DEMETER team, indeed confirm more recent results by the same team after re-analyzing the same data in a different way.

Freq. Bnd = f1, Stacked Eqs = 622, Sat.pass/bin = 36
CORR YES Night-Hours Shallow-Depths Time-PrePost MinM-6

Figure 2 (see main text)

Freq. Bnd = f2, Stacked Eqs = 622, Sat.pass/bin = 36
CORR YES Night-Hours Shallow-Depths Time-PrePost MinM-6

Figure 3 (see main text)

Freq. Bnd = f3, Stacked Eqs = 622, Sat.pass/bin = 36
CORR YES Night-Hours Shallow-Depths Time-PrePost MinM-6

Figure 4 (see main text)

Freq. Bnd = f4, Stacked Eqs = 622, Sat.pass/bin = 36
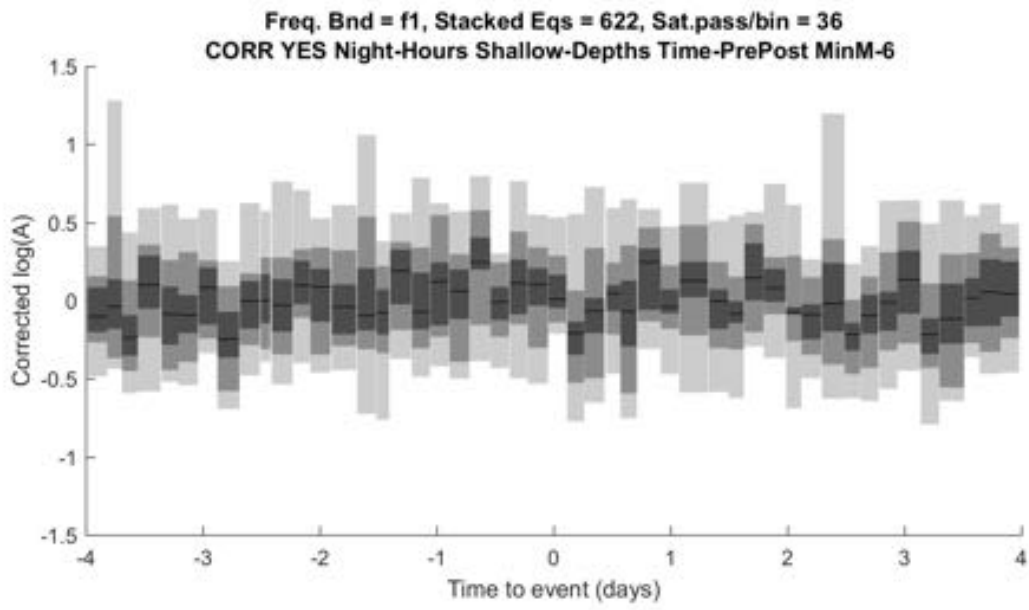CORR YES Night-Hours Shallow-Depths Time-PrePost MinM-6

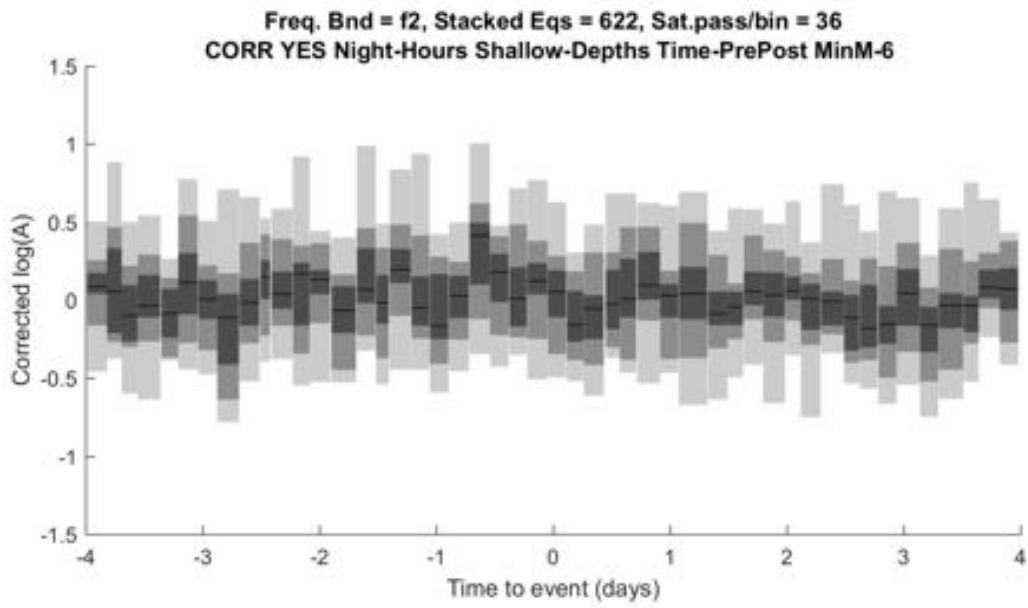Figure 5 (see main text)

Figure 6 (see main text)

Figure 7 (see main text)

Figure 8 (see main text)
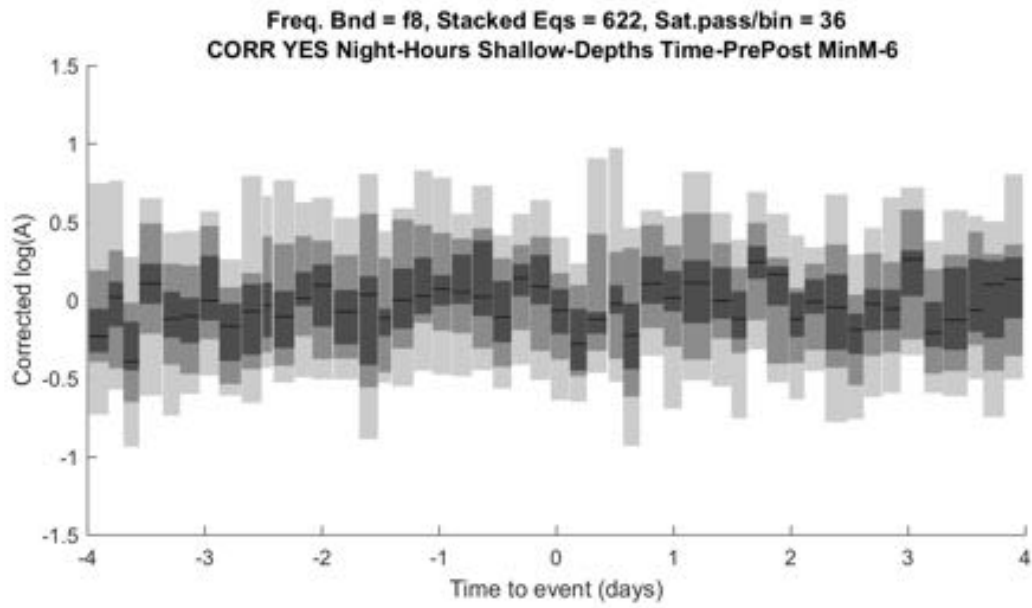
Figure 9 (see main text)
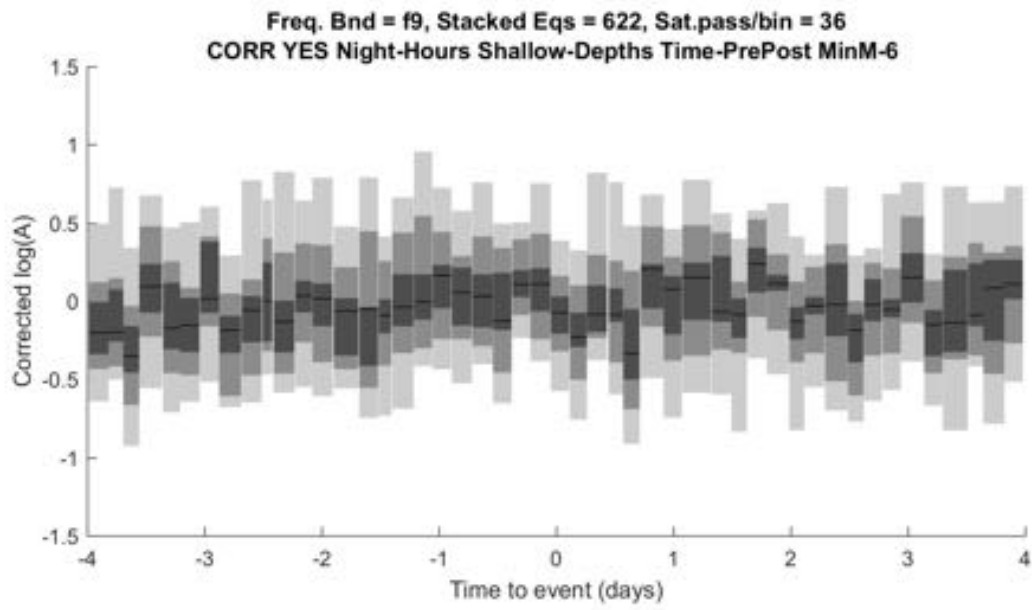
Figure 10 (see main text)
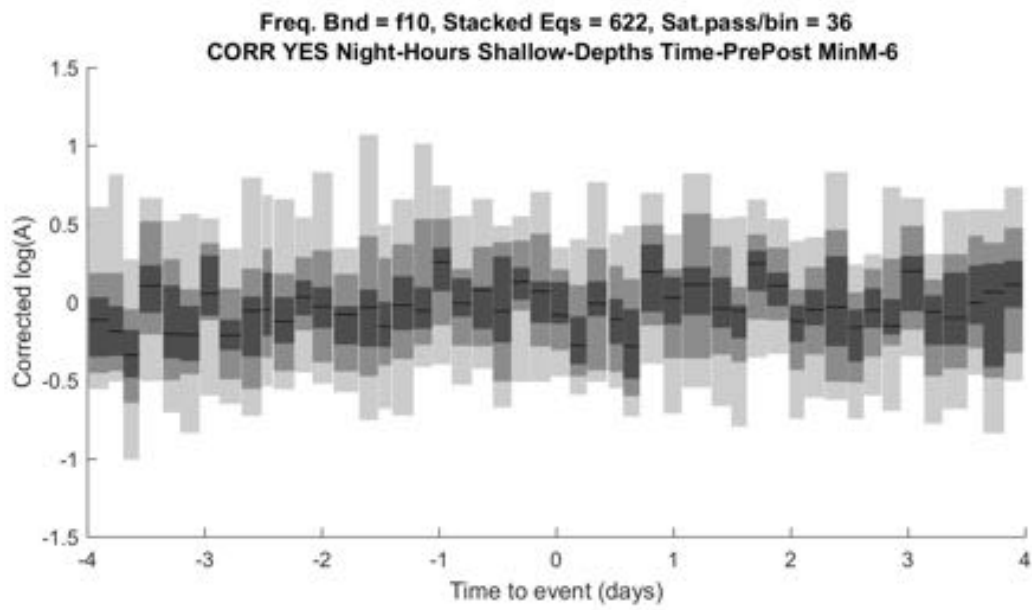
Figure 11 (see main text)

Freq. Bnd = f11, Stacked Eqs = 622, Sat.pass/bin = 36
CORR YES Night-Hours Shallow-Depths Time-PrePost MinM-6

Figure 12 (see main text)

Freq. Bnd = f12, Stacked Eqs = 622, Sat.pass/bin = 36
CORR YES Night-Hours Shallow-Depths Time-PrePost MinM-6

Figure 13 (see main text)

Freq. Bnd = f13, Stacked Eqs = 622, Sat.pass/bin = 36
CORR YES Night-Hours Shallow-Depths Time-PrePost MinM-6

Figure 14 (see main text)

Freq. Bnd = f14, Stacked Eqs = 622, Sat.pass/bin = 36
CORR YES Night-Hours Shallow-Depths Time-PrePost MinM-6
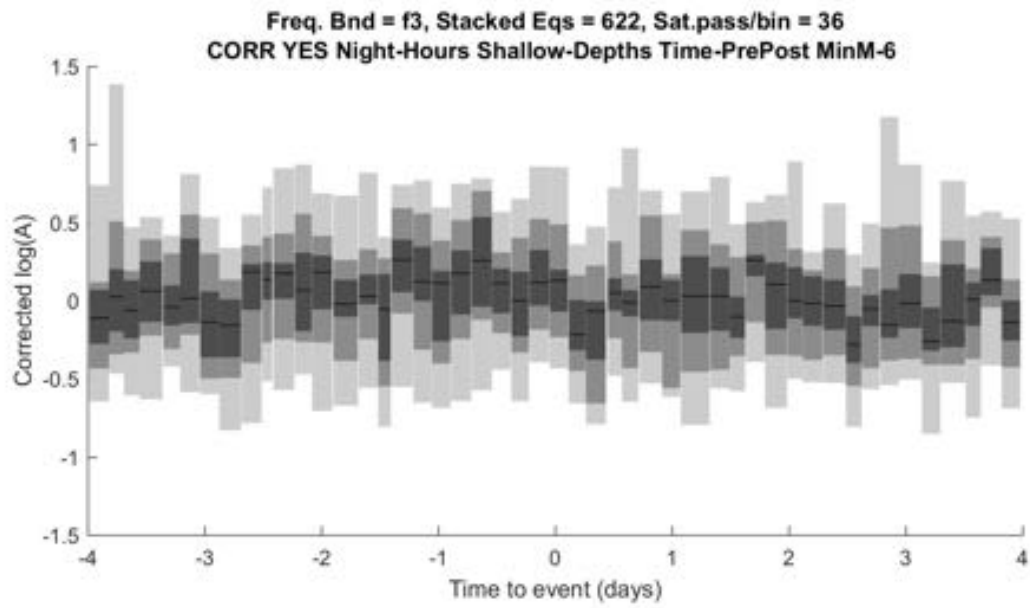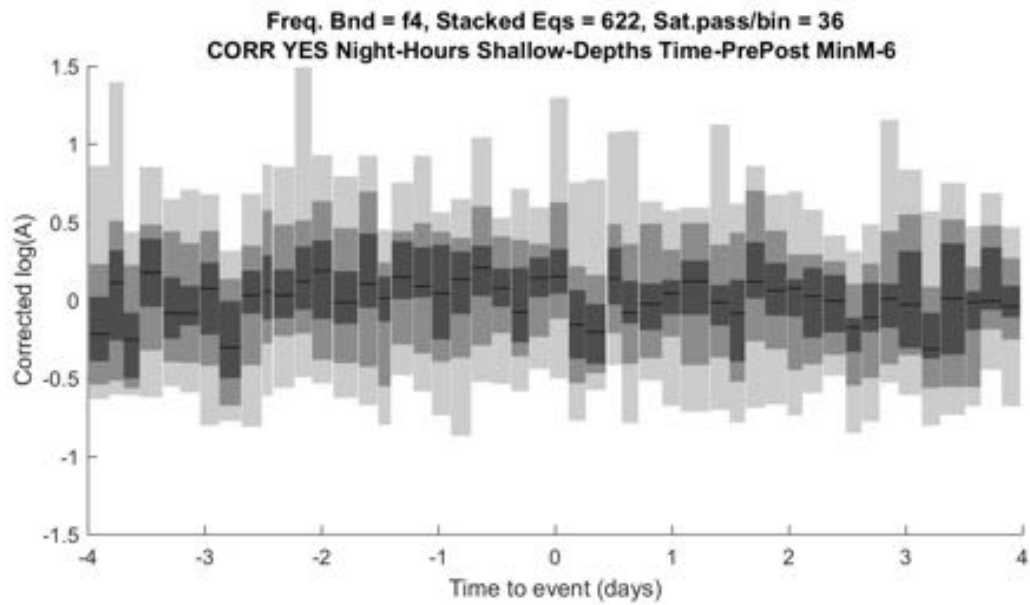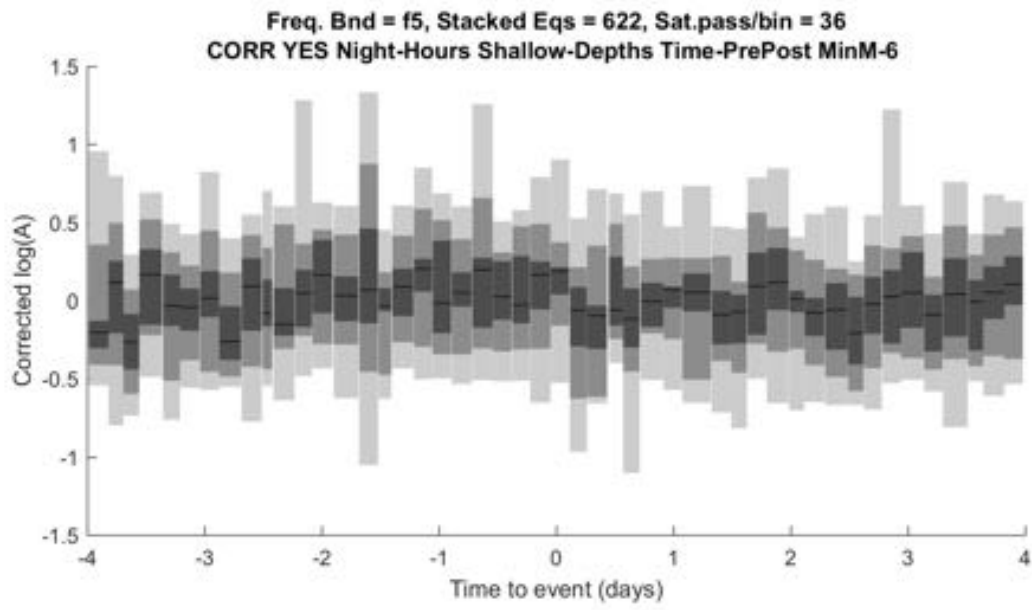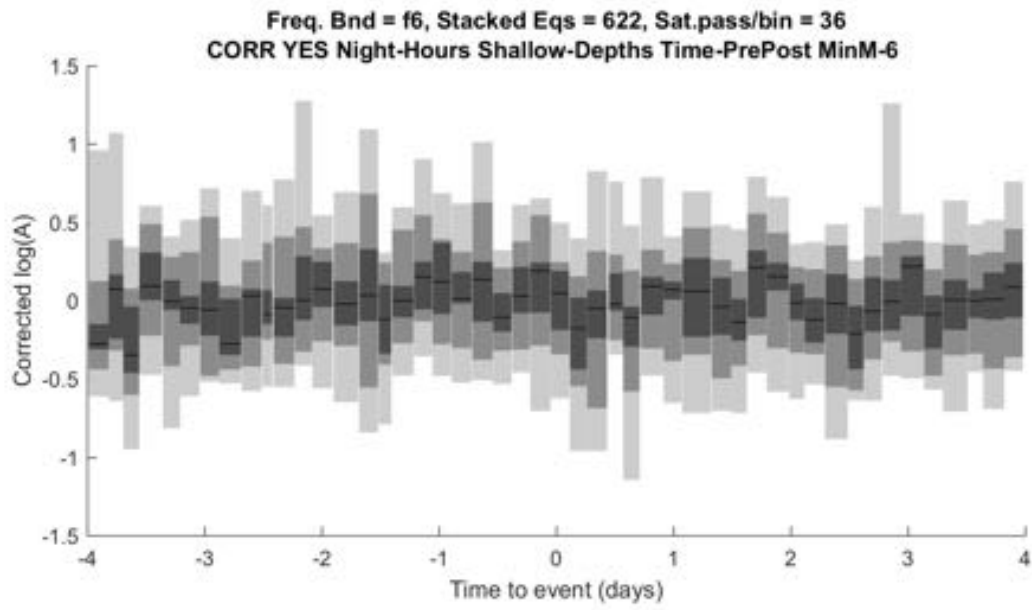
Figure 15 (see main text)

Figure 16 (see main text)

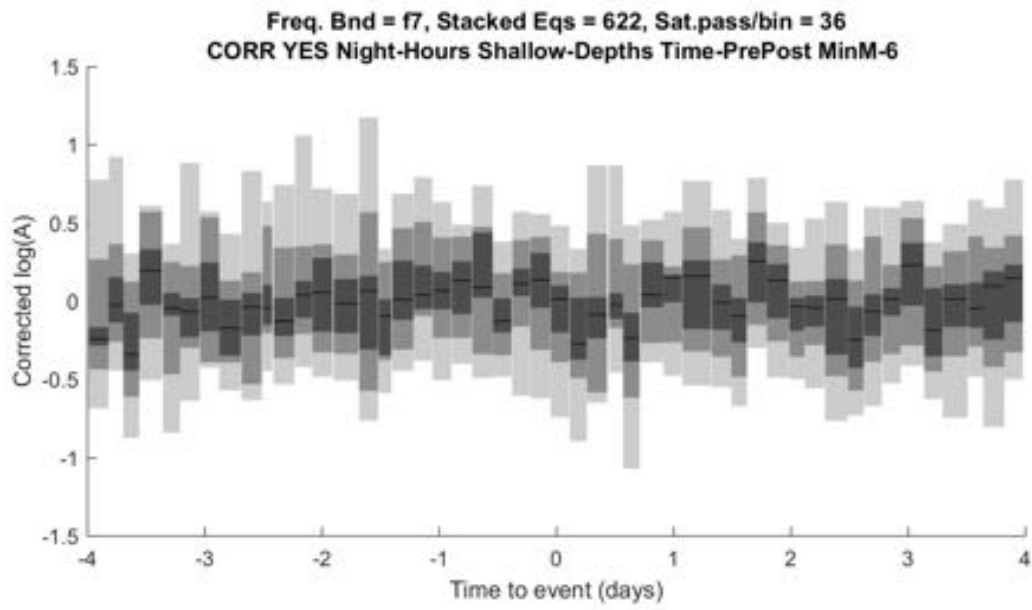
Figure 17 (see main text)

Freq. Bnd = f17, Stacked Eqs = 622, Sat.pass/bin = 36
CORR YES Night-Hours Shallow-Depths Time-PrePost MinM-6

Figure 18 (see main text)

Freq. Bnd = f18, Stacked Eqs = 622, Sat.pass/bin = 36
CORR YES Night-Hours Shallow-Depths Time-PrePost MinM-6

Figure

19 (see main text)

Freq. Bnd = f1, Stacked Eqs = 7412, Sat.pass/bin = 872
CORR YES Night-Hours Shallow-Depths Time-PrePost

Figure 20 (see main text)

Freq. Bnd = f2, Stacked Eqs = 7412, Sat.pass/bin = 872
CORR YES Night-Hours Shallow-Depths Time-PrePost

Figure 21 (see main text)

Freq. Bnd = f3, Stacked Eqs = 7412, Sat.pass/bin = 872
CORR YES Night-Hours Shallow-Depths Time-PrePost

Figure 22 (see main text)

Freq. Bnd = f4, Stacked Eqs = 7412, Sat.pass/bin = 872
CORR YES Night-Hours Shallow-Depths Time-PrePost

Figure 23 (see main text)

Freq. Bnd = f5, Stacked Eqs = 7412, Sat.pass/bin = 872
CORR YES Night-Hours Shallow-Depths Time-PrePost

Figure 24 (see main text)

Freq. Bnd = f6, Stacked Eqs = 7412, Sat.pass/bin = 872
CORR YES Night-Hours Shallow-Depths Time-PrePost

Figure 25 (see main text)

Freq. Bnd = f7, Stacked Eqs = 7412, Sat.pass/bin = 872
CORR YES Night-Hours Shallow-Depths Time-PrePost

Figure 26 (see main text)

Freq. Bnd = f8, Stacked Eqs = 7412, Sat.pass/bin = 872
CORR YES Night-Hours Shallow-Depths Time-PrePost

Figure 27 (see main text)

Freq. Bnd = f9, Stacked Eqs = 7412, Sat.pass/bin = 872
CORR YES Night-Hours Shallow-Depths Time-PrePost

Figure 28 (see main text)

Freq. Bnd = f10, Stacked Eqs = 7412, Sat.pass/bin = 872
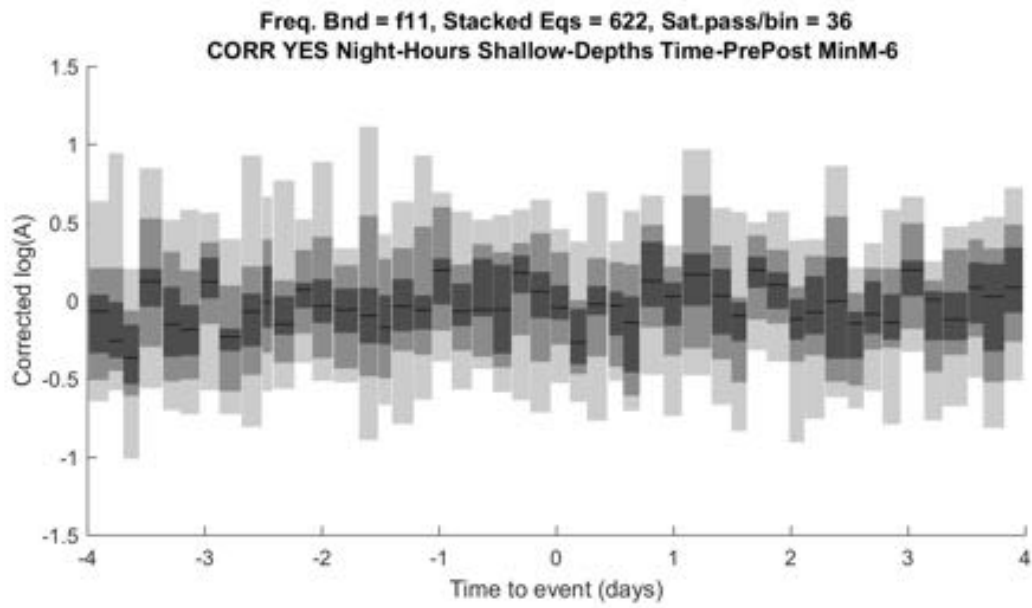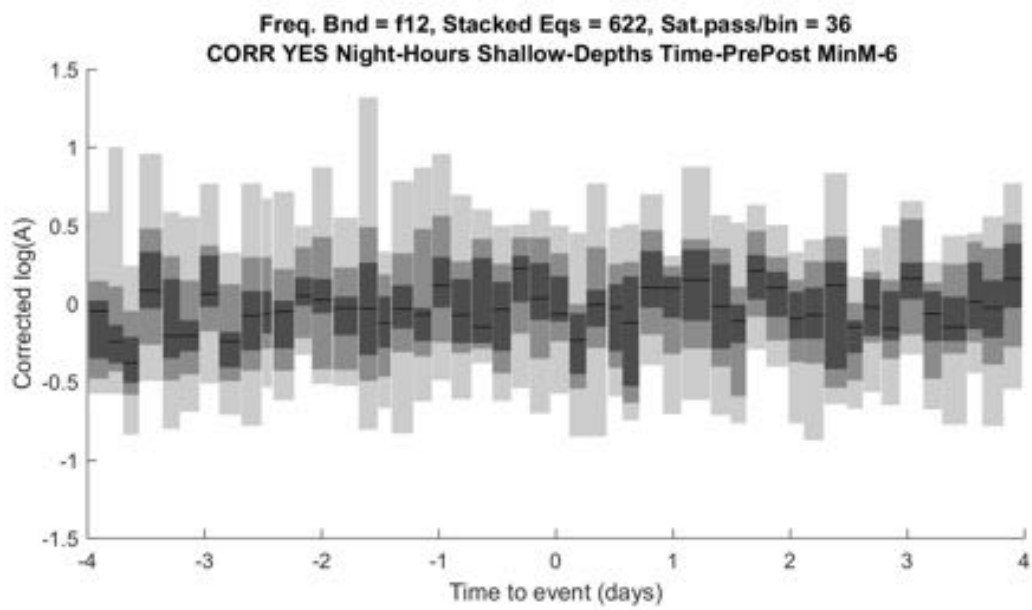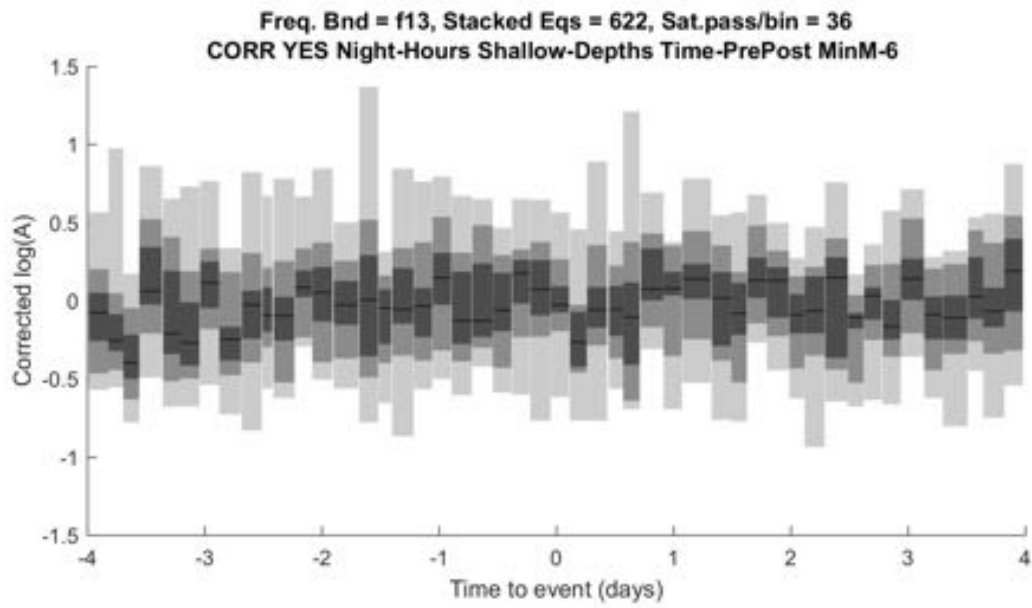CORR YES Night-Hours Shallow-Depths Time-PrePost

Figure 29 (see main text)

63

Figure 30 (see main text)

Figure 31 (see main text)

Freq. Bnd = f13, Stacked Eqs = 7412, Sat.pass/bin = 872
CORR YES Night-Hours Shallow-Depths Time-PrePost

Figure 32 (see main text)

Freq. Bnd = f14, Stacked Eqs = 7412, Sat.pass/bin = 872
CORR YES Night-Hours Shallow-Depths Time-PrePost

Figure 33 (see main text)

Freq. Bnd = f15, Stacked Eqs = 7412, Sat.pass/bin = 872
CORR YES Night-Hours Shallow-Depths Time-PrePost

Figure 34 (see main text)

Freq. Bnd = f16, Stacked Eqs = 7412, Sat.pass/bin = 872
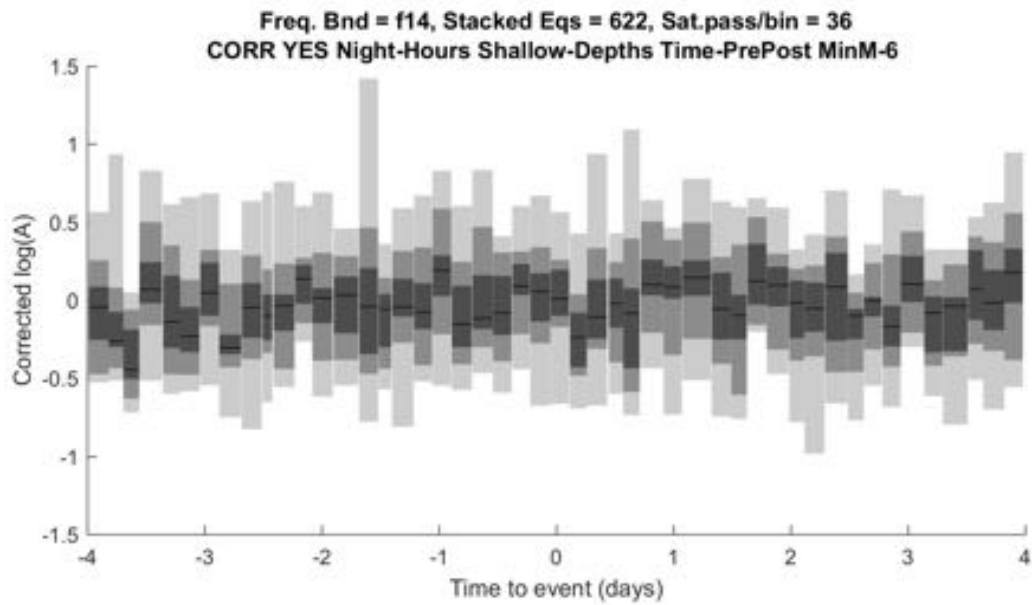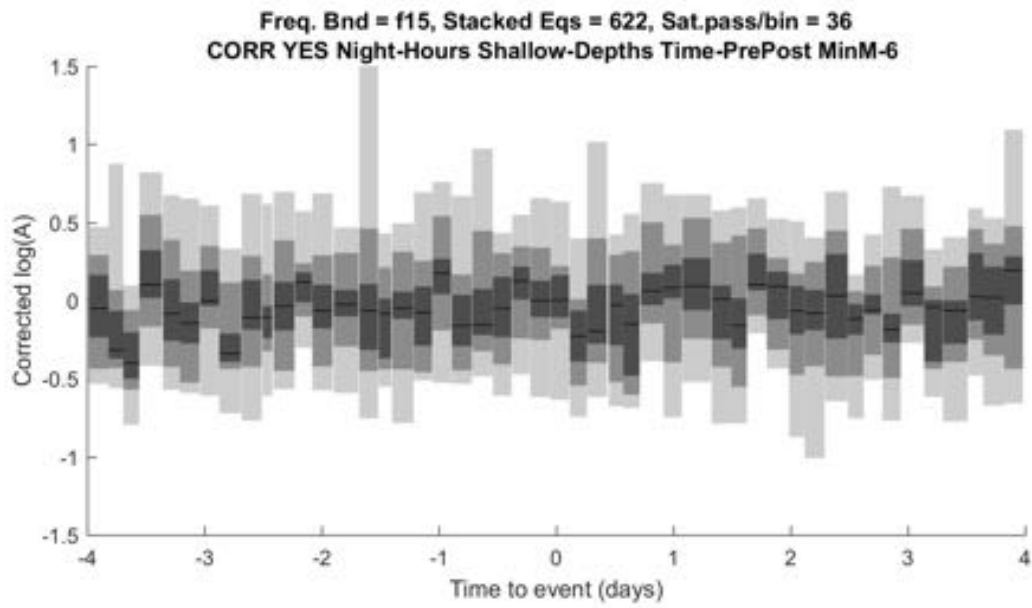**CORR YES Night-Hours Shallow-Depths Time-PrePost**
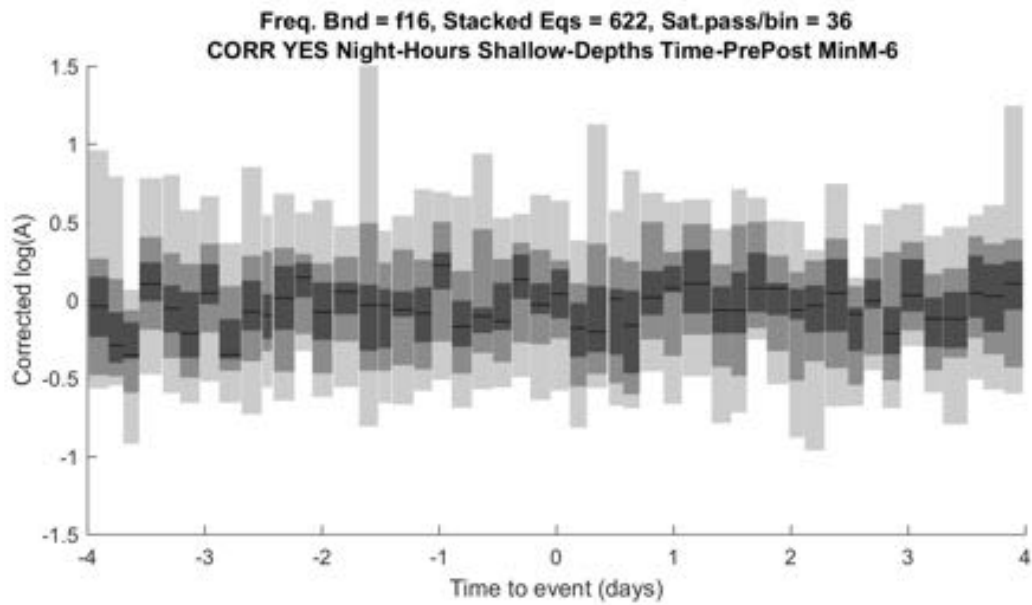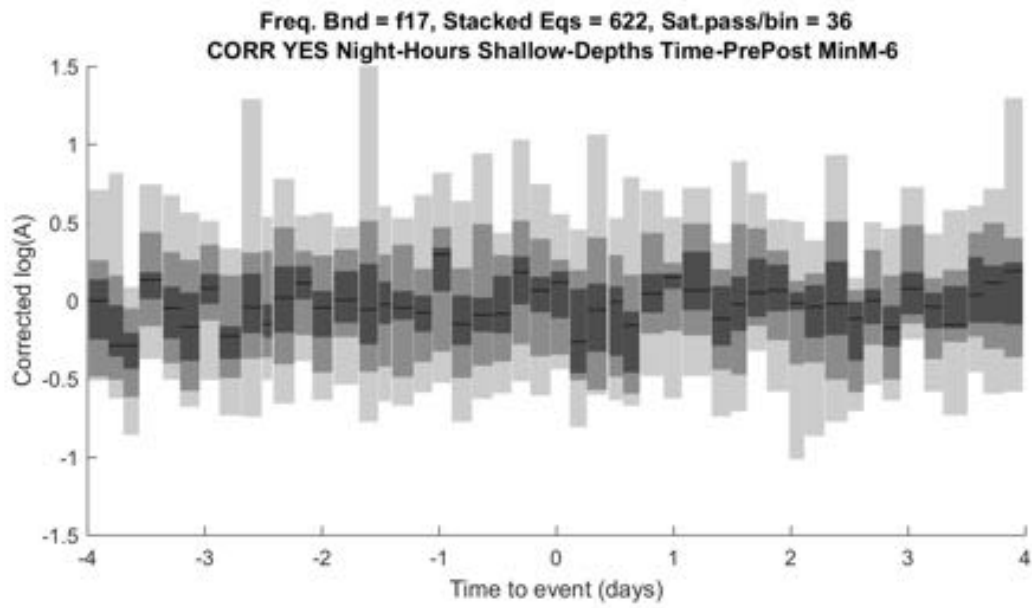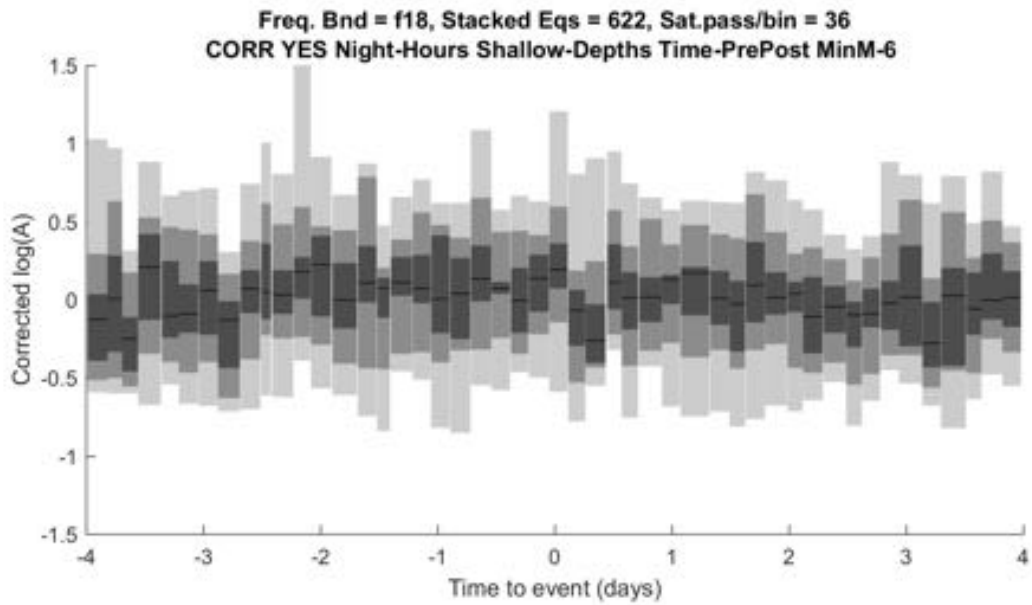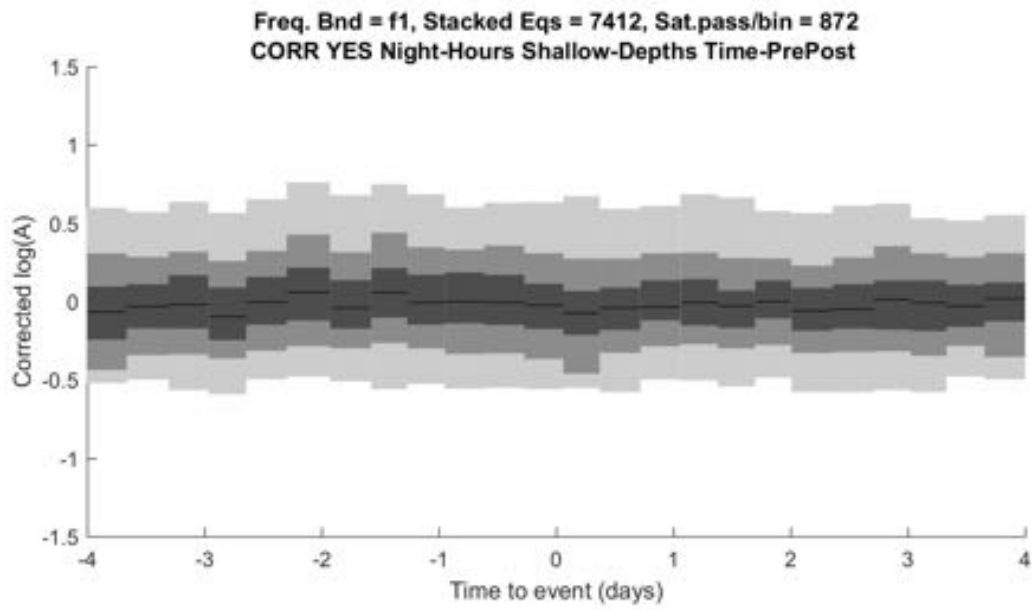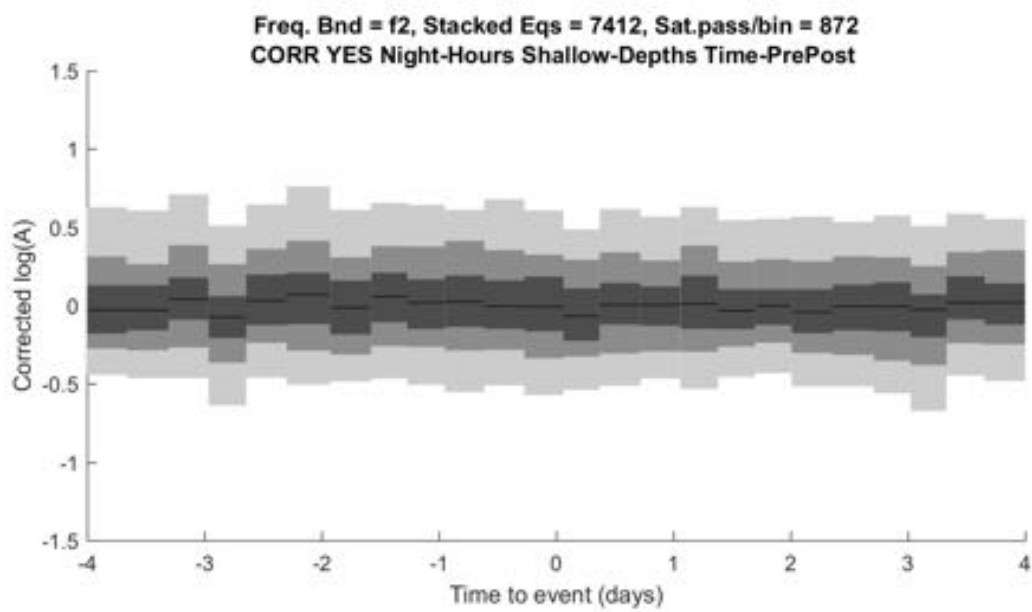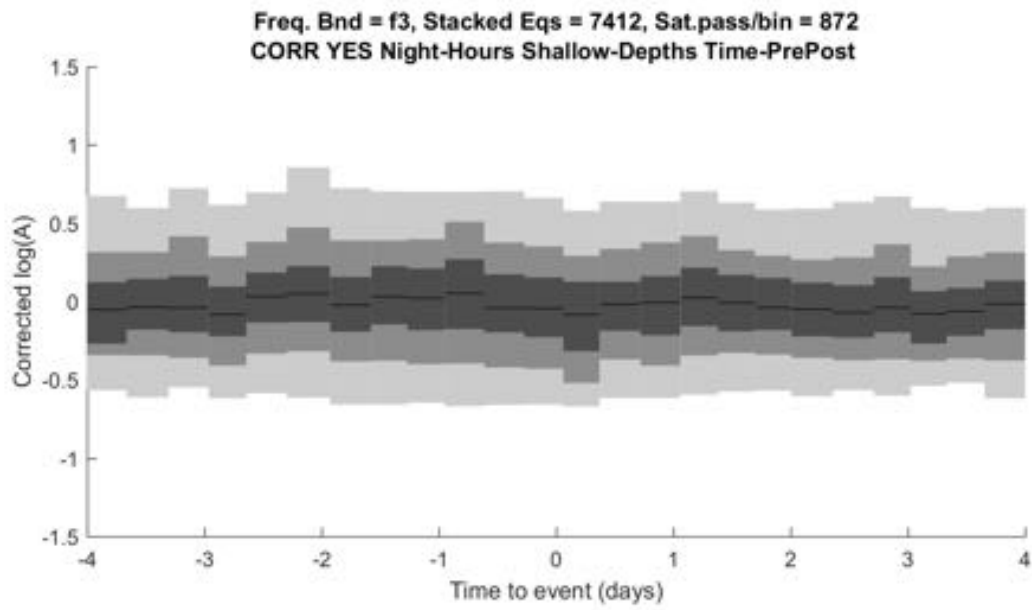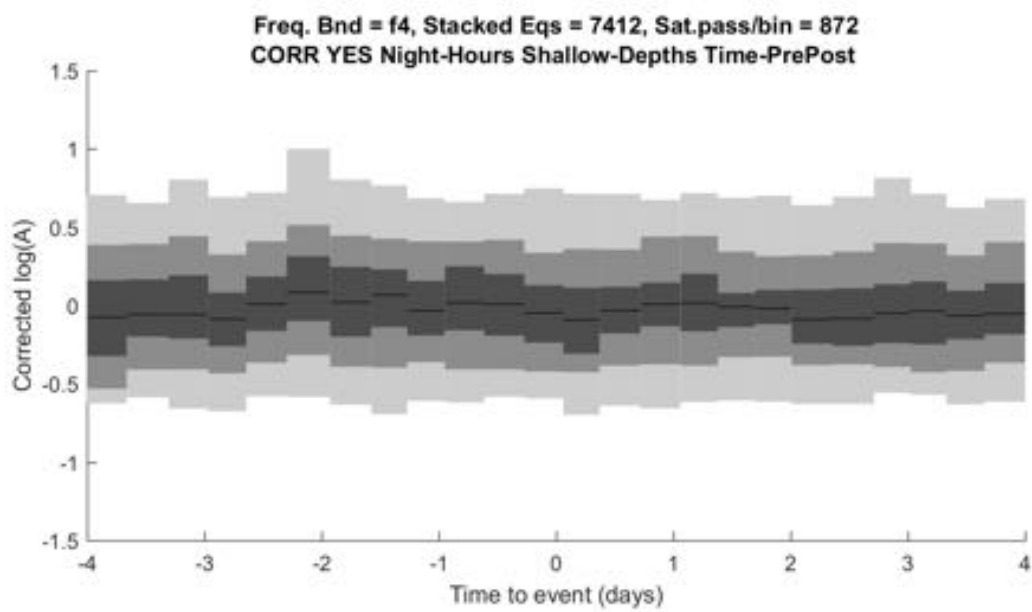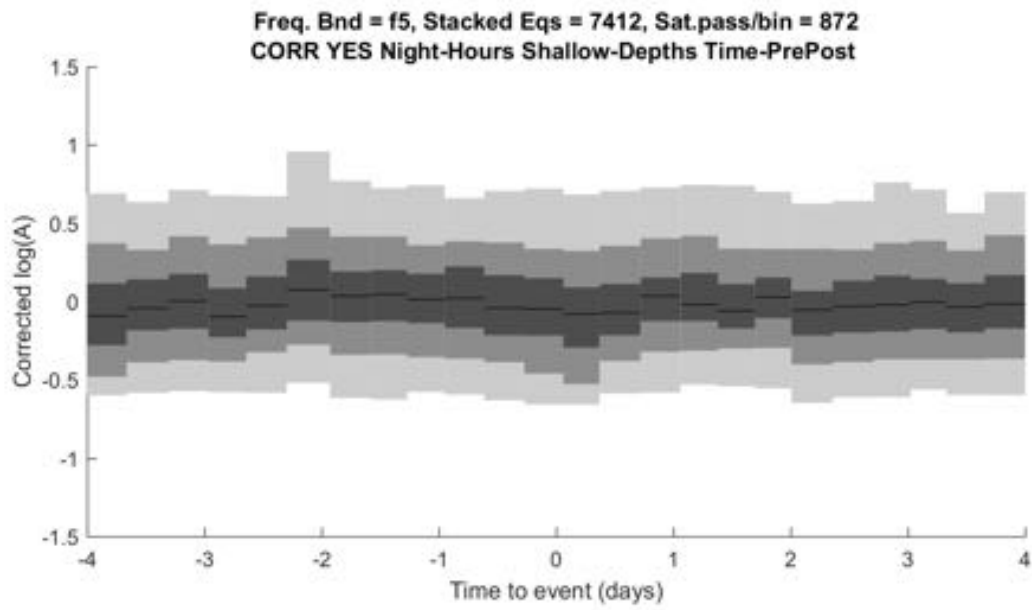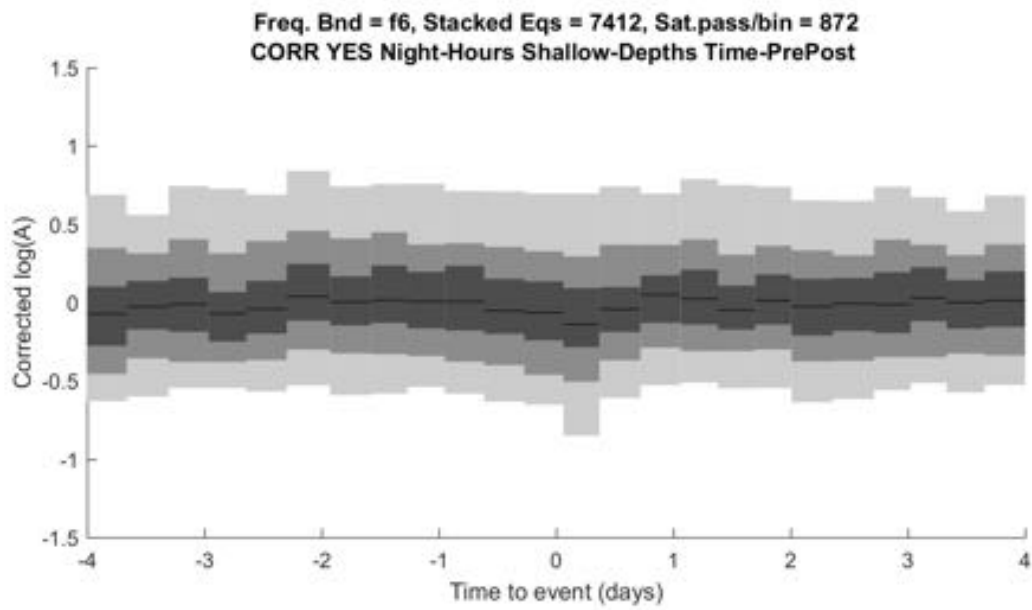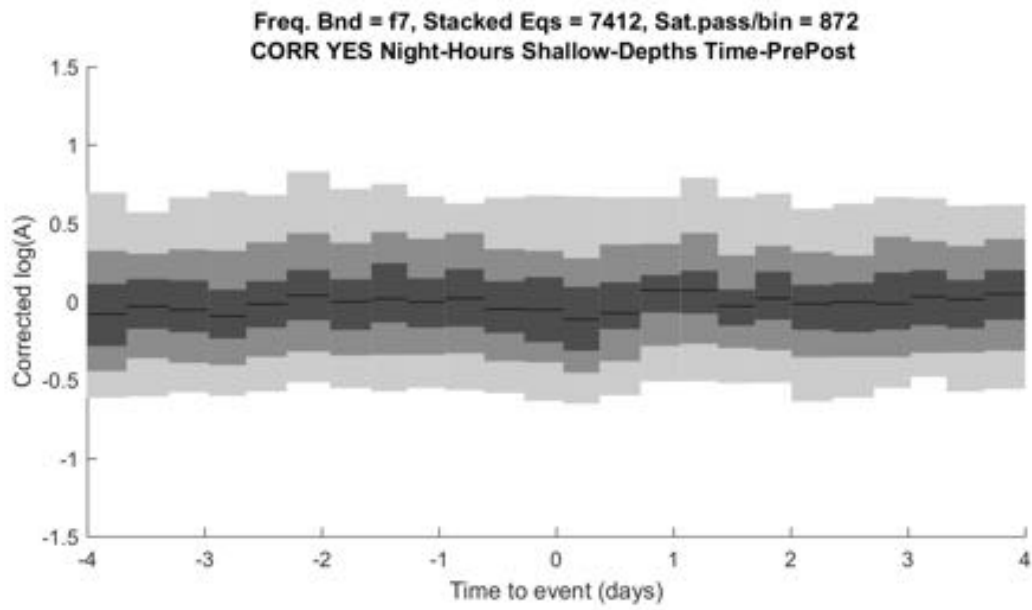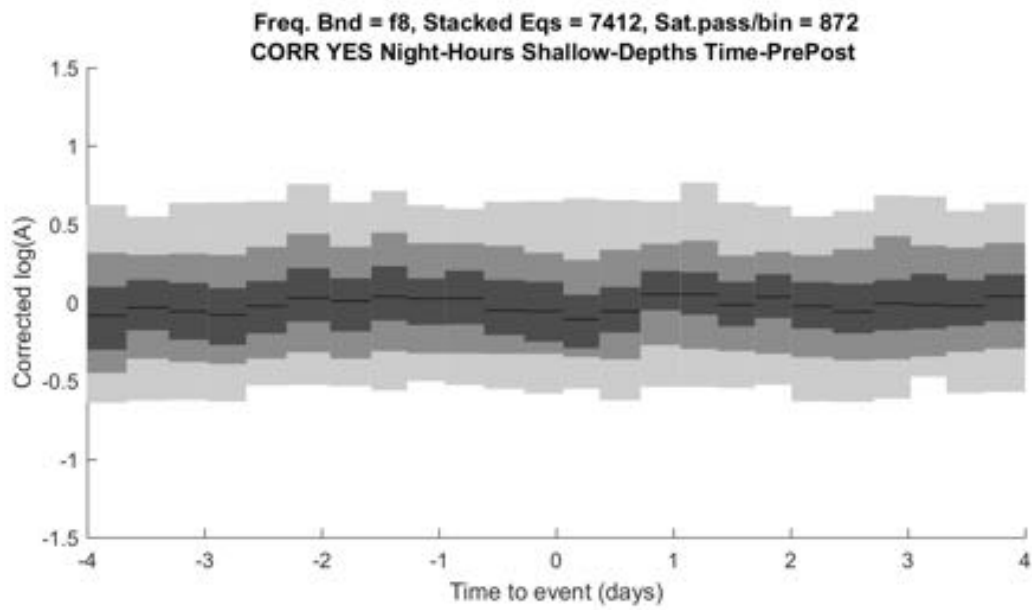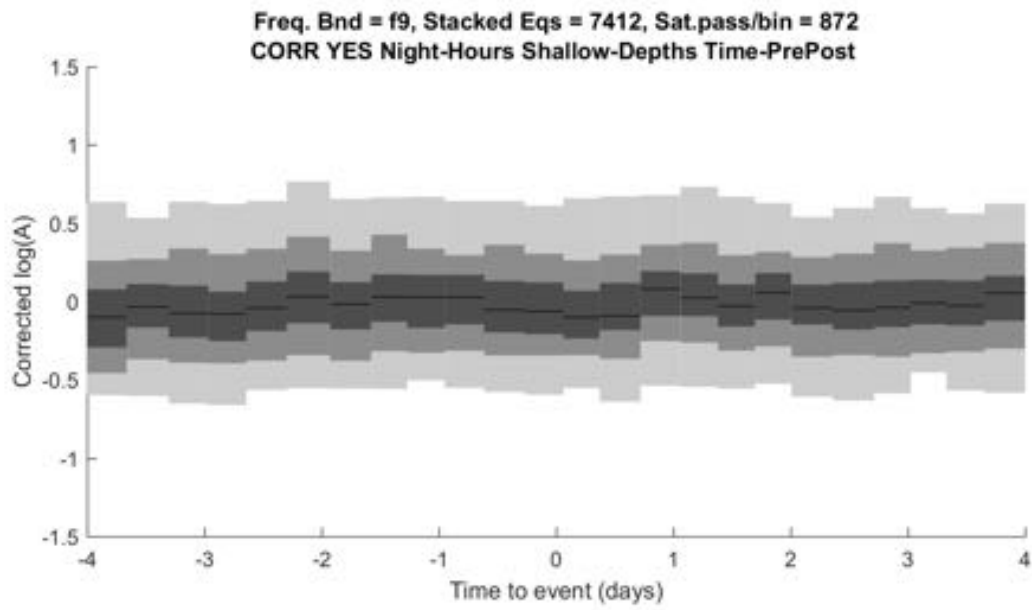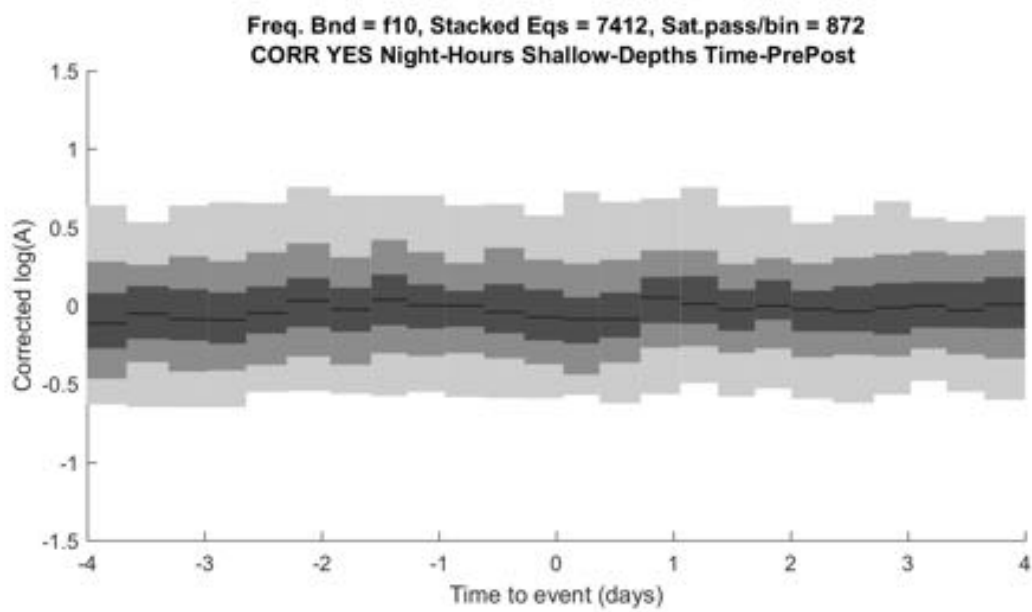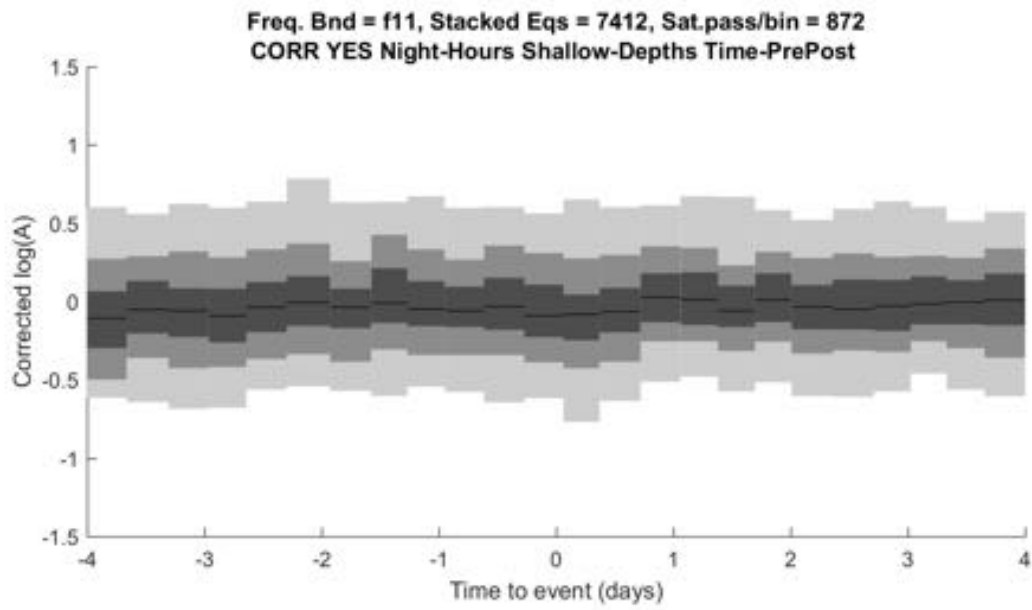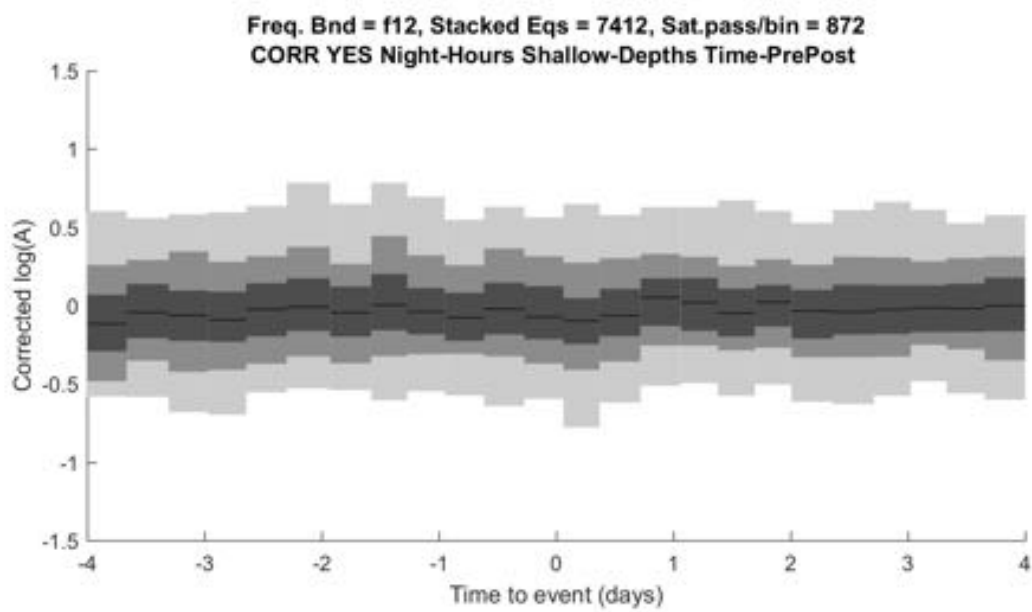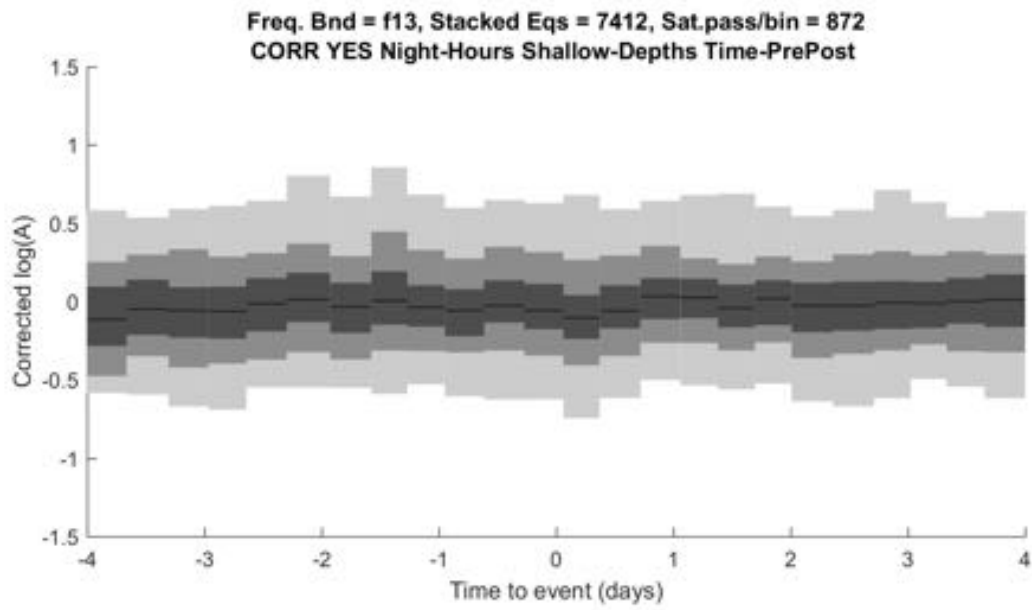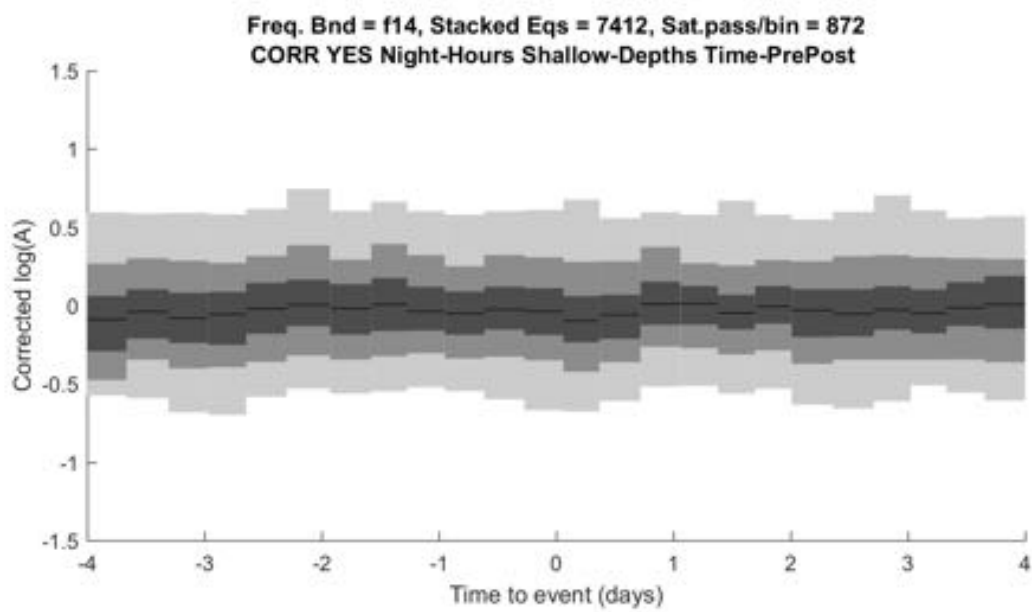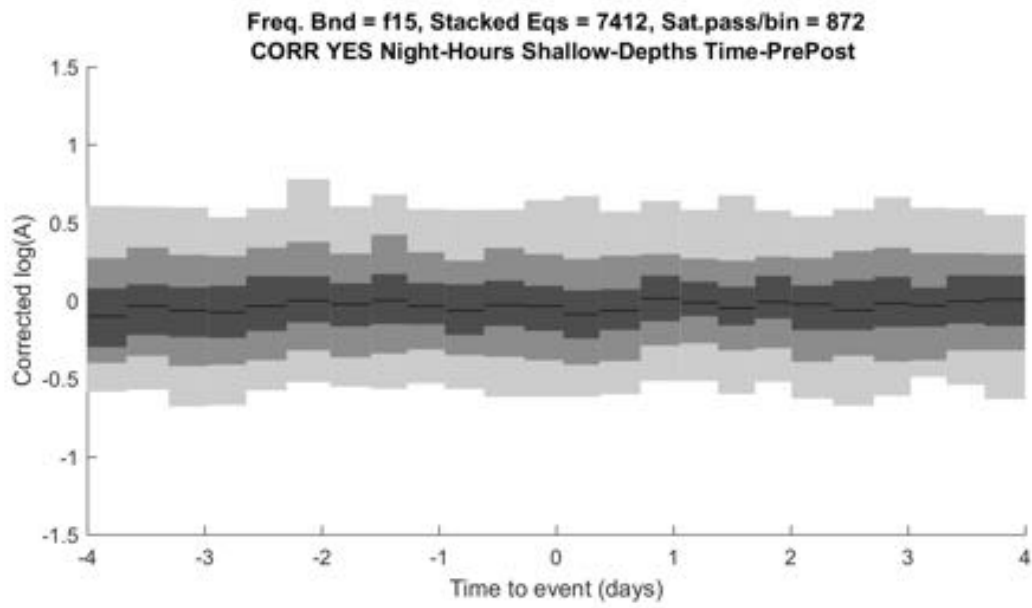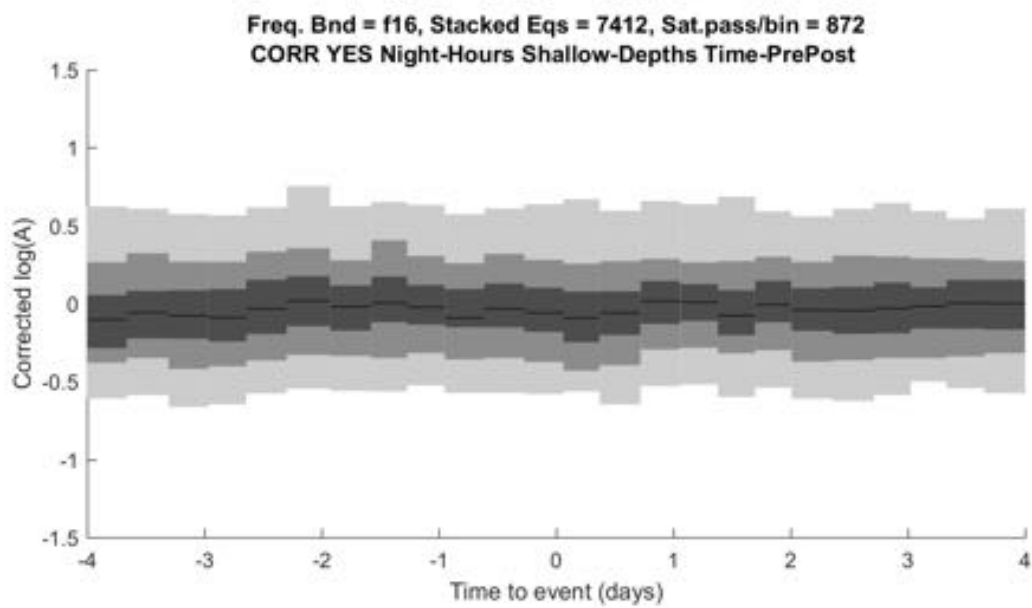
Figure 35 (see main text)
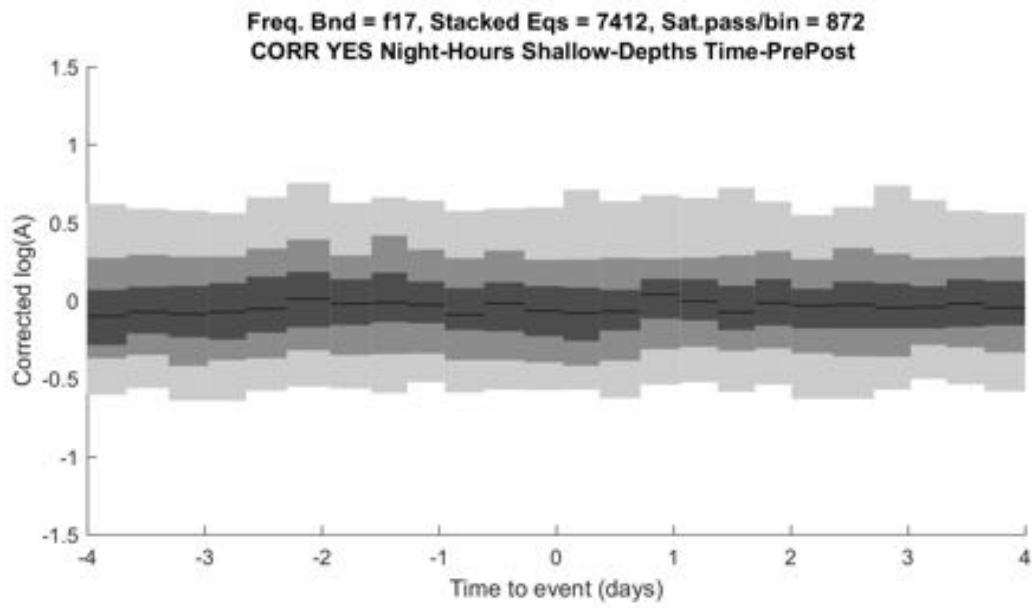
Figure 36 (see main text)
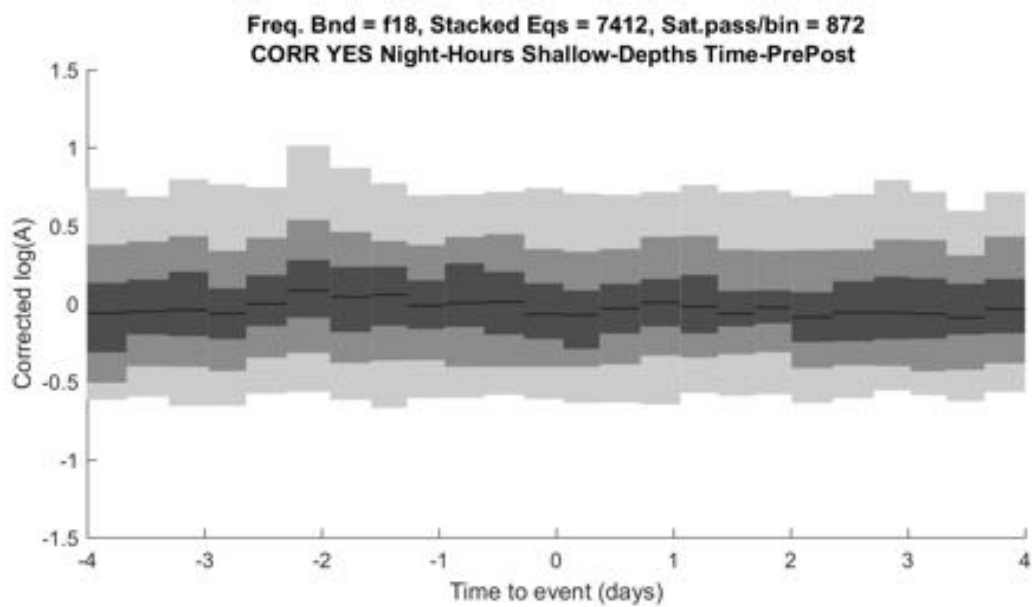
Figure 37 (see main text)

Annex C:
Earthquake prediction experiment in Taiwan using geoelectric data
(Hong-Jia Chen, Chien-Chih Chen, Guy Ouillon, Yaver Kamer, Didier Sornette)
A previously published paper is available in Annex G.

This work is the continuation of the collaboration initiated with the National Central University of Taiwan (Pr. Chien-Chih Chen), which already led to a publication joined to the last report (Chen et al., 2017), and since officially published. The goal is to improve the GEMSTIP earthquake prediction algorithm previously introduced by defining a joint station methodology. Hong-Jia Chen, who spent a year at ETH, will defend his PhD this Summer.

Geoelectric data

Since 2012, several geoelectric stations have been installed and uniformly distributed on the Taiwan Island (Fig. 1), with a mesh size of approximately 50km. This network is dubbed as the GeoElectric Monitoring System (GEMS). Each station continuously records self-potentials (referred to as geoelectric fields hereafter), which are naturally occurring electric potential differences in the Earth, i.e. passive sources. The geoelectric fields are measured by a non-polarized electrode, buried at about 1-2m depth, relative to a fixed reference one. Each site features two horizontal components, together with GPS synchronization. The dipole length of each component is within hundreds of meters to a few kilometers. Due to site-dependent limitations, the azimuth of each component is not exactly North or East. The collected data are digitized at 24 bit A/D converters. The accuracy of the measured voltages reaches 1μV, while the sampling rate is 15Hz.

Earthquake data

The seismological network of Taiwan is the densest in the world. Because $M_L \geq 5$ earthquakes usually lead to regional disasters, we focus only on $M_L \geq 5$ earthquakes during 2012/01/01 to 2016/12/31, within the region 119.5-122.5°E and 21.5-25.5°N, and at all depths, which amounts to 105 events. The distribution of the selected earthquakes is also shown in Fig. 1. Among those events, the strongest earthquake is the M_L=6.62 which occurred on 2012/06/10 at 122.31°E, 24.46°N. Furthermore, there are five inland earthquakes with M_L>6: (i) M_L=6.35, 2012/02/26, 120.75°E, 22.75°N (see Chen et al., 2013), (ii) M_L=6.24, 2013/03/27, 121.05°E, 23.90°N, (iii) M_L=6.48, 2013/06/02, 120.97°E, 23.86°N, (iv) M_L=6.42, 2013/10/31, 121.35°E, 23.57°N, and (v) M_L=6.60, 2016/02/06, 120.54°E, 22.92°N. The reported spatial location uncertainty for the 105 selected events is, in average, 0.21km horizontally and 0.23km vertically.

Detection of geoelectric anomalies before earthquakes

Statistical indices of geoelectric fields

We first resample the geoelectric data of the N- and E-components using a sampling rate of 1Hz, and calculate the mean (μ), variance (V), skewness (S), and kurtosis (K) of the daily N- and E-components of the geoelectric fields:

$$\mu = \frac{1}{N}\sum_{i=1}^{N} x_i \quad ,$$
$$V = \frac{1}{N-1}\sum_{i=1}^{N}|x_i - \mu|^2,$$
$$S = \frac{\frac{1}{N}\sum_{i=1}^{N}(x_i-\mu)^3}{\left(\sqrt{\frac{1}{N}\sum_{i=1}^{N}(x_i-\mu)^2}\right)^3} \quad , \tag{1}$$

$$K = \frac{\frac{1}{N}\sum_{i=1}^{N}(x_i-\mu)^4}{\left(\frac{1}{N}\sum_{i=1}^{N}(x_i-\mu)^2\right)^2} \quad ,$$

where x_i is a given component of the geoelectric field, and i stands for the 1st-86400th sec for each day. Figure 2 shows the time series of the four indices of the N- and E-components for the PULI station. $M_L \geq 5$ earthquakes occurring within 60km to this station are also plotted.

The daily mean series in Fig. 2 shows smooth variations, precluding the determination of clear anomalies prior to large earthquakes. Hence, we focus on the time series of skewness and kurtosis. For simplicity, we consider the absolute values of skewness ($|S|$).
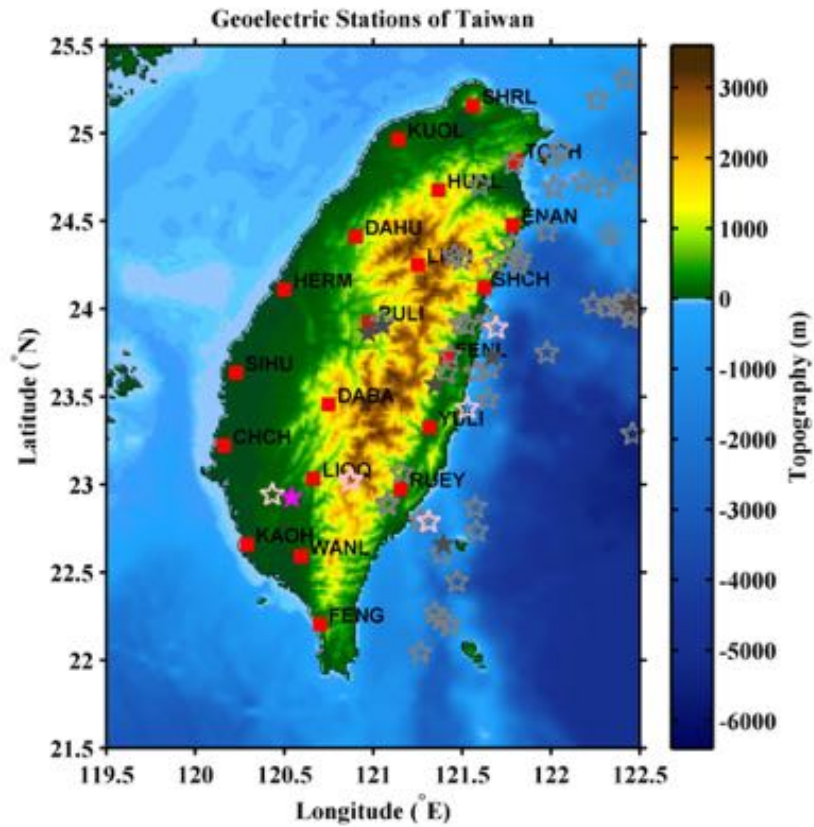
Figure 1. Spatial distributions of the geoelectric stations (red squares) and the ML≥5 earthquakes (pentagrams). The open and solid pentagrams are ML∈[5,6) and ML≥6 events, respectively.
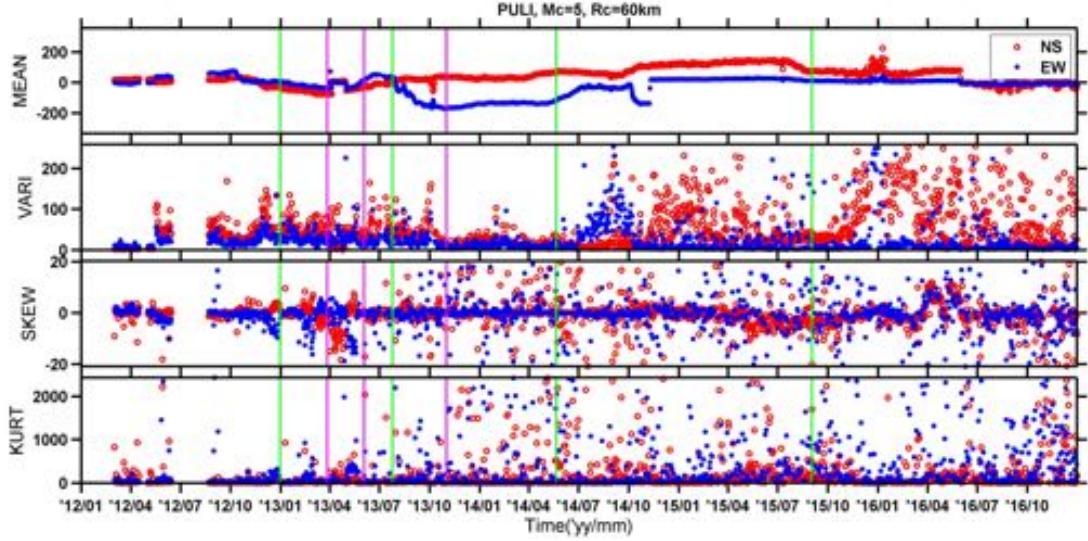
Figure 2. Time series of statistical indices and earthquakes at the PULI station. The red circles and blue dots stand for the N- and E-components, respectively. The green and magenta lines correspond to ML∈[5,6) and ML≥6 events, respectively. The distances of those events to the PULI station are smaller than or equal to 60 km.

Definition of anomalies of geoelectric fields using skewness and kurtosis

We consider the median and interquartile range (IQR) of both the skewness and kurtosis variables. Given the time series of a statistical index (y), we define the upper threshold (θ) above which we consider the variable as anomalous:

$$\theta(t; y) = Median(y_i) + A_{thr} \cdot IQR(y_i), \quad i = t - \Delta t \text{ to } t, \tag{2}$$

where t is the time in days, y_i is $|S|$ or K within the time interval Δt days, and A_{thr} is a factor to tune the level of the upper threshold.

We test the effect of the choice of Δt on calculating the median and IQR of $|S|$ and K. We consider values of Δt from 100 to 1,200 days, with a step of 100 days, expliciting ranges of parameters using the format {start:increment:end}, so that $\Delta t \in \{100{:}100{:}1{,}200\}$ (day). For a given station, from its onset time, we compute the medians and $IQRs$ of $|S|$ and K within intervals of length Δt by shifting the time windows by a lag of $0.05\Delta t$. We compute the statistics (mean ± 1 standard deviation) of those medians and $IQRs$, and plot them versus Δt, as shown in Fig. 3. We show the results for the PULI station, but other stations provide similar results. The medians and $IQRs$ of $|S|$ and K are relatively stable when $\Delta t \geq 1{,}000$ days. Hence, we consider $\Delta t = 1{,}000$ days to estimate the upper thresholds hereafter. $|S|$ or K is then defined as anomalous whenever $|S(t)| > \theta(t; |S|)$ or $K(t) > \theta(t; K)$.

The parameter A_{thr} controls the value of the upper thresholds. Consider PULI's $|S|$ parameter, for example: we estimate the upper thresholds corresponding to different A_{thr} ($A_{thr} \in \{1{:}1{:}5\}$), as shown in Fig. 4. We observe that, when $A_{thr}=1$, four anomalous points are found in the N-component of $|S|$ ($|S|_N$ for short) and 11 anomalous points in $|S|_E$ prior to the 2012/12/31, M_L=5.28 earthquake, whose distance to the PULI station is less than 60 km, within the 30 days preceding it. However, some of those anomalies are not anomalous anymore when increasing A_{thr}. Similar results are observed for the 2013/03/27, M_L=6.24 and the 2013/06/02, M_L=6.48 earthquakes. Moreover, when A_{thr}=4, fragmentary anomalies still appear prior to the 2013/06/02, M_L=6.48 earthquake within 53 days, while there are no anomalies prior to the 2013/03/27, M_L=6.24 earthquake. We explain in a later section how to determine the optimal value of A_{thr} for a given dataset.

Daily numbers of anomalous indices versus earthquakes

At each geoelectric station, the four indices ($|S|_N$, $|S|_E$, K_N, K_E) are used to state if a day is labeled as anomalous or not. First, at any time, we estimate the Anomaly Index Number (AIN), which is the

number of indices greater than their upper thresholds. Figure 5a shows the time series of *AIN* when A_{thr}=1 for the PULI station. We observe that the *AIN* prior to large earthquakes might be larger than during periods of relative quiescence. On the other hand, we label a day as anomalous if the *AIN* of that day is greater than or equal to a threshold number (N_{thr}). Figure 5b shows, when A_{thr}=1, the days labeled as anomalous corresponding to different values of N_{thr} ($N_{thr}\in\{1:1:4\}$) for the PULI station. It is obvious that the number of anomalous days decreases with increasing N_{thr}.
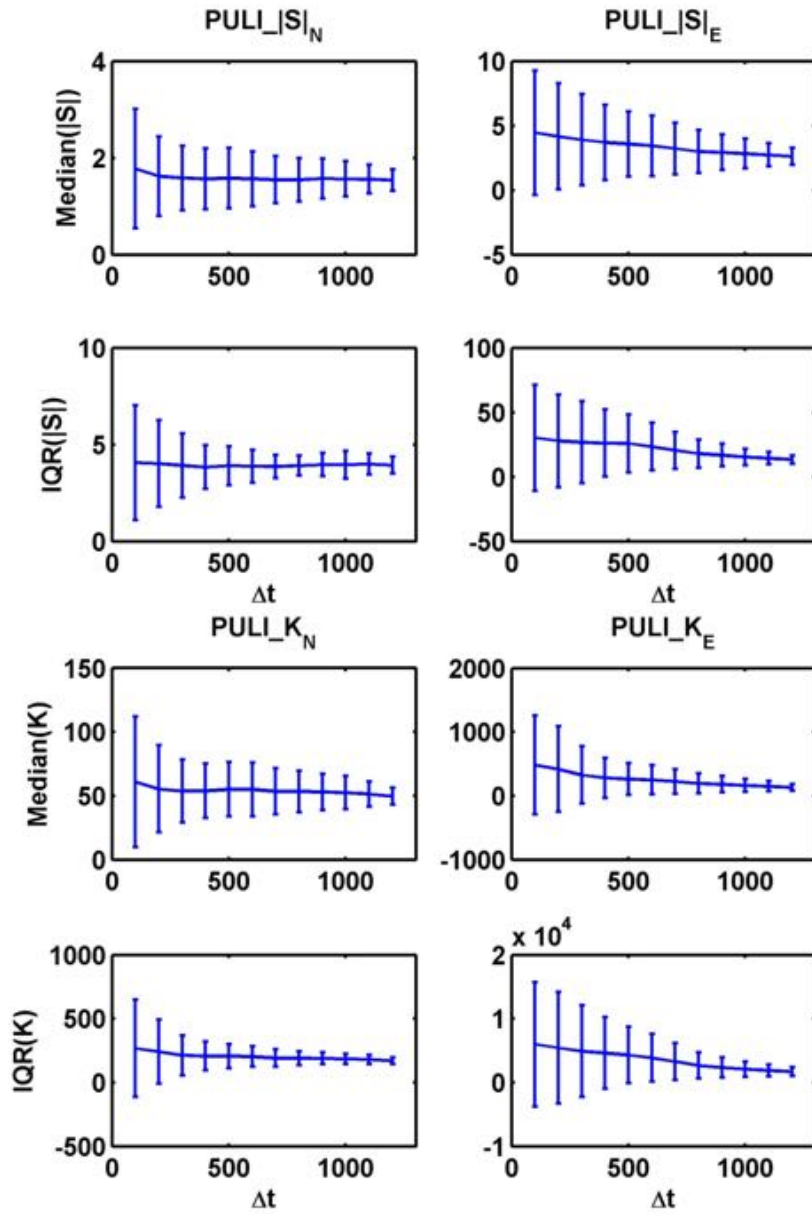
Figure 3. Sensitivity of the medians and interquartile ranges of |S| and K on Δt at the PULI station.
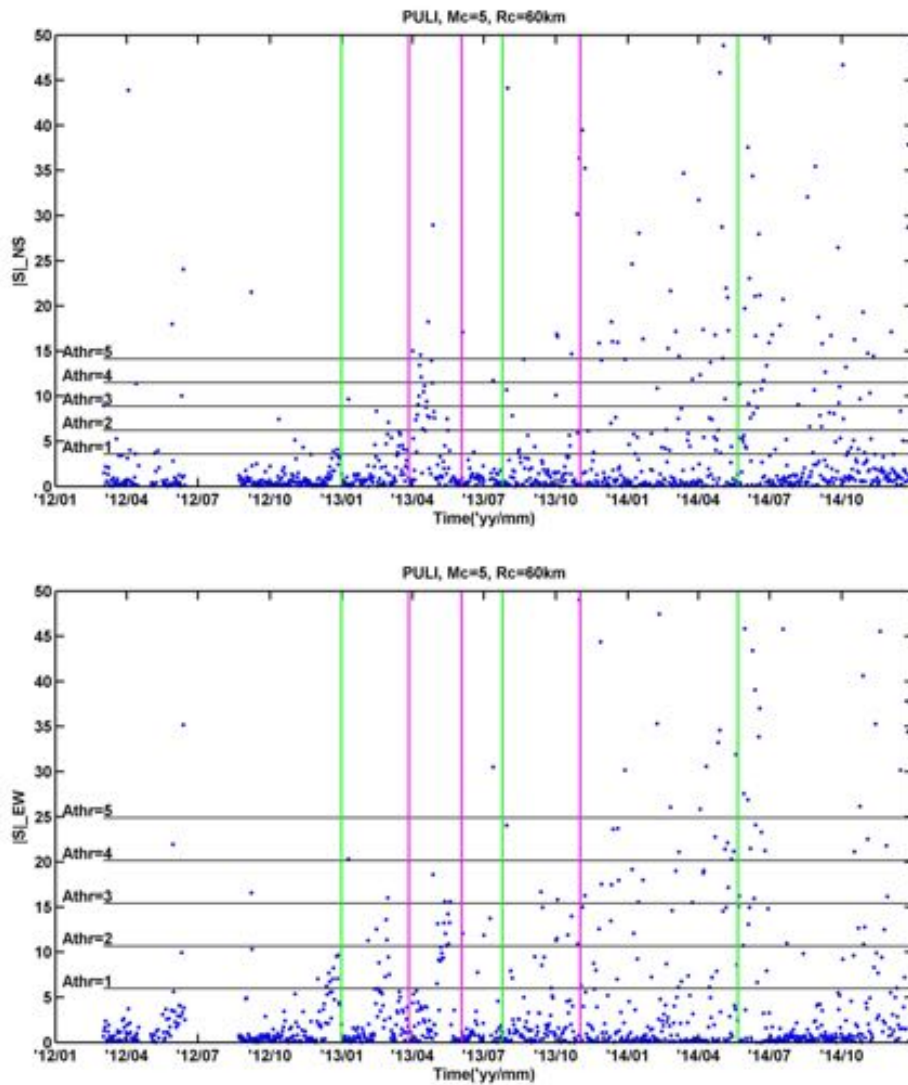
Figure 4. Time series of the absolute values of the skewness (blue dots) for the N- and E-components for the PULI station and their upper thresholds corresponding to different Athr (black lines). The green and magenta lines correspond to ML∈[5,6) and ML≥6 events, respectively. The distances from those events to the PULI station are smaller than or equal to 60 km.

Spatial range of geoelectric precursors

The recorded geoelectric fields at a given station are affected by instruments themselves, local human activities, geological and hydrological structures, and so on. Thus, provided that rock fracturing generates electric signals, we expect that some stations could miss the fracture-induced electric signals, possibly overprinted by other transients or screened during their propagation. Moreover, the amplitudes of the fracture-induced electric signals may decay with distance, limiting again the detection potential of each station.

Figure 6 shows the time series of days labeled as anomalous at the PULI station for A_{thr}=1 and N_{thr}=1. $M_L \geq 5$ earthquakes are also plotted, and are selected when the source-to-station distance is smaller than or equal to different cut-off distances ($R_c \in \{30:10:100\}$ km). The number of selected earthquakes naturally increases with R_c, which value at each station remains to be optimised in order to guess the relationship between seismic events and geoelectric signals
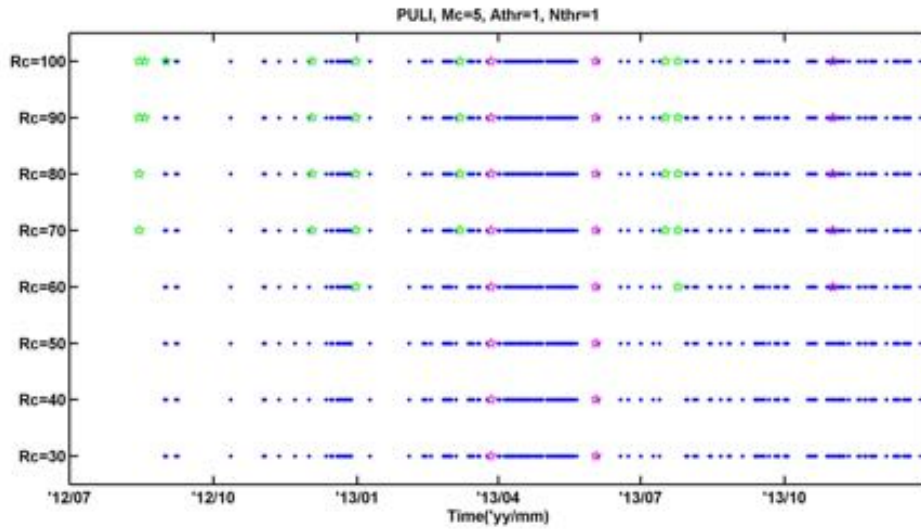
Figure 6. Time series of anomalous days versus earthquakes for different detection distances (Rc) at the PULI station. Anomalous days (blue dots) are defined at Athr=1 and Nthr=1 in this example. The green and magenta symbols correspond to ML∈[5,6) and ML≥6 events, respectively. The distances of those events to the PULI station are smaller than or equal to Rc km (vertical axis).

Observation time windows and numbers of anomalous days versus earthquakes

The number of anomalous days prior to large earthquakes is different from event to event. Figure 7 shows the days labeled as anomalous for A_{thr}=1 and N_{thr}=1 at the PULI station. We target the period from 2013/03/01 to 2013/03/28 in detail, which only includes the 2013/03/27, M_L=6.24 earthquake which occurred near that station. First, we focus on the window from 2013/03/24 to 2013/03/27 with an observation time length T_{obs}=4 days: one anomalous day within this window is thought to correspond to the earthquake. For T_{obs}=10 days (from 2013/03/18 to 2013/03/27), 3 anomalous days seem to be related to the earthquake; for T_{obs}=14 days (from 2013/03/14 to 2013/03/27), we get 6 days of anomaly; for T_{obs}=16 days (from 2013/03/12 to 2013/03/27), we get 7 days. If the number of anomalous days before an earthquake is greater than or equal to a threshold number (T_{thr} in day) within a window T_{obs}, we consider that the anomalous days are related to the earthquake. On the other hand, we also observe that an earthquake does not occur immediately after a given anomalous period, as shown in Fig. 7. The time delay between the end of an anomalous time window and the event is is referred to as a leading time window (T_{lead} in day).

We consider six main parameters (A_{thr}, N_{thr}, R_c, T_{obs}, T_{thr}, T_{lead}) to study the relationships between geoelectric anomalies and earthquakes. We further build up a predictive model based on these six parameters and optimize their values on a training dataset.
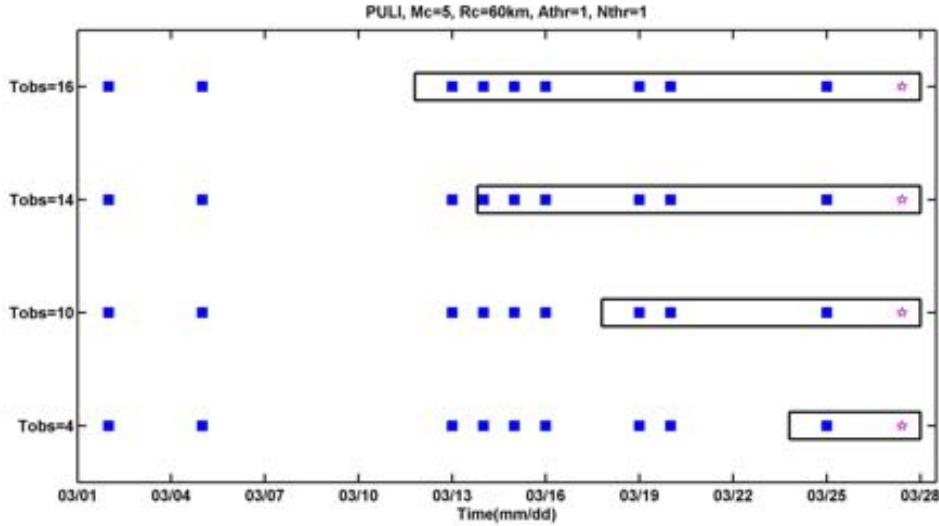
Figure 7. Time series of the lengths of the observation time window (T_{obs}, black rectangles) and number of anomaly days (blue squares), for the 2013/03/27, ML6.24 earthquake (magenta pentagram).

Relationship examination between anomalies and earthquakes

We improve the GEMSTIP algorithm presented in Chen et al. (2017) from a single station method to a joint stations method and propose another evaluation of model performance. This new version of the GEMSTIP algorithm consists of supervised machine learning and binary classification, meaning that the algorithm learns an optimal model from a training dataset, and predicts future events as one adds new data. The training dataset consists of known input data (geoelectric statistical anomalies) and corresponding output data (earthquakes). This algorithm features two main parts. In the first one, we establish a predictive model. This model labels days as anomalous based on given anomalous statistical indices, and then provides alarms based on those anomalies. In the second part, we evaluate the model by comparing alarmed earthquakes with observed earthquakes temporally and spatially. Before data analysis, we divide the dataset into two independent subsets: the training set and the validation set. The algorithm evaluates the fit of predictive models using different model parameters on the training dataset, and then selects the optimal parameters. The models with the optimal parameters are then used to process the validation dataset, and provide the forecasting scores. Conducting significance tests, we assess the practicability of the predictive model for the forecasting strategy.

GEMSTIP algorithm: Single station method

Establishing a predictive model

We presented above the factors used to define earthquake alarms based on geoelectric anomalies. For the sake of generalization, we take into account the magnitude of an event and the length of a predictive window. Hence, the model parameter vector $\boldsymbol{g}$ of each station is as follows:

$$\boldsymbol{g} = \left[M_c, R_c, A_{thr}, N_{thr}, T_{thr}, T_{obs}, T_{lead}, T_{pred}\right] \tag{3}$$

This predictive model possesses 8 parameters, and the illustrative meaning of each parameter is shown in Fig. 8. M_c is the minimum magnitude of events which can be predicted (here set to M_c=5.0).

(a)

(b)
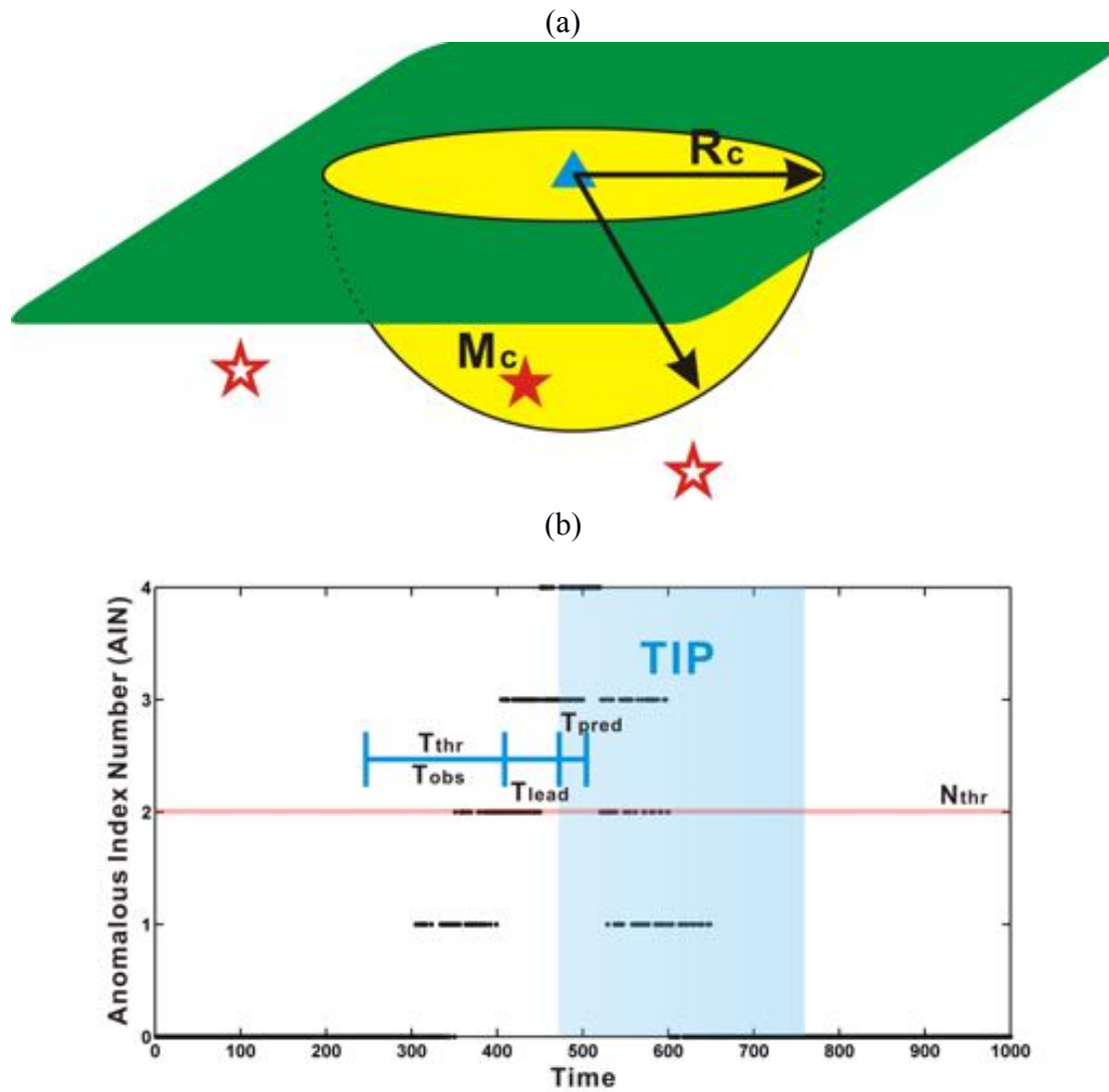
Figure 8. Schematic diagrams of (a) selection of target earthquakes, and (b) definition of 'Time of Increased Probability (TIP).', i.e. alarm times. The solid pentagon is the target event with a source-to-station distance smaller than or equal to Rc and with magnitude greater than or equal to Mc. An anomalous day is defined when the quantity AIN is greater than or equal to Nthr. The TIPs (blue region) within Tpred days are alarmed when the number of anomalous days is greater than or equal to Tthr within Tobs days. Tlead represents the delay between the end of anomalies and the occurrence of the event.

Considering a parameter vector $\boldsymbol{g}$, we define:

$$Q(t|\boldsymbol{g}) = \begin{cases} Q(t = t_i) = 1, \\ if \ M_{Li} \geq M_c \cap \|(x_i, y_i, z_i) - (x_{sta}, y_{sta}, 0)\| \leq R_c, i = 1 \ to \ N_{EQ}, \\ Q = 0, otherwise \end{cases} \qquad (4)$$

where Q is the time series of 0 (no target earthquake) or 1 (target earthquake), t is the time in days, (x_i, y_i, z_i), t_i, and M_{Li} are the location, occurrence time (in days), and magnitude of the ith target earthquake, respectively, N_{EQ} is the number of earthquakes, and (x_{sta}, y_{sta}) is the location of the considered station. The parameter M_c is the cut-off magnitude of target earthquakes, and R_c is the cut-off distance of target earthquakes to a station as we select earthquakes within a source-to-station distance smaller than or equal to R_c, as shown in Fig. 8a. We then define the 'Anomaly Index Number' as:

$$F_{AIN}(t|\boldsymbol{g}) = \sum_{i=1}^{2} \left(I\left(|S_i(t)| > \theta(t; |S_i|)\right) + I\left(K_i(t) > \theta(t; K_i)\right) \right), \qquad (5)$$

where F_{AIN} can take up to 5 values (from 0 to 4), t is the time in days, i is the N- or E- component, θ is the threshold value defined by Eq. (2), and $|S|$ and K are the absolutes of skewness and kurtosis, respectively, and $I(\Omega)$ is a logical function:

$$I(\Omega) = \begin{cases} 1, \ \Omega \ is \ true \\ 0, otherwise \end{cases}. \qquad (6)$$

The expression of 'Anomalous Time' is then defined as:

$$F_{AT}(t|\boldsymbol{g}) = I(F_{AIN}(t|\boldsymbol{g}) \geq N_{thr}), \qquad (7)$$

where F_{AT} is a time series of 0 (non-anomalous time) or 1 (anomalous time), t is the time in days, and N_{thr} is an integer threshold number smaller than or equal to 4. The expression of 'Sum of Anomalous Times' within a moving observation time window (T_{obs}) is defined as:

$$F_{SAT}(t|\boldsymbol{g}) = \sum_{i=t-T_{obs}+1}^{t} F_{AT}(t_i|\boldsymbol{g}), \qquad (8)$$

where F_{SAT} is an integer time series, t and t_i are times in days, T_{obs} (in days) is the length of the observation time window. The 'Time of Increased Probability (TIP),' illustrated in Fig. 8b, is thus defined as:

$$T_{TIP}(t|\boldsymbol{g}) = \begin{cases} T_{TIP}\left(t = t_i + T_{lead} \ to \ t_i + T_{lead} + T_{pred}\right) = 1, if \ F_{SAT}(t_i) \geq T_{thr} \\ T_{TIP}\left(t = t_i + T_{lead} \ to \ t_i + T_{lead} + T_{pred}\right) = 0, \ if \ F_{SAT}(t_i) < T_{thr} \end{cases}, \qquad (9)$$

where T_{TIP} is the time series of 0 (non-TIP) or 1 (TIP), t and t_i are the times in days, and T_{thr} (in days) is a threshold number. We issue alarms between t_i+T_{lead} and $t_i+T_{lead}+T_{pred}$ when $F_{SAT} \geq T_{thr}$ at time t_i. We adopt the concept of a grid search, meaning that hundreds of thousands of parameter vectors are generated within the value ranges. We then evaluate the score on a training dataset for each vector considered as a fit to the observations.

Scoring of models

The score of each model parameter vector is evaluated as:

$$d(\boldsymbol{g}) = 1 - \tau(\boldsymbol{g}) - n(\boldsymbol{g}). \qquad (10)$$

The function $\tau(\boldsymbol{g})$ is:

$$\tau(\boldsymbol{g}) = \frac{\sum_t I(T_{TIP}(t|\boldsymbol{g})=1)}{\sum_t I(T_{TIP}(t|\boldsymbol{g}) \geq 0)}, \qquad (11)$$

which is the fraction of alarmed time cells. The function $n(\boldsymbol{g})$ is:

$$n(\boldsymbol{g}) = \frac{\sum_t I(T_{TIP}(t|\boldsymbol{g})=0 \cap Q(t|\boldsymbol{g})=1)}{\sum_t I(T_{TIP}(t|\boldsymbol{g}) \geq 0 \cap Q(t|\boldsymbol{g})=1)}, \qquad (12)$$

which is the fraction of missed earthquakes. The smaller $\tau(\boldsymbol{g})$ and $n(\boldsymbol{g})$, the better, meaning that the

model catches target earthquakes with a high success rate and a small time resolution. The two functions are similar to Molchan scores (see Molchan, 1997), for which we can also provide confidence intervals as proposed by Zechar and Jordan (2008). Figure 9 shows the scatterplot of (τ, n) for the PULI station for the training phase from its onset to 2015/03/31. Each dot corresponds to the performance of a single model as defined above.

The fit between the two time series of Q and T_{TIP} is quantified by $d \in [-1,1]$. The case $d > 0$ means that the model successfully and non-randomly forecasts events, whereas $d \leq 0$ means that the prediction of the model is no better than a random guess (=0) or even worse than random. We thus rank the model parameter vectors according to their corresponding d values, select the top 10 model parameter vectors of each station, and further analyze validation datasets using the selected parameter vectors in a joint stations approach.
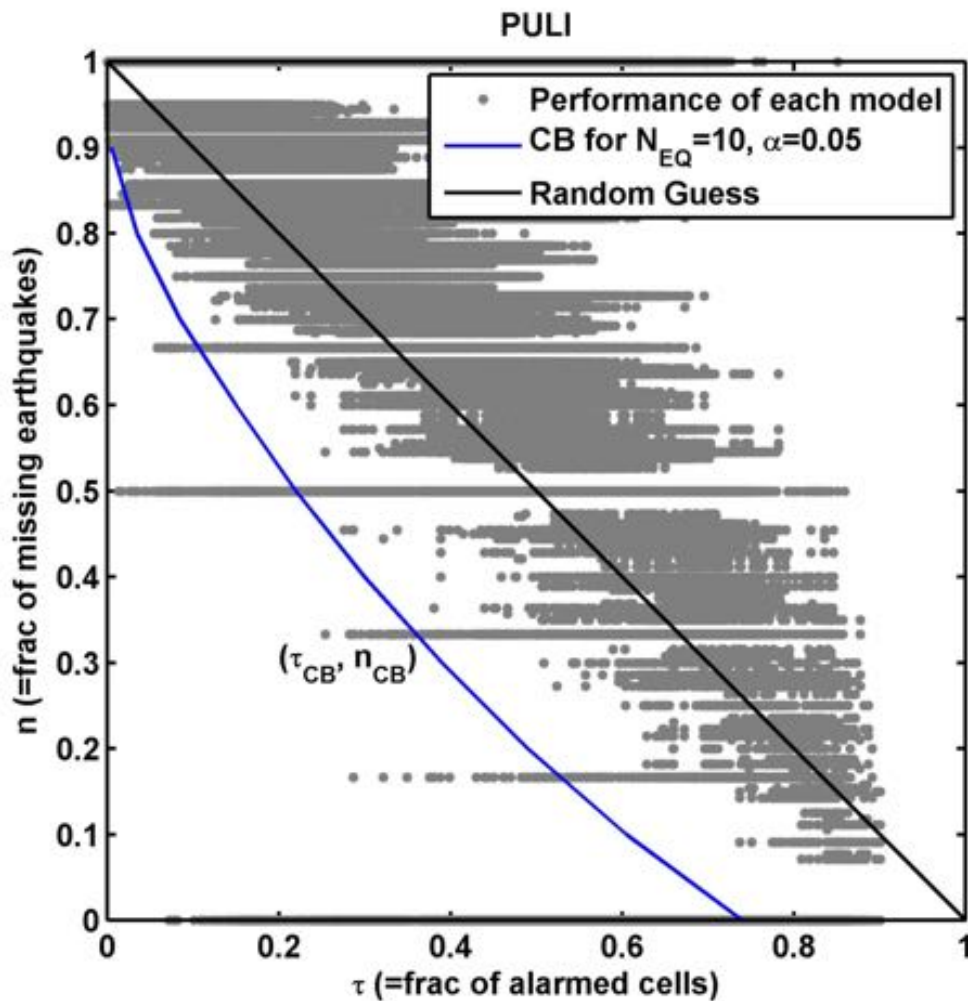
Figure 9. Molchan error diagram of the PULI station (gray dots) for the training datasets from its onset to 2015/03/31 with a confidence bound (blue line). This bound is defined at significance level α=0.05, and the number of target events NEQ=10. The black diagonal line stands for a random guess.

GEMSTIP algorithm: Joint stations method

Description

In the joint stations method, the selected optimal parameter vectors of each station (see previous section) are combined in order to build a parameter tensor for the Taiwan area. In this way, the spatial variations of Q and T_{TIP} are also considered. A model with a given parameters tensor is then scored

using the validation dataset in order to evaluate the overall fit for the Taiwan area. Figure 10 shows the schematic diagram describing the joint stations method. Station B in Fig. 10 misses event E2, so that event E2 is not predicted in the single station method applied to that station. However, station C hits event E2 successfully, so that event E2 is predicted when considering the joint stations method using both stations B and C. A similar case is shown for event E4 and stations A and C. The advantage of the joint stations method is that if an earthquake occurs within the detectable distances (R_c) of two stations and that one station issues an alarm for the earthquake, while the other does not, the joint stations method still considers the earthquake as successfully alarmed. This non-simultaneous alarms of stations might result from electric preferential propagations due to rupture directivity and conductive structure complexity.

The selected optimal vector $\boldsymbol{g}$ of each station composes the parameter tensor $\boldsymbol{G}$ for the Taiwan area, which is described as follows:

$$\boldsymbol{G} = \{\boldsymbol{g_i}, \quad i = 1 \; to \; N_{sta}\} \quad , \tag{13}$$

where N_{sta}=20 is the number of all stations in this paper. The formulaic description of the joint stations method is similar to that of the single station method. The expressions of Q and T_{TIP} for the joint stations method include spatial variables, use the data of all stations, and are modified as follows:

$$Q(x, y, t | \boldsymbol{G}) = \\ \begin{cases} Q\big(x = x_{i,j}, y = y_{i,j}, t = t_{i,j}\big) = 1, \\ if \; M_{Li,j} \geq M_{cj} \cap \left\| \big(x_{i,j}, y_{i,j}, z_{i,j}\big) - \big(x_j, y_j, 0\big) \right\| \leq R_{cj}, i = 1 \; to \; N_{EQj}, j = 1 \; to \; N_{sta}, \\ Q = 0, otherwise \end{cases} \tag{14}$$

In Eq. (14), Q is the space and time grids of 0 (no target earthquakes, or no pentagons in Fig. 10) or 1 (target earthquakes, or pentagons in Fig. 10); ($x_{i,j}$, $y_{i,j}$, $z_{i,j}$), $t_{i,j}$, and $M_{Li,j}$ are the location, occurrence (in day), and magnitude of the ith earthquake for the jth station, respectively; (x_j, y_j) is the location of the jth station; N_{EQj} is the number of selected earthquakes for the jth station, as we select earthquakes with magnitude greater than or equal to a cut-off magnitude for the jth station (M_{cj}) within a source-to-station distance smaller than or equal to a cut-off distance for the jth station (R_{cj}).

$$T_{TIP}(x, y, t | \boldsymbol{G}) = \begin{cases} T_{TIP}\big(\left\|(x, y) - (x_j, y_j)\right\| \leq R_{cj}, t = t_i + T_{lead} \; to \; t_i + T_{lead} + T_{pred}\big) = 1, \\ \quad if \; F_{SATj}(t_i) \geq T_{thrj}, j = 1 \; to \; N_{sta} \\ T_{TIP}\big(\left\|(x, y) - (x_j, y_j)\right\| \leq R_{cj}, t = t_i + T_{lead} \; to \; t_i + T_{lead} + T_{pred}\big) = 0, \\ \quad if \; F_{SATj}(t_i) < T_{thrj}, j = 1 \; to \; N_{sta} \\ T_{TIP} = nan, otherwise \end{cases} \tag{15}$$

In Eq. (15), T_{TIP} is the space and time grids of 0 (non-TIP, or white regions within a dotted circle of a station in Fig. 10), 1 (TIP, or yellow regions in Fig. 10), or not-a-number (nan, or white regions out of dotted circles in Fig. 10). For the jth station, we issue alarms within a distance R_c km between $t_i + T_{lead}$ and $t_i + T_{lead} + T_{pred}$ when $F_{SAT} \geq T_{thr}$ at time t_i. On the other hand, the evaluation of the agreement between Q and T_{TIP} for the joint stations method are similar to the single station case, which is conditioned to $\boldsymbol{G}$ instead of $\boldsymbol{g}$:

$$\tau(\boldsymbol{G}) = \frac{\sum_x \sum_y \sum_t I(T_{TIP}(x, y, t | \boldsymbol{G})=1)}{\sum_x \sum_y \sum_t I(T_{TIP}(x, y, t | \boldsymbol{G}) \geq 0)},$$

$$n(\boldsymbol{G}) = \frac{\sum_x \sum_y \sum_t I(T_{TIP}(x, y, t | \boldsymbol{G})=0 \cap Q(x, y, t | \boldsymbol{G})=1)}{\sum_x \sum_y \sum_t I(T_{TIP}(x, y, t | \boldsymbol{G}) \geq 0 \cap Q(x, y, t | \boldsymbol{G})=1)}, \tag{16}$$

$$D(\boldsymbol{G}) = 1 - \tau(\boldsymbol{G}) - n(\boldsymbol{G}).$$

Note that the score D is used for the joint stations method, while d stands for the single station method.
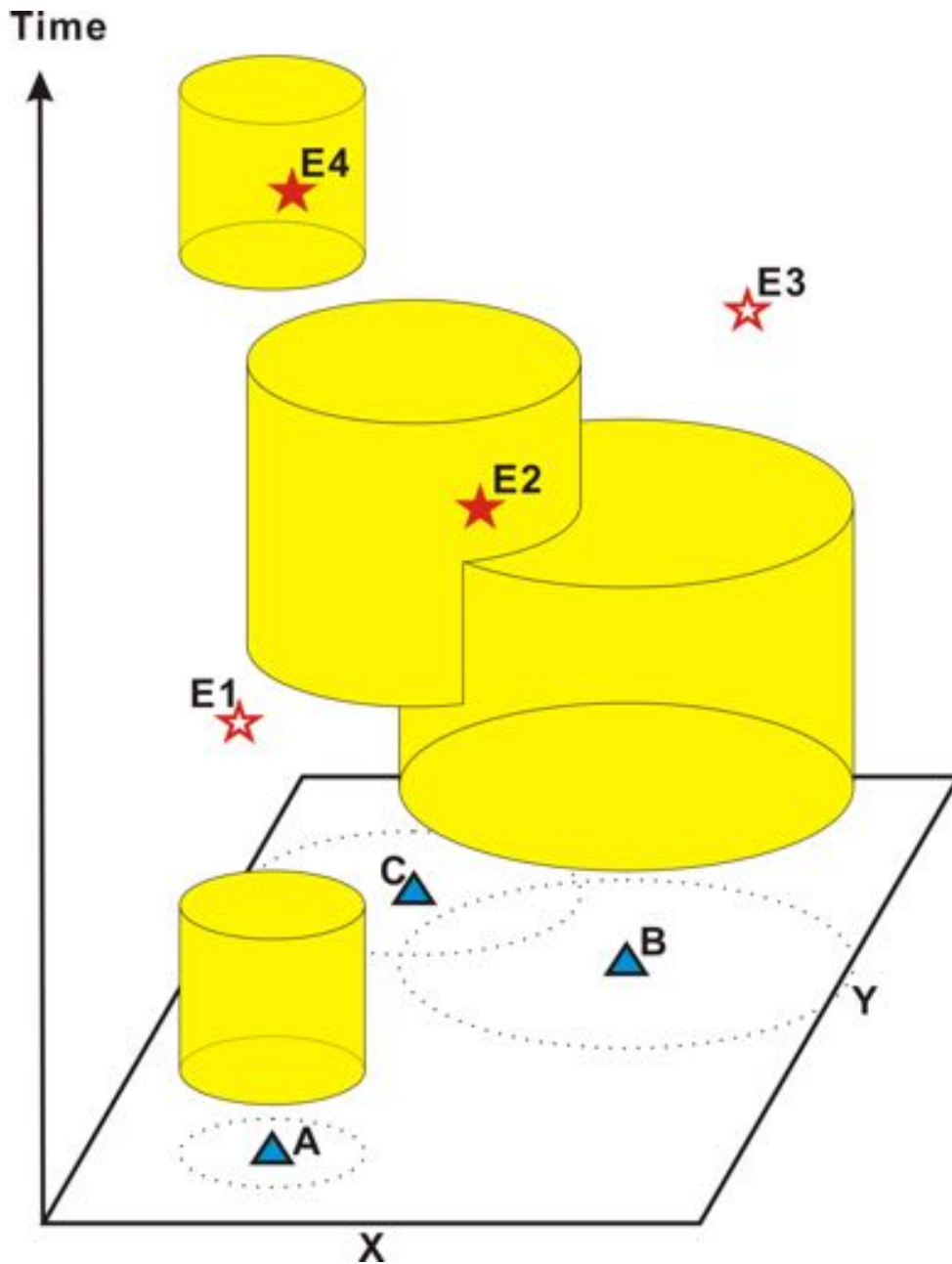
Figure 10. Schematic diagram of a joint stations method of the GEMSTIP algorithm. For example, event E2 is missed for a single station method at station B, while it is a hit considering a joint stations method using stations B and C.

Results using the joint stations method

According to the sensitivity analysis of Sec. 3.1, we opt for $\varDelta t$=1,000 days to define the threshold $\theta(t; y)$ of a given index y. We define a training phase from the onset time of each station up to 2014/06/30, labelled as Trn of case 01 in Table 1 (see below for the definition of all cases). For that period, 15 stations have recorded more than 1,000 days of data. In order to study the effect of the lengths of training phases, the latter are also extended by 3 months case by case, as shown in Table 1; that is, the ending times of the training phases are 2014/06/30, 2014/09/30, 2014/12/31, 2015/03/31, 2015/06/30, 2015/09/30, and 2015/12/31, which amount to 7 cases (labelled from 01 to 07 in Table 1). On the other hand, the lengths of the validation phases are tested by selecting 3, 6, 9, and 12

months following their corresponding training phases (labelled as Vld03, Vld06, Vld09, and Vld12, respectively). The number of earthquakes in each phase is also listed as the number within bracket in the Time column in Table 1.

Case	Training Phase (Trn)		Validation Phase of 3 months (Vld03)		Validation Phase of 6 months (Vld06)		Validation Phase of 9 months (Vld09)		Validation Phase of 12 months (Vld12)	
	Time	D	Time	D	Time	D	Time	D	Time	D
01	sta. onset-2014/6/30 (47)	0.85± 0.24	2014/7/1-2014/9/30 (4)	0.66± 0.14	2014/7/1-2014/12/31 (8)	0.63± 0.15	2014/7/1-2015/3/31 (14)	0.61± 0.18	2014/7/1-2015/6/30 (19)	0.61± 0.18
02	sta. onset-2014/9/30 (51)	0.85± 0.15	2014/10/1-2014/12/31 (4)	0.84± 0.17	2014/10/1-2015/3/31 (10)	0.83± 0.17	2014/10/1-2015/6/30 (15)	0.83± 0.17	2014/10/1-2015/9/30 (20)	0.83± 0.17
03	sta. onset -2014/12/31 (55)	0.82± 0.14	2015/1/1-2015/3/31 (6)	0.86± 0.10	2015/1/1-2015/6/30 (11)	0.87± 0.10	2015/1/1-2015/9/30 (16)	0.87± 0.10	2015/1/1-2015/12/31 (22)	0.78± 0.22
04	sta. onset -2015/3/31 (61)	0.85± 0.03	2015/4/1-2015/6/30 (5)	0.88± 0.03	2015/4/1-2015/9/30 (10)	0.88± 0.03	2015/4/1-2015/12/31 (16)	0.82± 0.17	2015/4/1-2016/3/31 (23)	0.78± 0.22
05	sta. onset -2015/6/30 (66)	0.86± 0.04	2015/7/1-2015/9/30 (5)	0.89± 0.03	2015/7/1-2015/12/31 (11)	0.82± 0.18	2015/7/1-2016/3/31 (18)	0.79± 0.28	2015/7/1-2016/6/30 (30)	0.75± 0.32
06	sta. onset -2015/9/30 (71)	0.86± 0.03	2015/10/1-2015/12/31 (6)	0.82± 0.18	2015/10/1-2016/3/31 (13)	0.78± 0.22	2015/10/1-2016/6/30 (25)	0.73± 0.27	2015/10/1-2016/9/30 (25)	0.72± 0.27
07	sta. onset -2015/12/31 (77)	0.79± 0.18	2016/1/1-2016/3/31 (7)	0.78± 0.18	2016/1/1 -2016/6/30 (19)	0.69± 0.21	2016/1/1-2016/9/30 (19)	0.68± 0.21	2016/1/1-2016/12/31 (28)	0.60± 0.27

Table 1. Periods, scores, and number of earthquakes for different training sets and their corresponding validation sets. The quantity D is represented by mean ± 2 standard deviations. The number within brackets in the Time column is the number of earthquakes during that time period.

First of all, using a single station method as described in a previous section, we estimate the *d* values of different parameter vectors **g** for each station within the training phase of case 01. According to the *d* values for each station, we select the top 10 ranking parameter vectors. We combine the top 1 vectors of all stations into the first parameter tensor **G₁** for the Taiwan area, the top 2 vectors of all stations into the second parameter tensor **G₂**, and so on, which amounts to ten sets of parameter tensors **Gᵢ** for *i*=1 to 10. Using the joint stations method described in Sec. 4.2, we then estimate the overall *D* values for the Taiwan area within the training phase and its following four kinds of validation phases for case 01. There are ten *D* values for each phase, and they are reported as mean ± 2 standard deviations in Fig. 11 and in Table 1 for case 01. Repeating the abovementioned procedure, we obtain the results for cases 02-07. We find out that the average values of *D* for the training phases of cases 01-07 are similar, approximately 0.80 to 0.85. The standard deviations of *D* in the training phases are relatively small in cases 04-06, approximately 0.035. In the validation phases for all cases, we observe a trend in the *D* values, i.e. Vld03>Vld06>Vld09>Vld12, meaning that the forecasting time period cannot be too long, or its associated score decreases. The Vld03 in cases 04 and 05 and the Vld06 in case 04 perform well. Not only are the average values of *D* quite high (approximately 0.885), but the standard deviations of *D* are relatively small (approximately 0.03).

As shown above, the fitting scores in cases 04 and 05 perform well in both the training and validation phases, suggesting that the length of the training phase for optimizing the parameter vectors is approximately between 1,000 and 1,200 days. Except for the Vld12 of cases 01, 05, 06, and 07, the ranges of *D* for both the training and validation datasets are above the confidence bound $D_{CB}^{max} = 0.46$ for N_{EQ}=5 and α=0.05. Note that the number of target earthquakes of most phases is larger than 5, so that the D_{CB}^{max} value for more earthquakes would be much lower. This means that the predictive model proposed in this study is meaningful and practical, i.e. there is a significant 'hidden correlation' in the seismoelectric pattern.

Frequency bands of earthquake-related geoelectric signals

We also studied the influence of the underlying frequency bands on the performance of the forecasting scheme, using Butterworth filters. Their main properties are that the frequency response is maximally flat in the passband, and gradually rolls off toward zero in the stopband. The filter response is flat, close to DC signals, decays to -3dB at the cut-off frequency, and decreases with a decaying rate of -20ndB/decade, where n is the number of poles in the filter. We use third-order low-, high-, and band-pass Butterworth filters.

GEMSTIP analysis results

The Butterworth filters are applied with different cut-off frequencies from 10^{-4} to $10^{-0.5}$Hz with a step of 0.25 in log scale. When loading the raw data of the geoelectric fields, we first apply the low- and high-pass filters with different cut-off frequencies. Next, we calculate the skewness and kurtosis of the filtered data, and repeat the analysis of the GEMSTIP algorithm proposed in the sections above.

Results of low- and high-pass filtered data

We select the optimal training phase from the onset time of each station up to 2015/03/31, and the optimal validation phase from 2015/04/01 to 2015/06/30. We get the averages and standard deviations of D values of the joint stations method versus the different cut-off frequencies, as shown in Fig. 12 (red lines). The D values for the low-pass filtered datasets for both the training and validation phases are similar, suggesting again that the algorithm is robust and that its optimal parameter tensors are informative. On the other hand, the average values of D remains relatively stable and high (approximately 0.85) with $f_c \leq 10^{-1.75}$ Hz, while they show a slightly decreasing trend from ~0.85 to ~0.78 when $f_c > 10^{-1.75}$ Hz, suggesting that the earthquake-related signals could be contaminated by noise at higher frequencies.

Subsequently, the abovementioned procedure is carried on the high-pass filtered datasets. Their D values versus different cut-off frequencies are also shown in Fig. 12 (blue lines). The gaps between the average values of D of both the training and validation phases for the high-pass filtered datasets are larger than those for the low-pass filtered datasets. Furthermore, the standard deviations of D for the high-pass filtered datasets are larger than those for the low-pass filtered datasets. Those results confirm that the earthquake-related signals are perturbed by high frequency noise.
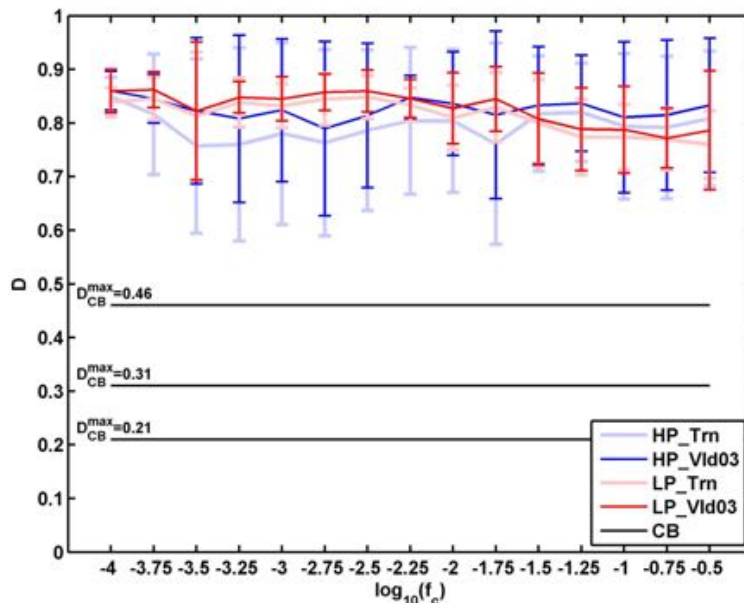
Figure 12. D scores (mean ± 2 standard deviations) for the low- and high-pass filtered datasets versus cut-off frequencies fc (in Hz). The blue lines represent the results of the high-pass filtered datasets, while the red ones stand for the low-pass filtered datasets. The light colors show the results of the training datasets from the onset time of each station up to 2015/03/31, while the thick ones stand for the validation datasets from 2015/04/01 to 2015/06/30.

Results of optimal band-pass filtered data

We select two different frequency bands for band-pass filtering. The first one is $f_1=10^{-3.5}$ Hz and $f_2=10^{-1.75}$ Hz (denoted as Bapass3.5 data), and the other one is $f_1=10^{-4.0}$ Hz and $f_2=10^{-1.75}$ Hz (Bapass4.0 data). We calculate the skewness and kurtosis of the two band-pass filtered datasets. We select again the same training phase (denoted as Trn) as in the previous section, and the four validation phases following the training phase (denoted as Vld03, Vld06, Vld09, and Vld12). Through the GEMSTIP analysis procedure, we get the D values for the two band-pass filtered datasets for the 5 different phases, as shown in Fig. 13. The D values for the raw data for the 5 phases are also shown in Fig. 13 as reference. The standard deviations of D for all phases for the Bapass4.0 data are smaller than those for the Bapass3.5 data, suggesting that the earthquake-related signals with $f \leq 10^{-3.5}$ Hz are more significant and more informative than others, an important information to constrain the prediction model. Moreover, the standard deviations of D for the Bapass4.0 data remain relatively small in the Vld09 and Vld12, compared to those for the raw and Bapass3.5 data, suggesting that the optimal parameter tensors obtained from the training datasets including low frequency components and less high frequency components could be used to forecast for a longer future time horizon.
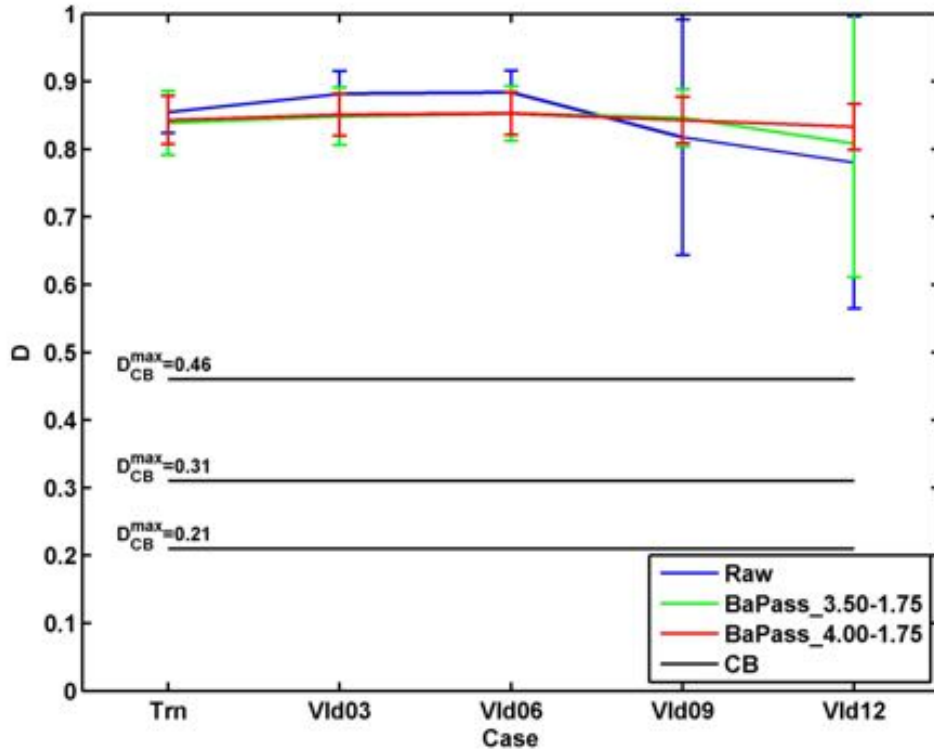
Figure 13. D scores (mean ± 2 standard deviations) for the raw data (blue line) and two optimal band-pass filtered datasets. One frequency band is from 10-3.5 to 10-1.75 Hz (green line), and the other from 10-4.0 to 10-1.75 Hz (red line). The training phase is from the onset time of each station up to 2015/03/31 (denoted as Trn in the x-axis). The validation phases are 3, 6, 9, and 12 months following the training phase (denoted as Vld03, Vld06, Vld09, and Vld12, respectively).

Precursor-based probabilistic forecasts

In order to build up a precursor-based probability of a future event, we define the hit rate v for a given parameter tensor $\boldsymbol{G}$ as:

$$v(\boldsymbol{G}) = 1 - n(\boldsymbol{G}), \tag{17}$$

where n is the rate of missed earthquakes as in Eq. (12). Then, the precursor-based probability $P(x, y,$

t) is naturally defined as:

$$P(x, y, t) = \frac{1}{N_{top}} \sum_{i=1}^{N_{top}} v(\boldsymbol{G_i}) \cdot T_{TIP}(x, y, t | \boldsymbol{G_i}), \qquad (18)$$

where N_{top}=10 is the number of the top model parameter tensors, $\boldsymbol{G_i}$ is the ith optimal parameter tensor for the joint stations method, and T_{TIP} is an index of 'Time of Increased Probability' described as in Eq. (15). Using Eq. (18), we can estimate a probabilistic forecast at time t using the geoelectric data before time t. Figure 14 shows the spatio-temporal probability maps for the optimal parameter tensors obtained from the raw, Bapass3.5, and Bapass4.0 datasets using the training phase extending from the onset time of each station up to 2015/03/31. Two target earthquakes in 2013/06/02 are located in the middle part and southern part of Taiwan, respectively, which coincide with high probabilities for the three forecasts. Note that the probabilities in the three figures increase from 2013/05/15 to 2013/06/01 before the two earthquakes, and decrease from 2013/06/03 to 2013/06/13.

(a)   (b)

(c)
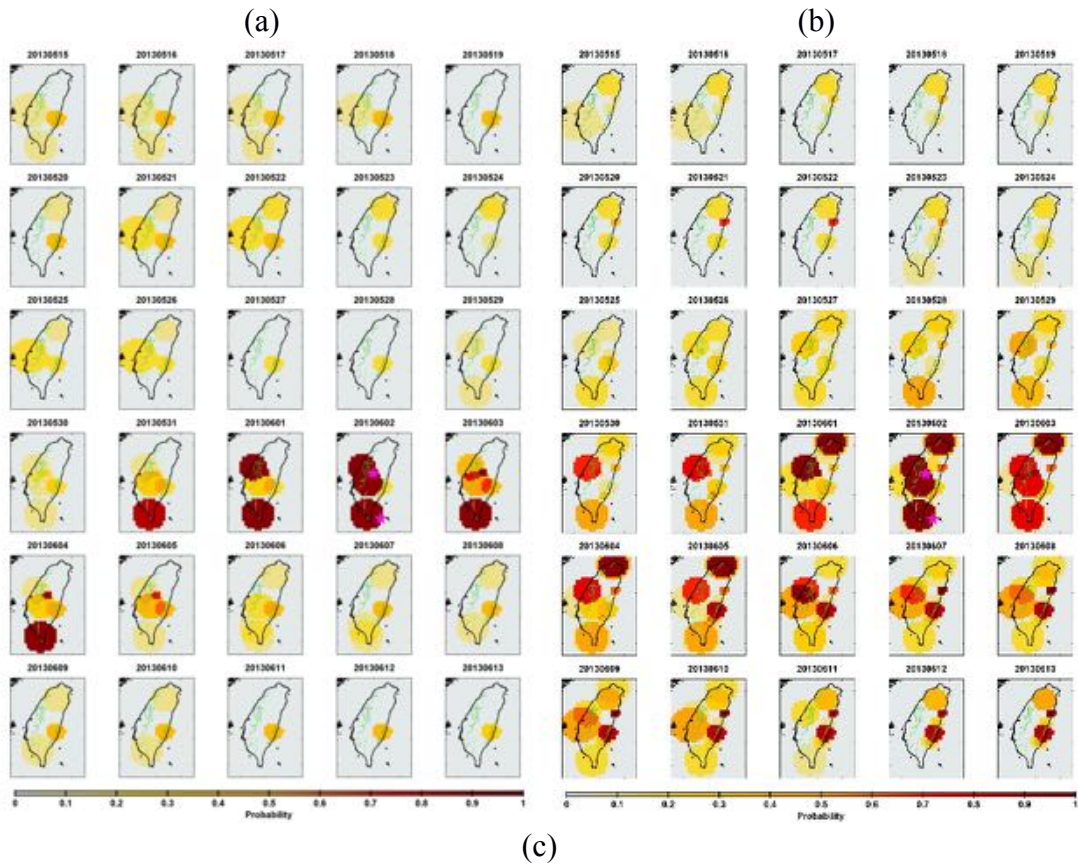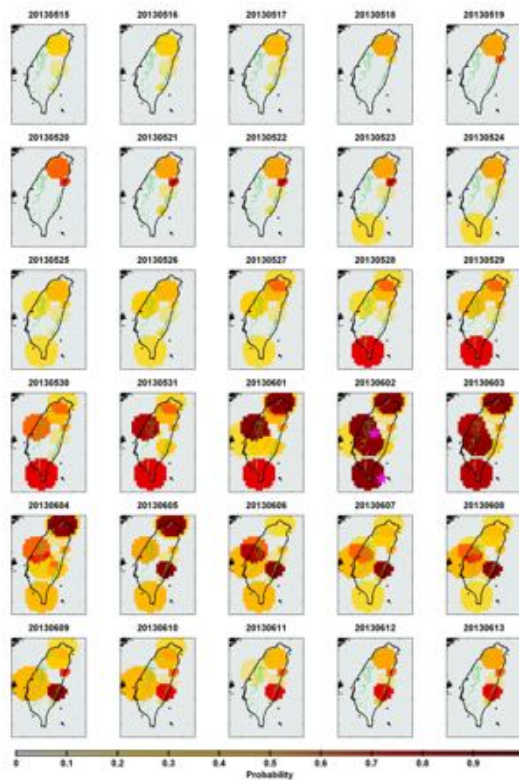
Figure 14. Temporal and spatial probability map of future events for (a) the raw data, (b) the band-pass filtered data with frequency from 10-3.5 to 10-1.75 Hz, and (c) the band-pass filtered data with frequency from 10-4.0 to 10-1.75 Hz.

Conclusions

The improved GEMSTIP algorithm presented in this report is useful to test the correlations between geoelectric anomalies and earthquake occurrences, as shown by the impressive d and D scores of the optimal models on validation datasets featuring several earthquakes M>5. We also showed that the frequency band within $10^{-4.0} \leq f \leq 10^{-1.75}$ Hz may be less contaminated by non-earthquake-related signals. This study thus lays the foundation of very promising earthquake forecasting techniques using non-seismic signals.

Our future work will then focus on applying this general algorithm to other types of recorded signals, possibly optimizing the parameters during daytime and nighttime separately to eliminate solar influence. Of course, the model will be updated as new data are acquired.

Annex D:
Stress-Activated Infrared Emission from Rock Surfaces in the Thermal Infrared (TIR) Window.

In this study, we report on infrared emission experiments that have been conducted to measure the spectral responses of various rocks in response to stresses applied via a hydraulic press and via expanding cement. The data were analyzed using principal components analysis and fluctuation spectroscopy. We report on several previously unknown phenomena, in particular a series of IR emission bands, possibly due to vibrationally excited states of the peroxy bond, and on pink noise suggestive of electron/hole trapping as in a semiconductor.

Introduction

We conducted experiments to test the hypothesis that the infrared emission coming off the surface of the unstressed portion of large rock samples is due to de-excitation of pairs of positive holes recombining to return to the peroxy state. Electrical conductivity studies indicate that the energy needed to break a peroxy bond is about 2.2+/-0.2eV. Conversely, when a peroxy bond forms, a fraction of this dissociation energy will be recovered, probably about 2eV.

Due to this exothermal recombination, the two O^- in the newly formed peroxy bond will be in a vibrationally highly excited state. If this recombination reaction takes place at the surface, de-excitation can take place either (i) by emission of infrared photons at energies corresponding to the downward transitions of the excited O^- pair within the vibrational manifold of the peroxy bond or (ii) by transfer of energy to the neighbors of the peroxy bond leading to local heating by phonon transfer.

The energy of the Si-OO-Si bond is accurately known from quantum mechanical calculations of the peroxy defect in $SiO2$ glass. As jumping more than one level is dipole forbidden, the highest energy quantum, equivalent to 920-930 cm^{-1} or 10.7μm, is associated with the last downward transition from quantum level 1 to the ground state, quantum level 0. Hot transitions within the vibrational manifold from n=2 to n=1, from n=3 to n=2, from n=4 to n=3 etc. are expected to give rise to a series of infrared emission bands at progressively lower transition energies. In addition to the emission of IR, photons at energies corresponding to transitions in the vibrational manifold of the peroxy bond, a broad background of longer wavelength IR emission is expected due to the transfer of energy onto neighboring atoms during thermalization.

Analytical methods

Measuring low levels of non-equilibrium phenomena (e.g. emission) in the presence of a large thermal background can be problematic because the relative intensities can lead to an unfavorable signal-to-noise ratio. Throughout this study, conducted at room temperature, a large thermal background was present due to emission of ambient air, resulting in raw emission spectra that appear to a casual observer to be the ubiquitous graybody spectrum of air at room temperature. In order to overcome this obstacle, we analyzed time-series of spectra in order to separate rapidly changing non-equilibrium quantities from more slowly varying equilibria. Two analytical approaches were considered to accomplish this. The first being principal components analysis (PCA), a common analytical technique that finds routine application in remote sensing spectroscopy. The second is an application of fluctuation spectroscopy. Fluctuation spectroscopy finds application in a variety of regimes, from the analysis of femtoliters of solution, where it can resolve single molecules, to astrophysics.

We believe this to be a novel application of the principles of fluctuation spectroscopy to geophysics. In this approach, the random or nonlinear behavior associated with the non-equilibrium part of the spectrum is characterized by parameterizing the distribution of its associated random variables and observing the manner in which these parameters change over time.

Fluctuation Spectroscopy

We use fluctuation spectroscopy to separate transient non-equilibrium quantities from slowly varying equilibria. By parameterizing the time-dependent moments or cumulants of a time series of spectra, we are able to measure phenomena that would be difficult or impossible to glean from raw spectra or traditional methods.

Given a time-series of measurements of a particular spectral band, it is convenient to detrend the series to a zero-mean process, separating these measurements into the band's mean (equilibrium) value, $S_0(t; v)$, and a zero-mean stochastic process $X(t; v)$. Each element of $X(t; v)$ is a random variable having a zero-mean distribution:

$$S(t; v) = S_0(t; v) + X(t; v) \qquad (1)$$

In the above, the expectation value of $X(t; v)$ is zero and the mean spectrum, $S_0(t; v)$ corresponds to a graybody spectrum, also a function of time. The random variable X describes the spectrum's fluctuations about equilibrium.

In order to analyze the statistical distribution of spectral fluctuations from equilibrium, it is useful to parameterize the distribution of the evolutionary spectral process $X(t; v)$ in terms of moments or cumulants. The nth (raw) moment may be estimated from data as the expected value of X^n. Without correcting for sample bias, this is:

$$m_n = E[X^n] \qquad (2)$$

As long as the distribution decays no slower than exponentially, knowledge of all the moments is equivalent to knowledge of the full distribution of X. For a zero-mean distribution, such as $X(t; v)$, the raw moments are also central moments, which correspond to common statistics: the second moment is the variance, the third moment the skewness, and the fourth the kurtosis.

Since the probability density associated with the spectral fluctuation $X(t; v)$ depends on frequency and time, its moments, cumulants, and other parameters are also functions of both frequency and time to allow for statistical non-stationarity. Local estimates of the distribution of X may be calculated from data. One simple approach is to sample a local neighborhood of the time series within a sliding window of width W and estimate moments or cumulants within this window. For example, time-dependent moments may be estimated as:

$$m_n(\nu, t, W) = \frac{1}{W} \sum_{j=0}^{W} X(t+j, \nu)^n \qquad (3)$$

The width of the sliding window should be small compared to the total time period as the temporal resolution is limited by the width of the sliding window. Shorter windows tend provide better temporal resolution, but the window needs to contain enough data to produce accurate parameter estimates. Within each window, the local value of S_0 corresponds to the average of S.

For each spectral band, a sliding window of fixed length was passed over the time series associated with that band and the distribution of spectral fluctuations was characterized in terms of sample moments within that band. Unless otherwise specified, fluctuations in the second moment (i.e. spectral variance) are presented.

Morse Potential

The simplest quantum mechanical potential energy function capable of representing effects such as bond dissociation is the Morse potential. The functional form of this potential is, up to an additive constant:

$$V(r) = D_e(1 - e^{-a(r-r_0)})^2 \tag{4}$$

Here, D_e is the dissociation energy of the bond, r_0 is the equilibrium bond distance, and the constant a may be expressed in terms of an effective spring constant, k_e, and the dissociation energy as $a = \sqrt{\frac{k_e}{2D_e}}$.

The Schrödinger equation may be solved analytically in this case, and the energy levels of the bound states have the eigenvalues:

$$E(n) = hv_0(n + \frac{1}{2}) - \frac{(hv_0(n + \frac{1}{2}))^2}{2D_e} \tag{5}$$

$$v_0 = \frac{a}{2\pi}\sqrt{\frac{2mD_e}{m}}$$

and the expression holds only for a finite number of energy levels that are less than the dissociation energy. Radiative transitions have frequencies corresponding to differences in energy between these levels. Since the energy levels are quadratic in n, the differences between subsequent levels are linear in n:

$$E(n+1) - E(n) = hv_0(1 - (n+1)\frac{hv_0}{2D_e}) \tag{6}$$

For this reason, the vibrational spectrum associated with a Morse potential consists of a finite number of evenly spaced spectral lines. By performing linear regression, a Morse potential can be fit to a set of observed spectral lines, revealing information about a bond, such as its dissociation energy.

Experimental results

Two sets of experiments were conducted: (1) with rectangular blocks of various rocks, typically 10x10x40-60cm^3, and (2) with large irregular gabbro-norite boulders, up to 7 tons, extracted from the Granite Rock quarry in Aromas, CA, located on the San Andreas Fault.

Rocks Stressed in a Hydraulic Press

Using a hydraulic press with manual controls delivering up to approximately 70,000lbs, rectangular blocks of rocks were stressed at one end via 2-4 rows of up to twenty 6.3 mm diameter stainless steel ball bearings arranged over an area of about 10x10cm^2. The ball bearings served to concentrate the stresses and achieve mechanical failure. The load was increased at a rate sufficient to achieve failure of the stressed end within a few minutes. The IR emission was recorded from the unstressed end of the blocks. After tests had shown that ambient lighting did not affect the spectra or intensity of the IR recorded off the rock surfaces, the experiments were carried out in the fully lighted Engineering Evaluation Laboratory, EEL, at the NASA Ames Research Center, though the movements of people were restricted during stressing to avoid reected IR radiation from warm bodies.

For both sets of experiments, a Bruker VERTEX 70 FT-IR spectrometer was used to collect the ambient temperature IR emission. The VERTEX 70 was equipped with a 5cm diameter, 2m long articulated emission attachment, internally Au-plated, the front end of which holds a 5cm diameter KBr window. This window was placed about 5cm off the rock surface, preferentially above an protruding spot or a rough area produced by a previous fracture. The spectrometer housing and the attachement were ashed with dry N$_2$, but air filled the 5 cm space between the KBr window and the rock surface.

The emission spectra were continuously recorded at 2cm^{-1} resolution over the 600 to 2500cm^{-1} range, or about 16µm to 4µm.

Figure 1 shows the loading force applied to a sample of red granite as a function of time. Fractures can be seen as discontinuous decreases in the applied load. The average spectral variance versus time is shown in Figure 2.

For comparison, PCA was also applied to this data. By applying a variant of PCA in which principal components are calculated within a sliding window, the weight of the first principal component is in close agreement with second-moment fluctuation spectroscopy, as shown in Figure 3. Indeed, close agreement is expected since the component weights in PCA correspond to second moments of a multivariate Gaussian fit to the data. Compared to PCA, fluctuation spectroscopy seems to produce a lower baseline level of noise.

Figure 4 shows the average variance of each spectral band before and during loading. An increase in the amplitude of low frequency noise was a common feature of these experiments. Effectively, the infrared spectral noise became colored in response to stress.
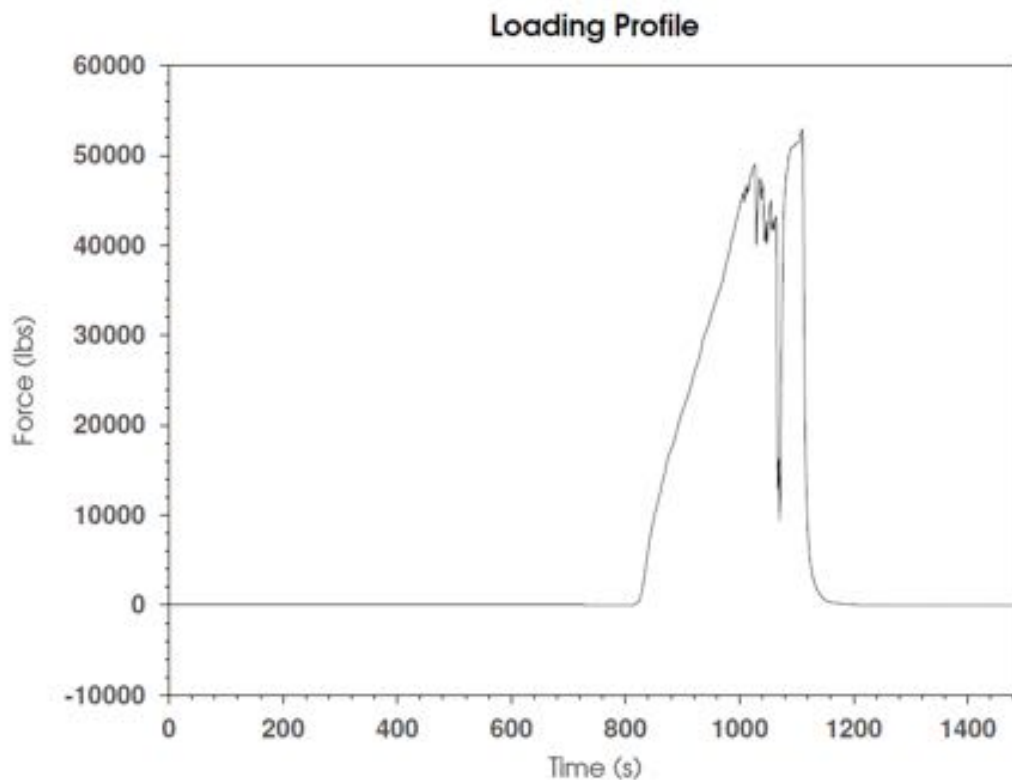
Figure 1. Applied load as a function of time for the red granite sample.
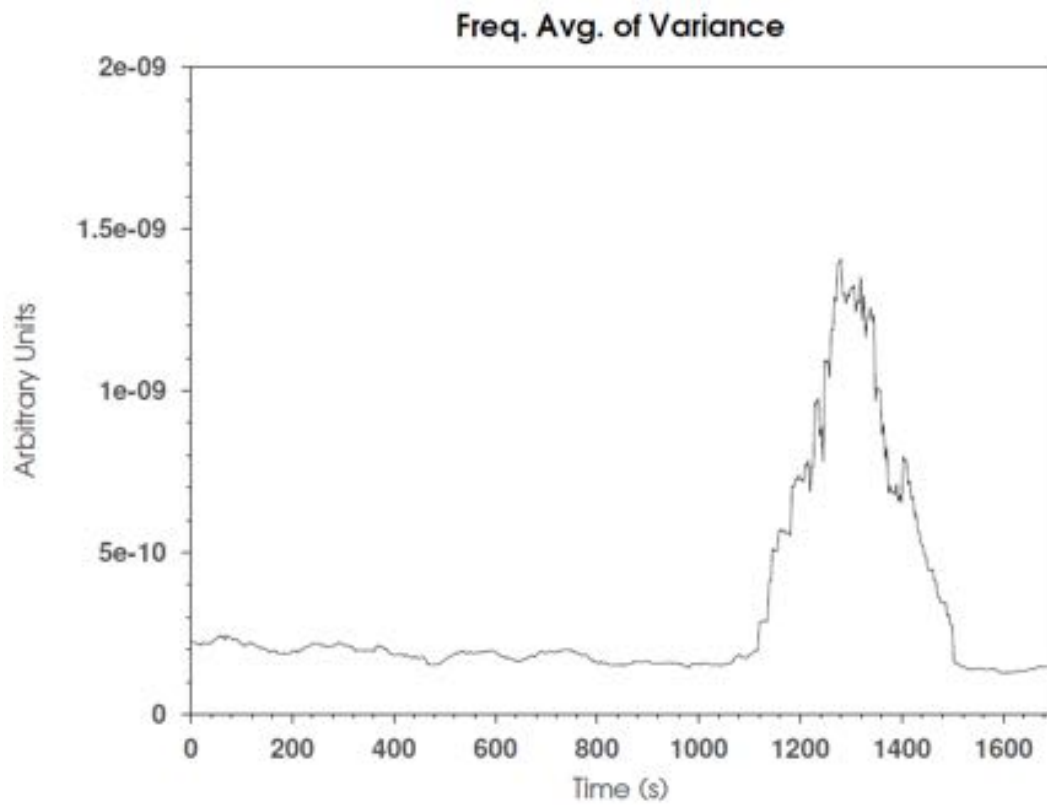
Figure 2. *Red Granite in hydraulic press. Average spectral variance versus time, calculated in a 30-sample sliding window. The rock was eventually pulverized by the press, leading to high levels of TIR activity.*
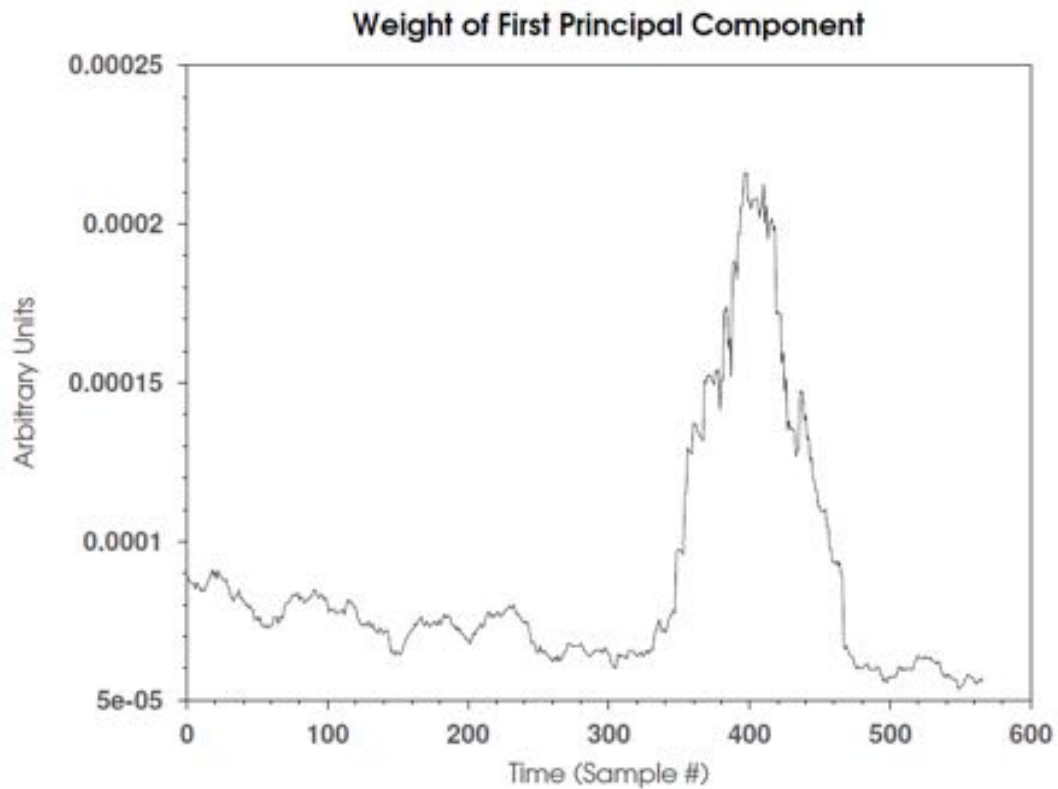
Figure 3. *Red Granite in hydraulic press. Weight of the largest principal component versus time, calculated in a 30-sample sliding window. This is in close agreement with the fluctuation spectroscopy result shown in Figure 2.*
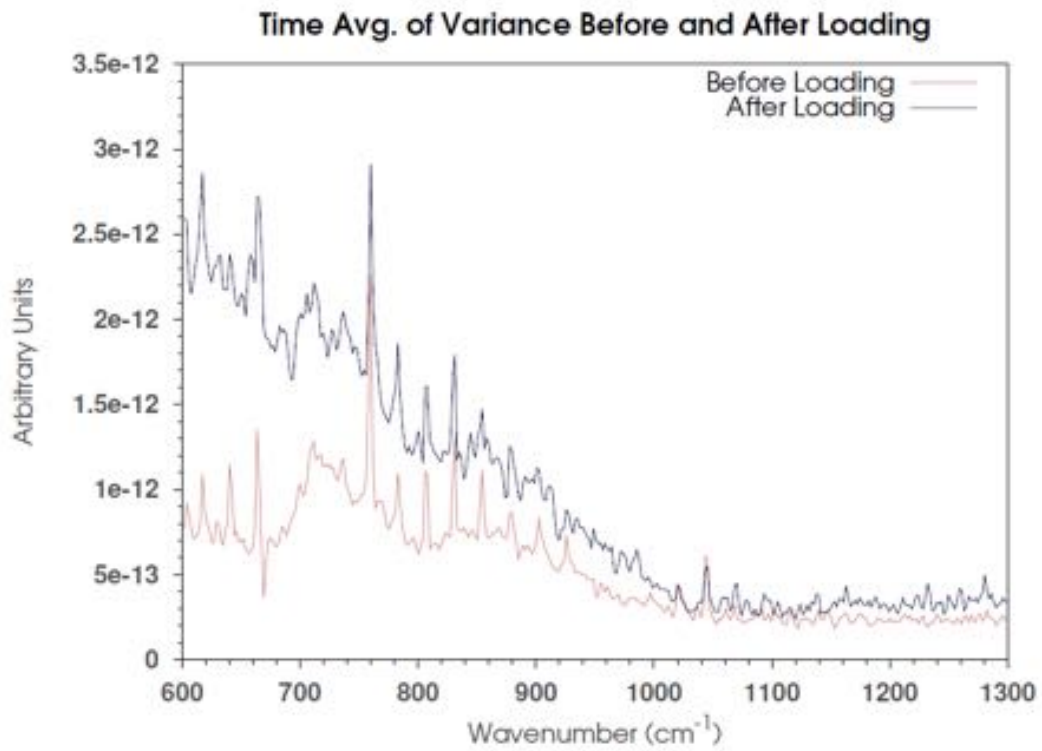
Figure 4*. Red Granite in hydraulic press. Emission activity (average variance) versus frequency. Note the sharp, evenly spaced lines at 760, 783, 807, 831, 854, 878, 902, and 926 cm⁻1.*

Figure 5 shows the loading force applied to a sample of black gabbro as a function of time. The average spectral variance versus time is shown in Figure 6. At the onset of stress, well before failure, the average spectral variance increases (and later decreases) discontinuously. Due to the finite width (30 samples or about 80 seconds) of the sliding window, the IR activity appears to commence prior to loading. This is an artifact due to the finite sampling width of the sliding window.

In all cases, time resolution is limited to the width of the sliding window. A common spectral signature of stress found in these experiments is that the spectrum of noise changes from nearly white noise to colored noise. Lower frequencies generally exhibit wider ranges of fluctuation than higher frequencies, up to a characteristic 'cut-off' or 'corner' frequency that seems to coincide with the 1->0 radiative transition of the peroxy bond around 920-930cm^{-1}. Spectral analysis reveals that, under stress, infrared noise as measured by the VERTEX 70 spectrometer changes from nearly white to colored noise having a 'pink' to 'brown' spectrum. Pink noise is associated with electron and hole trapping in semiconductors, and the appearance of pink noise in the rock could indicate that the rock has undergone a transition from an insulating state to a semiconducting state in response to stress.

A series of sharp peaks was repeatedly noted in these experiments at wavenumbers of 760, 783, 807, 831, 854, 878, 902, and 926 cm^{-1}. The peaks are evenly spaced, so by performing linear regression we obtain an essentially perfect fit to the energy eigenvalues of a Morse potential with $r^2>0.999$. The corresponding molecular bond has 40 bound states and a dissociation energy of 2.29eV.

A 2.29eV dissociation energy agrees with the 2.2+/-0.2 eV dissociation energy obtained from electrical conductivity experiments. Additionally, the ground state transition of 926 cm^{-1} is in good agreement with the 920cm^{-1} derived from computational chemistry calculations of peroxy defects, as well as the suspected ground state transition measured earlier by us at 930cm^{-1}. While a definitive characterization may be premature due to the relative novelty of the analysis presented here, these facts are not inconsistent with the hypothesis of radiative de-excitation of peroxy bonds.
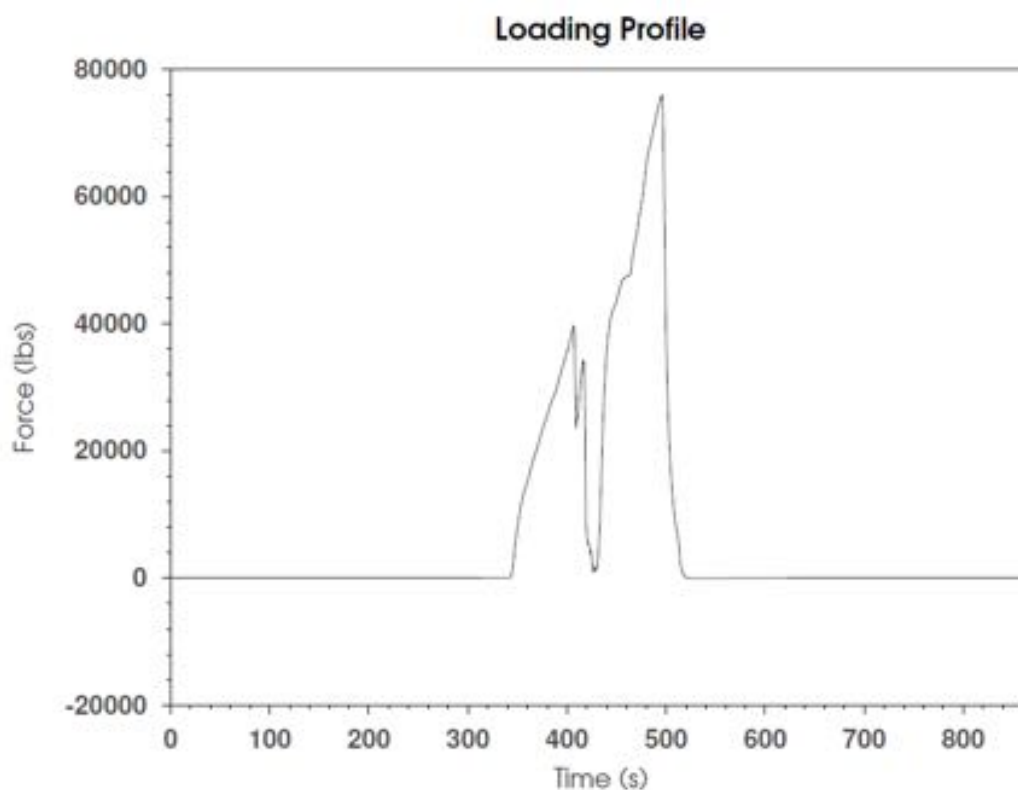
Figure 5. Applied load as a function of time for the red granite sample.
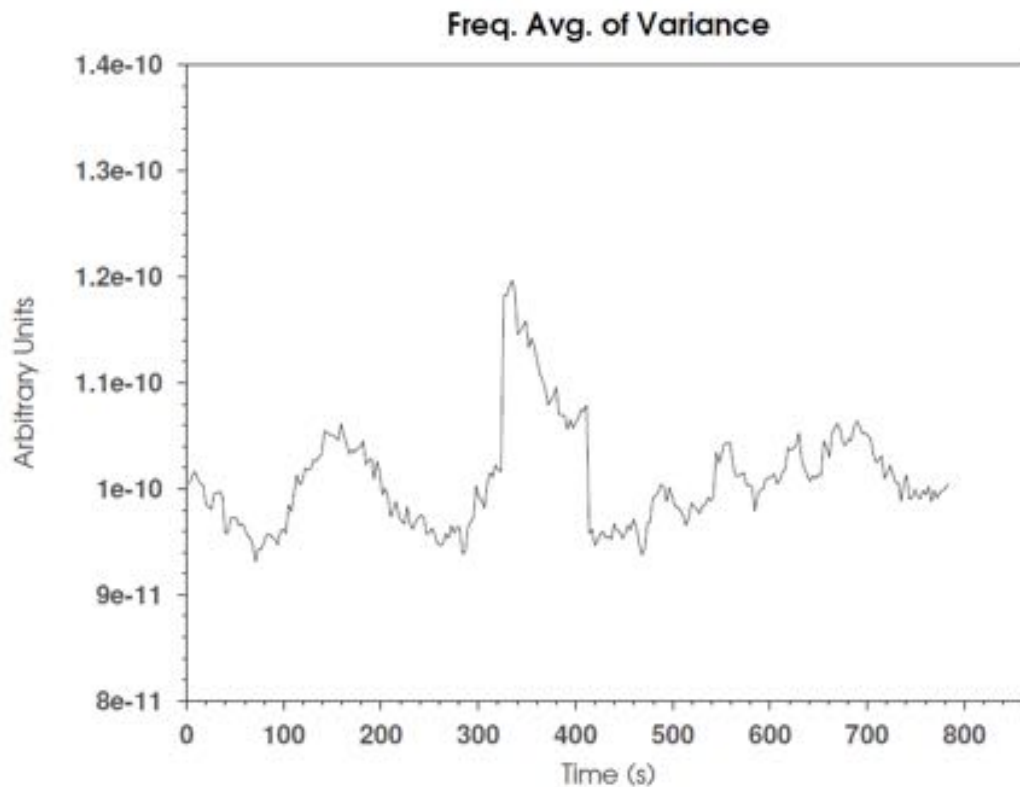
Figure 6. *Black Gabbro in hydraulic press. Average spectral variance versus time, calculated in a 30-sample sliding window.*

Gabbro-Norite Boulders Stressed with BUSTAR

Large boulders (up to 7 tons) were stressed from the inside using BUSTAR expanding cement poured into rows of four 75 cm deep, 6-7 cm diameter boreholes, placed on one side of the boulders, while the IR emission was recorded from the opposite side, about 1m from the boreholes. We conducted 8 runs, each lasting for 8-12 hrs from filling the BUSTAR slurry into the boreholes to final rock failure. The experiments were carried out overnight in a large unheated machine shop hall at the NASA Ames Research Center with the ambient temperatures decreasing from about 18°C around 10pm to around 14°C around 6-7am. The rock boulders were tied up with straps to prevent damage to near-by equipment by falling pieces during failure. While the IR emission was recorded, the boulders were surrounded by screens to shield against stray radiation from the surroundings. The lights in the hall were dimmed to a minimum level and the movement of people in the room was restricted to avoid adventitious IR radiation from body heat reflected off the boulders.

Analyzing the frequency dependence of the time series of each band and averaging over all frequencies, we see that the spectrum of the time series approximately follows a power law, specifically, it exhibits the 'pink' noise profile associated with thermoelectric fluctuations in semiconductors rather than the 'white' noise associated with thermoelectric fluctuations in insulators. A log-log plot, shown in Figure 7, illustrates that the critical exponent of the power law (the slope of the line in log-log scale) is between -1 and -2, colloquially referred to as 'pink' noise.

Applying fluctuation spectroscopy to the data collected from this experiment, we see long periods of low-level thermal fluctuations punctuated by episodes of spectroscopically distinct TIR emission activity. The results of this process can be seen in Figures 8 to 11 (displaying emission spectral variance at various times) for a single TIR event. Analysis of the data confirm the highly dynamic nature of the TIR emission processes, consistent with the preceeding discussion of the mechanisms of the various processes that take place at the rock surface. In particular the TIR emission intensity at low wavenumbers, long wavelengths, confirms that there is a significant rise of the intensity of the stress-induced radiation emitted below 930 cm^{-1}. In addition there are intermittent increases of infrared intensity emitted in the higher wavenumber, higher

energy range, in particular around 1000-1200 cm^{-1}, typical of Si-O and Al-O stretching vibrations and, bursts of emission activity in the 1400-1600 cm^{-1} region, typical for the H_2O bending modes of gas-phase H_2O molecules released from the rock surface. A special feature, which will have to be studied further, is the imbalance between Stokes and anti-Stokes emission lines, indicating that the H_2O molecules released from the rock surface may already be in highly excited states with respect to their bending modes.
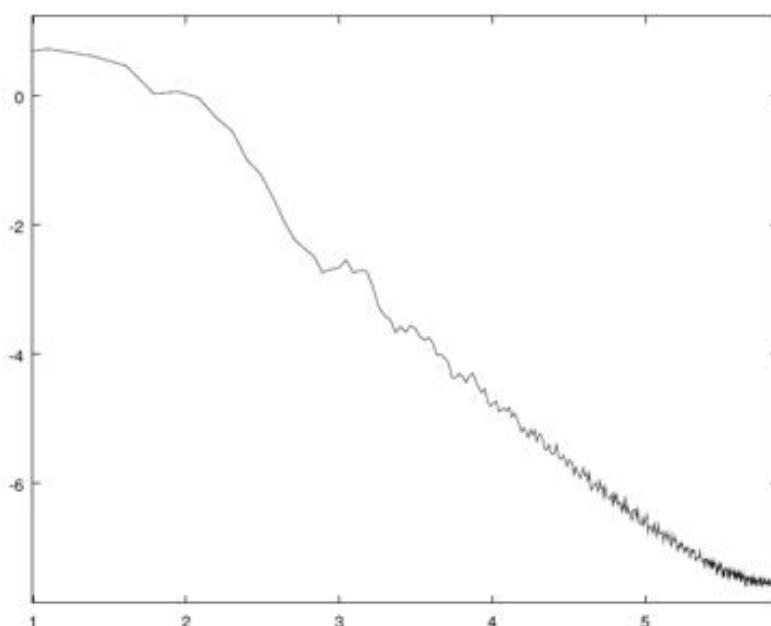
Figure 7. This shows log-frequency (horizontal) vs. log-amplitude (vertical) for the spectrum of the entire Bustar experiment. The slope of the line, corresponding to the critical exponent of the power law, is between -1 and -2, indicating that pink noise dominates the process.

The images shown in Figures 8 to 20 show spectral variance as a function of frequency at various times during the BUSTAR experiment number 5. As the internal stresses built up to the point of causing small fractures about 3.5 hours after start, bursts of infrared emission occurred below 1200 cm^{-1} and in the 1400-1600 cm^{-1} range, interrupted by longer periods of relative calm. About 8 hrs into the run, at 6:40 am, when internal cracking became quite audible (as recorded by the geophone), the intensity of fluctuations in the H_2O rotational emission bands increased drastically. By 6:48 am this H_2O emission had largely subsided, and by 6:50 am it has stopped altogether. At the same time, a strong infrared emission started in the 800-1200 cm^{-1} range, growing through 6:54 am and leading to an off-scale burst of broad-band infrared emission when the boulder broke.

Three major spectral features can be seen. Two are readily identified as the rotational fine structure of the water lines and the CO_2 stretching mode. The third is in the TIR band below 1000cm^{-1} and exhibits an unusual behavior as the rock is being stressed. This long wavelength IR emission band appears to move up and down the spectral range, changing amplitude and shape during TIR emission events. It has a sharp upper cutoff frequency around 1000cm^{-1} that is not exceeded until the final rock failure.

A sequence of snapshots illustrating key features of TIR emission behavior, as revealed by the spectral kurtosis, is seen in Figure 21. At first, a TIR peak can be seen around 900-950cm^{-1} and drifting to lower frequencies. At the onset of a major TIR event, the peak grows and moves upward in frequency before hitting its upper limit of 1000cm^{-1} at the end of the TIR event. The reason for this dynamic response is not fully understood, but could be related to the ground state of the peroxy bond around 920-930cm^{-1}.

Once the rock begins to fail as indicated by cracks forming at an increasing rate, the TIR peak appears to 'break through' the 1000cm^{-1} barrier, propagating upward to higher frequencies, possibly filling energy levels vacated during rupture. Another energy barrier around 770cm^{-1} can be seen during this final stage.

In contrast to the hydraulic press experiments, which collected the IR emission spectra every 2-3 seconds, a 1 minute sampling time was used during the BUSTAR experiments. Thus, by averaging out short fluctuations the fluctuation spectra from the BUSTAR experiments look smoother.

Similar observations were made during the other BUSTAR experiments of this series, testifying to the dynamic and spectral complexity of the stress-induced infrared emission. The Stokes region of the H_2O bending mode emission tended to be more strongly populated than the anti-Stokes region. The reason for this deviation from thermodynamic equilibrium is not presently understood. It may be related to the fact that the gas-phase H_2O molecules emitting under these conditions were in a highly excited vibrational state with respect to their bending mode. Further work will be needed to clarify this and other new features of the IR emission experiments.

Conclusions

By analyzing subtle fluctuations in the infrared emission spectrum of rocks, several previously unknown phenomena have been observed, offering confirmation of a number of earlier studies and hypotheses regarding the nature of positive hole charge carriers in stressed rock.

While at rest, in their normal insulating state, rocks exhibited TIR fluctuations similar to white noise. Thermal fluctuations produce white noise in insulators due to Johnson-Nyquist thermoelectric noise currents. As rocks were loaded, however, it was found that lower frequencies had greater fluctuations (variances) during periods of stress, up to a cutoff (or 'corner') frequency around $1000cm^{-1}$, beyond which white noise dominates. This suggests that some underlying physical process was producing colored noise. Pink noise is consistent with electron/hole trapping during direct current flow in semiconductors, a mechanism that has been proposed by us for thermal infrared emission and other electromagnetic phenomena in rocks. Observations of higher-order fluctuations (such as spectral kurtosis) also reveal activity in the $900-1000cm^{-1}$ range. Spectral lines are observed, starting at $926cm^{-1}$, and these lines have a nearly perfect fit to a Morse potential with a 2.29eV dissociation energy.

All these observations are consistent with activity near the ground state transition of the peroxy bond, theoretically calculated to be $920cm^{-1}$, as well as the experimentally measured dissociation energy of 2.2+/-0.2 eV.

Thus, more than 25 years after the first reports were published on TIR anomalies associated with active faults and earthquakes, a comprehensive picture of the underlying physical processes begins to emerge. The early ideas that emanation of warm gases might be the cause of these remarkable TIR anomalies, can be put to rest in view of the wealth of data presented in this study. What has emerged instead is a story of a series of complex solid state and interfacial processes that start with

the presence of peroxy defects in most, if not all rocks in the Earths crust down to about 35-45 km, including the depth range, 7-45 km, where a large majority of tectonic earthquakes originate. Available evidence suggests that many of these peroxy defects sit on grain boundaries or even straddle adjacent mineral grains. Therefore, when stresses are applied, those peroxy defects are particularly susceptible to activation, releasing positive hole charge carriers that can flow out of the stressed rock volume.

When the positive hole charge carriers arrive at the surface, they become trapped at the ground-to-air interface and build up a positive surface-subsurface charge. Because positive holes repel each other electrostatically, they accumulate on surfaces, especially at points of high curvature. For this reason they accumulate preferentially on topographic highs such as mountain ridges. If more positive holes arrive, their number density in the surface-subsurface layer reaches a critical value above which they will begin to recombine, returning to the peroxy state. This recombination, which is exothermal, leads to vibrationally highly excited states of the oxygen anions participating in this reaction. The exothermal recombination in turn leads to the emission of IR photons at energies representative of the radiative de-excitation of the peroxy bonds and of other bonds excited in the process.

At the same time, as peroxy bonds form in the surface, each deposits two positive charges into the surface, limiting and eventually stopping the resupply of positive hole charge carriers from below. As a result the IR emission from the surface must stop.

However, at sufficiently high positive surface-subsurface charges and sufficiently high electric fields another process sets in: field ionization of air molecules, probably O_2 leading to O^+_2 . The delivery of electrons to the surface reduces the positive surface charge, thereby setting the stage for a resumption of the flow of positive holes to the surface. Their exothermal recombination will lead to a renewed IR emission from the surface. In essence, it becomes clear that the IR emission from the rock surface is controlled by a complex interplay of at least two major processes, coupled in space and time, plus possibly other processes that have an effect on the wavelength (energy) of the IR emission.
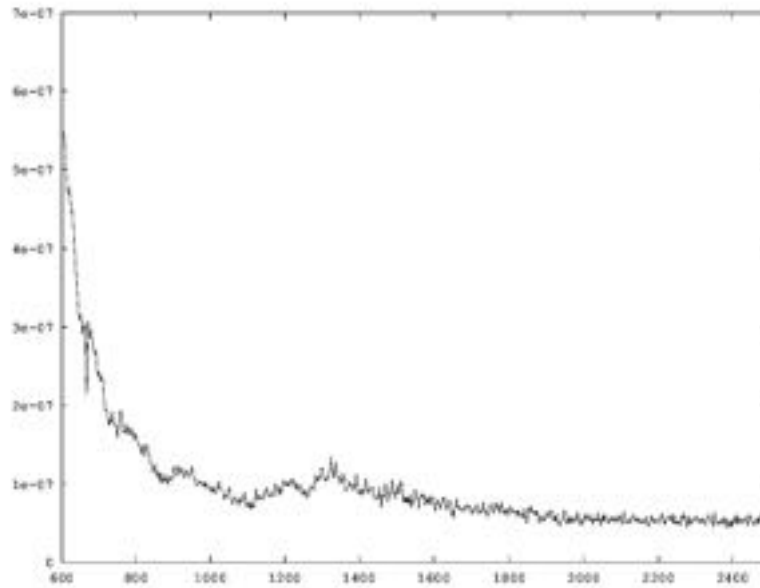
Figure 8: *This image, approximately 30 minutes after the start of the experiment, shows a typical background. (spectral variance as a function of frequency)*
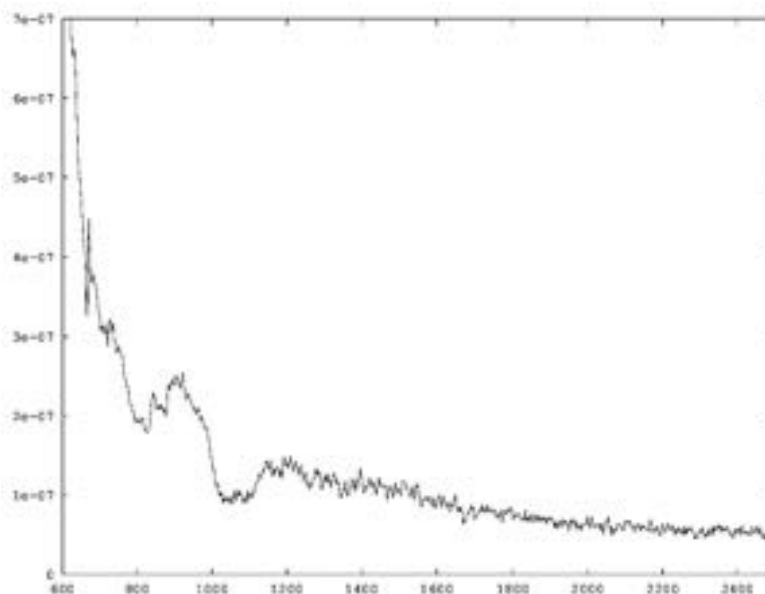
Figure 9: *This image, approximately 4 hours after the start of the experiment, shows the onset of a TIR event. (spectral variance as a function of frequency)*
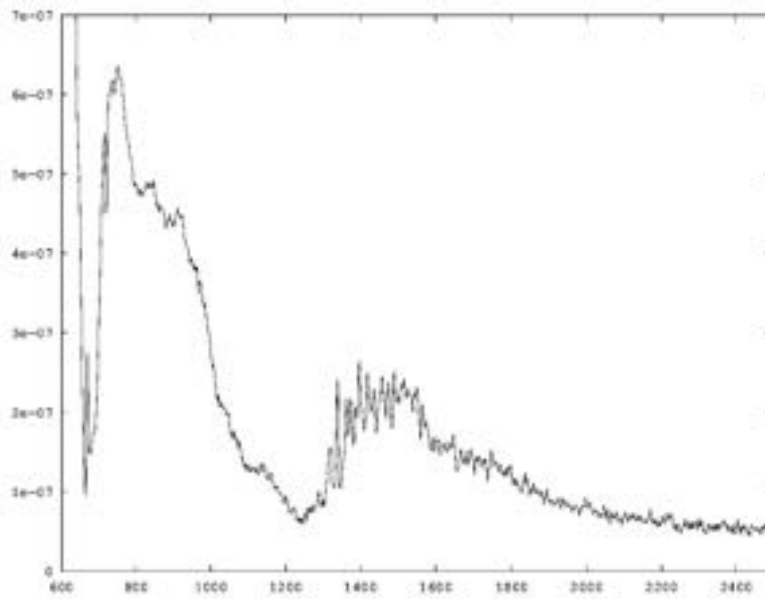
Figure 10: *This image, approximately 4 hours and 15 minutes into the experiment, shows the peak activity of a TIR event.*
(spectral variance as a function of frequency)
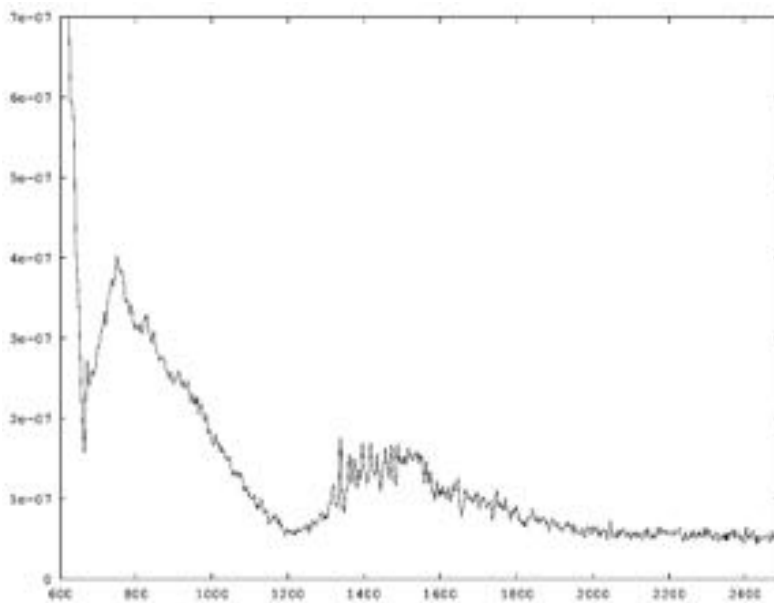
Figure 11: *This image, around 4 and a half hours into the experiment, shows the decline of a TIR event.*
(spectral variance as a function of frequency)
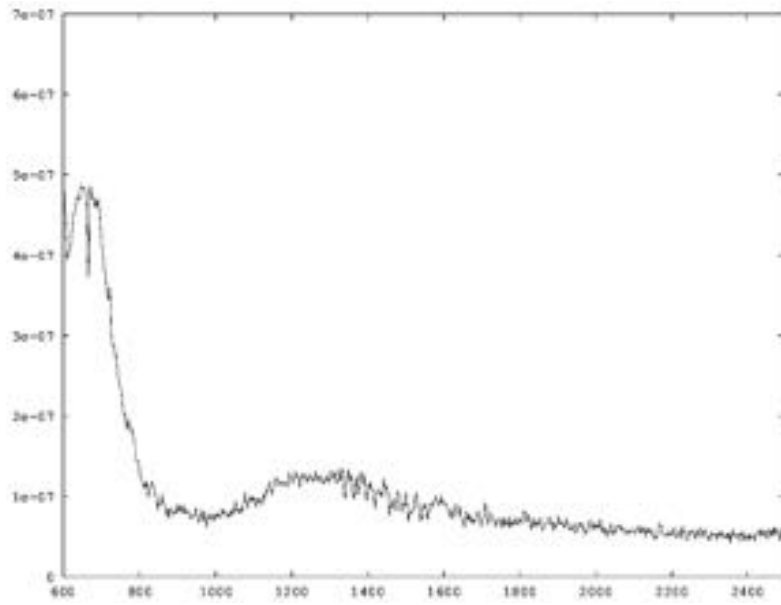
Figure 12: *This image, from about 5:20, shows spectral activity just prior to another TIR event.*
(spectral variance as a function of frequency)
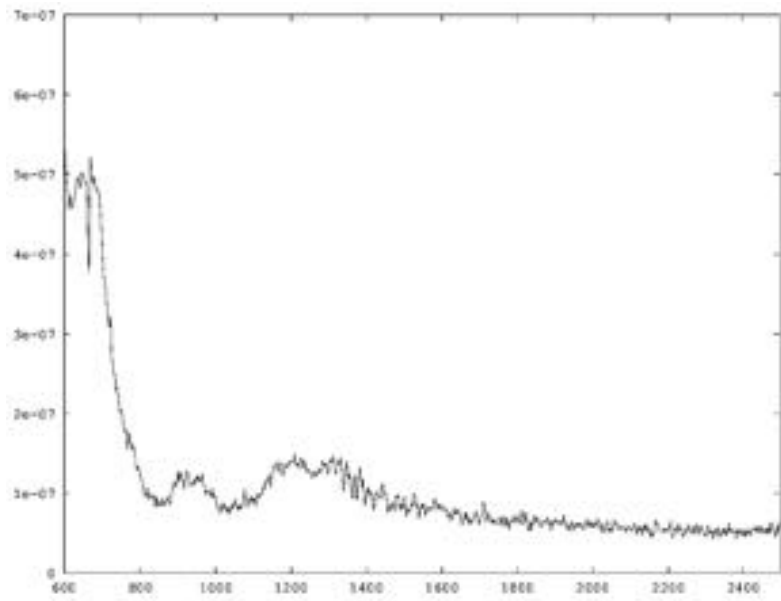
Figure 13: *This image, from 5:25, shows the onset of a TIR event.*
(spectral variance as a function of frequency)
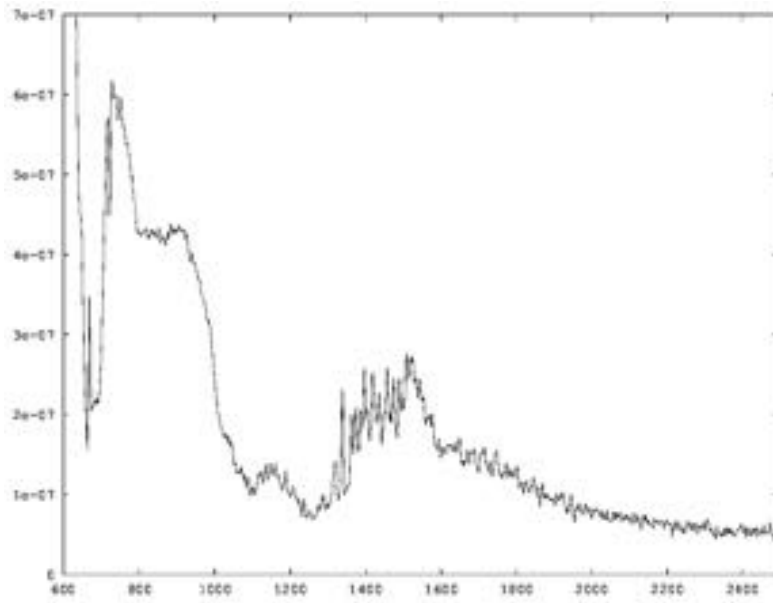
Figure 14: Peak of a TIR event at 5:42.
(spectral variance as a function of frequency)
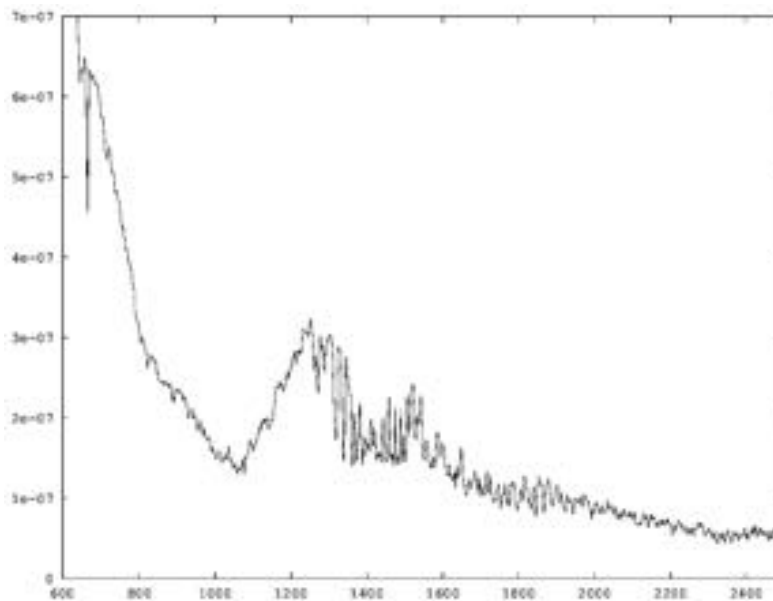
Figure 15: This image, from 6:07, shows the onset of TIR activity associated with a
fracture event.
(spectral variance as a function of frequency)
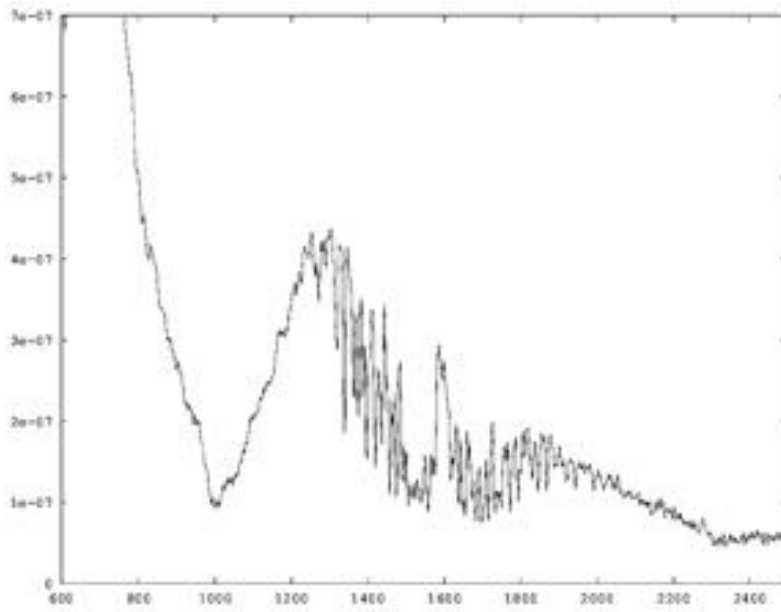
Figure 16: This image, from 6:40, shows the peak of TIR activity associated with a
fracture event, distinct from the earlier TIR events. Note the increased presence of water lines.
(spectral variance as a function of frequency)
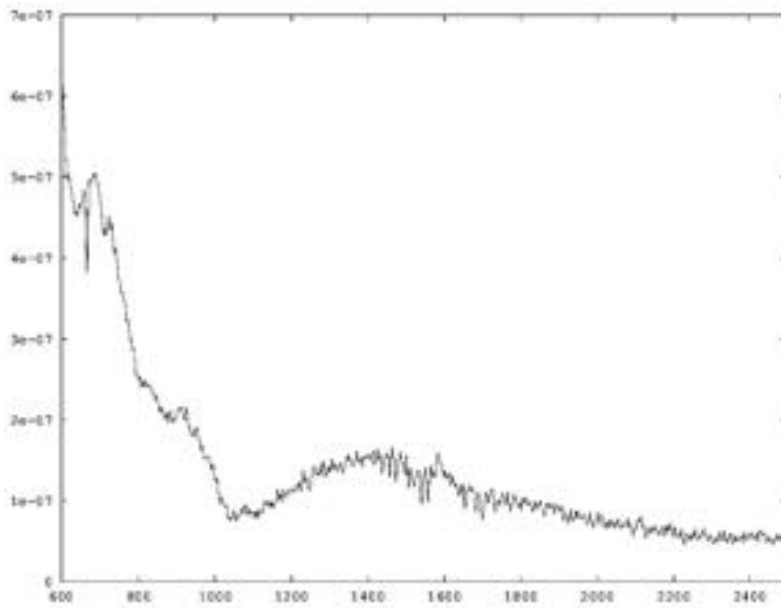
Figure 17: This image, from 6:48, shows TIR activity after a fracture event.
(spectral variance as a function of frequency)
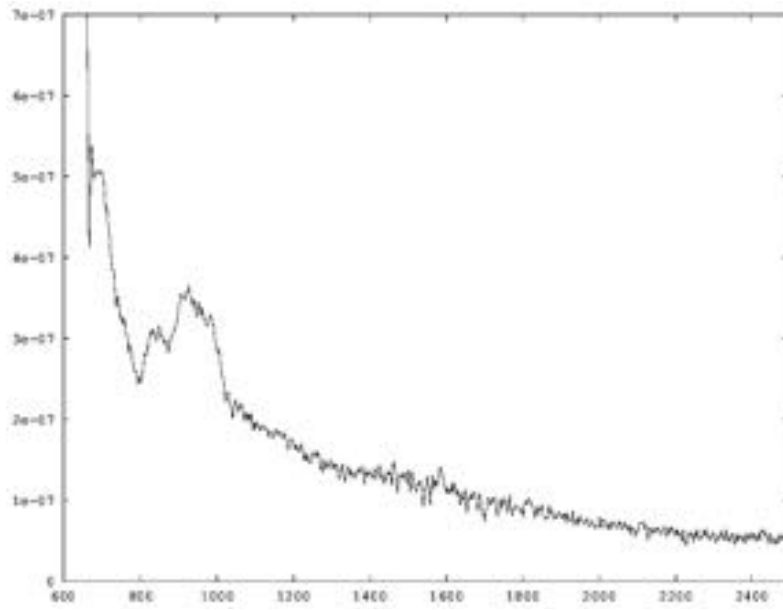
Figure 18: *This image, from 6:50, shows the onset of TIR activity from a fracture that destroyed the rock.*
(spectral variance as a function of frequency)
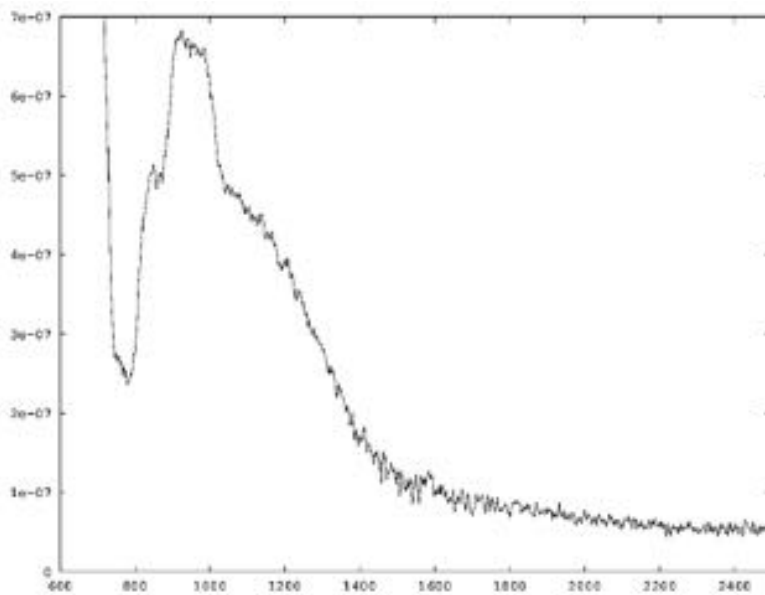
Figure 19: *This image from 6:54 shows TIR activity from a fracture that destroyed the rock.*
(spectral variance as a function of frequency)
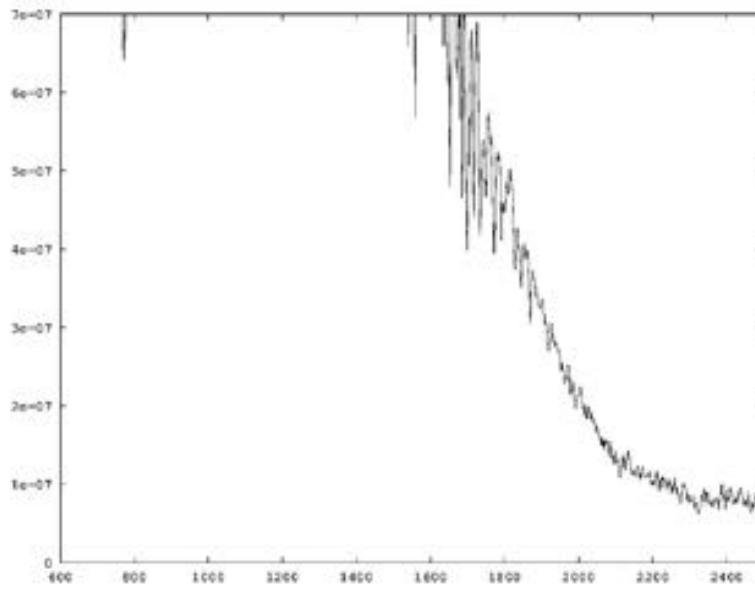
Figure 20: This image from the end of the 8-hour experiment shows continued TIR activity, mostly off the scale of the graph, from the fracture that destroyed the rock. (spectral variance as a function of frequency)
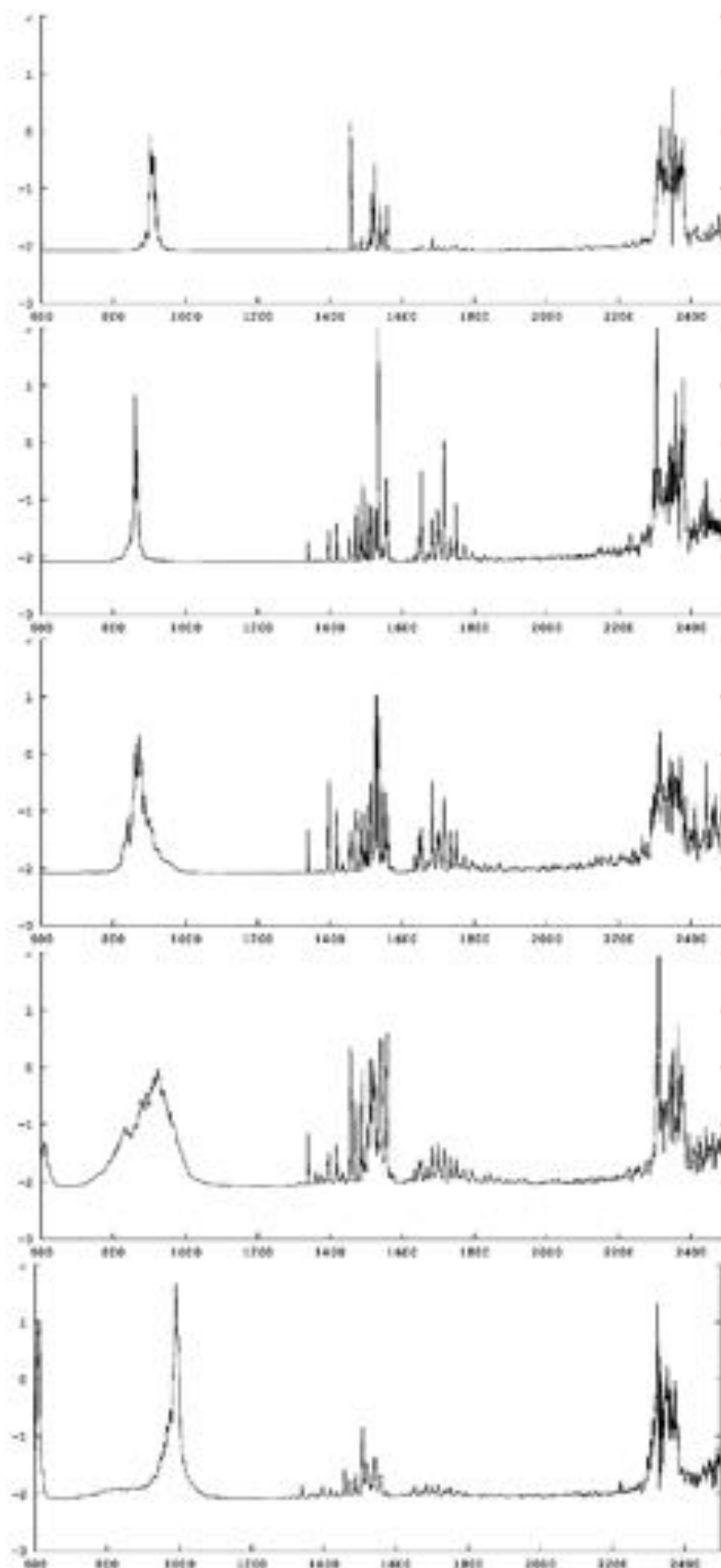
Figure 21: These plots show changes in spectral kurtosis (horizontal axis: frequency). In the first image, a dynamic peak can be seen just around 900-950cm^{-1}. In the second, The dynamic peak has drifted below 900cm^{-1}. In the third, the peak grows and changes shape. The fourth shows the continued evolution of this peak. In the last figure, the peak seems to hit an upper cutoff around 1000cm^{-1}.

Annex E:
Coupled electrokinetic Burridge-Knopoff model of fault sliding events and transient geoelectric signals.
(Hong-Jia Chen, Chien-Chih Chen, Guy Ouillon, Didier Sornette)

This work is the continuation of the collaboration initiated with the National Central University of Taiwan (Pr. Chien-Chih Chen). The goal is to study the possible morphology of anomalous signals before large earthquakes. Hong-Jia Chen, who spent a year at ETH, will defend his PhD this Summer. We introduce the first fully self-consistent model combining the seismic micro-ruptures occurring within a generalized Burridge-Knopoff spring-block model with the nucleation and propagation of electric charge pulses within a coupled electrokinetic system. This model provides a general theoretical framework for modeling and analysing geoelectric precursors to earthquakes. In particular, it is able to reproduce the unipolar pulses that have often been reported before large seismic events, as well as various observed anomalies in the statistical moments of the ambient electric fields.

Spring-block system

To begin with, we introduce a one-dimensional spring-block system. We consider a linear chain of N blocks of identical mass m pulled over an interface at a velocity v_L by a loading plate as shown in Fig. 1. Each block is connected to the loading plate by a spring with stiffness K_L, while adjacent blocks are connected to each other by a spring with stiffness K_C. In our study, geometrical boundary conditions are assumed to be periodic so that the Nth block is linked with the 1st one.

The blocks slide over a perfectly flat frictional interface. The static stability condition for each block is given by:

$$K_L x_i + K_C(2x_i - x_{i-1} - x_{i+1}) < F_{Si}, \quad i = 1 \text{ to } N, \qquad (1)$$

where F_{Si} is the threshold static frictional force of the ith block, and x_i is the position of the ith block relative to the loading plate. During strain accumulation due to the loading by the plate motion, all blocks are motionless relative to the interface and witness the same increase of their coordinates relative to the loading plate:

$$\frac{dx_i}{dt} = v_L, \quad i = 1 \text{ to } N, \qquad (2)$$

When the resulting force of the springs connected to the ith block exceeds the static threshold F_{Si}, the block begins to slide. The dynamic slip of the ith block, including inertia effects, is now given by:

$$m\frac{d^2 x_i}{dt^2} + K_L x_i + K_C(2x_i - x_{i-1} - x_{i+1}) = F_{Di}, \quad i = 1 \text{ to } N, \qquad (3)$$

where $F_{Di} < F_{Si}$ is the dynamic frictional force acting on the ith block. The sliding of one block can trigger the instability of the other blocks, thus forming a multi-blocks event. When the velocity of a block is zero, it sticks to the interface with zero velocity if the static friction criterion Eq. (1) is satisfied; if not satisfied, the block continues to slip according to Eq. (3).
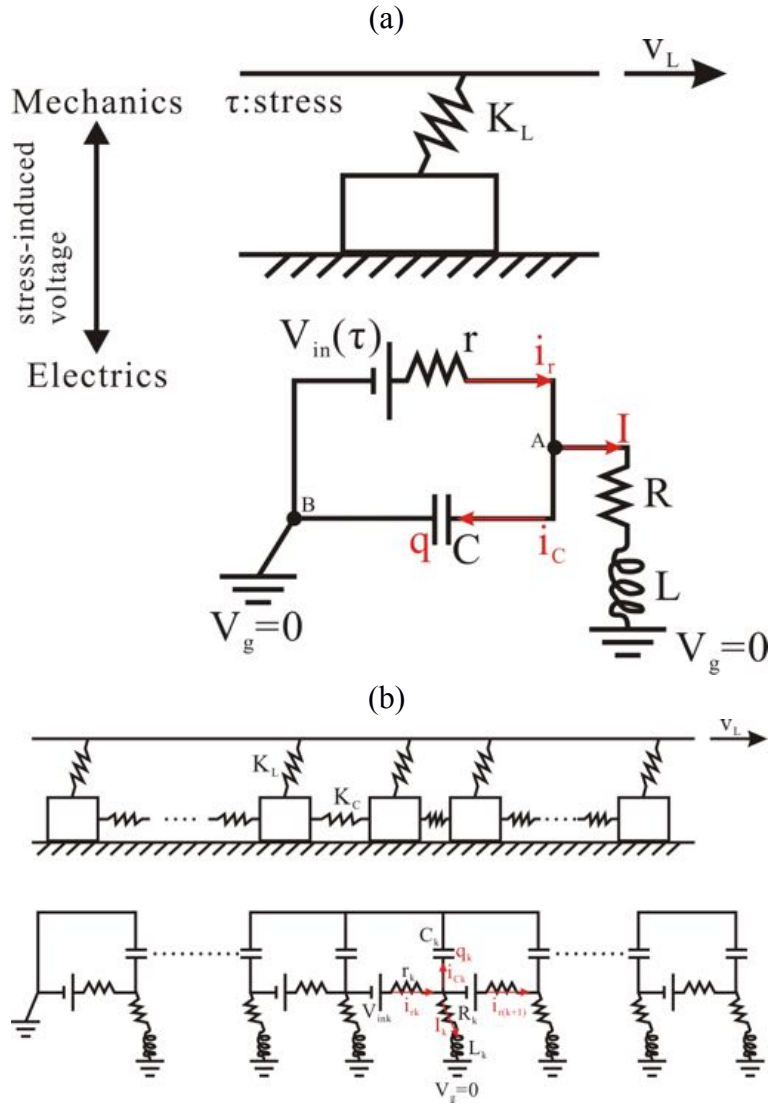
Figure 1. Schematic diagram of the Chen-Ouillon-Sornette model, combining a spring-block system and an electrokinetic system (a) for a single-block case, and (b) for a multi-blocks case.

In order to scale the above-mentioned equations, we introduce the following non-dimensional variables and parameters:

$$T_f = t\sqrt{\frac{K_L}{m}}, \; T_s = \frac{tK_Lv_L}{F_S^{ref}}, \; X_i = \frac{K_Lx_i}{F_S^{ref}}, \; \phi = \frac{F_{Si}}{F_{Di}}, \; s = \frac{K_C}{K_L}, \; \mu_i = \frac{F_{Si}}{F_S^{ref}}. \tag{4}$$

The parameter s is the stiffness ratio, representing the level of conservation of energy in the system. A larger stiffness ratio indicates a higher level of conservation or a lower level of dissipation of energy in the system, while the probability of multi-blocks, larger-sized events increases with s. The ratio ϕ of static to dynamic frictional forces is assumed to be the same for all blocks, but the quantity μ_i varies from block to block with F_S^{ref} being a reference value for the static frictional force (here, the minimum value of all the F_{Si}'s). Stress accumulation takes place during the 'slow time T_s' when all blocks are stable, and slipping of blocks occurs during the 'fast time T_f' when the loading plate is assumed to be approximately immobile. In terms of these non-dimensional variables and parameters, the static stability condition Eq. (1) becomes:

$$X_i + s(2X_i - X_{i-1} - X_{i+1}) = \tau_i < \mu_i, \quad i = 1 \; to \; N, \tag{5}$$

where τ_i stands for the stress acting on the ith block. The strain accumulation Eq. (2) becomes:

$$\frac{dX_i}{dT_s} = 1, \quad i = 1 \ to \ N. \tag{6}$$

The dynamic slip Eq. (3) becomes:

$$\frac{d^2X_i}{dT_f^2} + X_i + s(2X_i - X_{i-1} - X_{i+1}) = \frac{\mu_i}{\phi}, \quad i=1 \ to \ N. \tag{7}$$

Finally, we define the total amount of slip within the spring-block system as:

$$D_{SB}^{(t)} = \sum_{i=1}^{N}\left(X_i^{(t)} - X_i^{(t-1)}\right), \tag{8}$$

where t stands for the slipping time points.

In this work, we set $N=128$, $s=30$, $\phi=1.5$, while the μ_i's are assigned to blocks using a uniform random distribution within the range $1<\mu_i<3.5$.

Electrokinetic system: single-block problem
Description and governing equations
Experiments on positive hole charge carriers in rocks provide evidence that the production of electric charges (hence voltage, the equivalent of an electrical pressure) is proportional to the applied stress, due to the constant resistance of the compressed material. Hence, we consider that the mechanical and electrical variables within the crust are coupled through a stress-induced voltage (V_{in}), such that:

$$V_{in}(\tau) = \beta \cdot \tau, \tag{9}$$

where β is a positive constant and τ is the stress. We also assume that each block plays the role of a resistor with resistance r and of a capacitor with capacitance c, as shown in Fig. 1a. The block capacitor charges or discharges depending on the stress acting on the block. On the other hand, the block is embedded in the Earth's crust, i.e. is electrically grounded. The grounded current (I) passes through a grounded resistor with resistance R and a grounded inductor with inductance L.

According to the above-mentioned scheme, the equations of the RLC-type circuit for $N=1$ (Fig. 1a) are derived as follows. First, Kirchhoff's voltage law in the block provides:

$$V_{in} - i_r r - \frac{q}{c} = 0. \tag{10}$$

Second, the current-charge relation in the block capacitor yields:
$$i_c = \frac{dq}{dt}. \tag{11}$$

Third, using Kirchhoff's current law between the block and the ground (at node A in Fig. 1a), we get:

$$i_r = I + i_c. \tag{12}$$

Finally, the equality of the voltage of the block capacitor and the grounded component (using nodes A and B in Fig. 1a) gives:

$$IR + \frac{dI}{dt}L = \frac{q}{c}.$$ (13)

The quantity V_{in} is the stress-induced voltage as mentioned above, i_r is the current flowing away from the anode and passing through the block resistor (r), q stands for the stored charges of the block capacitor (c), and i_c is the current flowing towards the block capacitor (c). The unknown time-dependent variable vector is $G=[q, i_c, i_r, I]$ with the initial condition $G(t=0)=\vec{0}$.

This new model combining the mechanics of stick-slip in a spring-block system with the generation and propagation of electric charges within a coupled RLC circuit, is coined the Chen-Ouillon-Sornette (COS) model hereafter. The mechanical component of the system is essentially a one-dimensional Burridge-Knopoff model, which is used to simulate stick-slip motions and earthquake ruptures. On the other hand, the electrokinetic component consists of a series of RLC-type circuits, while the peroxy-defect theory is used to motivate the description of the coupling between the stress acting on blocks with the amount of electric charges newly created. The model is sketched on Fig. 1a for a single-block case and on Fig. 1b for a multi-blocks case.

Analytical solutions
Using the four Eqs. (10)-(13), we solve the problem analytically in the single-block case. In order to reduce the number of control parameters [r, c, R, L], we scale all of them by the grounded resistance R:

$$\hat{r} = \frac{r}{R}, \hat{c} = cR, \hat{L} = \frac{L}{R}, \widehat{V_{in}} = \frac{V_{in}}{R}.$$ (14)

Therefore, the R-scaled electrokinetic equations are:

$$\widehat{V_{in}} - \hat{r}i_r - \frac{q}{\hat{c}} = 0,$$
$$i_c = \frac{dq}{dt},$$ (15)
$$i_r = I + i_c,$$
$$I + \hat{L}\frac{dI}{dt} = \frac{q}{\hat{c}}.$$

In order to study the Green's function of such an electrokinetic system, we set $\widehat{V_{in}}(t)$ as a Dirac delta function $\delta(t)$, and use the Laplace transform rather than the Fourier transform because the electric behavior of the system is transient, not periodic. Taking the Laplace transform of Eqs. (15), they become, respectively:

$$1 - \hat{r}\tilde{i}_r - \frac{\tilde{q}}{\hat{c}} = 0,$$
$$\tilde{i}_c = s\tilde{q},$$ (16)
$$\tilde{i}_r = \tilde{I} + \tilde{i}_c,$$
$$\tilde{I} + \hat{L}s\tilde{I} = \frac{\tilde{q}}{\hat{c}},$$

where $\tilde{f}(s) = L[f(t)]$ is the notation for the Laplace transform. Note that the initial conditions are set to $G(t=0)=\vec{0}$. After combination of these equations, we get:

$$\tilde{q}(s) = \frac{\hat{c} + \hat{c}\hat{L}s}{(1+\hat{r}) + (\hat{L} + \hat{r}\hat{c})s + (\hat{r}\hat{c}\hat{L})s^2},$$ (17)

which finally yields:

$$\tilde{q}(s) = \frac{\left(s + \frac{1}{\hat{L}}\right)}{\hat{r}\left[s^2 + \left(\frac{1}{\hat{r}\hat{c}} + \frac{1}{\hat{L}}\right)s + \left(\frac{1}{\hat{r}\hat{c}\hat{L}} + \frac{1}{\hat{c}\hat{L}}\right)\right]}. \tag{18}$$

By setting $\zeta = \frac{1}{\hat{r}\hat{c}} + \frac{1}{\hat{L}}$, $\eta = \frac{1}{\hat{r}\hat{c}\hat{L}} + \frac{1}{\hat{c}\hat{L}}$, and $\Delta = \zeta^2 - 4\eta$, we obtain three different cases for the Green function $q_{gf}(t)$ as follows:

Case 1 ($\Delta > 0$) - overdamping solution:

$$q_{gf}^{(od)}(t) = \frac{e^{\frac{-\zeta+\sqrt{\Delta}}{2}t}\left(\frac{-\zeta+\sqrt{\Delta}}{2} + \frac{1}{\hat{L}}\right) + e^{\frac{-\zeta-\sqrt{\Delta}}{2}t}\left(-\frac{1}{\hat{L}} - \frac{-\zeta-\sqrt{\Delta}}{2}\right)}{\hat{r}\sqrt{\Delta}}. \tag{19}$$

Case 2 ($\Delta = 0$) - critical damping solution:

$$q_{gf}^{(cd)}(t) = \frac{e^{-\frac{\zeta}{2}t}\left[t\left(-\frac{\zeta}{2} + \frac{1}{\hat{L}}\right) + 1\right]}{\hat{r}}. \tag{20}$$

Case 3 ($\Delta < 0$) - underdamping solution:

$$q_{gf}^{(ud)}(t) = \frac{e^{-\frac{\zeta}{2}t}\left[\omega\cos(\omega t) + \left(-\frac{\zeta}{2} + \frac{1}{\hat{L}}\right)\sin(\omega t)\right]}{\omega\hat{r}}, \tag{21}$$

where $\omega = \frac{\sqrt{|\Delta|}}{2}$ is the natural frequency.

For criticality, we set $\left(\hat{r}, \hat{c}, \hat{L},\right) = (r_c, c_c, L_c)$, so that:

$$\Delta(r_c, c_c, L_c) = 0. \tag{22}$$

Expanding and summarizing Eq. (22), we have:

$$L_c^2 - 2r_c c_c L_c + r_c^2 c_c^2 - 4r_c^2 c_c L_c = 0. \tag{23}$$

Solving Eq. (23) for L_c, we get:

$$L_c = \begin{cases} \left(2r_c + 1 + 2\sqrt{r_c^2 + r_c}\right)r_c c_c \\ \left(2r_c + 1 - 2\sqrt{r_c^2 + r_c}\right)r_c c_c \end{cases}. \tag{24}$$

Therefore, we obtain the resistance-capacitance-inductance phase space, as shown in Fig. 2a. The set of (r_c, c_c, L_c) values forms two critical surfaces (CD1 and CD2) in the phase space, separating this phase space into three regions, i.e. two overdamping regions (OD1 and OD2) and one underdamping region (UD).

(a)
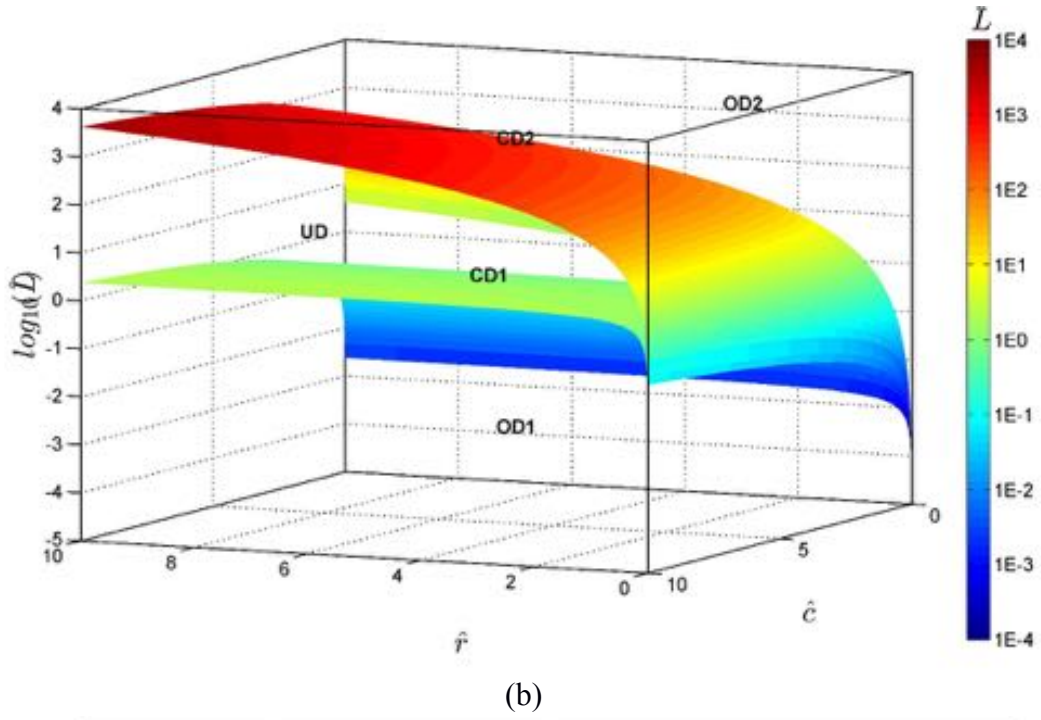
(b)
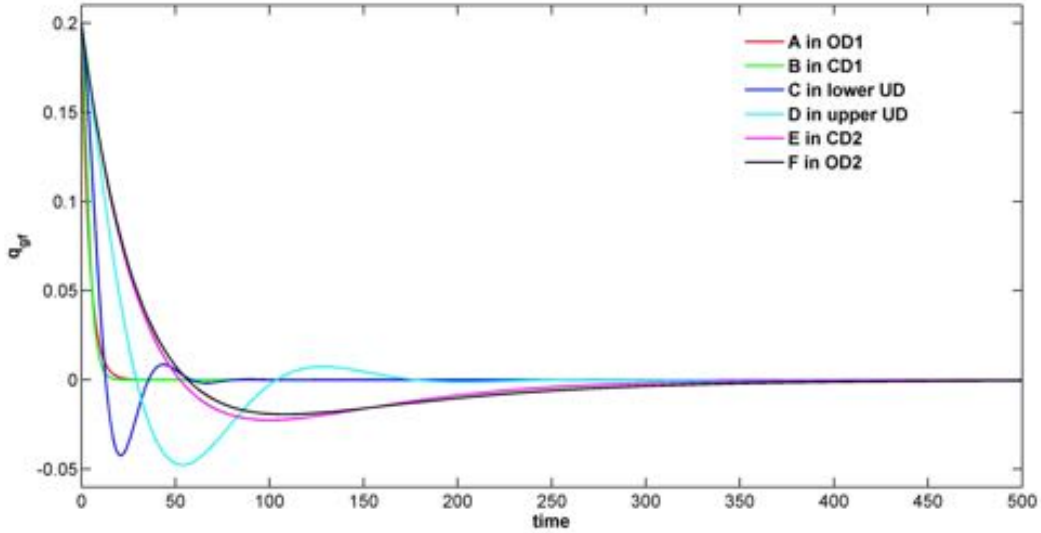
Figure 2. (a) Resistance-capacitance-inductance phase space, and (b) Green functions of charge series $q_{gf}(t)$ corresponding to different damping regions of the phase space. Information of sets A to F is listed in Table 2.

We select, for instance, six sets of $(\hat{r}, \hat{c}, \hat{L},)$ values to calculate their corresponding Green functions of charge series $q_{gf}(t)$ according to Eqs. (19)-(21), and shown on Fig. 2b. The six sets are A (5, 5, 0.1) in the lower overdamping region (OD1), B (5, 5, ~1.1387) on the lower critical damping surface (CD1), C (5, 5, 10) in the lower underdamping region (lower UD), D (5, 5, 100) in the upper underdamping region (upper UD), E (5, 5, ~548.8613) on the upper critical damping surface (CD2), and F (5, 5, 700) in the upper overdamping region (OD2), respectively. Information on the six selected sets, including ζ, η, Δ, are also listed in Table 1. The time series A and B for $q_{gf}(t)$ decay much faster and without oscillations, whereas for C and D, $q_{gf}(t)$ decays while oscillating around zero, but $q_{gf}(t)$ decays faster for C than for D. Finally, $q_{gf}(t)$ for E and F decay much slower with overshooting below zero and rebounding close to zero.

Set	$\hat{r}$	$\hat{c}$	$\hat{L}$	Damping Region	ζ	η	Δ	ω	Q1 (%)	Q2 (%)	Q3 (%)	Q4 (%)	b (slope)
A	5	5	0.1	OD1	10.04	2.40	91.20		6.85	93.15	26.32	73.68	2.12±0.39
B	5	5	$\widehat{L_{c1}}$	CD1	0.92	0.21	0		6.96	93.04	26.32	73.68	2.16±0.42
C	5	5	10	UD	0.14	0.024	-0.0764	0.14	8.67	91.33	26.32	73.68	2.05±0.24
D	5	5	100	UD	0.05	0.0024	-0.0071	0.04	15.95	84.05	21.49	78.51	1.77±0.04
E	5	5	$\widehat{L_{c2}}$	CD2	0.418	4.37E-4	0		13.60	86.40	18.42	81.58	1.72±0.03
F	5	5	700	OD2	0.414	3.43E-4	3.45E-4		13.17	86.83	16.23	83.77	1.72±0.03

Table 2. Information of the electrokinetic parameters of the six selected sets in the Chen-Ouillon-Sornette model.
Note: (i) $\widehat{L_{c1}}$=~1.1387 and $\widehat{L_{c2}}$=~548.8613. (ii) Q1+Q2=1 and Q3+Q4=1, respectively. (iii) The range of b value is mean ± 1 standard deviation.

Relationship between stress drops and voltage fluctuations

We assume a given stress time series (τ), which is the simulated stress from a spring-block system, as shown in the upper panel of Fig. 3a. If the ratio $\beta=1$, the time series also represents the stress-induced voltage. Now, we convolve the stress-induced voltage with a Green function $q_{gf}(t)$, as derived above. Dividing this convolution series by the block capacitance (c), we obtain a block voltage series (V_{SB}), as shown in the lower panel of Fig. 3a. The different series represent the block voltages of sets A to F, whose parameters are listed in Table 1. At the beginning of those series, a short-term transient state exists during the period 0-2000 time units. This transient state is ignored in the later analysis.

By differentiating the stress time series, we get the stress drops ($\Delta\tau$), as shown in the upper panel of Fig. 3b:

$$\Delta\tau_t = \tau_t - \tau_{t-1}, \tag{25}$$

where t is any time point. On the other hand, we also consider relative voltage fluctuations (V_{fluc}), as shown in the lower panel of Fig. 3b, defined as:

$$V_{fluc}^{(t)} = \left| \frac{V_{SB}^{(t)} - V_{SB}^{(t-1)}}{V_{SB}^{(t)}} \right| \cdot 100, \tag{26}$$

where t is any time point. In order to compare the stress drop of an event with its corresponding relative voltage fluctuation, we define the maximal value of V_{fluc} associated to an event:

$$V_{fluc}^{max}(i) = max\{V_{fluc}^t, \quad t(i) \le t < t(i+1)\}, \tag{27}$$

where $t(i)$ is the occurrence time of the ith event. Figure 3c shows the relationship between the stress drop of an event and its corresponding maximal relative voltage fluctuation. Overall, the stress drops and maximal voltage fluctuations follow a linear relationship.
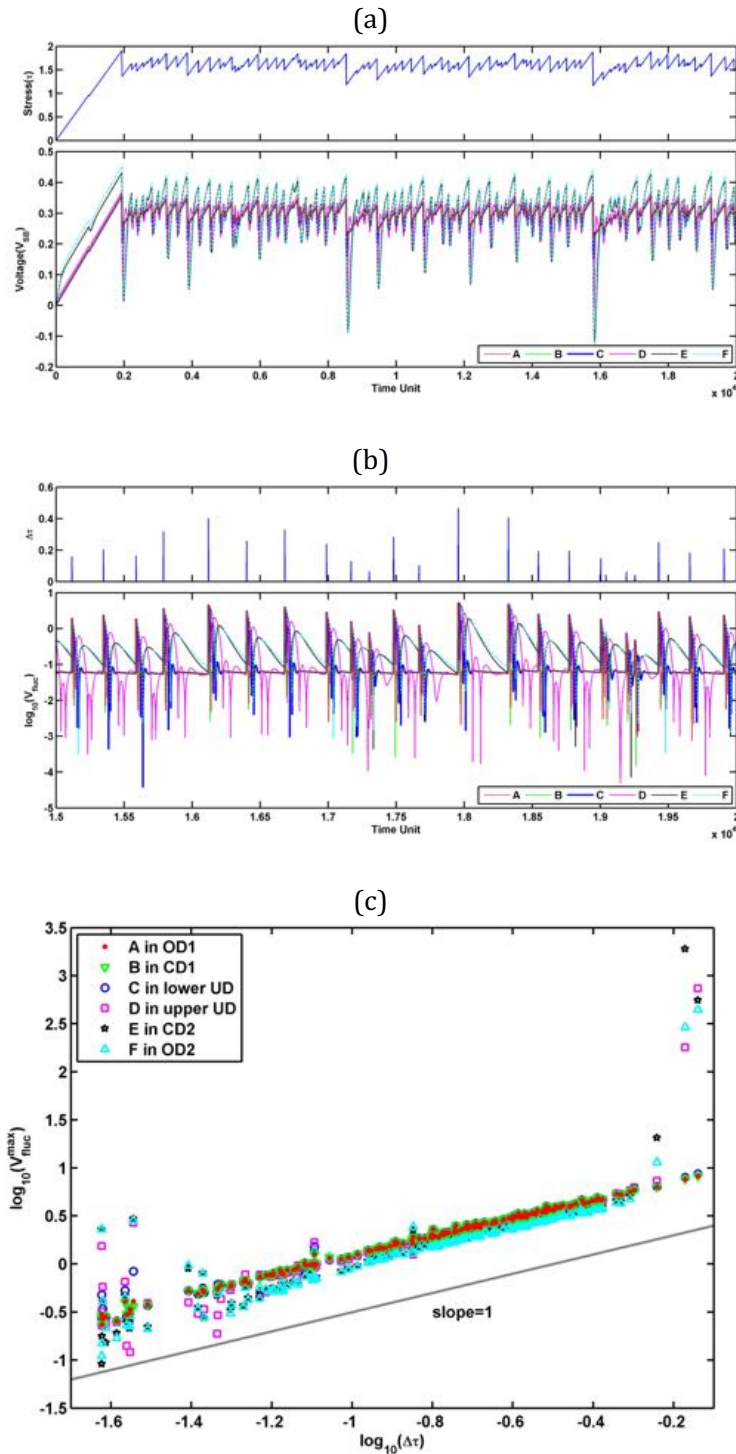
Figure 3. In the single-block model, (a) time series of stress (τ) and its block voltage (VSB) for sets A to F. (b) Time series of stress drop (Δτ) and relative voltage fluctuation (Vfluc) for sets A to F. (c) Scatter plot of the stress drop of an event and its corresponding maximal voltage fluctuation in a log-log scale. The gray line with slope=1 is plotted as reference.

Intuitively, we expect that small and large stress drops generate small and large voltage fluctuations, respectively. In fact, such a simple relationship may not always hold in the presence of complex spatio-temporal dynamics of the interacting blocks. In a heterogeneous multi-blocks COS model, it is possible that relatively small ruptures generate locally relatively large voltage fluctuations, especially for the blocks located in the upper UD, CD2, and OD2 regions of the phase space. This phenomenon would allow us to detect foreshock-induced electric signals, while the foreshocks themselves are below the detection threshold of seismic networks.

Electrokinetic system: multi-blocks problem

Governing equations

It is easy to expand the previous single-block model to a multi-blocks system, as shown in Fig. 1b. All notations remain the same, except that we add a subscript k relative to each block. Furthermore, the polarization direction (p_d) of stress-induced voltages should be considered here, so that Eq. (9) becomes:

$$V_{ink}(\tau_k) = p_{dk}\beta_k\tau_k, \tag{28}$$

where $p_{dk} = \begin{cases} 1, & \tau_{k-1} \geq \tau_{k+1} \\ -1, & \tau_{k-1} \leq \tau_{k+1} \end{cases}$, which is roughly consistent with the observation of Freund's experiments that positive holes flow from more stressed areas to less stressed ones. Note that p_d in the kth block is assigned randomly to 1 or -1 when $\tau_{k-1} = \tau_{k+1}$. The Kirchhoff's voltage law in the kth block gives:

$$\begin{cases} V_{in1} - i_{r1}r_1 - \frac{q_1}{c_1} = 0 \\ V_{ink} - i_{rk}r_k - \frac{q_k}{c_k} + \frac{q_{k-1}}{c_{k-1}} = 0, \quad k = 2 \ to \ N \end{cases} \tag{29}$$

For the current-charge relation in the kth block capacitor, we have:

$$i_{ck} = \frac{dq_k}{dt}, \quad k = 1 \ to \ N. \tag{30}$$

We then write the Kirchhoff's law for the current flowing towards the neighboring blocks or ground:

$$\begin{cases} i_{rk} = I_k + i_{ck} + i_{r(k+1)}, \quad k = 1 \ to \ N-1 \\ i_{rN} = I_N + i_{cN} \end{cases} \tag{31}$$

The equality of the voltages of the kth block resistance, stress-induced voltage, and RL components becomes:

$$\begin{cases} I_1 R_1 + \frac{dI_1}{dt}L_1 = V_{in1} - i_{r1}r_1 \\ I_k R_k + \frac{dI_k}{dt}L_k - I_{k-1}R_{k-1} - \frac{dI_{k-1}}{dt}L_{k-1} = V_{ink} - i_{rk}r_k, \quad k = 2 \ to \ N \end{cases} \tag{32}$$

The multi-blocks unknown variable vector is $\textbf{\textit{G}}=[q_k, i_{ck}, i_{rk}, I_k]$ for $k=1$ to N, with the initial condition $\textbf{\textit{G}}(t=0)=\vec{0}$. Finally, we define the total voltage of the electrokinetic system as follows:

$$V_{SB} = \frac{1}{N}\sum_{k=1}^{N}\left(R_k I_k + L_k \frac{dI_k}{dt}\right) = \frac{1}{N}\sum_{k=1}^{N}\frac{q_k}{c_k}. \tag{33}$$

The total voltage V_{SB} is analog to the voltage measured in real field experiments, which we propose to be associated with the leakage of currents into the ground. In the COS model, that voltage is proportional to the sum of the grounded currents (I_k) through grounded resistors (R_k) and grounded inductors (L_k), which is also equal to the voltage due to the charges stored in the block capacitors (c_k). Again, we use the grounded resistance R_k to scale the other parameters, as done in Sec. 3.2. We introduce a scaled parameter for the mechanical-electrical coupling:

$$\widehat{\beta_k} = \frac{\beta_k}{R_k}, \quad k = 1 \ to \ N. \tag{34}$$

The stress-induced voltage Eq. (28) becomes:

$$\widehat{V_{ink}}(\tau_k) = p_{dk}\widehat{\beta_k}\tau_k, \quad k = 1 \ to \ N.$$ (35)

Equations (29)-(33) now become:

$$\begin{cases} \widehat{V_{in1}} - i_{r1}\widehat{r_1} - \frac{q_1}{\widehat{c_1}} = 0 \\ \widehat{V_{ink}} - i_{rk}\widehat{r_k} - \frac{q_k}{\widehat{c_k}} + \frac{q_{k-1}}{\widehat{c_{k-1}}} = 0, \quad k = 2 \ to \ N \end{cases}$$ (36)

$$i_{ck} = \frac{dq_k}{dt}, \quad k = 1 \ to \ N,$$ (37)

$$\begin{cases} i_{rk} = I_k + i_{ck} + i_{r(k+1)}, \quad k = 1 \ to \ N-1 \\ \qquad i_{rN} = I_N + i_{cN} \end{cases}$$ (38)

$$\begin{cases} I_1 + \frac{dI_1}{dt}\widehat{L_1} = \widehat{V_{in1}} - i_{r1}\widehat{r_1} \\ I_k + \frac{dI_k}{dt}\widehat{L_k} - \alpha_{k-1}I_{k-1} - \alpha_{k-1}\frac{dI_{k-1}}{dt}\widehat{L_{k-1}} = \widehat{V_{ink}} - i_{rk}\widehat{r_k}, \quad k = 2 \ to \ N \end{cases}$$ (39)

$$\widehat{V_{SB}} = \frac{1}{N}\sum_{k=1}^{N}\left(I_k + \widehat{L_k}\frac{dI_k}{dt}\right) = \frac{1}{N}\sum_{k=1}^{N}\frac{q_k}{\widehat{c_k}}.$$ (40)

The parameter α in Eq. (39) is the ratio of adjacent grounded resistances ($\alpha_k = R_k/R_{k+1}$), which we set to unity, meaning that the grounded resistance is spatially homogeneous. For the sake of simplicity, we set the same parameters $[\widehat{\beta_k}, \widehat{r_k}, \widehat{c_k}, \widehat{L_k}]$ for all blocks, i.e. $[\hat{\beta}, \hat{r}, \hat{c}, \widehat{L}]$. We also set $\hat{\beta} = 1$, as it will act as a simple scaling factor for all voltages, and are left to study the effects of varying $\hat{r}$, $\hat{c}$, and $\widehat{L}$ on the simulated voltage $\widehat{V_{SB}}$.

Numerical analysis results

In the COS model, the multi-blocks problem is far more complicated than the single block one due to interactions among elements. Hence, we solve all the differential equations of the mechanical and electrokinetic systems numerically (using a 4th order Runge-Kutta method). We first implement the spring-block system in order to generate the stress (τ_k) acting on each block and use Eq. (35) to generate the stress-induced voltage ($\widehat{V_{ink}}$). We simulate the fully coupled COS model using the values of electrokinetic parameters listed in Table 1. In these simulations, the number of blocks is N=128, and the stiffness ratio is s=30.

We observe how the simulated voltage behaves at different damping conditions, as shown in Fig. 4. Figure 4a shows the simulated slips (D_{SB}), simulated voltage ($\widehat{V_{SB}}$), and relative voltage fluctuations (V_{fluc}) as defined in Eq. (26). Repeating the same analysis of correlations between slips and relative voltage fluctuations as above on the multi-blocks case, we get the empirical relationship between the slip during an event and its corresponding maximal V_{fluc} value (defined as in Eq. (27)), as shown in Fig. 4b. The scatterplot of Fig. 4b is separated into four quadrants (Q1 to Q4), whose boundaries are set by gaps on slip and voltage fluctuation ($D_{SB}^{thr} = 1$ sets the vertical threshold separation, while $V_{fluc}^{thr} = 100$ sets the horizontal one). For the relatively small slip cases, we consider the ratios Q1/(Q1+Q2) and Q2/(Q1+Q2), respectively. Quadrant Q1 features events with small slips but large voltage fluctuations, while Q2 features events with small slips and small voltage fluctuations. For the relatively large slip case, we compute Q3/(Q3+Q4) as well as Q4/(Q3+Q4). The results are listed in Table 1. One can observe that the ratios defined above for cases A to C are different than for cases D to F. This suggests that there exists a transition of slip-voltage relationships between the lower and upper UD regions as defined on the phase space on Fig. 2a. This predicts a possible variability of slip-induced voltage

statistics depending on local constitutive parameters. This variability explains in turn why large earthquake slips are not systematically followed by large electric signals, as the crust is not in a damping state favorable to such dynamics. On the other hand, our results clearly suggest that precursory electromagnetic signals may be observed before large events if: (i) there are slip foreshocks, i.e. small earthquakes that would be too small to be detected seismically; (ii) the local damping conditions allow them to leave a measurable electromagnetic fingerprint. The COS model thus offers a nice opportunity to test for this feature, provided we modify its mechanical part in order to allow for such small precursory slips.

(a)

(b)

Figure 4. In the multi-block model, (a) time series of slips (DSB) and block voltage (VSB) and relative voltage fluctuations (Vfluc) for sets A to F. (b) Scatter plot of the slip amount of an event and its corresponding maximal voltage fluctuation. (c) Proportions of small or large voltage fluctuations corresponding to small or large slips for sets A to F. Note that Q1+Q2=1 and Q3+Q4=1, respectively.

Discussion

Field observations of electromagnetic signals suggest the existence of propagating unipolar pulses prior to earthquakes. The proposed COS model generates unipolar voltage changes due to local stress drops, which could be analogous to the real observations. Furthermore, the small-scale ruptures before a large event could generate unipolar signals with different properties, depending on the underground electrokinetic parameters, their amplitudes and shapes being controlled by the underground resistance, capacitance, and inductance. Besides, the background values of the spring-block voltage $\widehat{V_{SB}}$ is not zero (see Figs. 3a and 4a), suggesting that the measurement of mean values of natural occurring geoelectric fields in a certain period might be used to infer to the stress level of the region. Hence, it would be possible to use the geoelectric field in order to invert for the stress level.

Relationships between the geoelectric field skewness and kurtosis, in one hand, and earthquakes, in the other hand, have been recently reported, suggesting that the statistical distribution of amplitudes of geoelectric signals is perturbed during the preparation stage of earthquakes. Figure 5 shows the time series of the event slips, as well as the skewness and kurtosis of the $\widehat{V_{SB}}$ series for the multi-blocks COS model described above. Using a moving window technique, we calculate the skewness and kurtosis within a window length of 131 time units, which is the median of inter-event times of events with $D_{SB}>1$. It seems that slips, and even micro-slips, perturb electric signals, as both skewness and kurtosis time series display quite ample fluctuations. The proposed COS model thus also provides an explanation for similar transients observed in real systems.
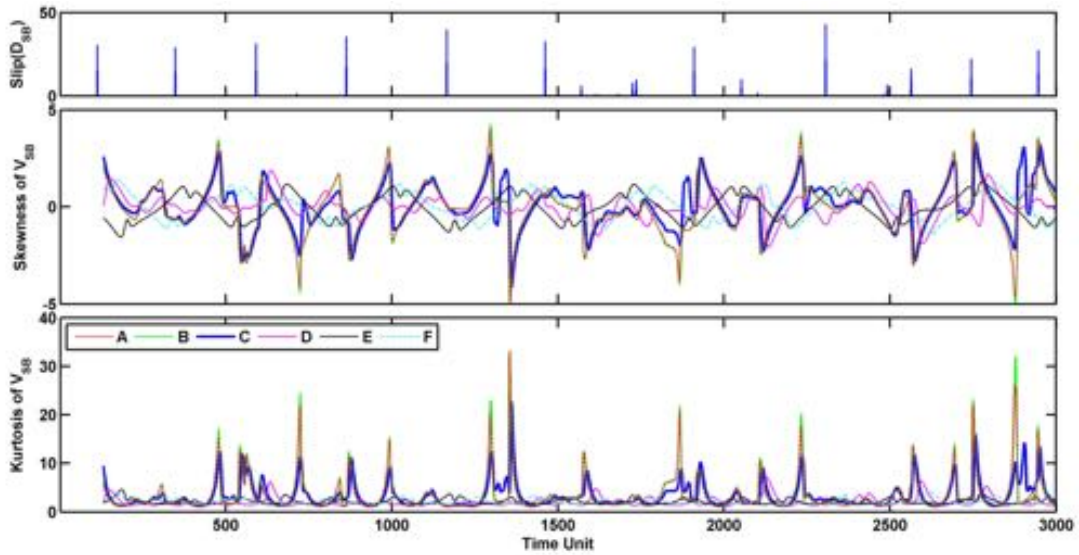
Figure 5. Time series of slips, skewness, and kurtosis for sets A to F.

Power spectrum analyses of electromagnetic signals before, during, and after a large earthquake, suggest an increase of the low-frequency energy content, as well as a power-law-shaped spectrum prior to large events. If the underlying mechanism of the electromagnetic signals obeys critical dynamics, then its spectrum is expected to behave as $S(f) = a \cdot f^{-b}$. The exponent b of the power-law spectrum in field observations is observed to get closer to 2 during the pre-seismic critical stage, a value separating regimes of anti-persistent and persistent behavior of the electromagnetic time series. From the COS model's view point, the slopes of the power-law fit to the power spectra depend on the damping conditions of the underground electrokinetic parameters, as shown in Fig. 6. We thus consider a full voltage time series excluding its transient initial state, and divide it into 305 non-overlapping segments using, as above, a window length of 131 time units. We estimate the power spectrum and its exponent b for each time window by fitting $log(S) = log(a) - b \cdot log(f)$ using a least square method. Analyzing statistically the 305 power spectra and b values, we get the average of the power spectra (Fig. 6a) as well as the statistics of their slopes (Fig. 6b) for sets A to F. It seems that, once again, there is a transition between the lower and upper UD regions of the phase space (see also the last column of Table 1). In our study, even a homogeneous system can also produce anomalous and complex voltages, depending on the state of the electrokinetic parameters. This suggests that heterogeneity of a system is not necessary to produce the complicated fracture-induced electromagnetic emissions prior to large earthquakes. The stress change indeed appears to be the key to produce geoelectric variations. However, future studies might also focus on stress-induced damage and fluid flow, which would make underground kinetic parameters dependent on space and time as well.

(a)

(b)
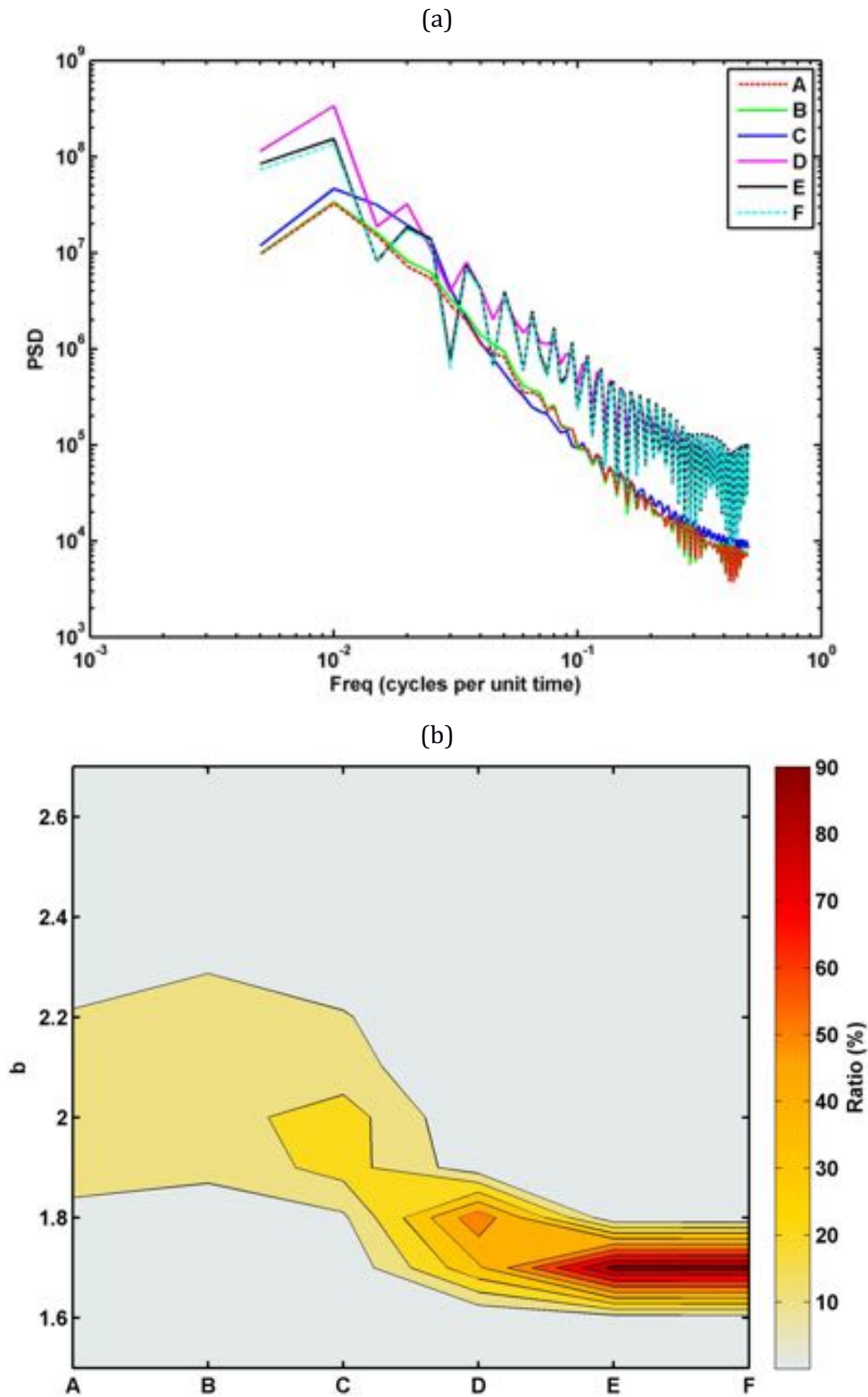
Figure 6. (a) Average of power spectrum densities (PSDs) of the 305 non-overlapping segments, whose length is 131 time units per segment. (b) Statistical distributions of power-law exponents (b value) of power-law fitting in the 305 PSDs.

Annex F:
Earthquake precursors in the light of peroxy defects theory: critical review of systematic observations.
(Friedemann Freund, Guy Ouillon, John Scoville, Didier Sornette)

To be published in the European Physical Journal (EPJ) 2018

Abstract: Forecasting earthquakes implies that there are time-varying processes, which depend on the changing conditions deep in the Earth's crust prior to major seismic activity. These processes may be linearly or non-linearly correlated. In seismology, the research has traditionally been centered on mechanical variables, including precursory ground deformation (revealing the build-up of stress deep below) and on prior seismic events (past earthquakes may be related to or even trigger future earthquakes). Since the results have been less than convincing, there is a general consensus in the geoscience community that earthquake forecasting on time scales comparable to meteorological forecasts are still quite far in the future, if ever attainable.

The starting point of the present review is to acknowledge that there are innumerable reports of other types of precursory phenomena ranging from emission of electromagnetic waves from ultralow frequency (ULF) to visible (VIS) and near-infrared (NIR) light, electric field and magnetic field anomalies of various kinds (see below), all the way to unusual animal behavior, which has been reported again and again. These precursory signals are intermittent and seem not to occur systematically before every major earthquake and reports on pre-earthquake signals are not widely accepted by the geoscience community at large because no one could explain their origins. In addition, the diversity of the signals makes them look disparate and unrelated, hampering any progress.

We review a credible, unifying theory for a solid-state mechanism, which is based on decades of research bridging semi-conductor physics, chemistry and rock physics. This theory, which we refer to as the "peroxy defect theory", is capable of providing explanations for the multitude of reported pre-earthquake phenomena. A synthesis has emerged that all pre-earthquake phenomena could trace back to one fundamental physical process: the activation of electronic charges (electrons and positive holes) in rocks subjected to ever-increasing tectonic stresses prior to any major seismic activity, via the rupture of peroxy bonds. The holes are unusual inasmuch as they are able to flow out of the stressed rock volume, into and through surrounding unstressed or less stressed rock, forming electric currents, traveling fast and far, and causing a wide range of physical and chemical follow-on processes along the way, which can be measured, ranging from electrical ground potentials, stimulated infrared emission, massive air ionization, to increased levels of ozone and toxic levels of carbon monoxide (CO).

In the second part of the review, we critically examine satellite and ground station data, recorded before past large earthquakes, as they have been claimed to provide evidence that precursory signals tend to become measurable days, sometimes weeks before the disasters. We review some of the various phenomena that can be directly predicted by the peroxy defect theory, namely, radon gas emanations, corona discharges, thermal infrared emissions, air ionization, ion and electron content in the ionosphere, and electro-magnetic anomalies.

Our analysis demonstrates the need for further systematic investigations, in particular with strong continuous statistical testing of the relevance and confidence of the precursors. Only then, the scientific community will be able to assess and improve the performance of earthquake forecasts.

Table of contents

I-Introduction

1.1 The cost of earthquakes

Large earthquakes are, by far, the deadliest of all natural disasters, claiming an average of 60,000 lives a year, featuring gigantic fluctuations (e.g. 80,000 victims from 1994 to 2004, and 780,000 from 2001 to 2010; see e.g. Knopoff and Sornette, 1995, for the size distribution of death tolls related to seismic events), which partly mirrors the highly intermittent distribution of seismicity in space, time, and magnitude. On more economic grounds, such disasters are also causing colossal property and industrial damage, with that of the 1989 Loma Prieta earthquake in California alone estimated at $6 billions (over €4 billions), the 1995 Kobe event in Japan estimated at $200 billions (€150 billions), while the 2011 Tohoku earthquake followed by its great tsunami already stands with much higher losses, with costs continuing to rise with the on-going management of the Fukushima nuclear disaster, which is likely to last several decades. Taking into account lost productivity, lost income, lost tax revenue, as well as the cost of rebuilding all infrastructures, the economic impact of a magnitude 7 or larger earthquake is expected to exceed €100 billions. The situation can only become more acute with the on-going growth and concentration of human populations in urban centers often found in seismic regions.

In this backdrop, if it were possible to warn of an impending major earthquake days or even weeks in advance, damage to industry, transportation and the power grid could be significantly reduced by taking appropriate mitigation measures. Numerous lives could be saved. By allowing recovery to begin sooner, the post-disaster restoration phase could also be made more cost-effective and more efficient.

1.2 Seismology: a very short historical introduction

Instruments to detect earthquakes appeared quite early in History, such as the Chinese seismoscope invented by Zhang Heng in 132 CE. However, those prototypes were unable to record and store any signal, hence did not allow their contemporaries (nor us) to provide precise location, origin time or energy estimation for the observed events. For a long period of time (i.e. until the late XIXth century), human beings and edifices have played the role of rudimentary seismographs (and accelerometers): through the numerous reports that one may find in historical archives, historians and scientists are able to list a catalog of large past events in inhabited areas. The amount of observed damage and perceptions of the people allow one to draw earthquake intensity maps, from which one can deduce estimations of the location of the epicenter and, according to quite dispersed empirical laws, its magnitude and depth. Even if genuine seismological networks appeared only during the XXth century, allowing a quantitative description of seismic ruptures, some important aspects of modern seismology appear to be rooted in philosophical reflections (about what we now coin as *seismic risk*) during the French Renaissance, in the wake of the great Lisbon earthquake in 1755, when a famous controversy opposed French philosophers François-Marie Arouet (better known as Voltaire) and Jean-Jacques Rousseau. The former (Voltaire, 1756) possessed what we would now qualify as a more hazard-oriented state of mind (claiming that such disasters occur randomly), while the latter (Rousseau, 1756) certainly formulated the very first ideas about risk, i.e. that man could protect himself from such calamities by coming up with better-thought building and urbanization policies. This hazard and risk dichotomy and terminology still defines nowadays the two main classes of approaches to natural catastrophes in the academic and engineering worlds, respectively.

1.3 Seismology as a science

On the side of hard science, a first major advance has been the model published by Reid (1910) who, for the first time, bridged different physical phenomena known both in nature and in the laboratory: earthquakes, faulting, and friction. Reid's elastic rebound theory not only allowed to explain the phenomenology of earthquakes, it also provided huge hopes in the possibility of predicting the large, devastating events that were threatening California and many other places worldwide. Reid viewed a seismic prone region as containing an isolated fault considered as a perfectly periodic relaxation oscillator with threshold dynamics, with each relaxation event constituting a large characteristic earthquake. His simple model has indeed more or less survived until now, with many refinements, for instance through the stress transfer approach to earthquake forecasting based on a deterministic analysis of fault-fault interactions (King et al., 1994; Nandan et al., 2016). While this approach can explain *a posteriori* some space-time features of some observed aftershock sequences following some large events (see for instance Bhloscaidh and McCloskey, 2014), it never provided any reliable prediction of similar earthquake sequences.

On the other hand, earthquake data began to accumulate at the turn of XIXth to XXth century, allowing the use of purely statistical descriptions (with many of them quite abusively and unfortunately ending up as so-called *laws* in the earthquake science terminology). The first of these laws quantifies the temporal rate of earthquakes following a large main event (and known as the Omori law; see Omori, 1894), and has been since similarly extended to space. The second one is the famous Gutenberg-Richter law, which is nothing but the power-law shaped energy distribution of observed events (Gutenberg and Richter, 1956). Combining these two robust statistical features (complemented by few other ones, like the productivity law (Helmstetter, 2003) quantifying the number of aftershocks directly triggered by a given event as a function of its magnitude) allowed the new branch of statistical seismology (and forecasting) to emerge.

Forecasting in seismology can be subdivided into two branches: (i) time-independent forecasting (which simply approximates seismicity as a constant-rate Poisson process in a given region, an approach initially popularized by Cornell, 1968), and (ii) time-dependent forecasting, which models seismicity as a linear superposition of generations of events triggered by all past events, allowing to forecast the seismicity rate at future times (see for instance Ogata, 2011). Time-independent and

time-dependent approaches are now evaluated and compared within a well-defined framework which allows one to test their mutual performances (see the Collaboratory for the Study of Earthquake Predictability, http://www.cseptesting.org). All these techniques continue to be improved and now feature impressive degrees of sophistication. However, they only allow to define probabilities of occurrence within a time scale of a few years at least. This is clearly insufficient as one goal of earthquake prediction is to define efficient short-term mitigation strategies such as temporary population evacuation or critical infrastructures shutdown. This severe drawback is mainly due to the complete lack of constraint on the magnitudes of upcoming events: the time-varying poissonian rate of occurrence of the next event can be modelled with some reasonable accurracy, but its magnitude is simply modelled by a random sampling of the time-invariant Gutenberg-Richter law (Helmstetter and Sornette, 2003). This is why such approaches do not define any prediction methodology *per se*.

Another branch independently emerged in the 1990s, pushing forward analogies between the many power-laws observed in the phenomenology of earthquakes and the dynamics of critical phase transitions (see e.g. Bowman et al., 1998). This approach led to consider the time of large events as critical points (or at least finite-time singularities), thus suggesting some predictability especially for large earthquakes, implying that the larger the event, the better their predictability (Huang et al., 1998). While this concept seemed to apply well in the laboratory or small-scale systems such as mines (Ouillon and Sornette, 2000) and under stress-controlled conditions, its applicability to large scale, strain-controlled systems such as tectonic plates is still debated (Mignan, 2011). Other approaches based on pattern recognition are also in use but do not provide really convincing results yet as they have not been thoroughly tested in real time. The Russian team around Keilis-Borok and Kossobokov has developed a rigorous testing framework (see http://www.mitp.ru/en/predictions.html), but the time scale of the prediction uncertainty (6 months) is only of scientific interest with little or no concrete societal impact. This led many in the seismological community to conclude that earthquakes cannot be predicted (Geller, 1997; Mulargia and Geller, 2003). See however Sornette (1999) and other contributions of the 1999 debate in the journal Nature coordinated by Ian Main.

1.4 Solid state physics: is it the key?

Much before and well after seismology developed into a hard science, mainly based on mechanical concepts of static and dynamic deformation of materials, solid state physics may have provided another way to consider the preparatory stages to large earthquake occurrences (for instance, one can trace the connection of earthquakes and electromagnetic phenomena back to the papers of Shida, 1886, and Milne, 1890). Countless reports of precursory phenomena have been accumulated through time, first witnessing visual observations, then recorded by an ever increasing number of ground stations or remote satellites. Those precursory signals are thought to reflect the time-varying processes associated with the slow tectonic stress accumulation in the Earth's crust. Such reported pre-seismic earthquake precursors recorded on the ground or from space are compiled in Table 1 and concern very diverse categories such as variations of the magnetic field, electromagnetic fluctuations over various frequency bands, gas emanation from the ground, changes of ionospheric properties, earthquake lights, night glows, up to the controversial reports of weird behavior of domestic or wild animals.

Satellites observations	Ground stations observations
Thermal Infrared (TIR) anomalies	Medium-term magnetic field variations
Total Electron Content (TEC) anomalies	ULF emission from within the Earth crust
Changes in ionospheric ion concentrations	Tree potentials and ground potentials
Ionospheric electric field turbulences	Soil conductivity changes
Atmospheric Gravity Waves (AGW)	Groundwater chemistry changes
CO release from the ground	Trace gas such as CO release from the
Ozone formation at ground level	ground
VLF attenuation due to air ionization	Radon emanation from the ground

Mesospheric lightning	Positive and negative air ionization	**Table 1:**
Lineaments in the VIS-NIR	Sub-ionospheric VLF/ELF propagation	
	Nightglow amd chromatic shifts	

types of anomalous signals usually reported prior to seismic events.

Unfortunately, the seismological community never considered such precursors as being reliable or meaningful, which led to an unfortunate disconnection, if not a definitive dialog breakage, between the two communities. The main concerns and criticisms raised within the seismological community include: (i) non-seismic precursors were not properly tested in a statistical sense, since the published cases mostly referred to single case events, and were presented without much quantification of the errors (such as false alarms and missed predictions); (ii) the reported phenomena displayed quite a wide diversity but no clear physical model had been formulated that could explain them in a coherent fashion. The latter argument is strongly reminiscent of Wegener's 1915 continental drift theory that reported so many clear and documented arguments, but was not accepted by the geophysical community until the 1960's when the fundamental process of mantle's convection was recognized. Solid-state earthquake physics thus still has to overcome its own Wegenerian bottleneck.

Based on decades of research, one of us (see Freund, 2010 for a review) has derived a credible, unifying theory for a physical mechanism that is capable of providing explanations for the multitude of reported pre-earthquake phenomena mentioned above. A clear synthesis has emerged that all pre-earthquake phenomena can be traced back to one fundamental physical process: the activation of electronic charges (electrons and positive holes) in rocks by the activation or break-up of peroxy defects during the ever-increasing tectonic stresses prior to any major seismic activity. The positive holes are unusual inasmuch as they are able to flow out of the stressed rock volume, into and through surrounding unstressed or less stressed rock, forming electric currents, traveling fast and far, and causing a wide range of secondary physical and chemical processes all along their way. These processes range from electrical ground potentials, stimulated infrared emission, and massive air ionization, to increased levels of carbon monoxide (CO) and ozone. The theoretical framework provided allows one to rationalize previous analyses of satellite and ground station data that were recorded before large earthquakes. These recordings seem to provide clear evidence that precursory signals tend to become measurable days, and sometimes weeks before the disasters.

The goal of this paper will thus be to present, in a shortened but pedagogical way, the microscopic theory of peroxy defects and its consequences at macroscopic, observable scales, as well as a critical review of observations themselves. Notice that many other theoretical models have been previously proposed (see for instance Gershenzon et al., 1989; Molchanov et al., 1995, 2001; Molchanov and Hayakawa, 1998; Sorokin et al., 2001; Pulinets et al., 2003), but will not be described nor discussed in the present paper to preserve its coherence and consistence. As pointed out above, the immense majority of observations have not been systematic in space nor time, so that even a synthesis of the related litterature, which amounts to really gigantic proportions, would amount to fall in a time and energy "black hole", and would not even be fully convincing. Such partial work compilations already exist (Hauksson, 1981; Cicerone et al., 2009) and will be cited when relevant in this paper. We shall thus provide instead a non-exhaustive review of observations in the sense that we shall focus on previously published results obtained using continuous measurements over a time period that allows one to correlate them with a significant number of events occurring within a well-defined spatial domain. The very last section will provide a discussion about these observations, as well as a presentation of our novel ideas about the way this research should continue, insisting on the proper quantitative analysis and necessary statistical testing of the correlations between non-seismic observations and earthquakes.

II-Theoretical model: peroxy defects flow in stressed rock

We shall now present the mechanism within which we propose that most if not all reported non-seismic precursory phenomena are rooted. We choose to not present all details as they will be more meticulously described in a forthcoming book, together with many laboratory experimental results.

2.1 Peroxy bonds and defects in rocks

The most common minerals in the Earth's crust are silicates including quartz, feldspar, mica, amphibole, pyroxene, olivine…, abundantly present in igneous and metamorphic crustal rocks. Their structures link oxygen anions O^{2-} with Si^{4+} or Al^{3+}, typically forming $(X.Y)O_4$ or $O_3X-O-YO_3$ entities, where X and Y can be Si^{4+} or Al^{3+} (Freund, 1985; Freund, 2010). These minerals contain a type of defects that has largely escaped attention: peroxy links, $O_3X-OO-YO_3$, where one O^{2-} is replaced by a pair of O^-, forming an $O-O$ bond. Special about peroxy defects is that, while they are hard to detect in their inactive state, their presence has far-reaching consequences for the physical properties of minerals and rocks, specifically for their electrical response to stress and other variables.

Peroxy defects were first observed in nominally highest purity (99.99%) melt-grown MgO single crystals [*F. Freund and Wengeler*, 1982]. They were shown to derive from the incorporation of traces of fluid phase components such as H_2O into the MgO matrix during crystallization from an ever so slightly fluid-laden melt. The solute H_2O turn into OH^-. During cooling, in the temperature range around 500°C, OH^- pairs at Mg^{2+} vacancy sites undergo an electronic rearrangement in the form of a redox conversion, whereby the hydroxyl protons extract one electron from their respective parent hydroxyls, turning into H, which combine to H_2, while the hydroxyl oxygens – now in the 1– valence state – combine to O_2^{2-}. This redox conversion has been confirmed by replacing OH^- with OD^- [*F. Freund et al.*, 1982]. Evidence for peroxy defects was subsequently obtained for silica and silicates such as feldspars, pyroxenes, olivine etc. and a variety of rocks (F. Freund and Masuda, 1991; F. Freund and Oberheuser, 1986; F.T. Freund, 2003; Lerski et al., 1988).

Figure 1: Part of a 2-component phase diagram "Mineral + H_2O", indicating that the melting point of the dry system T_{melt} is lowered to T_{cryst}, the crystallization temperature, through formation of a solid solution (ss). The ss stability field shrinks with decreasing temperature. At T_{freeze}, the system freezes and leaves thermodynamic equilibrium. At this point, ss turns into a supersaturated solid solution sss. In the sss field $(X.Y)O_4$ redox conversion takes place during further cooling, converting pairs of solute OH^- into peroxy plus H_2.

According to thermodynamic principles, when a solid crystallizes from a melt or, more specifically, when a mineral crystallizes from a magma that is naturally laden with dissolved gases or fluids, a finite concentration of the gas/fluid components will enter the solid matrix, forming a solid solution (ss) as depicted in **Figure 1**. The solid solution stability field is widest at T_{cryst}, the temperature of crystallization. With decreasing T, the solid solution stability field shrinks – a process that can only be achieved by diffusional processes, which allow the gas/fluid "impurities" to segregate, preferentially to dislocation, subgrain boundaries and grain surfaces. Eventually however, regardless of how slow the cooling rate, the diffusional processes cannot keep up. At this point the

system freezes at T_{freeze}, and the solid solution turns into a supersaturated solid solution (sss) marked in **Figure 1** by yellow and red. Upon entering the supersaturated solid solution field, the system leaves thermodynamic equilibrium and enters the realm of metastability.

Under metastable conditions, reactions can take place that are disallowed under equilibrium conditions. Of interest here is an electronic rearrangement known as a redox conversion, which involves pairs of solute hydroxyls, OH^- or $O_3(X,Y)\text{-}OH$. In a silicate matrix the solute species is $O_3Si\text{-}OH$. Upon cooling to temperatures around 500°C, these hydroxyl pairs undergo a redox conversion, in the course of which each hydroxyl proton, H^+, steals an electron from its parent hydroxyl oxygen, O^{2-}: $OH^- \Leftrightarrow O^- + H$. The two H combine to H_2, while the two O^- snap together to form an $O^-\text{–}O^-$ bond. In the case of MgO, this becomes a peroxy anion, O_2^{2-}. In the case of silicate matrices, it becomes a peroxy defect, generically $O_3Si\text{-}OO\text{-}SiO_3$.

$$O_3Si\text{-}OH\ HO\text{-}SiO_3 \Leftrightarrow O_3Si\text{-}OO\text{-}SiO_3 + (H_2)_i \qquad [1]$$
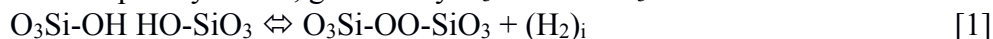
The redox conversion is reversible as long as the H_2 molecules remain at or close to the site, where they have been born, here marked by subscript i for "interstitial". Since interstitial H_2 is diffusively mobile, even in dense mineral matrices, they may diffuse away, here marked by an arrow, making this redox conversion irreversible:

$$O_3Si\text{-}OH\ HO\text{-}SiO_3 \Rightarrow O_3Si\text{-}OO\text{-}SiO_3 + H_2\Uparrow$$
$$[2]$$
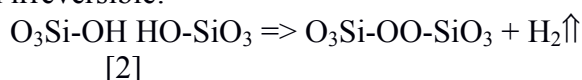
The temperature interval, in which this redox conversion takes place, around 500°C, is marked in gray in **Figure 1**.

Introduced into the mineral structures during cooling over geological times along the geotherm, peroxy defects such as $O_3Si\text{-}OO\text{-}SiO_3$ replacing $O_3Si\text{-}O\text{-}SiO_3$ can therefore be expected to exist in essentially all igneous and high-grade metamorphic rocks. When igneous rocks are transported to the Earth surface and erode, detrital mineral grains laden with peroxy defects such as quartz, feldspars etc. become incorporated into sedimentary rocks. As a consequence, even sedimentary rocks commonly contain minerals with peroxy bonds.

The presence of peroxy defects is an important geophysical factor in the sense that they will affect, even control, many features of the rocks, especially their electric transport properties. Mechanical stresses are highly effective in perturbing peroxy defects that are sitting at grain boundaries or may even bridge grain boundaries. Mechanical stresses cause grains to slide relative to each other. Any ever so slight movement will bend peroxy bonds and cause them to break up.

Electric charges in rocks are either ionic or electronic. Those that are electronic fall into two categories: electrons (usually noted as e') and positive holes or p-holes, the latter standing for a defect electron (usually noted as $h^\bullet$). Crustal rocks mostly consist of silicate minerals or contain detrital silicate minerals, characterized by O^{2-} anions. However, as argued above, there will always be some O^{2-} that have given away an electron and turned into O^-. Two O^- atoms bond together in a peroxy link represent a pair of trapped p-holes, which are dormant and electrically inactive in their dormant state.

As long as peroxy bonds are intact, they are electrically inactive. When peroxy bonds are perturbed, they can break up. A type of perturbation that leads to During the break-up an electron, e', is transferred from a neighboring O^{2-} into the broken peroxy bond. In eq. [3] the peroxy bond is represented by two dots, **:**, each dot standing for a hole state. During break-up the electron becomes trapped in the now broken peroxy bond, here represented by a single dot, $\cdot$:

$$O_3Si\text{-}O\mathbf{:}O\text{-}SiO_3 + O^{2-} \qquad \Leftrightarrow \quad O_3Si\text{-}O\bullet O\text{-}SiO_3 + O^- \qquad [3]$$
$$\quad\quad\quad\quad\quad\quad\quad\quad\text{e'}\quad\quad\quad\quad\quad\text{h}^\bullet$$
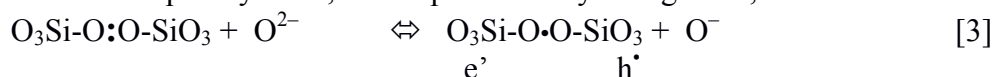
At the same time the O^{2-} that has donated the electron turns into an O^-. This quasi-free O^- represents a defect electron in the oxygen anion sublattice, e.g. a hole-type charge carrier, symbolized by $h^\bullet$, which we call a "positive hole" or p-hole for short.

The transport properties of the trapped electron e' and of the quasi-free hole, $h^{\bullet\cdot}$, are of interest In the constext of earthquake-related electrical properties.

The energy levels of the unbroken peroxy defects are associated with O 2sp-symmetry states that form the upper edge of the valence band. Likewise, the new e' and $h^\bullet$ states, created during the

break-up of the peroxy bonds, exist at or near the upper edge of the valence band. The e' become trapped by shifting downward to new energy levels slightly below the surface of the valence band. Their conjugated mirror states e'* shift upward into the band gap, slightly above the edge of the valence band. It is important to note that the e' and e'* states are available only where peroxy bond breakage occurs, i.e. where mechanical stresses are applied the rocks, which cause peroxy bonds to break. Hence, the e' are mobile only within the stressed rock volume.

By contrast, the h$^\bullet$ are associated with energy levels that form the very edge of the valence band. Their wavefunctions are highly delocalized and they have the remarkable ability to spread out of the stressed rock volume.

Subjecting a rock to deviatoric stress reveals the existence of those dormant p-holes (Freund et al., 2006). If the stressing rate is sufficiently small, which is the case in tectonics, rock will at first deform continuously with a visco-elasto-plastic bulk rheology (i.e. in the ductile regime, as opposed to the brittle regime where deformation is mainly accommodated by elasticity and the formation of cracks and fractures). Most of the ductile deformation is irreversible and consists, at the microscopic level, in sliding of grains relative to each other and in motion of dislocations, a thermally activated process. To the extent peroxy bonds decorate grain boundaries or dislocations, every so slight motion of mineral grains relative to each other will tend to break the O$^-$-O$^-$ bonds. As described by eq [3] the broken peroxy bonds will take over an electron from a neighboring site, for instance a nearby O^{2-} acting as donor. While the electron becomes trapped in the broken peroxy bond, the donor O^{2-} turns into an O$^-$, equivalent to a defect electron on the O^{2-} sublattice, i.e. a p-hole. This p-hole state is not bound to the broken peroxy bond but can diffuse away via a phonon-coupled electron hopping mechanism [*Shluger et al.*, 1992] at a speed on the order of 100 m.s^{-1} [*John Scoville et al.*, 2015]. The p-holes are capable of traveling over large distances. Since their speed of propagation is controlled by diffusion, they will slow down, if they propagate in a plane or into 4π space [*John Scoville et al.*, 2014; *John Scoville et al.*, 2015].

The break-up of peroxy bonds will naturally enhance the electric conductivity of the rocks, in particular within the stressed rock volume, where e' and h$^\bullet$ jointly act as mobile charge carriers, less so in the surrounding rocks, through which only h$^\bullet$ can travel. To the extent that the presence of the e' and h$^\bullet$ charge carriers affect other physical properties of rocks, for instance the speed of P and S waves, this process may provide a new and different explanation of the widely reported pre-earthquake changes in the V_P/V_S ratios (Catchings, 1999; Scafidia et al., 2009). The most common explanations considered so far are that, when rocks deep in the crust are subjected to stress, they undergo microfracturing,. This process is thought to allow fluids to penetrate, which would lead to changes in the speed with which P and S waves propagate (Kranz, 1983; Scholz, 1968). The alternative explanation offered here is that, when peroxy bonds become activated and p-hole charge carriers with highly delocalized wavefunctions become activated, the average bonds between oxygen anions and cations become slightly less ionic. Increased covalency makes the bonds slightly more ductile, leading to changes in the mechanical properties of the rocks that have been described as "softening" (Freund et al., 2010).

Once e' and h$^\bullet$ charge carriers become activated in a given rock volume, they will start to recombine, returning to the inactive peroxy state. By conducting laboratory experiments at different stress rates spanning 8 orders of magnitude, it has been shown that, inside the stressed rock volume, the lifetimes of stress-activated p-holes vary widely from milliseconds to several months [*John Scoville et al.*, 2015]. If the stress rates are very high, the number of p-hole charge carriers activated and available to flow out of the stressed subvolume is very high. Once outside the stressed subvolume, the p-holes are expected to have indeterminate lifetimes, possibly very long, allowing them to propagate far afield. This suggests that observable signals rooted in the physics of p-hole migration may display a wide range of patterns at different stress rates.

In laboratory experiments, uniform loading of a sample of dry granite under uniaxial stress conditions leads first to a nearly 5-fold increase of its electric conductivity until the stress reaches a moderate value of about 25 MPa. Beyond this stress value, the conductivity increases much more gradually and indeed quickly reaches an almost constant value (Freund, 2010). In another

experiment, only a small part of a rock slab is loaded while the rest is kept unstressed (Freund, 2010). Voltage is measured across the plate at two different locations (within stressed and unstressed domains). The stressed domain shows a monotonic but irregular increase of the measured voltage, up to a very sharp peak whose onset and maximum value coincide with major cracking events preceding the final failure of the sample. In the unstressed domain, the temporal pattern of voltage is completely different: it first rises very quickly to its maximum value as soon as loading is applied on the other part of the sample, then decreases irregularly with large fluctuations to finally reach its pre-stress background value, and reverses slightly its sign just before failure. Freund (2010) showed that the most significant part of the electric signal is thus observed before reaching failure stress, suggesting that electrical anomalies in nature would not necessarily continue to build up towards earthquakes but precede them by a finite time depending on the loading rate. In a similar but constant stress experiment, Freund et al. (2006) observed that the current intensity measured across the sample mimicked closely the time variation of the imposed stress.

As already mentioned, the existence and mobility of p-holes should increase the electric conductivity. In a heating experiments (Kathrein and Freund, 1983; Freund, 2010) conducted with MgO single crystals, the number of p-holes started to increase around 430° and further increase over the 450-600°C temperature range, causing the conductivity of the MgO single crystals to increase by up to 6 orders of magnitude. The current carried by these p-holes has a characteristic 1eV activation energy. Interpreting laboratory experiments by Parkhomenko and Bondarenko (1986) who monitored the electric conductivity of various rock samples as a function of temperature, Freund (2010) notices a similar energy activation from 200 to 600°C, suggesting that the same migration of p-holes process also holds in crustal rocks. Transposing this temperature range onto the average geotherm, i.e. the depth–temperature profile, in the stable continental crust, this roughly corresponds to the depth range of 7-40 km. Incidentally, this fits well with the depth range over which most earthquakes are observed to nucleate.

2.2 Flow of positive holes in the crust

Freund (2002) and Freund et al. (2006) suggested that, when activated by stress (and temperature, but we shall from now on only focus on stress), nucleated p-holes start to flow towards the less stressed regions while electrons will remain trapped locally. The unstressed rock volume thus becomes positively charged relative to the stressed volume, making the system behave like a battery. The potential difference that emerges creates an electric field counteracting the flow of p-holes. As the latter naturally repel each other, positive charges will pile up at the surface of the Earth. A side-effect is a significant electrical conductivity increase within the stressed volume, and a smaller increase across the unstressed domain (Freund, 2010).

No sustained outflow of p-holes can occur when the battery circuit is not closed to allow for a return current. In laboratory experiments it is easy to achieve circuit closure by connecting the stressed and unstressed parts of a given rock sample with a wire. Electrons in the stressed portion of the rock then use this wire to flow to the unstressed portion and recombine with the p-holes that have traversed the unstressed rock. In the field the situation is more complicated. Three scenarios can be envisioned.

First, in the case of large to very large earthquakes the actively stressed rock volume may extend downward to the deeper layers of the crust, where the temperatures are sufficiently high so that electrons are thermally activated causing the rocks to become electron-conductive. In this case an electron current can flow deep in the crust paralleling the stress-activated p-hole current and thereby closing the circuit (Freund, 2007a, 2007b).

Second, if an electrolytically conductive path exists, for instance through the water-saturated gouge along a fault plane, circuit closure can be achieved through the flow of H_3O^+ and water-soluble ions (Freund, 2009). This mechanism is plausible as active faults may permit deep penetration of water along fault planes.

Third, if large-scale air ionization occur at the Earth surface, the conductivity of the air may become large enough to provide for a return path for the p–hole charges flowing in the crust.

2.3 Accumulation of p-holes at the Earth surface and air ionization

While accumulating at the free surface the positive charges form thin surface/subsurface charge layers associated with steep electric (E) fields. Due to the intrinsic nature of E fields (represented mathematically as Laplacian fields), corners, edges, or any other positive (i.e. upward) topographic fluctuation (such as hills or high mountains in areas of tectonic convergence) amplify these E fields, which can locally reach values as high as a few millions $V.cm^{-1}$.

As these high E fields build up, they will lead to two processes (Freund et al., 2009):

(i)   Field ionization of air molecules. Among the main constituents of air O_2 has the lowest ionization potential and, hence, is expected to become most easily field-ionized to O_2^+.

(ii)   Corona discharges. When the local E fields become so large that they can accelerate free electrons (which are always present due to cosmic rays and radioactive decay processes) to energies sufficiently high to impact-ionize gas neutrals, discharge avalanches will occur, commonly known as corona discharges.

Air ionization has been shown to set in once the surface potential reaches +3V (Freund et al., 2009). Further influx of positive holes leads to fluctuations of the surface potential, indicative of impulsive field-ionization of positive airborne ions at the surface and injection of electrons into the surface. If the influx continues, corona discharges are triggered, leading to a break-down of the positive surface potential (Freund et al., 2009).

It is expected that topographic fluctuations where ionization is maximum will then allow a lot of air electrons to be driven to the rock surface from above, causing the upward flow of p-holes from the bulk rock to increase correspondingly. Laboratory experiments show that the generation of positive airborne ions at the surface of stressed gabbro samples displays a pulse-like dynamics and also a major peak at sample failure, due to the sudden release of a large amount of airborne ions by the fracture surface. The reversal of the surface potential before failure is accompanied by light flashes emanating from the rock sample as well as by radio-frequency pulses, confirming the occurrence of corona discharges so that conditions are fulfilled to get air ionization.

This ultimate step in the life of p-holes is evidenced by another set of laboratory observations. Close to the free surface p-holes can recombine and return to the peroxy state. The recombination is an exothermal process, in the course of which part of the energy is recovered that had been expended in the stressed rock to break the peroxy bonds. This energy leads to vibrationally highly excited states of the newly formed peroxy bonds, which de-excite by emitting photons at discrete energies corresponding to the downward transitions in the vibrational manifold (Ricci et al., 2001). an experimental confirmation of these infrared "hot bands" has been reported for anorthosite (Freund, 2007).

2.4 First-order predictions of the model

The model presented above provides a very plausible overview of the 'life, works, and death' of positive charge carriers in the Earth crust, namely the p-holes. Unfortunately, there exists no direct means of investigation in order to validate this scenario, and microscopic entities such as p-holes are not detectable *in situ*. However, if rock material in geological conditions obeys the physical picture described in the previous section when being slowly loaded by tectonic stress, the resulting positive charges accumulation and massive air ionization at the free surface would induce a wealth of corollary phenomena that we shall now describe in more details. Most of them are fairly measurable and have been claimed to be widely observed before seismic events of various magnitudes. Published works reporting them will be reviewed in the next section.

The most obvious expected consequence of the arrival of p-holes at the free surface would be an increase of the electric conductivity of the most superficial soil layers, i.e. a change of a physical properties. A more subtle consequence is of chemical nature, as soils generally feature high contents of organic matter, i.e. of carbon atoms. The latter is often present in the form of triple bonded carbon, which is able to retain Radon (^{222}Rn) atoms. Radon is a noble gas with a half-life time of

about 3.8 days, generated from the radioactive decay of Radium (^{226}Ra), and which can display chemical reactivity (Li et al., 2008). As Radium itself is a decay product of Uranium, it follows that Radon is geologically mainly confined over continental areas. Freund (2010) speculates that, because p-holes are highly oxidizing, they should oxidize triple-bonded carbon to double-bonded carbon. As the latter is unable to retain Radon atoms within the soil, this allows the release of Radon atoms, which can then freely percolate within the soil and escape at the free surface. Such Radon emanation in the vicinity of future epicenters have been reported a countless number of times as a genuine earthquake precursor. Note that observations of Radon concentration increase certainly reflect very local conditions as its short life-time doesn't allow it to travel over very large distances, certainly a few meters at most (Woith, 2015). Another expression of the highly oxidizing nature of p-holes can be found in the fact that, prior to major earthquakes, carbon monoxide, CO, has been found to emanate from the ground, probably due to the oxidative interaction of p-holes with organic matter in the soil [*Singh et al.*, 2010].

As observed in some of the laboratory experiments reported in the previous section, infrared emissions are expected to occur when p-holes recombine with electrons at the free surface. As such recombination should occur at higher rates at narrow topographic heights, where the inward flow of p-holes is predicted to be the largest, we should thus observe a correlation between the topography and Infrared emissions, which are usually misinterpreted as an increase in actual ground temperature. Such a model rationalizes the night-time thermal anomalies that have been observed using Infrared satellite imagery (Ouzounov et al., 2006; Ouzounov and Freund, 2004; Qiang et al., 1999; Saraf et al., 2008; Singh, 2008; Tramutoli et al., 2005; Tronin, 2000; Tronin et al., 2004), without the need to use a specifically thermal model (examples of which can be found in Pulinets et al., 2006; Saraf et al., 2008; Singh, 2008; Tramutoli et al., 2005; Tronin, 1999). An excellent example of strong pre-earthquake thermal infrared emission from the mountain tops has recently been reported for the case of the magnitude 6.3 L'Aquila earthquake [*Luca Piroddi et al.*, 2014a; *L. Piroddi et al.*, 2014b]. Though pre-earthquake radon emanation might be sufficient to locally change the heat capacity of the air, this does not the fact that the most intense infrared emissions come from topographic highs and not from the valleys that are dissected by active faults.

Increasing the electric field at the ground surface up to the possible triggering of corona discharges suggests that transient phenomena usually reported as earthquake lights may also occur (Galli, 1910; Losseva and Nemchinov, 2005; Mack, 1912; St Laurent, 2000; Terada, 1931; Tsukuda, 1997; Derr, 1986). Such corona discharge are also speculated to generate a significant amount of RF (Radio Frequency) noise (Freund, 2010) which should be recorded. A more speculative consequence is the water droplet condensation expected to occur around nuclei constituted by airborne ions. This condensation will be accompanied by a release of latent heat, causing the rise of this air mass (Dunajecka and Pulinets, 2005). Under favorable conditions of humidity, clouds can form and remain close to the future epicenter zone. Such cloud formation has been documented before earthquakes (Lu, 1988; Ondoh, 2003; Tramutoli, 1998; Guo and Wang, 2008).

At last, once the massive ionization of air occurs, this would lead to an upward migration of charged particles, i.e. to a vertical current flow in the atmosphere that Freund (2010) estimates to be of the order of 10-100 A km^{-2} and which would produce noticeable electromagnetic anomalies. Those anomalies would not be restricted to the atmosphere as the ascending positive charges would then also pull downward electrons located at the bottom of the ionosphere, thus modify its physical properties by influencing the vertical distribution of electrons and ions in the ionospheric plasma (Chen et al., 1999; Hayakawa, 2007; Hayakawa et al., 2005; Liperovsky et al., 2000; Pulinets, 2007; Sorokin et al., 2006; Zakharenkova et al., 2007).

III-Empirical tests

3.1 Observations

The previous section exposed a consistent theoretical model of stress-dependent electric charge activation and migration, potentially leading to a wealth of phenomena which would be observable prior to earthquakes. We are very aware that the upscaling from the microscopic and laboratory scales up to the size of interest for natural earthquakes is far from obvious, in view of the structural complexity of the Earth's crust. The latter is crisscrossed by innumerable cracks, fractures, joints and faults over the full observable range of scales (typically from microns up to thousands of kilometers). Those discontinuities are thought to be often filled by fluids of various chemical compositions. This pervasive disorder might itself induce a high complexity in the geometry of the path over which electric charges may travel in rock. Charge flow might be highly focused in some zones and nearly completely screened in others, possibly leading to a very heterogeneous structure of the distribution of charges close to the surface. We are still far from a complete forward modelling of such a process, and we should be aware that observations can by no means be as smooth in space, time or amplitude as those that could be deduced from a similar process in a homogeneous medium. The association of anomalous phenomena and earthquakes will thus necessarily be imperfect, which is why we chose to report here only works dealing with systematic analyses that allow one to assess the statistical significance of the underlying physical assumptions.

To be fully consistent with the previous section where we explained the theoretical model, we shall review only some of the various phenomena that can be directly predicted to hold, namely: radon gas emanations, corona discharges, thermal infrared emissions, air ionization, ion and electron content in the ionosphere, and electro-magnetic anomalies.

One should keep in mind that all these observations rely on different methods of measurement, which can make interpretation difficult. For instance, ground stations are usually run continuously in time, but the spatially covered area is ill-defined. Several such stations are generally run simultaneously (defining a local network), but the spatial area they cover is similarly blurred, as some recorded anomalies might have their source located far outside of the network. Correlations with seismicity are thus difficult to assess. On the other hand, satellites have the advantage to perform repetitive recordings over much wider areas on the Earth over long time periods. Some satellites are stationary or define a constellation so that almost any point on Earth can have a measurement of a given parameter continuously. This is for example the case for GPS data, which can be used to compute the Total Electron Content. Some other satellites are single and non-stationary, such as DEMETER. In that case, the embarked instruments do not provide a continuous recording of a given parameter at all locations, but a continuous sampling along the satellite's trajectory. It follows that the sampling above the location of a given point on Earth will turn out to be highly discontinuous in time.

Most of the papers dealing with non-seismic precursors refer to the work of Dobrovolsky et al. (1979) in order to check the consistency between the size of an earthquake and the maximum distance up to which anomalies have been reported. Based on the compilation of previously published data, this paper proposes that this maximum distance between an earthquake source and a precursor is given by $D=10^{0.43M}$ in km. Dobrovolsky et al. (1979) proposed a theoretical explanation to this empirical "law" (which is certainly another abusive and unfortunate terminology), by assuming that the earthquake preparation zone scales with the size of the upcoming event, and can be modelled as a soft inclusion in an elastic medium that perturbs the distribution of stresses and strains. They show that the aforementioned precursory distance corresponds to a strain perturbation of about 10^{-8}. The idea behind the soft inclusion model is that a multitude of microcracks nucleate or open close to the future event, so that the mechanism underlying the various precursors should be of mechanical nature. Similarly, in the time domain, Rikitake (1986) proposed a relationship between the earthquake magnitude and its precursor time T: $\log(T)=0.76M-1.83$, based on the observation of many reported precursors of various nature.

As a final remark before starting our review of the main non-seismic precursors, we stress that only

papers written in english have been considered, whereas most of those anomalies have been studied for decades in China, India, Japan, Russia, Taiwan, etc. so that, many papers and reports published in the corresponding languages will not be summarized or listed, representing an unfortunate western bias.

3.3 Radon gas emanations

The measurement of Radon gas content is one of the most often reported earthquake precursors, and is generally based on the detection of the alpha particles that are emitted by the radon decay. The very first measurements have been performed by Shiratoi (1927) and Imamura (1947) in ground water, and by Hatuda (1953) in soil along a Japanese active fault. Radon concentrations have often been reported to increase (sometimes up to a factor 10) before seismic events, on the time scale of days to months, either over large areas or in the close surroundings of an active fault (Okabe, 1956; Chyi et al., 2002; Inan et al., 2008; King, 1980; Nagarajaa et al., 2003; Tsvetkova et al., 2001; Yasuoka et al., 2009). Riggio and Santulin (2015) classify Radon anomalies into two categories according to their shapes. Type A anomalies correspond to a slow but regular drift that can take place over several years. Type B corresponds to shorter-lived anomalies (with a duration of few hours to days) that can precede earthquakes. The latter anomalies are reported to be either positive or negative. An important challenge is the removal of external influences such as meteorological conditions, as Woith (2015) claims that such externally induced anomalies look strikingly similar to those associated with seismotectonic processes.

Radon indeed seems to be a very sensitive *in situ* stress gauge. For instance, Teng and McElrath (1977) report an experiment where Radon concentration in a hot spring is measured every 2 hours over a total time period of 9 days. A simple harmonic analysis suggests that the dataset features diurnal as well as semidiurnal fluctuations, i.e. closely related to Earth tides. Shapiro et al. (1980) analyze 20 months of continuous monitoring at the Kresge site in Pasadena, covering 1977 and 1978. Data are sampled three times a day, allowing them to show evidence of an annual cycle, which they interpret as being due to the thermoelastic stresses emerging from changes in the subsurface temperature. The corresponding estimated strain is of the order of 5×10^{-6}, i.e. within the range proposed by Dobrovolsky et al. (1979). Trique et al. (1999) study two lakes in the French Alps, with water levels varying with amplitudes of, respectively, 50m and 70m. The two sites are equipped with instruments allowing to measure Radon emanations, electric potential variations, as well as the strain induced by the fluctuating water levels over a period of nearly 3 years. They find that Radon emanation bursts are highly correlated with episodes of strain acceleration: positive peaks of both time series occur within 10 days of each other in 63% of the cases (16 events in all; the score decreases to 27% if one distributes the same number of radon bursts randomly in time). A similar but slightly weaker association is found for fluctuations of the electric potential (the correlation score is 53%, and decreases down to 30% when randomizing the electric data), while the tiltmeters indicate strain amplitudes of about 5 to 7×10^{-6}.

A rough correlation of Radon emanation and seismicity is documented by Inan et al. (2008), who report a continuous monitoring at a soil radon station along the North Anatolian fault during the full 2002 year. They notice that many peaks of concentration are correlated with the occurrence of M≥4 events within a radius of 100km from the recording station. Interestingly, all earthquakes occur between January and October 2002, when the radon signal is characterized by quite large fluctuations. From early October to the end of December, the radon signal returns back to a low and nearly constant background level, while seismicity coincidentally shuts down. Some seismic events occur right at the same time as the Radon peaks, sometimes a few days afterwards, or shortly before such peaks. One should also mention that two of the nine detected seismic events clearly occur at a local minimum of the Radon signal.

Instead of considering cases of continuous monitoring and systematic correlation with earthquakes, some authors prefer to perform statistical analyses after building a compilation of previously published studies. In most of the cases, anomaly detection is performed using the method of Igarashi and Wakita (1990), which consists in estimating the long term average of the signal, and

looking for times when the signal deviates by more than two standard deviations. Hauksson (1981) provides a compilation of many data collected in the literature, devoted to single case analyses, in order to put in evidence general relationships between the properties of the recorded anomalies and the magnitude of the associated earthquakes. As he points out, in most analyses that have been performed by various teams across the world, the rate of false alarms as well as the absence of anomalies are generally not reported, which certainly biases his statistics. Such a data compilation is thus by no means equivalent to a systematic analysis. Hauksson (1981) claims that, in the case of Radon anomalies, the relationship of Rikitake (1976) for the anomaly lead time is much more often the exception than the rule. His compilation suggests that the amplitude of the Radon anomaly for events with magnitude between 6.0 and 8.0 tends to peak at distances of 200 to 500km from the epicenter, but does not give any indication about its azimuthal position. We shall see below that such a distance also emerges in the case of electric field anomalies recorded by satellites. This distance is observed to grow with time and with the magnitude of the event, which is compatible with the empirical law of Dobrovolsky et al. (1979), as the zone where Radon anomalies exist corresponds to strain values of about 10^{-8} to 10^{-6}. However, the amplitudes of the anomalies do not show any correlation with the magnitude of the event. Woith (2015) also provides such a meta-analysis of 93 papers relating radon precursor anomalies, and suggests that the precursor time interval before events can reach up to 18 years, but data selection suffers the same limitations as Hauksson (1981). Cicerone et al. (2009) provide a statistical analysis of 125 previously published observations linked to 86 earthquakes. They conclude that the temporal organization of the anomalies does not allow to foretell the time of the event, despite the fact that most anomalies seem to occur within the previous month and last less than 200 days. Larger precursory times (with maximum values varying from 0 to 200 days when magnitude increases from 2 to 8) as well as longer duration of the Radon anomalies (with corresponding maximum values from 200 to 1000 days) appear to be correlated with larger magnitude seismic events. They also suggest that larger anomalies tend to occur closer to the epicenter, and confirm that the amplitudes do not correlate with the magnitude of the event. Data are anyway very scattered, and most of the anomalies exhibit amplitudes of the order of 50% to 100% of the background level. See also Petraki et al. (2015) for another similar review of published works.

Looking at a continuous recording, Teng (1980) provides a contrasting account of the use of Radon anomalies for earthquake prediction purposes. He first analyses data recorded along the locked part of the San Andreas fault, where Radon is sampled weekly since 1974. At the time of his paper, he notices that no clear correlation can be assessed between earthquakes and the Radon signal. For instance, at the Switzer Camp station, three positive anomalies are detected, but only one seems to correspond to a seismic event. Moreover, no correlation among anomalies recorded at different stations seems to exist. He also reports the case of the Kutzan station, located West of the Szechuan province in China, close to a large active fault where nine events with magnitude between 5.2 and 7.9 occurred during the time period 1972-1976. Prior to eight of them, anomalous spikes in Radon concentration have been recorded from 6 to 13 days before the events, and only one anomaly was not followed by any seismic event. Those anomalies stood from 36% to 120% above the long-term average level. Teng (1980) acknowledges that many anomalies worldwide do not seem to be linked to any event, so that the rate of false alarms in a prediction set-up might be quite high.

Shapiro et al. (1980), whose experiment has been described above, show that only 3 out of a set of 11 events with M≥2.0 and depth within 2-15 km, within a 25km distance from the station, have been preceded by a Radon anomaly. Four are reported to be preceded by possible fluctuations due to some external cause (such as rain), while four came without any precursory signal. Note that, in this work, anomalies have been detected by a simple visual inspection.

Hauksson and Goddard (1981) collect data from nine stations located in Iceland, with most stations being spaced by less than 15km, sampled once a week in 1978 and 1979. In order to associate recorded Radon anomalies and observed earthquakes, they propose a relationship to relate the minimum earthquake magnitude M that is able to trigger an anomaly at a recording station, as a function of the epicenter-to-station distance D. They find that M≥2.4 $\log_{10}$(D)-0.43 (which, when

inverted, yields an estimation of D that is a bit larger than the one initially proposed by Dobrovolsky et al., 1979). This relationship is fitted on data reported in the literature for large earthquakes occurring in China, USSR and Japan, and simply extrapolated to smaller magnitudes for their observations in Iceland. When earthquakes are clustered, only the largest one is taken into account, or the first one of the sequence if their magnitudes are similar. Radon anomalies are then detected using the criterion of Igarashi and Wakita (1990). When considering all events (23 earthquakes with magnitude ≥1.0) and stations, they are then left with a database of 57 potential observable radon anomalies, from which they deduce a set of 9 observed precursory anomalies, 48 cases of lack of anomaly (false negatives), and 7 false alarms (or false positives). They also observe that the amplitude of the anomaly does not seem to change with distance. Anomalies last from about 2 weeks to a month, their amplitudes relative to the background level being about 40% to 380%. When considering only events with M≥2, 65% of the latter can be associated with at least one anomaly, and both the duration of anomalies and the maximum distance where they are observed increase with the size of the event.

Steinitz et al. (2003) report an eight years (1994-2002) experiment near the Dead Sea rift fault, where 796 events with magnitude between 0 and 4.6 have been detected. They first remove events with a location uncertainty larger than 4km (thus selecting 82% of the whole catalog) and exclude events that appear to be clustered with previous ones. They compute a running average of the Radon time series using a 25h long window. From this time series, they determine the local minima and maxima. For each locally maximum value, they compute the ratio between that value and the preceding minimum value (which is considered as the onset of the corresponding anomaly). They then show that only anomalies ≥1.9 are correlated with earthquakes, which constitutes a set of 110 anomalies, considering events occurring as far as 270km from the monitoring station. They then show that events occurring outside of the Dead Sea rift valley do not show any specific clustering relative to the anomalies, whereas those occurring within the rift do display such a clustering within the three days following the onset of the anomaly. This result is validated by generating random earthquake sequences, showing that the natural observations have a probability of being due to chance of only p=0.006%. This result is stable with respect to the specific rules employed to remove clustered events.

Torkar et al. (2010) use the data of a Radon station in Slovenia, operating from June 2000 to January 2002, with an hourly sampling rate. For each earthquake, they compute the radius predicted by Dobrovolsky et al. (1979) and look for prior anomalies before this event within twice this distance. The time series of Radon concentration and other meteorological data during non-seismic periods are then fed into a multilayer perceptron (i.e. a multilayer neural network) in order to decipher the effect of external non-seismic environmental parameters on the Radon signal. The parameters of the neural network are then applied to the set of environmental parameters during seismic periods in order to predict what the Radon concentration should be, and compare it to the observed one. The difference between the two defines the potential anomaly. This technique then allows one to associate 10 of the seismic events (i.e. 77% of the total) to a Radon anomaly, within +/-7 days.

Let us also mention the report by Igarashi et al. (1995) of the fourfold increased Radon concentration in ground water over several months before the 1995 southern Hyogo Prefecture (Kobe) earthquake on 17 January 1995. On 8 January, 9 days before the earthquake, the radon concentration reached a peak of more than 10 times that at the beginning of the observation, before starting to decrease. Johansen et al. (1996) found that the dynamical evolution of the Radon concentration is well-represented by log-periodic accelerated peaks, suggesting a kind of critical behavior (Freund and Sornette, 2007).

3.4 Ground measurement of electromagnetic fields

3.4.1 Electric field
In the DC to ULF range (i.e. up to 10Hz), Myachkin et al. (1972) report variations of the electric

field amplitude of the order of 100-300 mV.km^{-1}, during the 3-16 days before events in Kamchatka, but not systematically. Sobolev (1975) similarly noticed a decrease of the electric field prior to events in Kamchatka, using hourly means. In contrast, Miyakoshi (1985) reports an increase of amplitude on just one of the two components in Japan. This corresponds to variations at periods of a few hours to days. At higher frequencies, no such variations are noticed (Honkura et al. (1976) report daily variations of 50% at periods 60-7200s without any associated seismicity; variations of up to 100% are observed by Sims and Bostick (1969) in Texas without any event too). In Greece, Varotsos and Alexopoulos (1984a, 1984b, 1987) and Varotsos and Lazaridou (1991) reported square pulses of up to 250 mV.km^{-1} preceding events by 7-260 hours (so-called Seismic Electric Signals, SES). Scaling of the observed signals on dipole gauges of different sizes are used to discriminate true signals from noise.

3.4.2 Magnetic field

The release of positive holes from a source volume generates currents that are accompanied by corresponding changes in the magnetic field. If the magnetic field changes rapidly, transient magnetic pulses are observed. In fact, it is this phenomenon that allowed Shockley et al. (1949) to verify the diffusive behavior of charges in semiconductors. Such pulses were computationally modeled in the context of positive hole flows by Scoville et al. (2015) and were found to have the characteristic diffusive form of pulses observed before several earthquakes in Peru, within an order of magnitude in amplitude and duration.

Similar pulses were observed with increased frequency prior to the M = 5.4 Alum Rock California earthquake of 30 October 2007. A magnetometer located about 2 km from the epicenter recorded a series of unipolar magnetic pulses reaching amplitudes up to 30 nT, as reported in Bleier et al. (2009). Bleier et al. (2009) shows that, in the three weeks preceding the Alum rock earthquake, the incidence of pulses was higher than any other 3-week period from 2006-2007 and that the pulse count falls rapidly after the earthquake. Bleier et al. (2009) also notes that there were no nearby lightning strikes at corresponding times, the pulses were much stronger than PC3 and PC4 geomagnetic pulsations, and were localized near the epicenter, which would not be the case for geomagnetic activity.

Johnston et al. (1973) offer a review of reported variations of the magnetic field amplitude before earthquakes, and show that their amplitudes decrease drastically with time after 1960. This is interpreted as resulting from higher quality instruments, and from the removal of anomalies due to ionospheric and magnetospheric disturbances. Honkura et al. (1976) show that, below 0.1Hz, the spectrum of the natural field has a 1/f spectrum, which explains the existence of many fluctuations superimposed on the DC component, so that anomaly detection might be difficult in this frequency range. For instance, Dea et al. (1993) successfully correlate ULF signals with 29 events with M>3.5 in California and Nevada during 18 months. However, they report associated signals for only 7 of the 67 events with M>3.5 in Southern California during the same period.

Chen et al. (2004) study the variations of the total geomagnetic field recorded by eight ground stations in Taiwan during 1989-2001 with a sampling rate of one measurement every 10 minutes (except one station, with a sampling interval of 5 minutes). They compute the yearly drift of the amplitude of the magnetic field, and data are compared with the international geomagnetic reference field model (Barton, 1977). The drift is found to be less than 5nT/yr for all stations but one after 1997, thus defining a zero isoporic zone (ZIZ) as defined by Zeng et al. (2001) who claim that 80% of events with magnitude larger than 6.0 occur within 9 months to 2.5yrs after the onset of a ZIZ. Chen et al. (2004) claim that such a ZIZ appears in Taiwan after 1997, coinciding with the onset of seismicity, while the ZIZ disappears after the Chi-Chi earthquakes and its aftershocks sequence. Zeng et al. (2002) claim that a ZIZ appeared within 2.5 years before the Haicheng and Tangshan earthquakes in China, while Ispir et al. (1976) report a similar process about 1 year before M>=6.0 events in Turkey during 1966-1969. Tazima et al. (1976) report the same behavior within 2.5 years before 80% of events in Japan during 1954-1966.

Johnston (1989) reports a continuous experiment of magnetic field monitoring along 800km of the

San Andreas fault system, with only one event with M=5.2 preceded by a magnetic anomaly on two independent instruments (which happened to be the closest to the epicenter), while a nearby event with M=5.9 gave no precursory signal. The recording system of the USGS operated for 14 years.

Smith et al. (1978) failed to correlate creep events on the San Andreas fault with signals recorded by nearby magnetometers using 3 years of data. However, Johnston (1989) suggests that, when detrended, changes in creep rates over time scales of several months appear to be correlated to similar changes in the magnetic field, which is interpreted as the effect of the tectonic load. Creep events are also not associated with local variations of the electric field.

Han et al. (2014) use geomagnetic data in the ULF range (i.e. around 1Hz) recorded by a single ground station in Japan during the time period 2001-2010. The quantity they study at a given station is not a standard one and is derived from Hattori et al. (2006). They first consider each event and its associated co-seismic energy release. The quantity that such an event transfers to a station is its energy divided by the squared hypocentral distance. Coarse-graining at the scale of 1 day, they thus compute a daily cumulative energy index at each station, and consider only cumulated values larger than 10^8 (unfortunately, no unit is provided), which are then labeled as earthquake events, and consider only seismic events with a depth shallower than 60km. They consider two spatial subgroups of events: the closest 50 ones, and the next closest 50 ones. For the magnetic signal, they only consider data recorded from 2:30am to 4:00am in order to remove external magnetic pollution. The recording of the vertical component sampled at 1Hz is then wavelet-transformed at about 0.01Hz, and its power is coarse-grained at a daily scale too. Another station, located in an aseismic area, is used as a reference in order to remove the effect of global magnetic fluctuations. Using a simple linear regression model to link both magnetic signals, they are able to compute a reference signal at the observation station, and simply use the ratio between the observed and modeled values at that station in order to define an anomaly. An anomaly is defined when the ratio is beyond the median of its distribution plus 1.5 times its interquantile range. This thus means that only energy enhancements are considered as anomalous, without any consideration of energy drops. They are thus left with a set of 324 anomalies. They then use a superposed epoch analysis by considering consecutively each earthquake as the origin of time, in order to check the average distribution of anomalous geomagnetic days before and after the event. A similar procedure is conducted by randomizing the times of earthquakes using a uniform distribution. Unfortunately, they do not decluster the events (or only partially, thanks to their daily coarsegraining). Repeating this last step several times allows them to compute error bars on the surrogate sets. The results show a clear clustering of anomalies in the two weeks before and 2 days after earthquake events. Coarse graining at scale of 5 days yields an anomalous period of 6-15 days before earthquake events. When considering the dataset that is the most distant to the station, those correlations disappear, suggesting that only events close to a station can generate magnetic anomalies. Varying the threshold of the energy index, they find that only earthquake events which induce values larger than 10^7 are significantly associated with anomalies that precede them. They propose to quantify their results by plotting them onto a Molchan error diagram, considering only the case where, once an anomaly is evidenced, an alarm is triggered within a time window extending 11-15 days after it. This should lead to a single point on the diagram, but the authors plot a continuous line from which they deduce that their gain is around 1.6 when compared to a random prediction. The parameter used to get that curve is not mentioned, so their conclusion is a bit unclear. We can guess that the parameter is the threshold value defining if an anomaly is observed.

In a subsequent paper, Han et al. (2017) use exactly the same dataset and processing in order to test for the influence of the leading time and window size of the alarms to get the best prediction when an anomaly is observed. They use a slightly different version of the Molchan diagram by plotting the ratio of the correctly predicted events versus the ratio of the alarm time rate. As a bonus, they compute the 90% and 95% confidence level curves of the random guess case in order to check the significance of a prediction that is observed to be better than random. They then show that the most significant results are obtained when the alarm time rate is rather large, within 0.25-0.45. For a comparison, they also simply use the same prediction algorithm but replace the detected anomalies

in the magnetic signal by earthquake days themselves, so using seismicity itself as a predictor of future activity. This shows that the latter performs always worse, close to a random forecast. In order to investigate the influence of the parameters defining the position and size of the alarm window, they use the skilled area score of Zechar and Jordan (2008). From these computations, they deduce that several combinations of parameters may lead to an increased prediction power: the first one is characterized by a leading time of a week and an alarm window of less than four days; the other one by a leading time of 14-14 days and an alarm window of less than a week. The absolute optimum corresponds to a leading time of 8 days and an alarm window of 1 day, which seems to be amazingly precise for a prediction method. For those parameters, the Molchan curve is above the 95% confidence level when the alarm rate is within 0.10-0.57. However, the maximum probability gain is not very large, only 1.78 when the alarm rate is 5%. Indeed these results do not constitute a real prediction experiment, but rather the training phase of a potential prediction method. The optimal parameters provided by the authors should be validated by analyzing the success and failure rates on an independent dataset. Moreover, the results might change when considering the size of the area around the station (here, 100km).

3.4.3 Visible Spectrum (Earthquake Lights)
There have been numerous credible reports of luminous phenomena associated with earthquakes dating back for centuries, and high-quality images and video are now available due to the proliferation of digital imaging (Derr et al., 2014). Since light emission is necessarily associated with the motion of electric charge carriers, earthquakes lights provide conclusive and visible evidence of electromagnetic phenomena prior to and during earthquakes. Thériault et al. (2014) make a systematic study of these reports of earthquake lights and find that more than 90% of earthquake lights are reported near rift environments, marked by the prevalence of subvertic mafic dykes that have been enplaced during past periods of extensional tectonics.

Though early photographs of earthquake lights as described in Derr (1973) were met with skepticism, digital photography has now documented many instances. Precise timing of seismic waves and photography of earthquake lights in Peru has established that light emission is correlated with the arrival of seismic waves (Lira, 2008).

3.5 Thermal Infrared (TIR) anomalies
Eleftheriou et al. (2016) provide the only long-run experiment attempting to correlate earthquakes with TIR anomalies in Greece over the time period from May 2004 to December 2013, using the MeteoSat Second Generation–Spinning Enhanced Visible and Infrared Imager (MSG–SEVIRI). They consider 3151 TIR images acquired in the 9.80-11.80μm wavelength from 2am to 2:15am (local time). Data are first conditioned according to the month and time of the day of recording, as well as their type of geographical location (i.e. inland or offshore). This not only allows them to remove the background variations of temperature, but also to reduce the effect of other external parameters such as the vegetation cover. Anomalies are defined by comparing each conditional measurement to space and time averages, and their standard deviation. Note that all measurements affected by the presence of clouds are excluded from all those calculations. Side effects of the presence of such clouds (such as the cold spatial average effect, which results from the possible correlation of the clouds location with the ground temperature distribution) are also eliminated. Thermal anomalies are detected when the observed signal deviates more than four standard deviations from its reference value, and checked for spatial and temporal consistence (covering an area of at least 150km^2 within a 1°x1° cell, and occurring at least twice within a week).

This leads to the identification of 62 anomalies. A given anomaly is considered to be correlated with an earthquake with M≥4 if the latter occurs within a time window extending from 15 days before the anomaly to 30 days after it, and within the distance provided by the Dobrovolsky et al. (1979) law. Results show an amazing correlation between anomalies and earthquakes, as 93% of the alarms correlate with seismic events, and only 7% constitute false alarms. However, their correlation procedures allow sequences of anomalies to occur (1) only before events, (2) only after

them, or (3) to start before events and stop after they occurred. For events with M≥4, category (3) features less than 5% of the anomalies, while this share increases up to 15% in average for increasing magnitude thresholds. About 66% of the anomalies occur before events with M≥5.

In order to test the significance of their correlations, they use Molchan diagrams, which plot the fraction of missed events against the fraction of the space-time volume occupied by the alarms (which, in time, include 15 days before the anomaly and 30 days after it ended). They also consider a prevision mode, where they take only account of the 30 days following the anomaly. In both modes (correlation or prevision), they find that the observed associations have a significant gain over pure random ones. In correlation mode and M≥4, the gain is between 1.8 and 3.2, while in prevision mode it is between 1.5 (for M≥6) and 3.7 (for M≥5). In both cases, the largest gain is achieved when considering events with M≥5.5. In this case, the fraction of space-time filled with alarms is within 8-11%. Unfortunately, no study of the time distribution of anomalies is performed, and the earthquake catalog they use is not declustered beforehand. This latter feature may artificially increase their success rate.

One detailed example of a TIR anomaly prior to a major earthquake is found in the work of Piroddi et al. (2010, 2012, 2014). This study concerns the spatial and temporal distribution of TIR anomalies preceding the M=6.3 L'Aquila earthquake of April 06, 2009 in central Italy using the Nighttime Thermal Gradient (NTG) technique of Bryant et al. (2002, 2003, 2004a, 2004b). The NTG technique is based on the recognition that, under clear skies, the Earth's surface tends to cool during the night. This cooling trend can be obtained from geostationary weather satellites, which deliver calibrated TIR images every 15 min or 30 min. A linear regression of the implied radiation temperature versus time allows a slope ΔT to be derived, and this can be used to map nighttime temperature trends.

One notable result of this analysis is the fact that the recorded TIR anomalies are not present on the valley floor, where several active faults are located, including the Paganica Fault that produced the M=6.3 seismic event three nights later. The anomalies were associated with topographic highs on either side of the L'Aquila valley but not with the valley floor. This results suggests that the TIR anomalies are not due to warm gases emanating from the ground but rather the result of the accumulation of p-holes at topographic highs, where they undergo exothermal pairwise recombination to peroxy. The energy required to break the peroxy bond is on the order of 2.4 eV [*Kathrein and Freund*, 1983]. During pairwise p-hole recombination a fraction of this energy is regained, probably 2.1–2.2 eV. This energy will be deposited into the two oxygens participating in the recombination reaction, causing the

m to becomes vibrationally highly excited to the tune of ≈20,000K equivalent. Hence, as new peroxy bonds form at the Earth surface, in particular at topographic highs, they are expected to emit infrared photons corresponding to the radiative de-excitation of the vibrationally excited peroxy bonds.

3.6 Ionospheric disturbances

Correlations between earthquakes and ionospheric disturbances have been first proposed after the occurrence of the Great Alaska earthquake in 1964 (Davies and Baker, 1965; Leonard and Barnes, 1965). Since then there have been many related publications (see for instance Cahyadi and Heki, 2013; Calais and Minster, 1995; Ho et al., 2013; Hsiao et al., 2009, 2010; Le et al., 2013; Lin, 2010, 2011, 2012, 2013a; Liperovskaya et al., 2006; Liu et al., 2001, 2006b, 2008, 2009, 2010a, 2011a, 2012; Mekela et al., 2011; Ondoh, 1998; Pulinets et al., 2003; Pulinets et al., 2004, 2005; Pulinets and Boyarchuk, 2004; Pulinets, 2007; Sarkar et al., 2011; Silina et al., 2001; Yao et al., 2012; Yu et al., 2009; Zhao et al., 2008, 2010; Zhou et al., 2009; Zhu et al., 2013a, 2013b). As for radon studies, most of this work has been devoted to case studies, such as for the Wenchuan (M7.9) event (Hsiao et al. 2010; Jhuang et al. 2010; Jin et al. 2011; Kamogawa et al. 2012; Lin et al. 2009; Lin 2013a; Liu et al. 2009, 2012; Xu et al. 2010; Yu et al. 2009; Zhao et al. 2008; Zhou et al. 2009; Zhu et al.

2013b), or the Tohoku (M9.0) event (Chen et al. 2011; Gokhberg et al. 2011; Hayakawa et al. 2013; Kamogawa et al. 2012; Le et al. 2013; Lin 2012; Liu et al., 2011a; Yao et al. 2012; Zhu et al. 2013b).

Ionospheric perturbations constitute the core of many studies (Chen et al., 2004; Depuev and Zelenova, 1996; Hayakawa, 2007; Hayakawa et al., 2006; Liu et al., 2006a,b; Liu et al, 2004a,b; Maekawa et al., 2006; Oyama et al., 2008; Pulinets et al., 2005; Singh, 2008; Trigunait et al., 2004; Zakharenkova et al., 2007) and generally focus on the fluctuations of the Total Electron Content (TEC), as well as on the changes in the Very Low Frequency (VLF) properties of the electromagnetic field. They rely on datasets acquired by satellites such as DEMETER (Detection of Electro-Magnetic Emissions Transmitted from Earthquake Regions), featuring instruments to measure directly the physical properties of the ionosphere. This micro-satellite of the French National Agency (CNES), weighting about 130kg, was a low altitude satellite launched in June 2004 and stopped operating in December 2010. It was orbiting at low altitude (710km at first, then 660km from December 2005), on a nearly polar (98° inclination) and nearly sun-synchroneous orbit, with 14 orbits a day and nearly 35min long half-orbits. The upgoing orbits corresponded to nighttime, and the downgoing orbits to daytime. The satellite did not strictly return above the same points every day, so that such consecutive 'nearby' points could be more than 1000km apart from one day to the next, and measurements did not cover latitudes beyond +/-65°. The initial mission of DEMETER has been to study the seismo-electromagnetic effects on the ionosphere prior to earthquakes, not to perform predictions *per se*. It featured three electric and three magnetic sensors, two Langmuir probes, an ion spectrometer, and an energetic particle analyzer. The frequency ranges covered by the magnetic and electric field measurements are respectively 10Hz-17kHz and DC-3.5MHz, while the sampling rate of the Langmuir probe for TEC estimation is 1s (Lebreton et al., 2006).

Some other satellites serving other purposes can also be used to infer the TEC. The Global Positioning System (GPS) consists of a set of 24 satellites, evenly distributed within 6 orbital planes, flying at an altitude of 20,200km. Each satellite emits signals at two distinct frequencies and carrier phases. Due to the dispersive properties of the ionosphere, each signal has thus a different speed. The carrier phase advance and group delay of those waves in the ionosphere depend on the electron density integrated along the full propagation path. The TEC can then be derived by comparing the phase delays between the two signals. A final correction is then applied to derive the VTEC, which corresponds to the TEC which would have been measured if the waves' rays had been vertical (Sardon et al., 1994; Leick, 1995; Liu et al., 1996). VTEC maps can then be derived every 30s (Tsai and Liu, 1999), using the more than 1,000 GPS ground-based receivers worldwide. Most of the works presented below and using GPS data use the global ionosphere maps provided with a 2h time resolution by the International GNSS Service (IGS), at distinct grid points with a spatial resolution of 2.5° in latitude and 5° in longitude, covering the full longitude range and latitudes within +/-87.5°. This provides maps consisting of 71x73=5,183 points each.

3.6.1 Total Electronic Content (TEC) measurements
In the last two decades, interest has grown in the estimation of the TEC in the ionosphere and its relationship with earthquakes (Astafyeva and Heki, 2011; Calais and Minster, 1995; Chavez et al., 2011; Kim and Hegai, 1999; Oyama et al., 2008).

Measurements by DEMETER
He et al. (2011) study the ionospheric electron density directly recorded by DEMETER, with a time resolution of 1s (Lebreton et al., 2006), and use data from 2006 to the beginning of 2009 as the satellite changed altitude late 2005. This reduces the dataset to 30,000 half-orbits, as they only keep nighttime periods to avoid solar perturbations. During the same time window, earthquakes amount to about 7,000 events with M≥5.0. A grid is centered on each event, featuring 11x11 cells with a 2° resolution. TEC data are segmented in 30s long intervals, which are then sorted in space within this grid. This allows them to compute, in each cell, a background average and standard deviation by

considering data recorded from 31 to 75 days before the event and associated to a magnetic index Kp<2+. They then compute the average values in the last 30 days and Kp<3+ as the studied signal. This allows them to define a relative variation of the signal compared to the background (and normalized by the standard deviation of the latter) in each cell. This grid is then stacked and averaged over all considered events. This allows them to show evidence for a maximum anomaly close to the epicenter, located slightly to its North in the Northern hemisphere, and slightly to its South in the Southern hemisphere, while its spatial extent is about 350km. The anomaly is also more pronounced for offshore events, for larger magnitudes and shallower depths. Removing all data that follow an event within a day (to eliminate the effect of gravity waves possibly triggered by the latter), the effect is weaker but clearly identifiable. Looking more closely at their results, we can notice that the reported anomaly is positive, but that its normalized value (by the background's standard deviation) is only 0.68 at maximum, i.e. of about one standard deviation. We also notice that such a systematic shift between the event and the anomaly has also been documented for Radon anomalies (Hauksson, 1981), but He et al. (2011) did not look at any possible relationship between the amplitude of the shift and the size of the associated event.

Ryu et al. (2016) compute the equatorial ionization anomaly (EIA) and study its relationship with mid-latitude seismic activity. This is done by selecting a restricted zone in North-East Asia (roughly covering a 40° by 20° window centered on Japan) and earthquakes with magnitude M≥6.0 occurring therein during the DEMETER mission (35 events in all, previously part of the analysis of Liu et al., 2013). The quantity they consider is, for each orbit, the TEC measured near the geomagnetic equator region, by estimating the normalized equatorial plasma density (NEDP) which is ratio of electron density within 15° of the geomagnetic equator to the same averaged value at latitudes between +/-30° and +/-50°. Their analysis is based on plots of the TEC as a function of latitude for profiles distant to a given epicenter by less than 20° in longitude. They first perform a restricted set of individual case studies of 7 events with M≥6.8 in a time period extending from one month before to one month after each selected event. In a few cases, they outline that some anomalies could be due to the occurrence of other large events occurring outside of their spatial window (for instance in Solomon Islands, Taiwan, China, etc...), an hypothesis that is difficult to test. They finally claim that 5 out of the 7 events are associated with equatorial positive TEC anomalies within 10 days before their occurrence. Looking at individual TEC profiles for the M≥6.0 events, they do not observe such an increase. Anomalies appear more clearly if one selects only M≥6.5 events (i.e. 16 events in all, with only one not showing such an increase, which can be explained by its larger focal depth). The effect seems to be absent for hypocentral depths larger than 30km. They conclude that mid-latitude seismicity affects the equatorial ionosphere in the morning.

Measurements by GPS

Saroso et al. (2008) study correlations between TEC and earthquakes occurring in Sulawesi during the time period 1993-2002, using three ground-based GPS stations. The TEC is first estimated at the location of given events, and for any local time. The mean and standard deviation of this distribution are estimated, as well as upper/lower detection thresholds (corresponding to 1.34 standard deviations above or below the mean, i.e. a 82% confidence level). This reference state is then compared to TEC data derived at the same locations each of the 15 days preceding an earthquake, and allows one to infer that anomalies occur within 2-7 days before the events. However, the earthquake dataset which is chosen by the authors seems to be arbitrary, as they limit it to 11 seismic events with M≥5.9, but do not mention how they selected them, as well as to the Sumatra, 2004 event (M=9.3). They also do not mention any declustering of the catalog, so that some anomalies may be each related to several distinct events occurring as clusters (thus increasing the apparent success rate), and they do not test any null hypothesis (such as the distribution of anomalies within similar 15 days time windows in aseismic areas). A last criticism is that they do not further test whether some of the anomalies could correspond to some anomalous geomagnetic storms or other external disturbances.

The studies that follow have been conducted at a worldwide scale using the TEC maps provided by

the IGS and described above. Le et al. (2011) study TEC anomalies at the global scale before events with magnitude larger than 6, within the time period 2002-2010. Earthquakes occurring within 4 days after a magnetic storm are excluded from the analysis, as well as those occurring at nearly the same location and within 15 days in time, leaving a final and significant set of 736 events. The VTEC is interpolated linearly in time with a 1h step, before modeling them spatially using a spherical harmonics expansion. The grid point that is the closest to each event is considered as its associated TEC data point. At each time sample, they compute the mean and standard deviation of the signal within the 1 to 15 previous days, and the current point is considered as an outlier if it is beyond a single standard deviation from the mean. If there are more than 6 successive anomalous data within a given day, they associate to the latter the largest quantile reached by such a fluctuation (R=60%, 80% or 100%). Each of the 1-21 days preceding each selected earthquake is checked for its abnormality and quantile level R. The days with anomalous geomagnetic indices are excluded from the statistics, as well each of the three days following them. The results show that: (i) the rate of observed anomalous days increases with the magnitude of earthquakes for shallow depths (≤20km); (ii) the rate of anomalies is larger when time gets closer to the occurrence of the event; (iii) positive anomalies are observed twice as often as negative ones; (iv) the rate of anomalies decreases with the focal depth. No specific variation with latitude is observed. In order to check with a null hypothesis, the 61-300 days before each earthquake are considered as background days. If another earthquake associated to the same node occurred within these background days, the 15 days before it and after it are removed, as well as anomalous geomagnetic indices days and their three following days. The background rate of anomalous days is 2 to 4 times smaller than the rate of anomalies in the 1-2 days before the events, confirming the significance of the observed precursory signal.

Yao et al. (2012) provide a worldwide analysis of M≥7.0 events during the year 2010, considering only those that have not been preceded by another M≥7 event within a 15 days window (yielding a final set of seven events in all). The TEC maps are then linearly interpolated at the location of each event. A sliding window method is applied, allowing at any given time to compute the mean and standard deviation of the signal over a 30 days window before that time. Thresholds are defined at +/-1.5 standard deviations from the local mean (corresponding to a confidence level of 87%). They then check for TEC anomalies within 0-14 days before each event. This analysis is repeatedly performed at each node of the original data grid. While some anomalies are clearly correlated with external perturbations, some others are not. Using only the latter, they check that 5 out of 7 events are preceded by TEC anomalies, which may be either positive (4 cases) or negative (1 case). Anomalies occur during daytime (from 12:00 to 20:00, local time), within 2 days before the events. By looking at anomalies at all the grid points, they notice that they indeed occur all over the world. Yet, some anomalies repeat in time at some of the nodes, and the highest repeating rates tend to cluster spatially in regions close to the future events, even if the spatial mode of the anomalies' density does not coincide with the epicenter (yet no systematic shift is observed). In parallel, some weaker effects are observed in the magnetically conjugated region, while the strength of the effect does not seem to be correlated with the depth of events. Unfortunately, the authors offer no such analysis and results over locations and times with no earthquake activity.

Zhu et al. (2014) study the anomalies before M≥7.0 earthquakes worldwide during 2003-2012, which amount to 144 events in all (as events occurring within a 5° distance and within less than 15 days in time are excluded from the analysis). The nearest grid point is used as a proxy for each event for the TEC signal. They use a sliding window of 10 days before any given time to compute the mean and standard deviation of the TEC signal at that time. They apply this technique to each of the 15 days before each event, and consider a confidence level of 95% to detect outliers. They exclude days when magnetic disturbances occur, as well as their two following days. Computing the relative amount of events before which some anomalies have been observed, they observe a larger rate of anomalies when the magnitude increases, and that the rate of negative anomalies increases as the time of the event approaches. Yet, the effect is very weak as the increase is of the order of a few percent when M varies from 7.0 to 7.9. They also observe that most negative anomalies occur

between 12:00 LT and 18:00 LT while their duration is about 2 hours. No such specific pattern is reported for positive anomalies, and this effect seems to hold only for events with M≥7.6.

Ke et al. (2016) look at GPS-derived TEC anomalies before M>5.0 events in China from 2003 to 2013. They have unfortunately chosen arbitrarily only 24 events (as we can check that this set of events does not obey the Gutenberg-Richter distribution). Similarly to Yao et al. (2012), they use IGS maps published every 2h. They also use a sliding windows approach, but the chosen parameters are not indicated clearly, yet seem to be apparently the same as in Liu et al. (2010a,b), i.e. a time window of 5 days. Anomalies are defined by first computing the upper and lower quartiles of the TEC data within the 15 days before each event, and by defining upper and lower thresholds for detection by the quartiles-to-median distance multiplied by 1.5. Looking at anomalies from 15 days before to 5 days after the events, they observe that they can be positive or negative, occur before or after the events, and do not depend on earthquake magnitude. For 5<M<5.9, 33% of events have only positive anomalies, while 42% of events have only negative anomalies. The remaining 8% have both positive or negative anomalies. For 6.0<M<6.9, those ratios reach respectively 44%, 33% and 11%. For 7.0<M<8.0, they are 50%, 25% and 25%. Drawing spatial maps of TEC anomalies at the time of the events, they show that anomalies occur close to the events, but also at more distant locations. Unfortunately, no quantitative test of the significance of the results is provided. They also show that the amplitude of the anomalies fluctuates a lot within the 5 days before the events, and tend to be more uniform afterwards (but are not smaller, despite their claim). They finally note that more extreme solar and geomagnetic activities occur before most M>7 events, which they interpret by claiming (!) that these geomagnetic perturbations are indeed triggering those seismic events.

3.6.2 Ion density

The DEMETER satellite is also equipped with an instrument labelled IAP (Instrument Analyseur de Plasma; see Berthelier et al. , 2006) allowing to estimate the total ion density (i.e. the sum of H+, He+ and O+ ions), with a 4s time resolution in survey mode and twice that sampling rate in the burst mode. This allows them to get an alternative measurement of the TEC as both signals are assumed to fluctuate in opposite ways. The advantage of using ion density is that it is a less noisy signal than electron density, thus allowing to detect anomalies more efficiently. At the DEMETER altitude, the ion density is dominated by the O+ content (Li and Parrot, 2013).

Parrot (2011) analyzes a limited dataset extending from August 2004 to October 2009. They consider seismic events with M≥4.8 (17,366 earthquakes in all) and the measured ion density from 0 to 15 days before the events, keeping only the closest nighttime orbit within 1500km of each epicenter (which corresponds to a flight time of about 3 minutes). Sometimes, there is no such orbit within a given day (as the satellite is too far or recording failed). Anomalies are detected by a simple detection of local maxima of the ion density, and their amplitude is normalized by the background value along the same orbit segment. They compare their results to two reference datasets: the first one is obtained by switching the latitudes and longitudes of earthquakes but keeping their times (RAND1). Another dataset is obtained by shifting their longitude 25° to the West (RAND2), in order to keep the latitudinal structure of seismicity intact, as most events occur close to the Equator and as there are more anomalies of external origin around the Equator during nighttime. Such surrogate catalogs are designed to provide a background rate of spurious associations between anomalies and earthquakes. If N is the number of days between an event and an aftershock, and if N<15days, only ion density data within the N-1 days before the aftershock are used (but the aftershock is not eliminated from the catalog). For events occurring below the sea level, the amount of detected perturbations associated to events is always larger than the background rate. Inland, similarly high rates are observed only when considering M>6 events. Considering the average amplitudes observed before events, as well as the average maximum amplitude, both are found to be larger for the natural catalog, increase with the magnitude of the event, and are larger for offshore events (yet, no error bars are provided). This latter result is interpreted as the existence of a larger electric conductivity above the sea.

Parrot (2012) repeats the same analysis, but now splits events into three distinct categories: below the sea level, inland, and close to the coast, retaining only the closest orbit to each event, and eliminating data when $K_p>3+$. He then considers the median of the largest anomaly observed in the 15 days before each event. The observed anomalous effect increases with magnitude, decreases with focal depth, and is again stronger offshore.

Li and Parrot (2012) average consecutive values in the burst mode to get the same rate as in the survey mode. The data are then smoothed using a Savitzky-Golay algorithm (Savitzky and Golay, 1964). Anomalies are detected using the same methodology as above, with durations constrained to be between 23s and 2 minutes (corresponding to flight distances of up to 840km and at least 5 sampled points). Events are split according to their magnitude (M4.8-5.0; M5.1-6.0; M$\geq$6.1) and focal depth (larger and smaller than 20km). Anomalies are then associated (or not) to earthquakes according to the delay times T between them (<7 days or <15 days), and the epicenter-anomaly distance D (<500km, <1000km, or <1500km). For D<500km and T<7 days, the number of false alarms is 44,863 over a total of 46,446 i.e. 97%. The rate of good detections increases from 14% to 18% when the magnitude increases (see Tables 2 to 7) and decreases slightly with depth. Logically, it increases when cutoffs on time interval and distance increase. Unfortunately, the rate of false alarms is not systematically indicated and they do not provide the total amount of positive anomalies, in order to compare with the ones successfully associated to events.

Using a technique similar to Li and Parrot (2012), Li and Parrot (2013) present results about ion density variations, focusing on nighttime anomalies only, resulting in 96,863 half-orbits, with 27,257,933 samples. Different criteria are applied to define an anomaly: (i) a duration must be between 23 and 120s; (ii) the distance from the corresponding satellite position to the nearest seismic zone must be less than 1,500km (considering only events with M>4.8 during the satellite mission as defining seismic areas); (iii) on the day of the anomaly, K_p must be smaller than 3 in order to remove the effect of solar activity. Spurious peaks are also removed, without mentioning the criteria for their detection. The anomaly time window is defined by a local extremum bracketed by the two closest points where the derivative of the signal changes sign, while the values of the signal at the end points of this window define the local background signal. This allows them to present evidence for 56,139 such anomalies (which are observed to be either positive or negative), while the total number of earthquakes is 21,863 (using the USGS catalog from August 20, 2004 to December 31, 2010). Computing the ratio A between the anomaly's amplitude and the associated background value allows them to deal safely with problems such as a change of the satellite altitude. The comparison with earthquake activity is performed by computing the distance D between an anomaly and an event (with a maximum value of 1500km), the time delay T (considering a maximum value of 15 days), and the depth d of the event. If an earthquake can be associated to one or more anomalies, it is counted as a single detection. If not, it is a bad detection. If a perturbation corresponds to an event, this is a true alarm; if not, a false alarm.

Considering $A>10\%$ and targeting events with M=4.8 to 5, the number of false alarms amounts to 63% (26,877 alarms in all). The number of wrong detections is 64% (over 12,057events). If we take account of earthquakes with magnitude larger than 5, the false alarm rate drops to 19%. Counting all events with M>4.8, the rate of false alarms drops from 23% to 17% when A increase from 0 to 15%, but the rate of bad detections then increases. Anyway, the rate of good detection increases with the magnitude of events, and about 90% of the right alarms correspond to upward (positive) anomalies. The number of associated anomalies per earthquake is also observed to increase with their magnitude, while the amplitude of the anomalies is only weakly correlated with the magnitude of the events.

They then consider 3 types of events: inland, below the sea with a water depth larger than 1km, and below the sea but close to the coast. The percentage of good detections is larger under the sea and is the worst when close to the coast, confirming the results of Parrot (2012). Unfortunately, they do not mention anything about the rate of such correct alarms. In order to compare the results with a reference dataset, they shift events 25° Westward, and 1 month backward in the past (in order to keep intact the latitudinal structure). The ratio of good detections is then 42,27% (with a standard

deviation of 0.39), whereas the ratio is about 44.7% at worst with the true data. The observed effect is thus very weak. They also find that one perturbation is at most associated with a single event, while each event can be associated with more than one perturbation. Intracontinental seismicity features only events with less than 9 anomalies. Events with 10-19 anomalies occur mostly at plate boundaries, while events with more than 20 anomalies occur in a very specific zone in the southern hemisphere.

In order to complement their analysis, they also look at the number of perturbations before large events as a function of time. The total number of perturbations before events reaches 64% during the week before (78% over the Himalayas), while no such increase is observed in the southern zone mentioned above. The number of anomalies shows a maximum on the day of the event, and decreases for larger time delays. Results using electron density are about the same, except that the peaks are a bit less sharp. Both the rates of false alarms and good detections decrease when small anomalies are eliminated. As the satellite flies over any zone only a few minutes a day, chances are large to miss them (and have a wrong detection) if the anomalies do not occur continuously. They also notice (focusing on only two events of M=8.8 and 6.3) that the epicenter lies close to the barycenter of the associated anomalies. However, this could be due to the uniform random distribution of anomalies, which are constrained to sample a symmetric spatial zone around the earthquakes.

3.6.3 Electric and magnetic fields measurements

Electromagnetic perturbations

The DEMETER satellite was equipped to measure simultaneously the electric and magnetic fields using respectively the ICE (Instrument Champ Electrique, see Berthelier et al., 2006) and the IMSC (Parrot et al., 2006; Santolik et al., 2006). The ICE used two distinct modes of acquisition: (i) a survey mode, to record low bit rate data at 25kbits/s; (ii) a burst mode, triggered above predefined seismic regions, to record high bit rate data at 1.6Mbits/s. The seismic regions featured mainly the Southern American subduction zone, the Alps-Zagros-Himalaya mountain ranges, parts of the Asian pacific subduction zone, and a couple of other areas. The ICE featured four antennas to record the three components of the electric field. This analog signal was filtered into four frequency channels, then digitized and stored:

- DC/ULF (0-15Hz): the waveforms of the four measured potentials, digitized at 39Hz and stored for both modes of operation.
- ELF (15Hz-1kHz): three components of the field waveforms, sampled at 2.5kHz, in burst mode only.
- VLF (15Hz-17.4kHz): one component of the field waveform, or spectral data for one of the components, are sampled at 40kHz. In burst mode, the power spectrum is computed at a resolution of 19Hz. Forty such spectra are averaged and normalized, using a resolution of 2s, and both the waveform and spectra are stored. In survey mode, only the spectra are stored, according to three submodes: (0) identical to the burst mode; (1) the temporal resolution is 0.5s; (2) the time resolution is 2s but the frequency resolution is 78Hz.
- HF (10kHz-3.175MHz): the same field component as in the VLF channel is sampled at 6.66Mhz. Averaged power spectra are computed every 2s with a resolution of 3.25kHz over 40 intervals of 0.6ms. When in burst mode, the average spectrum is stored as well as the waveform of one of those intervals. In survey mode, only the average spectra are stored. There are three submodes: (0) power spectra with a resolution of 3.25kHz ; (1) same, but with a time resolution of 0.5s; (2) the time resolution is 2s and frequency resolution is 13kHz.

Nemec et al. (2008) use about 2.5 years of data, focusing on VLF band. The power spectra of one

electric and one magnetic component are computed onboard with a 19.5Hz resolution in frequency, and a 2s or 0.5s resolution in time. They use the electric component normal to the plane of the orbit, whereas the magnetic one is inclined 45° from the satellite velocity vector. Their analysis considers 11,500 hours corresponding to 20,000 half-orbits. The corresponding USGS catalog lists about 9000 events with M≥4.8. The dataset is first partitioned into a 6-dimensional matrix, defined by: geomagnetic longitude (res. 10°) and latitude (2°), frequency (16 bands for the electric component and 13 for the magnetic one, of 117Hz each, smaller than 10kHz in order to avoid the influence of terrestrial VLF transmitters), K_p index (0 to 1o, 1+ to 2+, and >3), magnetic local time, and season (October-April and May-September).

Within each cell of this matrix, they estimate the empirical cumulative and density distributions of the observed power spectrum amplitudes. For each considered observation E_i within a cell, the corresponding cumulative probability F_i can then be computed. Such F_i values are sampled only when the position of the satellite flies close to an earthquake epicenter (i.e. within 1,100km and up to 5 days before and 3 days after it occurred). Such datapoints are removed if some seismic events are too clustered, unfortunately without any mention of the rejection criteria in space and time. The sampled values of F_i are then binned as a function of frequency range (using the same bins as defined above), time to or from an event (using a 4h resolution), and distance to the event (using a 1°=110km resolution). The probabilistic intensity I_b is then defined within each bin, as the average value of F_i minus 0.5. Applying a correction to take into account the fact that all measurements are not independent, they detect anomalies of I_b beyond 3 standard deviations. The same method is applied on two types of surrogate catalogs: either keeping the real locations of earthquakes with random occurrence times, or keeping the real occurrence times with random locations. No specific pattern of I_b is noticed when using any of the random catalogs. The original data are then split according to day/night, and according to the focal depth of earthquakes (<40km and beyond 40km). Keeping only data recorded at night, they show that I_b decreases by about 3 standard deviations within a time window extending from 0 to 4 hours before seismic events with M>4.8. Using only superficial events with M>5.0, the observed decrease is about 4 standard deviations. The latter corresponds to a 4 to 6dB decrease of the power spectrum. The effect is weaker when using magnetic data, while no effect is observed during daytime or for deeper events. The effect is also observed to be stronger within a spatial window of about 350km, which corresponds well with similar estimations using ion density. Their interpretation is that during daytime, ionospheric ionization is so large that it masks all amplitude changes due to seismic activity. They argue that the 1.7kHz frequency corresponds to the cut-off frequency of the earth-ionosphere waveguide during the night (Budden, 1961), the low frequency cutoff being inversely proportional to the height of the ionosphere. Nemec et al. (2010) argue that the source of VLF radiation recorded by DEMETER during nighttime is due to electromagnetic waves generated by thunderstorm activity. If the height of the ionosphere decreases, then the cutoff frequency increases, and the power spectral density at 1.7kHz decreases.

Nemec et al. (2009), analyze the same dataset using 3.5 years of data (corresponding to 9,000 hours in nighttime for about 15,500 orbits), during which 9,500 earthquakes have been recorded, with a depth smaller than 40km and M≥4.8, and 5,500 events with M≥5.0. They first focus on the 200Hz-wide frequency band around 1.7kHz, nighttime recordings, M>=5.0 and depth <40km events, and a satellite-epicenter distance smaller than 3° (about 330km). Plotting I_b as a function of time, they still observe a sudden decrease beyond 3 standard deviations before the events. But the decrease is now only 2.4dB to 3.6dB, smaller than observed by Nemec et al. (2008). They interpret this change of amplitude as maybe due to some scarce but large contributions of the background level. Interestingly, they quantify the usual natural background variability of the raw signal to be about 11dB, which is much larger than the observed anomalies. The latter are indeed detected only because of their stacking procedure, but such anomalies could certainly not be detected individually when running, for instance, a genuine prediction experiment.

In a second analysis, they use a new data processing in order to study spatial patterns. They then re-estimate the F_i values taking account of a single time bin (0-4 hours before events) in order to infer

the spatial location of anomalies relative to the observed earthquakes. To do so, they consider any point P within 10° in latitude and longitude from a seismic event. For each orbit passing within 3° of such a point P, they check if the values of F_i are larger or smaller than usual. This is done by using the non-parametric Mann-Whitney U test, which tests if two populations have the same mean (see Sheskin, 2000), with a confidence level of 0.01 (their results being insensitive to this arbitrary choice). This allows them to compare the observed distribution of F_i values close to point P to their distribution along the rest of the same half-orbit, considered as a background signal. They then test if the observed Fi's are smaller, larger or indistinguishable from the values on the rest of the half-orbit, the latter cases being eliminated from the rest of the analysis, so that they only study cases where an anomaly is observed before an event. They then test the number of increases and decreases using a simple binomial distribution and assuming that both rates should not differ significantly if no effect holds. Despite the strong limitations of this test (as they exclude cases where no anomaly is observed before an event), they find a nonrandom, anomalous pattern about 1.5° North and 2° West of seismic events when stacking over all seismic events. The probability of random occurrences of increases and decreases of F_i is about 10^{-4} at this location. They finally focus on the most anomalous point (and its 3° surroundings) to check how the numbers of increases and decreases depend on earthquake magnitude, depth and altitude of the solid surface above the event. For M>5.5, there is most often a decrease, the pattern becoming more random for lower magnitude events. An observed decrease is also more probable for depths <20km. No dependence is found on the inland or offshore location of events. In a tentative explanation of the Westward drift of the anomaly relative to the earthquakes, they suggest that either aerosols are subjected to the Coriolis force, or that some ions are subjected to a magnetic field. But they offer no reason for the northward component of the drift. We can mention a similar shift of the anomaly on Radon anomalies recorded on the ground. In terms of statistics, it should be noted that, for 50% of events, no deviation occurs according to the Mann-Whitney test.

Pisa et al. (2012) use the same method as Nemec et al. (2008), now applied to the full DEMETER dataset. The data are initially sorted within the same 6-dimensional matrix. Data that can be related to more than one seismic event are removed. They focus on nighttime half-orbits, seismic events with M≥5.0 and depth ≤40km. They still observe a decrease of power within the same frequency band, with the strongest significance when distances are smaller than 440km, and still within the 4 hours window before events. The decrease is now about 3 standard deviations, which corresponds to about 1.8dB, while the natural background variation is estimated to about 7.5dB. The effect thus seems smaller as data accumulate. Yet, the probability to be a random positive/negative deviation is still only about 0.1%, using a t-test or a binomial test.

Pisa et al. (2013) provide additional observations using the survey mode during the whole mission. They consider different earthquake magnitude ranges (from M≥5, about 12,000 events, down to M≥3, with about 153,000 events in all). They still consider the 6-dimensional matrix to condition the data, but the satellite-epicenter distance varies from 0 to 440km, and the time interval from 2 days before to 1 day after each event. They also use quarters instead of semesters for conditioning on the season. Removing cases where data can be associated to more than one event, they are left with 8,400 events. They observe the same result as before: an attenuation of 2dB in the last 4 hours and within 440km, which is about 2.9 standard deviations (with a probability to be random of about 0.3%). In all other distance-time bins, the probability is found to be one to two orders of magnitude larger. Two surrogate catalogs are then submitted to the same analysis: one in which seismic events are shifted 10 days back in time, and another one where they are spatially shifted 25° to the West. No signal is observed for both surrogate catalogs. In the case of the natural catalog, the effect is much stronger between March and August, which is the season of lightning (Christian et al., 2003). It is also slightly stronger for larger latitudes (>20°), and for events below the sea surface. This is interpreted by the lower attenuation of the VLF waves in the Earth-ionosphere waveguide above the sea (Meyer et al., 2011), as the main contributing factor is the conductivity of the surface of the lower boundary of the waveguide. The effect is also stronger for events with shallow depth (≤33km), but many events are attributed an arbitrary depth at 10km (which happens when the

location algorithm fails to constrain depth). A more refined temporal analysis shows that the decrease is more pronounced 3 to 4h before the events, with an amplitude of about 2.3dB. The effect increases with the magnitude of the events and is significant when M≥4. As pointed out by Toledo-Redondo et al. (2012), the height of the lower boundary of the ionosphere exhibits a seasonal variation and depends on the position on Earth. Pisa et al. (2013) then claim that the electric conductivity of the lower troposphere increases, because of charge carriers emanating from stressed rocks before major events. The air conductivity increases, the electric current down from the ionosphere also increases, by Ohm's law (Rycroft and Harrison, 2012), so that the ionosphere lowers at night time at about 88km, by about 2km (Harrison et al., 2010). They propose that VLF radio waves originating from lightning and propagating in the Earth-ionosphere waveguide at night are cut-off at a slightly higher frequency (1.74kHz vs 1.7kHz): there is thus additional attenuation of signals from lightning propagating in this waveguide.

IV-Discussion and conclusion

This review provides a heterogenous but encouraging assessment of the correlations between many non-seismic signals with tectonic and earthquake activity, which are expected to occur according to the theory based on the activation of peroxy defects and flow of the associated p-holes.

To recapitulate, peroxy defects are point defects in the matrix of oxide and silicate materials, including the overwhelming majority of rock-forming minerals, in which pairs of oxygen anions have converted from the usual 2– valence state to the 1– valence state, forming a very short $O^-–O^-$ bond. Though peroxy concentrations have not yet been systematically studied, there is strong evidence that peroxy defects of the type O_3X-OO-YO_3 (with X and Y standing for Si^{4+} or Al^{3+} etc.) are ubiquitous in the constituent minerals of igneous and high-grade metamorphic rocks. The reason is that peroxy defects derive from hydroxyl "impurities", commonly O_3(X,Y)-OH, that become incorporated into the matrix of any minerals that crystallize from an H_2O-laden melt or magma or that recrystallize in any high temperature H_2O-laden metamorphic environment [*Friedemann T. Freund and Freund*, 2015]. The formative reaction involves a redox conversion of solute hydroxyl pairs as described by eq [1], whereby electrons rearrange in such a way that the two hydroxyl protons, H^+, take over an electron from their respective hydroxyl oxygens, O^{2-}, changing into two H which combine to form H_2, while the two O^{2-} change to O^-, which form a peroxy bond, $O^-–O^-$. This is a classical redox reaction that causes one part to become reduced and the other to become oxidized.

As long as the peroxy bond is intact, it is electrically inactive. When the peroxy bond is perturbed, for instance by bending during the application of mechanical stress, it breaks. In the process described by eq [2] the peroxy bond becomes unstable and takes over an electron, e', from a neighboring O^{2-}. The neighboring O^{2-} thereby changes into O^-, a defect electron in the oxygen anion sublattice, hence a hole. Because of its unusual transport properties, foremost its ability to spread out fast and far, this type of charge carrier has been called a "positive hole".

Many of these independent studies provide results that seem to be consistent with the prediction of the theory, even if some differences blur a bit the full picture.

First, even very tiny stress fluctuations in natural settings seem to possess a non-seismic signature, as revealed by Radon analysis and, to a somewhat lesser degree, electromagnetic fields. This is indeed compatible with the empirical relationship provided by Dobrovolsky et al. (1979), suggesting that strains as low as 10^{-8} may be associated with such signals. This provides a strong tie with all non-destructive laboratory experiments conducted under well-controlled mechanical and physical conditions. For instance, Scoville et al. (2015) report on rock stressing experiments changing the stress rate over 8 orders of magnitude. One of the most remarkable observation is that, when a fine-grained gabbro is subjected to stress, the outflow of p-holes from the stressed subvolume is extremely sensitive to very low stress level changes. A plausible explanation is that many peroxy bonds exist at grain boundaries and across grain boundaries. Ever so slight shifting of mineral grains relative to each other, such as during small stress changes, make these peroxy bonds

highly susceptible to dissociation and instant release of highly mobile p-holes.

The same paper [*John Scoville et al.*, 2015] also reports on the lifetimes of stress-activated p-hole charge carriers. It shows that, inside the stressed subvolume of the fine-grained gabbro rock, the p-hole lifetimes spread from milliseconds to several months. It is therefore quite conceivable that weak mechanical forces such as experienced during the tides will suffice to reversibly activate a fairly large number of p-hole charges in the deep crust, thereby providing an explanation for the diurnal and semi-diurnal patterns recognized, for instance, in radon release data (Teng and McElrath, 1977). The concept of peroxy bond breakage during grain-grain sliding is further supported by the observation that, when the stress is removed, allowing the grains to return to their starting positions, the p-hole charge carriers quickly recombine and return to their inactive peroxy state. However, the nature of the relationship between the size of the Dobrovolsky precursory zone and the magnitude of the upcoming events is not yet clearly established.

Combining a wide array of studies clearly indicate that earthquakes are often preceded by various anomalies a few days to weeks before they occur. Yet, there is no one-to-one relation between signal anomalies and earthquake nucleation. What most of pubished studies show is that, based on a single precursory indicator, the number of false alarms is large: anomalies can and do often occur without subsequent seismic event. However, it also appears that the rate and intensity at which anomalies are recorded increase as the time of the event approaches and as its magnitude increases. This statement holds even though, in many cases, the amplitude of any given precursory anomaly is not significantly correlated with the magnitude of the seismic event. The leading time of the anomalies, as well as their duration, also seem to correlate positively with the magnitude of the earthquake.

One complicating factor is that many studies report an offset between the spatial location of the anomalies and that of the future epicenter, often a few hundreds of kilometers. There are potentialy several mechanisms that could lead to such a shift. First, just as currents in the ground can induce changes in the ionosphere, it is well known that currents in the ionosphere or magnetosphere (or many other currents) can induce telluric currents in the ground. Several drivers of telluric currents are described in Helman (2013). Atmospheric precursors can be driven either by ionospheric currents, in the case of ionized species, or by winds, Coriolis forces, etc, in the case of neutral species. It is also possible that stress buildup may occur somewhere along a fault, leading to observed precursors, while rupture may occur somewhere else along the fault. A careful examination of more radon data is warranted, especially as the spatial density of continuously recording stations has increased since the compilation paper of Hauksson (1981).

Global analyses, which can only be achieved by the use of measurements by satellites, allowed for the most systematic analyses (typically at the scale of years to a decade) that can be compared with significant earthquake catalogs featuring tens to hundreds of thousands of events. Most of these works show that precursory anomalies tend to be more significant for larger magnitude events, when the focal depth is smaller, and when events are associated with offshore subduction zones. They diverge on the time at which such observations can be made. For instance, ionospheric perturbations deduced from GPS measurements suggest that TEC anomalies at the geomagnetic equator occur in the morning for events in the afternoon. Most TEC anomalies are reported to be negative, while ion content anomalies (as reported by the DEMETER satellite) tend to be positive, which is perfectly consistent. However, different satellite technologies come to different conclusions about specific topics: for instance, the DEMETER daytime data are systematically eliminated as they do not display specific patterns of anomalies, which is interpreted as due to noise arising from external influences. This finding questions the anomalies patterns found using GPS data, which provide evidence for anomalies only during day time. It also seems that, when using the DEMETER dataset for ion densities, the strength of anomalies seems to depend on whether the earthquake focus is offshore or inland. When analyzing data derived from the electron distribution this relation is not found.

The various methodologies used to detect anomalous behaviors are mostly local in time, meaning that the signal observed at a given time is compared to a background value that is estimated up to at

most a few weeks before. In contrast, a large part of the anomaly detection procedure using the DEMETER dataset estimates the statistics of the background signal using the whole dataset at hand. This last procedure can be prone to mistakes if the background signal itself is not stationary in time. As a result, increasing the size of the dataset would lead to fewer detected anomalies. This might explain why the electric field anomalies recorded in the VLF range are observed with smaller and smaller amplitudes as the size of the considered dataset increases. Indeed, preliminary results (Kamer et al., work in progress) indicate that the background signal is not stationary, even in aseismic areas such as Bostwana, for instance.

Another important aspect that has been neglected so far is the temporal and spatial clustering of earthquakes. Some works take this universal process into account in order to remove seismic events occurring too close in time in order to eliminate double counting of successes (or failures) when correlating them with anomalies. Unfortunately, all the techniques used for this declustering are somewhat primitive, if not arbitrary. One of the goals of statistical seismology is to model seismic catalogs with sets of well defined clusters whose seeds are distributed randomly in time. This allows one to compute the probability of any event to be either independent or to have been triggered by the cumulative effect of some previous events. Preprocessing seismic catalogs with the latest generation of such sophisticated declustering tools (Nandan et al., 2017) should certainly help in assigning probabilities of each detected anomaly to be associated to any observed earthquake.

Finally, a striking common feature of all these works is the absence of any assumption about the morphological features of the anomalies we should look for. In a sense, this allows one to be as objective and open minded as possible when looking for them. But this is also a severe drawback, as the probability is certainly high to mistake transient noise for anomalies. Some recent works suggest that anomalies in the magnetic field recorded by ground stations have the shape of unipolar pulses, an observation confirmed by experiments and numerical simulations. The latter either solve differential equations at the microscopic level (Scoville et al., 2015), or use a coarse-grained description of a frictional fault as an assembly of blocks separated by elastic springs (in the spirit of Burridge and Knopoff, 1967), each unit of the model being also modeled as a RLC circuit within which charge generation in each block depends on the applied stress upon it (Chen et al., 2017). These works need to be developed further in order to provide guidance concerning the various transfer functions that would help modelling signatures of seismic-induced anomalies.

V-References

Akhoondzadeh, M., Parrot, M., and M.R. Saradjian (2010): Electron and ion density variations before strong earthquakes (M>6.0) using DEMETER and GPS data, Nat. Hazards Earth Syst. Sci., 10, 7-18.

Asada , T., Baba, H., Kawazoe, M., and M. Sugiura (2001): An attempt to delineate very low frequency electromagnetic signals associated with earthquakes, Earth Planets Space, 53, 55-62.

Astafyeva, E., and K. Heki (2011): Vertical TEC over seismically active region during low solar activity, J. Atmos. Sol.-Terr. Phys., 73, 1,643-1,652.

Barton, C.E. (1997): International Geomagnetic Reference Field: The Seventh Generation, J. Geomag. Geoelectr., 49, 123-148.

Berthelier, J.J., Godefroy, M., Leblanc, F., Malingre, M., Menvielle, M., Lagoutte, D., Brochot, J.Y., Colin, F., Elie, F., Legendre, C., Zamora, P., Benoist, D., Chapuis, Y., Artru, J. and R. Pfaff (2006): ICE, the electric field experiment on DEMETER, Planet. Space Sci., 54, 456-471.

Bhloscaidh, M. N., and J. McCloskey (2014): Response of the San Jacinto Fault Zone to static stress changes from the 1992 Landers earthquake, J. Geophys. Res. Solid Earth, 119, 8914–8935, doi:10.1002/2014JB011164.

Bleier, T., Dunson, C., Maniscalco, M., Bryant, N., Bambery, R. and Freund, F. (2009): Investigation of ULF magnetic pulsations, air conductivity changes, and infra red signatures associated with the 30 October Alum Rock M5.4 earthquake, Nat. Hazard. Earth Sys., 9, 585–603.

Bortnik, J., Cutler, W., Dunson, C., and T.E. Bleier (2008): The possible statistical relation of Pc1 pulsations to earthquake occurrence at low latitudes, Ann. Geophys. 26, 2825-2836.

Bowman, D.D., Ouillon, G., Sammis, C.G., Sornette, A. & Sornette, D. (1998): An observational test of the critical earthquake concept, J. Geophys. Res., 103, B10, 24 349–24 372.

Bryant, N. A., T. L. Logan, A. L. Zobrist, W. L. Bunch, and J. Clark (2004b), Geosynchronous Weather Satellite Thermal IR Measurements Prior to Earthquakes, paper presented at Fall Meeting, American Geophysical Union San Francisco, CA.

Bryant, N., A. Zobrist , and T. Logan (2003), Automatic Co-Registration of Space-Based Sensors for Precision Change Detection and Analysis, paper presented at IGARSS 2003 Transactions, Toulouse, France, 21-26 July 2003.

Bryant, N., A. Zobrist , and T. Logan (2004a), Precision Automatic Co-Registration Procedures for Spacecraft Sensors, paper presented at Annual Meeting, American Society of Photogrammetry and Remote Sensing, Denver, CO, May 27, 2004.

Bryant, N. A., A. L. Zobrist, L. L. Logan, F. Freund, and S. Nishenko (2002), Observed weather satellite thermal IR responses prior to earthquakes, Eos Trans. AGU, 83(47), S71C-1106.

Budden, K.G (1961): Radio waves in the ionosphere: the mathematical theory of the reflection of radio waves from stratified ionised layers, Cambridge, England: Cambridge University Press, 542pp.

Burridge, R. and Knopoff, L. (1967): Model and theoretical seismicity, Bull. Seis. Soc. Amer. 57, 341-371.

Cahyadi, M.N., Heki, K. (2013): Ionospheric disturbances of the 2007 Bengkulu and the 2005 Nias earthquakes, Sumatra, observed with a regional GPS network. J. Geophys. Res., doi:10.1002/jgra.50208.

Calais, E., and J.B. Minster (1995): GPS detection of ionospheric perturbations following the January 17, 1994, Northridge Earthquake, Geophys. Res. Lett., 22, 1,045-1,048.

Catchings, R. D. (1999), Regional Vp, Vs, Vp/Vs, and Poisson's ratios across earthquake source zones from Memphis, Tennessee, to St. Louis, Missouri Bulletin of the Seismological Society of America, 89(6), 1591-1605.

Chavez, O., Pérez-Enriquez, R., Cruz-Abeyro, J.A., Millan-Almaraz, J.R., Kotsarenko, A., and E. Rojas (2011): Detection of electromagnetic anomalies of three earthquakes in Mexico with an improved statistical method, Nat. Hazards Earth Syst. Sci., 11, 2,021-2,027, doi:10.5194/nhess-11-2021-2011.

Chen, H.-J. , C.-C. Chen, G. Ouillon and D. Sornette (2017): Micro-slip on faults as a potential source of transient geoelectric signals, ETH Zurich working paper.

Chen, Y.L., J.Y. Chuo, J.Y. Liu, and S.A. Pulinets (1999): A statistical study of ionospheric precursors of strong earthquakes in the Taiwan area, 24th General Ass. URSI, URSI, 745 pp.

Chen, C.-H., Liu, J.-Y., Yen H.-Y., Zeng, X., and Y.-H. Yeh (2004): Changes of Geomagnetic Total Field and Occurrences of Earthquakes in Taiwan, TAO, Vol. 15, No. 3, 361-370.

Chen, C.H., Saito, A., Lin, C.H., Liu, J.Y., Tsai, H.F., Tsugawa, T., Otsuka, Y., Nishioka, M., Matsumura, M. (2011): Long-distance propagation of ionospheric disturbance generated by the 2011 off the Pacific coast of Tohoku earthquake, Earth Planets Space 63, 881–884.

Christian, H. J., et al. (2003): Global frequency and distribution of lightning as observed from space by the Optical Transient Detector, J. Geophys. Res., 108, doi:10.1029/2002JD002347

Chyi, L.L., Chou, C.Y., Yang, F.T. and C.H. Chen (2002): Automated radon monitoring of seimicity in a fault zone, Geofis. Int., 41, 4, 507-511.

Cicerone, R.D., Ebel, J.E., and J. Britton (2009): A systematic compilation of earthquake precursors, Tectonophysics, Volume 476, Issues 3–4, 25, Pages 371-396.

Clilverd, M.A., Rodger, C.J., and N.R. Thomson (1999): Investigating seismoionospheric effects on a long subionospheric path, J. Geophys. Res., 104(A12), 28,171-28,179.

Cornell, C.A. (1968). Engineering seismic risk analysis, Bull. Seism. Soc. Am., 58, 1583-1606.

Dautermann, T., Calais, E., Haase, J., and J. Garrison (2007): Investigation of ionospheric electron content variations before earthquakes in southern California, 2003-2004, J. Geophys. Res., 112, B02106, doi:10.1029/2006jb004447.

Davies, K., and D. M. Baker (1965): Ionospheric effects observed around the time of the Alaskan earth- quake of March 28, 1964, J. Geophys. Res., 70(9), 2251-2253.

Dea, J.Y., Hansen, P.R., and W.-M. Boerner (1992): Long-term ELF background noise measurements, the existence of window regions, and applications to earthquake precursor emission studies, Phys. Earth Planet. Int.

Depuev, V. and Zelenova, T. (1996): Electron density profile changes in a pre-earthquake period, Adv. Space Res., 18(6), 115–118.

Derr, J. S. (1973): Earthquake lights: a review of observations and present theories. Bulletin of the Seismological Society of America, 63, 2177–2187.

Derr, J.S. (1986): Rock mechanics: Luminous phenomena and their relationship to rock fracture, Nature 321, 470-471, DOI: 10.1038/321470a0.

Derr, J.S., F. St-Laurent, F.T. Freund and R. Thériault (2014): Earthquake Lights, Encyclopedia of Solid Earth Geophysics, 165-167.

Dobrovolsky, I.P., Zubkov, S.I., and V.I. Miachkin (1979), Estimation of the size of earthquake preparation zones, Pure Appl. Geophys., 117, 1025–1044, doi:10.1007/BF00876083.

Dunajecka, M.A., and S.A. Pulinets (2005), Atmospheric and thermal anomalies observed around the time of strong earthquakes in México, Atmósfera 18, 236-247.

Eleftheriou, A., Filizzola, C., Genzano, N. et al. (2016): Long-Term RST Analysis of Anomalous TIR Sequences in Relation with Earthquakes Occurred in Greece in the Period 2004–2013, Pure Appl. Geophys., 173: 285. https://doi.org/10.1007/s00024-015-1116-8

Freund, F. (1985): Conversion of dissolved "water" into molecular hydrogen and peroxy linkages, J. Non-Cryst. Solids 71, 1-3, 195-202, DOI: 10.1016/0022-3093(85)90288-1.

Freund, F. (2002): Charge generation and propagation in igneous rocks, J. Geodyn.33, 4-5, 543-570, DOI: 10.1016/S0264-3707(02)00015-7.

Freund, F. T. (2003), On the electrical conductivity structure of the stable continental crust, J. Geodynamics, 35, 353-388.

Freund, F.T. (2007a): Pre-earthquake signals: part 1. Deviatoric stresses turn rocks into a source of electric currents, Nat. Hazards Erath Syst. Sci., 7, 535-541.

Freund, F.T. (2007b), Pre-earthquake signals – Part II: Flow of battery currents in the crust, Nat. Hazards Earth Syst. Sci. 7, 543-548.

Freund, F.T. (2009), Stress-activated positive hole charge carriers in rocks and the generation of

pre-earthquake signals. In: M. Hayakawa (ed.), Electromagnetic Phenomena Associated with Earthquakes, Research Signpost, New Dehli, 41-96.

Freund, F. (2010): Toward a Unified Solid State Theory for Pre-Earthquake Signals, Acta Geophys., 58: 719. doi:10.2478/s11600-009-0066-x

Freund, F. T., and M. M. Freund (2015), Paradox of Peroxy Defects and Positive Holes in RocksPart I: Effect of Temperature, Journal of Asian Earth Sciences, 2015, 373-383, doi:10.1016/j.jseaes.2015.04.047.

Freund, F., and M. M. Masuda (1991), Highly mobile oxygen hole-type charge carriers in fused silica, J. Mater. Res., 6(8), 1619-1622, doi: http://dx.doi.org/10.1557/JMR.1991.1619.

Freund, F., and G. Oberheuser (1986), Water dissolved in olivine: a single crystal infrared study, J. Geophys. Res., 91, 745-761.

Freund, F. and D. Sornette (2007): Electro-Magnetic Earthquake Bursts and Critical Rupture of Peroxy Bond Networks in Rocks, Tectonophysics 431, 33-47.

Freund, F., and H. Wengeler (1982), The infrared spectrum of OH--compensated defect sites in C-doped MgO and CaO single crystals, J. Phys. Chem. Solids, 43, 129-145.

Freund, F., H. Wengeler, and R. Martens (1982), A hydrogen-deuterium fractionation mechanism in magnesium oxide., Geochim. Cosmochim. Acta, 46, 1821-1829.

Freund, F. T., I. Kulahci, G. Cyr, J. Ling, M. Winnick, J. Tregloan-Reed, and M. M. Freund (2009), Air ionization at rock surface and pre-earthquake signals, J. Atmos. Sol. Terr. Phys., 71, 1824–1834.

Freund, F.T., A. Takeuchi, and B.W.S. Lau (2006): Electric currents streaming out of stressed igneous rocks − A step towards understanding pre-earthquake low frequency EM emissions, Phys. Chem. Earth 31, 4-9, 389-396, DOI:10.1016/j.pce.2006.02.027.

Freund, F. T., S. A. Hoenig, A. Braun, R. P. Dahlgren, M. Momayez, and J. J. Chu (2010), Softening rocks with stress-activated electric current, in 5th International Symposium on In-situ Rock Stress (ISRSV) edited, Beijing, China.

Fujiwara, H., Kamogawa, M., Ikeda, M., Liu, J.Y., Sakata, H., Chen, Y. I., Ofuruton, H., Muramatsu, S., Chuo, Y.J., Ohtsuki, Y.H., 2004. Atmospheric anomalies observed during earthquake occurrences. Geophys. Res. Lett. 31.

Galli, I. (1910), Raccolta e classifzione di fenomeni luminosi osservati nei terremoti, Boll. Soc. Sism. Ital. 14, 221-448.

Geller, R.J. (1997): Earthquake prediction: a critical review, Geophys. J. Int., 131,425-450.

Gershenzon, N.I., Gokhberg, M.B., Karakin, A.V., Petviashvili, N.V., and A.L. Rykunov (1989): Modelling the connection between earthquake preparation processes and crustal electromagnetic emission, Phys. Earth Planet. Int., 57, 129-138.

Gokhberg, M.B., Steblov, G.M., Shalimov, S.L., Veis, V.A., Grekhova, E.A. (2011): Ionospheric response to submarine earthquake of March 11, 2011, in Japan according to GPS observations. Izv., Atmos. Ocean. Phys. 47, 929–940.

Guo, G., and B. Wang (2008): Cloud anomaly before Iran earthquake, Int. J. Remote Sensing 29, 7, 1921-1928, DOI: 10.1080/01431160701373762.

Gutenberg, B., Richter, C. F. (1956): Magnitude and Energy of Earthquakes, Annali di Geofisica, 9: 1–15

Han, P., K. Hattori, M. Hirokawa, J. Zhuang, C.-H. Chen, F. Febriani, H. Yamaguchi, C. Yoshino, J.-Y. Liu, and S. Yoshida (2014), Statistical analysis of ULF seismomagnetic phenomena at Kakioka, Japan, during 2001–2010, J. Geophys. Res. Space Physics, 119, 4998–5011, doi:10.1002/2014JA019789.

Han, P., Hattori, K., Zhuang, J., Chen, C.-H., Liu, J.-Y., and S. Yoshida (2017): Evaluation of ULF seismo-magnetic phenomena in Kakioka, Japan by using Molchan's error diagram, Geophys. J. Int., 208, 482–490.

Harrison, R. G., K. L. Aplin, and M. J. Rycroft (2010), Atmospheric electricity coupling between earthquake regions and the ionosphere, J. Atmos. Sol. Terr. Phys., 72, 376–381.

Hasbi, A.M., Mohd Ali, M.A., and N. Misran (2011): Ionospheric variations before some large

earthquakes over Sumatra, Nat. Hazards Earth Syst. Sci., 11, 597-611, doi:10.5194/nhess-11-597-2011.

Hattori, K., Serita, A., Yoshino, C., Hayakawa, M. & Isezaki, N. (2006): Singular spectral analysis and principal component analysis for signal discrimination of ULF geomagnetic data associated with 2000 Izu Island Earthquake Swarm, Phys. Chem. Earth, 31, 281–291.

Hattori, K., Wadatsumi, K., Furuya, R., Yada, N., Yamamoto, I., Ninagawa, K., Ideta, Y., and M. Nishihashi (2008): Variation of Radioactive Atmospheric Ion Concentration Associated With Large Earthquakes. AGU Fall Meeting, San Francisco, CA.

Hatuda, Z. (1953): Radon content and its change in soil air near the ground surface. Mem. College Sci., Univ. Kyoto, Series B, 20, 285-306.

Hauksson, E. (1981): Radon content of groundwater as an earthquake precursor: evaluation of worldwide data and physical basis, Journal of Geophysical Research, vol. 86, No. B10, pp. 9397-9410, October 10.

Hauksson, E., J.G. and Goddard (1981): Radon earthquake precursor studies in Iceland, J. Geophys. Res., 86, 7037-7054.

Hayakawa, M., Molchanov, O.A., Kodama, T., Afonin, V.V., Akentieva, O.A., 2000. Plasma density variations observed on a satellite possibly related to seismicity. Adv. Space Res. 28, 1277–1280.

Hayakawa, M. (2007): VLF/LF radio sounding of ionospheric perturbations associated with earthquakes, Sensors 7, 7, 1141-1158, DOI: 10.3390/s7071141.

Hayakawa, M., A.V. Shvets, and S. Maekawa (2005): Subionospheric LF monitoring of ionospheric perturbations prior to the Tokachi-oki earthquake and a possible mechanism of lithosphere-ionosphere coupling, Adv. Polar Upper Atmos. Res. 19, 42-54.

Hayakawa, M., K. Ohta, S. Maekawa, T. Yamauchi, Y. Ida, T. Gotoh, N. Yonaiguchi, H. Sasaki, and T. Nakamura (2006), Electromagnetic precursors to the 2004 Mid Niigata Prefecture earthquake, Phys. Chem. Earth, 31, 356–364.

Hayakawa, M., Rozhnoi, A., Solovieva, M., Hobara, Y., Ohta, K., Schekotov, A., Fedorov, E. (2013): The lower ionospheric perturbation as a precursor to the 11 March 2011 Japan earthquake. Geomat. Nat. Hazards Risk (2013). doi:10.1080/19475705.2012.751938

He, Y., Yang, D., Qian, J., and M. Parrot (2010): Response of the ionospheric electron density and temperature in ionosphere based on DEMETER ISL data, Earthq. Sci., 23(4), 349-355, doi:10.1007/s11589-010-0732-8.

He, Y., Yang, D., Qian, J., and M. Parrot (2011): Response of the ionospheric electron density to different types of seismic events, Nat. Hazards Earth Syst. Sci., 11, 2,173-2,180, doi:10.5194/nhess-11-2173-2011.

Helmstetter, A. (2003): Is earthquake triggering driven by small earthquakes? Phys. Res. Lett. 91, 058501.

Helmstetter, A. and D. Sornette (2003): Predictability in the ETAS Model of Interacting Triggered Seismicity, J. Geophys. Res., 108, 2482, 10.1029/2003JB002485.

Henderson, T.R., Sonwalkar, V.S., Helliwell, R.A., Inan, U.S., and A.C. Fraser-Smith (1991): A search for ELF/VLF emissions induced by earthquakes as observed in the ionosphere by the DE 2 satellite (abstract), Eos Trans. AGU, 72, Fall Meeting Suppl., 330, 1991.

Henderson, T.R., Sonwalkar, V.S., Helliwell, R.A., Inan, U.S., and A.C. Fraser-Smith (1993): A search for ELF/VLF emissions induced by earthquakes as observed in the ionosphere by the DE 2 satellite, J. Geophys. Res., 98(A6), 9503-9514.

Hsiao, C.C., Liu, J.Y., Oyama, K.I., Yen, N.L., Wang, Y.H., Miau, J.J. (2009): Ionospheric electron density anomaly prior to the December 26, 2006 M7.0 Pingtung earthquake doublet observed by FORMOSAT-3/COSMIC. Phys. Chem. Earth 34, 474–478.

Hsiao, C.C., Liu, J.Y., Oyama, K.I., Yen, N.L., Liou, Y.A., Chen, S.S., Miau, J.J. (2010): Seismoionospheric precursor of the 2008 Mw7.9 Wenchuan earthquake observed by FORMOSAT-3/COSMIC. GPS Solut. 14, 83–89.

Ho, Y.Y., Jhuang, H.K., Su, Y.C., Liu, J.Y. (2013): Seismo-ionospheric anomalies in total electron

content of the GIM and electron density of DEMETER before the 27 February 2010 M8.8 Chile earthquake, Adv. Space Res.. doi:10.1016/j.bbr.2011.03.031

Hobara, Y., Lefeuvre, F., Parrot, M., and O.A. Molchanov (2005): Low-latitude ionospheric turbulence observed by Aureol-3 satellite, Ann. Geophys., 23, 1259-1270.

Hollerman, W.A., B.L. Lau, R.J. Moore, C.A. Malespin, N.P. Bergeron, F.T. Freund, and P.J. Wasilewski (2006): Electric currents in granite and gabbro generated by impacts up to 1 km/sec, AGU Fall Meeting 2006, San Francisco.

Honkura, Y., Niblett, E.R., and R.D. Kurtz (1976): Changes in magnetic and telluric fields in a seismically active region of Eastern Canada: preliminary results of earthquake prediction studies, Tectonophysics, 34, 219-230.

Huang, Y., H. Saleur, C. Sammis, and D. Sornette (1998): Precursors, aftershocks, criticality and self-organized criticality, Europhys. Lett., 41, 43-48, 1998.

Igarashi G., and H. Wakita (1990): Groundwater radon anomalies associated with earthquakes. Tectonophys., 180, 237-254.

Igarashi G., Saeki S., Takahata N., Sumikawa K., Tasaka S., Sasaki G., Takahashi M. and Sano Y. (1995): Ground-water radon anomaly before the kobe earthquake in Japan, Science 269 (5220), 60-61.

Imamura, G. (1947): Report on the observed variation of the Tochiomata hot spring immediately before the Nagano earthquake of July 15, 1947. Kagaku, 11, 16-17.

Inan, S., T. Akgül, C. Seyis, R. Saatç?lar, S. Baykut, S. Ergintav, and M. Bas (2008), Geochemical monitoring in the Marmara region (NW Turkey): A search for precursors of seismic activity, J. Geophys. Res., 113, B03401, doi:10.1029/2007JB005206.

Ispir, Y., O. Uyar, Y. Gungormus, N. Orbay, and B. Caglayan (1976): Some results from studies on tectonomagnetic effect in NW Turkey, J. Geomag. Geoelectr., 28, 123-135.

Jhuang, H.K., Ho, Y.Y., Kakinami, Y., Liu, J.Y., Oyama, K.I., Parrot, M., Hattori, K., Nishihashi,M., Zhang, D.H. (2010): Seismo-ionospheric anomalies of the GPS-TEC. appear before the 12 May 2008 magnitude 8.0 Wenchuan.

Jin, S., Han, L., Cho, J. (2011): Lower atmospheric anomalies following the 2008 Wenchuan earthquake observed by GPS measurements. J. Atmos. Sol.-Terr. Phys. 73, 810–814.

Johansen, A., D. Sornette, H. Wakita, U. Tsunogai, W.I. Newman and H. Saleur (1996): Discrete scaling in earthquake precursory phenomena : evidence in the Kobe earthquake, Japan, J.Phys.I France 6, 1391-1402.

Johansen, A., H. Saleur and D. Sornette (2000): New Evidence of Earthquake Precursory Phenomena in the 17 Jan. 1995 Kobe Earthquake, Japan, Eur. Phys. J. B 15, 551-555.

Johnston, M.J.S (1989): Review of magnetic and electric field effects near active faults and volcanoes in the U.S.A., Phys. Earth Planet. Int., 57, 47-63.

Johnston, M.J.S., Smith, B.E., Johnson, J.R., and F.J. Williams (1973): A search for tectonomagnetic effects in California and western Nevada, in Proceedings of Conference on Tectonic Problems of the San Andreas fault system, edited by R.L. Kovach and A. Nur, pp. 225-239, Stanford Unibersity Press, 239.

Kamogawa, M., Kakinami, Y., Watanabe, S., Liu, J.Y., Watanabe, Y. (2012): Seismo-tsunamigenic ionospheric hole triggered by M 9.0 2011 off the Pacific coast of Tohoku earthquake. Terr. Atmos. Ocean, Sci. 23, 327–331.

Kathrein, H., and F. Freund (1983), Electrical conductivity of magnesium oxide single crystal below 1200 K., J. Phys. Chem. Solids, 44, 177-186.

Ke, F., Wang, Y., Wang, X., Qian, H., and C. Shi (2016): Statistical analysis of seismo-ionospheric anomalies related to Ms>5.0 earthquakes in China by GPS TEC, J. Seismol., 20, 137-149, DOI:10.1007/s10950-015-9516-x

Kim, V.P., and V.V. Hegai (1999): A possible presage of strong earthquakes in the nighttime mid-latitude region ionosphere, atmospheric and ionospheric electromagnetic phenomena associated with earthquake, Tokyo: Terra Scientific Publishing Company, 619-627.

King, C.Y. (1980): Episodic Radon changes in subsurface soil gas along active faults and possible

relation to earthquakes, J. Geophys. Res., 85, 3065-3078.

King, G., R. S. Stein, and J. Lin (1994): Static stress changes and the triggering of earthquakes, Bull. Seismol. Soc. Am., 84, 935–953.

Knopoff, L. and D. Sornette (1995): Earthquake Death Tolls, Journal de Physique I, EDP Sciences, 5(12), pp.1681-1668.

Kon, S., Nishihashi, M., Hattori, K. (2011): Ionospheric anomalies possibly associated with $M \geq 6.0$ earthquakes in the Japan area during 1998–2010: case studies and statistical study. J. Asian Earth Sci. 41, 410–420

Kranz, R. L. (1983), Microcracks in rock: a review, Tectonophysics, 100, 449-480.

Larkina, V.I., Migulin, V.V., Molchanov, O.A., Kharkov, I.P., Inchin, A.S., and V.B. Schvetcova (1989): Some statistical results on very low frequency radiowave emissions in the upper ionosphere over earthquake zones, Phys. Earth Planet. Int., 57, 100-109.

Le, H., Liu, J.Y., and L. Liu (2011): A statistical analysis of ionospheric anomalies before 736 M6.0+ earthquakes during 2002-2010, J. Geophys. Res., 116, A02303, doi:10.1029/2010ja015781.

Le, H.J., Liu, L.B., Liu, J.Y., Zhao, B.Q., Chen, Y.D., Wan, W.X. (2013): The ionospheric anomalies prior to the M9.0 Tohoku-Oki earthquake. J. Asian Earth Sci. 62, 476–484 (2013)

Lebreton, J.-P., Stverak, S., Trvnicek, P., Maksimovic, M., Klinge, D., Merikallio, S., Lagoutte, D., Poirier, B., Blelly, P.-L., Kozacek, Z., Salaquarda, M., 2006. The ISL Langmuir probe experiment processing onboard DEMETER: scientific objectives, description and first results. Planet. Space Sci. 54 (5), 472–486.

Leick, A., 1995: GPS satellite surveying, John Wiley, New York, 560 pp.

Leonard, R. S., and R. A. Barnes, Jr. (1965): Observation of ionospheric disturbances following the Alaskan earthquake, J. Geophys. Res., 70(5), 1250-1253.

Lerski, S., F. Batllo, R. C. LeRoy, T. Wydeven, and F. Freund (1988), Evidence for peroxy in a sanidine from the lower crust, EOS Trans. Amer. Geophys. Union, 69, 1468.

Li, M., and M. Parrot (2012): "Real Time analysis" of the ion density measured by the satellite DEMETER in relation with the seismic activity, Nat. Hazards Earth Syst. Sci., 12, 2957-1963, doi:10.5194/nhess-12-2957-2012.

Li, M., Parrot, M. (2013): Statistical analysis of an ionospheric parameter as a base for earthquake prediction, J. Geophys. Res. 118, 3731–3739.

Li, W.-K., G.-D. Zhou, and T.C.W. Mak (2008): Advanced Structural Inorganic Chemistry, International Union of Crystallography, Oxford University Press, 688 pp.

Lin, J., Wu, Y., Zhu, F.Y., Qiao, X.J., Zhou, Y.Y. (2009): Wenchuan earthquake ionosphere TEC anomaly detected by GPS. Chin. J. Geophys., 52(1), 297–300.

Lin, J.W. (2010): Ionospheric total electron content (TEC) anomalies associated with earthquakes through Karhunen-Loeve transform (KLT). Terr. Atmos. Ocean. Sci. 21, 253–265 (2010)

Lin, J.W.(2011): Latitude-time total electron content anomalies as precursors to Japan's large earthquakes associated with principal component analysis. Int. J. Geophys. 2011, 1–12

Lin, J.W. (2012): Ionospheric total electron content seismo-perturbation after Japan's March 11, 2011, M = 9.0 Tohoku earthquake under a geomagnetic storm; a nonlinear principal component analysis. Astrophys. Space Sci. 341, 251–258.

Lin, J.W. (2013a): Ionospheric anomaly at the occurring time of China's May 12, 2008, M = 7.9 Wenchuan earthquake using nonlinear principal component analyses and image decoding. Egypt. J. Remote Sens. Space Sci. (2013a). doi:10.1016/j.ejrs.2012.11.005

Lin, J.W. (2013b): Is it possible to detect earlier ionospheric precursors before large earthquakes using principal component analysis (PCA)?, Arab. J. Geosci. 6, 1091–1100.

Lin, J., Wu, Y., Zhu, F.Y., Qiao, X.J., Zhou, Y.Y. (2009): Wenchuan earthquake ionosphere TEC anomaly detected by GPS. Chin. J. Geophys., 52(1), 297–300.

Liperovsky, V.A., O.A. Pokhotelov, E.V. Liperovskaya, M. Parrot, C.-V. Meister, and O.A. Alimov (2000): Modification of sporadic E-layers caused by seismic activity, Surv. Geophys. 21, 5-6, 449-486, DOI: 10.1023/A:1006711603561.

Liperovskaya, E., Parrot, M., Bogdanov, V., Meister, C.-V., Rodkin, M., Liperovsky, V. (2006): On

variations of foF2 and F-spread before strong earthquakes in Japan. Nat. Hazards Earth Syst. Sci. 6, 735–739.

Lira A. (2008): time difference correlation between seismic waves and earthquake Lights. Seismological Research Letters 79(4), 516-519.

Liu, J.Y., Tsai HF, Jung TK (1996) Total electron content obtained by using the global positioning system. TAO 7:107–117

Liu, J.Y., Chen, Y.I., Pulinets, S.A., Tsai, Y.B., Chuo, Y.J. (2000): Seismoionospheric signatures prior to M ≥ 6.0 Taiwan earthquakes, Geophys. Res. Lett. 27, 3113–3116

Liu, J.Y., Chen, Y.I., Chuo, Y.J., Tsai, H.F. (2001): Variations of ionospheric total electron content during the Chi-Chi earthquake. Geophys. Res. Lett. 28, 1383–1386

Liu, J.Y., Chen, Y.I., Jhuang, H.K., Lin, Y.H. (2004a): Ionospheric foF2 and TEC anomalous days associated with M ≥ 5.0 earthquakes in Taiwan during 1997–1999. Terr. Atmos. Ocean. Sci. 15, 371–383.

Liu, J.Y., Chuo YJ, Shan SJ, Tsai YB, Chen YI, Pulinets SA, Yu SB (2004b) Pre-earthquake ionospheric anomalies registered by continuous GPS TEC measurements. Ann Geophys 22:1585–1593

Liu, J.Y., Chen, Y.I., Chuo, Y.J., Chen, C.S. (2006a): A statistical investigation of preearthquake ionospheric anomaly. J. Geophys. Res. 111, A05304, doi:10.1029/2005JA011333

Liu, J.Y., Tsai, Y.B., Chen, S.W., Lee, C.P., Chen, Y.C., Yen, H.Y., Chang, W.Y., Liu, C. (2006b): Giant ionospheric disturbances excited by the M9.3 Sumatra earthquake of 26 December 2004. Geophys. Res. Lett. 33, L02103, doi:10.1029/2005GL023963

Liu, J.Y., Chen, S.W., Chen, Y.C., Yen, H.Y., Chang, C.P., Chang, W.Y., Tsai, L.C., Chen, C.H., Yang, W.H. (2008): Seismoionospheric precursors of the 26 December 2006 M7.0 Pingtung earthquake doublet. Terr. Atmos. Ocean. Sci. 19, 751–759.

Liu, J.Y., Tsai HF, Jung TK (1996): Total electron content obtained by using the global positioning system. TAO 7:107–117

Liu J.Y. et al (2008) Seimo-ionospheric GPS total electron anomalies observed before the 12 May 2008 Ms7.9 Wenchuan earthquake. J Geophys Res 114:A04320. doi:10.1029/2008JA013698

Liu, J.Y., Chen, Y.I., Chen, C.H., Liu, C.Y., Chen, C.Y., Nishihashi, M., Li, J.Z., Xia, Y.Q., Oyama, K.I., Hattori, K., Lin, C.H. (2009): Seismoionospheric GPS total electron content anomalies observed before the 12 May 2008 Mw7.9 Wenchuan earthquake. J. Geophys. Res. 114, A04320 (2009), doi:10.1029/2008JA013698

Liu, J.Y., Chen, Y.I., Chen, C.H., Hattori, K. (2010a): Temporal and spatial precursors in the ionospheric global positioning system (GPS) total electron content observed before the 26 December 2004 M9.3 Sumatra-Andaman earthquake. J. Geophys. Res. 115, A09312, doi:10.1029/2010JA015313.

Liu, J.Y., Chen, C.H., Chen, V.I., Yang,W.H., Oyama, K.I., Kuo, K.W. (2010b): A statistical study of ionospheric earthquake precursors monitored by using equatorial ionization anomaly of GPS TEC in Taiwan during 2001–2007. J. Asian Earth Sci. 39, 76–80.

Liu, J.Y., Chen CH, Chen YI, Yang WH, Oyama KI, Kuo KW (2010c) A statistical study of ionospheric 249 earthquake precursors monitored by using 250 equatorial ionization anomaly of GPS TEC in Taiwan during 2001–2007. J Asian Earth Sci 39:76–80

Liu, J.Y., Chen YI, Pulinets SA, Tsai YB, Chuo YJ (2010d) Seismoionospheric signatures prior to Ms6.0 Taiwan earthquakes. Geophys Res Lett 27:3113–3116

Liu, J.Y., Chen, C.H., Lin, C.H., Tsai, H.F., Chen, C.H., Kamogawa, M. (2011a): Ionospheric disturbances triggered by the 11 March 2011 M9.0 Tohoku earthquake. J. Geophys. Res. 116, A06319 (2011a), doi:10.1029/2011JA016761

Liu, J.Y., Sun, Y.Y., Tsai, H.F., Lin, C.H. (2012): Seismo-traveling ionospheric disturbances triggered by the 12 May 2008 M 8.0 Wenchuan earthquake. Terr. Atmos. Ocean. Sci. 23, 9–15.

Liu, J.Y., Chen CH, Tsai HF, Le H (2013) A statistical study on seismo-ionospheric anomalies of the total electron content for the period of 56 M≥6.0 earthquakes occurring in China during 1998–2012. Chin J Space Sci 33(3):258–269

Liu, J.Y., Chen, C.H., Tsai, H.F., 2013. A statistical study on seismoionospheric precursors of the total electron content associated with 146 M 6.0 earthquakes in Japan during 1998–2011. In: Hayagawa, M. (Ed.), Earthquake Prediction Studies: Seismo Electromagnetics. TERRAPUB, Tokyo, pp. 17–30.

Losseva, T.V., and I.V. Nemchinov (2005): Earthquake lights and rupture processes, Nat. Hazard Earth Syst. Sci. 5, 649-656.

Lu, D. (1988): Impending Earthquake Prediction, Jinangsu Science and Publishing House, Nanjing, China.

Mack, K. (1912), Das süddeutsche Erdbeben vom 16. November 1911, Abschnitt VII: Lichterscheinungen, Würtembergische Jahrbücher für Statistik and Landeskunde, Stuttgart.

Maekawa, S., T. Horie, T. Yamauchi, T. Sawaya, M. Ishikawa, M. Hayakawa, and H. Sasaki (2006), A statistical study on the effect of earthquakes on the ionosphere, based on the subionospheric LF propagation data in Japan, Ann. Geophys., 24, 2219–2225, doi:10.5194/angeo-24-2219-2006.

Makela, J. J., et al. (2011), Imaging and modeling the ionospheric airglow response over Hawaii to the tsunami generated by the Tohoku earthquake of 11 March 2011, Geophys. Res. Lett., 38, L00G02, doi:10.1029/2011GL047860.

Matthews, J.P., and J.P. Lebreton (1985): A search for seismic related wave activity in the micopulsation and ULF frequency ranges using GEOS-2 data, Ann. Geophys., 3, 749-754, 1985.

Mignan, A. (2011): Retrospective on the Accelerating Seismic Release (ASR) hypothesis: controversy and new horizons, Tectonophysics, 505, 1–16.

Milne, J. (1890): Earthquakes in connection with electric and magnetic phenomena, Trans. Seismol. Soc. Jpn., 5, 135.

Miyakoshi, J. (1985): On some problems of the variation of self-potentials oberved in an active fault, the Yamasaki fault, Disaster Prev. Res. Inst. Annu., 28B, 127-132, 1985.

Molchanov, P.A., and M. Hayakawa (1998): On the generation mechanism of ULF seismogneic electromagnetic emissions, Phys. earth Planet. Int. 105, 201-210.

Molchanov, O.A., Mazhaeva, O.A., Goliavin, A.N., and M. Hayakawa (1993): Observation by the Intercosmos-24 satellite of ELF-VLF electromagnetic emissions associated with earthquakes, Ann. Geophys., 11, 431-440.

Molchanov, O.A., Hayakawa, M., and Rafalsky, V.A. (1995): Penetration characteristics of electromagnetic emissions from an underground seismic source into the atmosphere, ionosphere, and magnetosphere, J. Geophys. Res., 100(A2), 1,691-1,712.

Molchanov, O.A., Kulchitsky, A., and M. Hayakawa (2001): Inductive seismo-electromagnetic effect in relation to seismogenic ULF emission, Nat. Hazards Earth Syst. Sci., 1, 61-67.

Molchanov, O.A. et al. (2006): Global diagnostics of the ionospheric perturbations related to the seismic activity using the VLF radio signals collected on the DEMETER satellite, Nat. Hazards Earth Syst. Sci., 6, 745-753.

Mulargia, F., Geller, R.J. (Eds.) (2003): Earthquake Science and Seismic Risk Reduction, Kluwer, Dordrecht, 347 pp.

Myachkin, V.I., Sobolev, G.A., Dolbilkina, N.A., Morozow, V.N., and V.B. Preobrazensky (1972): The study of variations in geophysical fields near focal zones of Kamchatka, Tectonophysics, 14, 287-293.

Meyer, S. G., A. B. Collier, and C. J. Rodger (2011): Daytime VLF modeling over land and sea, comparison with data from DEMETER satellite, IEEE Conference publications, General Assembly and Scientific Symposium, 2011 XXXth URSI, doi:10.1109/URSIGASS.2011.6051108.

Nagaraja, K., Prasad, B. S. N., Madhava, M. S., Chandrashekara, M. S., Paramesh, L., Sannappa, J., Pawar, S. D., Murugavel, P., and Kamra, A. K.: Radon and its short-lived progeny: variations near the ground, Radiat. Meas., 36, 413–417, 2003.

Nandan, S., G. Ouillon, J. Woessner, D. Sornette, and S. Wiemer (2016): Systematic assessment of the static stress triggering hypothesis using interearthquake time statistics, J. Geophys. Res. Solid Earth, 121, 1890–1909, doi:10.1002/2015JB0 12212.

Nemec, F., Santolik, O., Parrot, M., and J.J. Berthelier (2008): Spacecraft observations of electromagnetic perturbations connected with seismic activity, Geophys. Res. Lett., 35, L05109, doi:10.1029/2007GL032517.

Nemec, F., Santolik, O., and M. Parrot (2009): Decrease of intensity of ELF/VLF waves observed in the upper ionosphere close to earthquakes: a statistical study, J. Geophys. res., 114, doi:10.1029/2008JA013972

Nemec, F., O. Santolík, M. Parrot, and C. J. Rodger (2010): Relationship between median intensities of electromagnetic emissions in the VLF range and lightning activity, J. Geophys. Res., 115, doi:10.1029/2010JA015296.

Ogata, Y. (2011). Significant improvements of the space-time ETAS model for forecasting of accurate baseline seismicity, Earth, Planets and Space, Vol.63, No.3, pp. 217-229, doi:10.5047/eps.2010.09.001.

Okabe, S. (1956): Time variation of the atmospheric radon content near the ground surface with relation to some geophysical phenomena, Mem. Coll. Sci. Univ. Kyoto, Ser. A, 28 (2), 99-115.

Omori, F. (1894): On the aftershocks of earthquakes, Journal of the College of Science, Imperial University of Tokyo. 7: 111–200.

Ondoh, T. (1998): Ionospheric disturbances associated with great earthquake of Hokkaido southwest coast, Japan of 12 July 1993, Phys. Earth and Planet. Inter., 105, 261–269.

Ondoh, T. (2003): Anomalous sporadic-E layers observed before M 7.2 Hyogo-ken Nanbu earthquake; Terrestrial gas emanation model, Adv. Polar Upper Atmos. Res. 17, 96-108.

Ouillon, G. & Sornette, D. (2000): The concept of 'critical earthquakes' applied to mine rockbursts with time-to-failure analysis, Geophysical Journal International, 143, 454-468.

Ouzounov, D., and F. Freund (2004), Mid-infrared emission prior to strong earthquakes analyzed by remote sensing data, Adv. Space Res. 33, 3, 268-273, DOI: 10.1016/S0273-1177(03)00486-1.

Ouzounov, D., N. Bryant, T. Logan, S. Pulinets, and P. Taylor (2006), Satellite thermal IR phenomena associated with some of the major earthquakes in 1999-2003, Phys. Chem. Earth 31, 4-9, 154-163, DOI: 10.1016/j.pce.2006.02.036.

Oyama, K.-I., Kakinami, Y., Liu, J.-Y., Kamogawa, M., and T. Kodama (2008): Reduction of electron temperature in low latitude ionosphere at 600km before and after large earthquakes, J. Geophys. Res., 113, A11317, doi:10.1029/2008ja013367.

Oyama, K.-I., Kakinami, Y., Liu, J.Y., Abdu, M.A., Cheng, C.Z., 2011. Latitudinal distribution of anomalous ion density as a precursor of a large earthquake. J. Geophys. Res. 116.

Park, S.K., Johnston, M.J.S., Madden, T.R., Morgan, F.D., and H.F. Morrison (1993): Electromagnetic precursors to earthquakes in the ULF band: a review of observations and mechanisms, Rev. Geophys., 31, 2, 117-132.

Parkhomenko, E.I., and A.T. Bondarenko (1986): Electrical conductivity of rocks at high pressures and temperatures, NASA, Washington, D.C., 292 pp.

Parrot, M., and M.M. Mogilevsky (1989): VLF emissions associated with earthquakes and observed in the ionosphere and the magnetosphere, Phys. Earth Planet. Int., 57, 86-99.

Parrot, M. (1994): Statistical study of ELF/VLF emissions recorded by a low-altitude satellite during seismic events, J. geophys. Res., 99(A12), 23,339-23,347.

Parrot, M. (2011): Statistical analysis of the ion density measured by the satellite DEMETER in relation with the seismic activity, Earthq. Sci., 24, 513–521, doi:10.1007/s11589-011-0813-3.

Parrot, M. (2012): Statistical analysis of automatically detected ion density veriations recorded by DEMETER and their relation to seismic activity, Ann. Geophys., 55(1), 149-155, doi:10.4401/5270.

Parrot, M., J.J. Berthelier, J.P. Lebreton, J.A. Sauvaud, O. Santolík and J. Blecki (2006): Examples of unusual ionospheric observations made by the DEMETER satellite over seismic regions, Phys. Chem. Earth, 31, 486-495; doi: 10.1016/j.pce.2006.02.011.

Petraki E, Nikolopoulos D, Panagiotaras D, Cantzos D, Yannakopoulos P, et al. (2015) Radon-222: A Potential Short-Term Earthquake Precursor. J Earth Sci Clim Change 6: 282, doi:10.4172/2157-7617.1000282

Piroddi, L. (2010), Sistimo di teleriilevamento termico per il montoraggion e la pervenzione dei rischi naturali: il caso sismico, Ph.D. thesis, 163 pp, Università degli Studi di Cagliari, Italy.

Piroddi, L., and G. Ranieri (2012), Night Thermal Gradient: A New Potential Tool for Earthquake Precursors Studies. An Application to the Seismic Area of L'Aquila (Central Italy), Selected Topics in Applied Earth Observations and Remote Sensing, 5(1), 307-312.

Piroddi, L., G. Ranieri, F. Freund, and A. Trogu (2014a), Geology, tectonics and topography underlined by L'Aquila earthquake TIR precursors Geophysical Journal International, 197(3), 1532-1536, doi:10.1093/gji/ggu123.

Piroddi, L., G. Ranieri, F. T. Freund, and A. Trogu (2014b), TIR, tectonics and geology in L'Aquila 2009, in EMSEV 2014, edited, Warsaw.

Pisa, D., Nemec, F., Parrot, M., and O. Santolik (2012): Attenuation of electromagnetic waves at frequency ~1.7kHz in the upper ionosphere observed by the DEMETER satellite in the vicinity of earthquakes, Ann. Geophys., 55(1), 157-163, doi:10.4401/ag5276.

Píša, D., F. Nemec, O. Santolík, M. Parrot, and M. Rycroft (2013): Additional attenuation of natural VLF electromagnetic waves observed by the DEMETER spacecraft resulting from preseismic activity, J. Geophys. Res. Space Physics, 118, 5286–5295, doi:10.1002/jgra.50469.

Pulinets, S.A. (2007): Natural radioactivity, earthquakes, and the ionosphere, EOS Trans. AGU, 88, 217-224.

Pulinets, S.A., and K. Boyarchuk (2004): Ionospheric precursors of earthquakes, Berlin: Springer, 2004.

Pulinets, S.A., Legen'ka, A.A., Gaivoronskaya, T.V., and V.K. Depuev (2003): Main phenomenological features of ionospheric precursors of strong earthquakes, J. Atmos. Sol.-Terr. Phys., 65, 1,337-1,347.

Pulinets, S. A., Liu, J. Y., and Safronova, I. A. (2004): Interpretation of a statistical analysis of variations in the foF2 critical frequency before earthquakes based on data from Chung-Li ionospheric station (Taiwan), Geomagn. Aeronom., 44, 102–106.

Pulinets, S. A., Leyva, A., and Ciraolo, L. (2005): GPS TEC variations around the time of the Colima earthquake of 21 January 2003, Geofisica Internacional, 369–377.

Pulinets, S.A., D. Ouzounov, L. Ciraolo, R. Singh, G. Cervone, A. Leyva, M. Dunajecka, A.V. Karelin, K.A. Boyarchuk, and A. Kotsarenko (2006): Thermal, atmospheric and ionospheric anomalies around the time of the Colima M7.8 earthquake of 21 January 2003, Ann. Geophys. 24, 835-849.

Qiang, Z., C. Dian, L. Li, M. Xu, F. Ge, T. Liu, Y. Zhao, and M. Guo (1999): Satellitic thermal infrared brightness temperature anomaly image – shortterm and impending earthquake precursors, Science in China, Series D: Earth Sciences 42, 3, 313-324, DOI: 10.1007/BF02878968.

Reid, H.F. (1910): The Mechanics of the Earthquake, The California Earthquake of April 18, 1906, Report of the State Investigation Commission, Vol.2, Carnegie Institution of Washington, Washington, D.C.

Ricci, D., G. Pacchioni, M.A. Szymanski, A.L. Shluger, and A.M. Stoneham (2001): Modeling disorder in amorphous silica with embedded clusters: The peroxy bridge defect center, Phys. Rev. B 64, 22, 224101-224108, DOI: 10.1103/PhysRevB.64.224104.

Riggio, A., and M. Santulin (2015): Earthquake forecasting: a review of radon as seismic precursor, Bollettino di Geofisica Teorica ed Applicata, Vol. 56, n. 2, pp. 95-114; June; DOI:10.4430/bgta0148.

Rikitake, T. (1976): Recurrence of great earthquakes at subduction zones, Tectonophys., 35, 335-362.

Rodger, C.J., Thomson, N.R., and R.L. Dowden (1996): A search for ELF/VLF activity associated with earthquakes using ISIS satellite data, J. Geophys. Res., 101(A6), 13,369-13,378.

Rousseau, J.J. (1756): Lettre sur la providence.

Rycroft, M., and R. Harrison (2012): Electromagnetic atmosphere-plasma coupling: The global atmospheric electric circuit, Space Sci. Rev., 168, 363–384, doi:10.1007/s11214-011-9830-8.

Ryu, K., Lee, E., Chae, J.S., Parrot, M., Pulinets, S. (2014b). Seismoionospheric coupling appearing

as equatorial electron density enhancements observed via DEMETER electron density measurements. J. Geophys. Res. Space Phys. 119 (10), 8524–8542.

Ryu, K., Oyama, K._I., Bankov, L., Minakshi, D., Koichi, C.-H., Liu, J.Y., and Liu, H. (2016): Precursory equatorial ionospheric density enhancement: contribution from Mid_latitude large earthquakes in the North_East Asian region. Adv Space Res 57:268–280.

Santolík, O., F. Nemec, M. Parrot, D. Lagoutte, and L. Madrias (2006): Analysis methods for multi-component wave measurements on board the DEMETER spacecraft, Planet. Space Sci., 54, 512–527, doi:10.1016/j.pss.2005.10.020.

Saraf, A.K., V. Rawat, P. Banerjee, S. Choudhury, S.K. Panda, S. Dasgupta, and J.D. Das (2008): Satellite detection of earthquake thermal infrared precursors in Iran, Nat. Hazards 47, 1, 119-135, DOI:10.1007/s11069-007-9201-7.

Sardon, E., A. Rius, and N. Zarraoa (1994): Estimation of the transmitter and receiver differential biases and the ionospheric total electron content from global posi-tioning system observations, Radio Sci., 29, 577-586.

Sarkar, S., Tiwari, S., and A.K. Gwal (2011): Electron density anomalies associated with M>=5.9 earthquakes in Indonesia during 2005 observed by DEMETER, J. Atmos. Sol. Terr. Phys, 73(16), 2289-2299, doi:10.1016/j.jastp.2011.06.004.

Saroso, S., Liu, J.-Y., Hattori, K., and C.-H. Chen (2008): Ionospheric GPS TEC anomalies and M>=5.9 earthquakes in Indonesia during 1993-2002.

Savitzky, A. and Golay, M.J.E. (1964): Smoothing and Differentiation of Data by Simplified Least-Squares Procedures, Analytical Chemistry, 36, 1627-1639.

Scafidia, D., S. Solarino, and C. Eva (2009), P wave seismic velocity and Vp/Vs ratio beneath the Italian peninsula from local earthquake tomography, Tectonophysics, 465(1-4), 1-23, doi:10.1016/j.tecto.2008.07.013.

Shockley, W. and Pearson, G. L., and Haynes, J. R. (1949). "Hole injection in germanium – Quantitative studies and filamentary transistors". Bell System Technical Journal. 28: 344–366. doi:10.1002/j.1538-7305.1949.tb03641.x

Scholz, C. H. (1968), Microfractures, aftershocks, and seismicity, Bulletin of the Seismological Society of America, 58(3), 1117-1130.

Scoville, J., J. Heraud, and F. Freund (2014), Pre-earthquake Magnetic Pulses, Nat. Hazards Earth Syst. Sci. Discuss., 2, 7367-7381, doi:10.5194/nhessd-2-7367-2014.

Scoville, J., J. Heraud, and F. Freund (2015): Pre-earthquake magnetic pulses, Natural Hazards and Earth System Sciences 15 (8), 1873-1880.

Scoville, J., J. Sornette, and F. T. Freund (2015), Paradox of peroxy defects and positive holes in rocks Part II: Outflow of electric currents from stressed rocks, Journal of Asian Earth Sciences, 114, Part 2, 338-351, doi:http://dx.doi.org/10.1016/j.jseaes.2015.04.016.

Shapiro, M. H., J. D. Melvin, T. A. Tombrello, and J. H. Whitcomb (1980): Automated radon monitoring at a hard-rock site in the southern California Transverse Ranges, J. Geophys. Res., 85, 3058-3064.

Shen, X., Zhang, X., Wang, L., Chen, L., Wu, Y., Yuan, S., Shen, J., Zhao, S., Qian, J., and J. Ding (2011): The earthquake-related disturbances in ionosphere and project for the first China seismo-electromagnetic satellite.

Sheskin, D.J. (2000): Handbook of parametric and nonparametric statistical procedures, 2nd Ed., CRC Press, Boca Raton, Fla.

Shida, R. (1886): On Earth currents, Trans. Seis. Soc., Vol. IX, Pt. I.

Shiratoi, K. (1927): The variation of radon activity of hot spring. Tohoku Imperial Univ., Scientific Report, Series 3, 16, 1725-1730.

Shluger, A. L., E. N. Heifets, J. D. Gale, and C. R. A. Catlow (1992), Theoretical simulation of localized holes in MgO, J. Phys.: Condens. Matter, 4(26), 5711-5722.

Silina, A.S., Liperovskaya, E.V., Liperovsky, V.A., and Meister, C.-V (2001): Ionospheric phenmena before stroing earthquakes, Nat Hazards Earth Syst. Sci., 1, 113-118, doi:10.5194/nhess-1-113-2001.

Sims, W.E., and F.X. Bostick, Jr. (1969): Methods of magnetotelluric analysis, Rep. 58, 86 pp., Electr. Geophys. Res. lab., Univ. of Texas at Austin.

Singh, B. (2008), Electromagnetic Phenomenon Related to Earthquakes and Volcanoes, Narosa Publ. House, New Delhi.

Singh, R. P., J. S. Kumar, J. Zlotnicki, and M. Kafatos (2010), Satellite Detection of Carbon Monoxide Emission Prior to the Gujarat Earthquake of 26 January 2001, Appl. Geochem., 25(4), 580–585.

Smith, B.E., Johnston, M.J.S. and Burford, R.O. (1978): Local variations in magnetic field, long term changes in creep rate, and local earthquakes along the San Andreas fault in central California, J. Geomagn. Geoelectr., 30, 539-548.

Sobolev, G.A. (1975): Application of electric method to the tentative short-term forecast of Kamchatka earhquakes, Pure Appl. Geophys., 113, 229-235.

Sornette, D. (1999) Towards a truly multidisciplinary approach to earthquake prediction, Nature debate April 1999, in "Is the reliable prediction of individual earthquakes a realistic scientific goal?", {http://www.nature.com/nature/debates/earthquake/equake_frameset.html)

Sorokin, V.M., Chmyrev, V.M., and A.K. Yaschenko (2001): Electrodynamic model of the lower atmosphere and the ionosphere coupling, J. Atmos. Sol.-Terr. Phys., 63, 1,681-1,691.

Sorokin, V.M., A.K. Yaschenko, and M. Hayakawa (2006b): Formation mechanism of the lower-ionospheric disturbances by the atmosphere electric current over a seismic region, J. Atmos. Sol.-Terr. Phys. 68, 11, 1260-1268, DOI:10.1016/j.jastp.2006.03.005.

St-Laurent, F. (2000): The Saguenay, Québec, earthquake lights of November 1988-January 1989, Seismol. Res. Lett. 71, 160-174.

Steinitz, G., Begin, Z.B., and N. Gazit-Yaari (2003): Statistically significant relation between radon flux and weak earthquakes in the Dead Sea rift valley, Geology 31, 505.

Tate, J., and W. Daily (1989): Evidence of electro-seismic phenomena, Phys. Earth Planet. Int., 57, 1-10.

Tazima M., H. Mizuno, and M. Tanaka (1976): Geomagnetic secular change anomaly in Japan, J. Geomag. Geoelectr., 28, 137-143.

Terada, T. (1931), On luminous phenomena accompanying earthquakes, Bull. Earthq. Res. Inst. Tokyo Univ. 9, 225-255.

Teng, T.L., and R.P. McElrath (1977): Variation of radon content in groundwater as induced by tidal stress changes, Rep. 77-2, Geophys. Lab., Univ. of S. Calif., Los Angeles, Calif.

Teng, T.L. (1980): Some recent studies on groundwater radon content as an earthquake precursor, Journal of Geophysical Research, vol. 85, No. B6, pages 3089-3099, June 10.

Thériault R, St-Laurent F, Freund FT, Derr J.S. (2014): Prevalence of earthquake lights associated with rift environments. Seismological Research Letters 85(1), 159-178.

Toledo-Redondo, S., M. Parrot, and A. Salinas (2012): Variation of the ?rst cut-off frequency of the Earth-ionosphere waveguide observed by DEMETER, J. Geophys. Res., 117, A04321, doi:10.1029/2011JA017400.

Torkar, D., Zmazek, B., Vaupotic, J., and I. Kobal (2010): Application of artificial neural networks in simulating radon levels in soil gas, Chem. Geol., 270, 1-8, doi:10.1016/J.chemgeo.2009.09.017.

Tramutoli, V. (1998): Robust AVHRR Techniques (RAT) for environmental monitoring: Theory and applications, EUROPTO Conference on Remote Sensing for Geology, Land Management, and Cultural Heritage III, Barcelona, Spain, September 1998, SPIE 3496.

Tramutoli, V., V. Cuomo, C. Filizzola, N. Pergola, and C. Pietrapertosa (2005): Assessing the potential of thermal infrared satellite surveys for monitoring seismically active areas: The case of Kocaeli (İzmit) earthquake, August 17, 1999, Remote Sens. Environ. 96, 3-4, 409-426, DOI: 10.1016/j.rse.2005.04.006.

Trigunait, A., M. Parrot, S. A. Pulinets, and F. Li (2004): Variations of the ionospheric electron density during the Bhuj seismic event, Ann. Geophys., 22 (12), 4123–4131.

Trique, M., Richon, P., Perrier, F., Avouac, J.-P., and J.-C. Sabroux (1999): Radon emanation and electric potential variations associated with transient deformation near reservoir lakes, Nature, 399,

137.

Tronin, A.A. (ed.) (1999): Satellite Thermal Survey Application for Earthquake Prediction, Terra Scientific Publ., Tokyo, 717-746.

Tronin, A.A. (2000), Thermal IR satellite sensor data application for earthquake research in China, Int. J. Remote Sens. 21, 16, 3169-3177, DOI: 10.1080/01431160050145054.

Tronin, A.A., O.A. Molchanov, and P.F. Biagi (2004): Thermal anomalies and well observations in Kamchatka, Int. J. Remote Sens. 25, 13, 2649-2655, DOI:10.1080/01431160410001665812.

Tsai, H. F., and J. Y. Liu (1999), Ionospheric total electron content response to solar eclipses, J. Geophys. Res., 104(A6), 12657–12668, doi:10.1029/1999JA900001.

Tsvetkova, T., Monnin, M., Nevinsky, I. and Perelygin, V. (2001): Research on variation of radon and gamma-background as a prediction of earthquakes in the Caucasus, Radiation Measurements, 33, 1-5.

Tsukuda, T. (1997): Sizes and some features of luminous sources associated with the 1995 Hyogo-ken Nanbu earthquake, J. Phys. Earth 45, 73-82.

Varotsos, P., and K. Alexopolous (1984a): Physical properties of the variations of the electric field of the earth preceding earthquakes, I, Tectonophys., 110, 73-98.

Varotsos, P., and K. Alexopolous (1984b): Physical properties of the variations of the electric field of the earth preceding earthquakes, II, Determination of epicenter and magnitude, Tectonophys., 110, 99-125.

Varotsos, P., and K. Alexopolous (1987): Physical properties of the variations of the electric field of the earth preceding earthquakes, II, Determination of epicenter and magnitude, Tectonophys., 136, 335-339.

Varotsos, P., Lazaridou, M. (1991): Latest aspects of earthquake prediction in Greece based on Seismic Electric Signals. Tectonophysics 188, 321–347

Voltaire (1756): Poème sur le désastre de Lisbonne.

Woith, H. (2015): Radon earthquake precursor: A short review; Eur. Phys. J., Special Topics, 224, 611–627, DOI: 10.1140/epjst/e2015-02395-9

Xu, T., Hu, Y., Wu, J., Wu, Z., Suo, Y., Feng, J. (2010): Giant disturbance in the ionospheric F2 region prior to the M8.0Wenchuan earthquake on 12 May 2008. Ann. Geophys. 28, 1533–1538.

Yao, Y.B., Chen, P., Zhang, S., Chen, J.J., Yan, F., and W.F. Peng (2012): Analysis of pre-earthquake ionospheric anomalies before the global M=7.0+ earthquakes in 2010, Nat. Hazards Earth Syst. Sci., 12, 575-585, 2012.

Yasuoka, Y., Y. Kawada, H. Nagahama, Y. Omori, T. Ishikawa, S. Tokonami and M. Shinogi (2009): Preseismic changes in atmospheric radon concentration and crustal strain, Phys. Chem. Earth, 34, 431-434.

Yu, T., Mao, T., Wang, Y., Wang, J. (2009): Study of the ionospheric anomaly before the Wenchuan earthquake. Chin. Sci. Bull. 54, 1080–1086.

Zakharenkova, I.E., I.I. Shagimuratov, and A. Krankowski (2007): Features of the ionosphere behavior before the Kythira 2006 earthquake, Acta Geophys. 55, 4, 524-534, DOI: 10.2478/s11600-007-0031-5.

Zechar, J.D., and T.H. Jordan (2008): Testing alarm-based earthquake predictions, Geophys. J. Int., 172, 2, 715-724, doi:10.1111/j.1365-246X.2007.03676.x.

Zeng, X., Y. Lin, C. Xu, and S. O. Yang (2001): Turning changes in evolution of geomagnetic field and infrastructural analysis of earthquake prediction, Kybernetes- Int. J. Systems & Cybernetics, 30, 365-377.

Zeng, X., M. Hayakawa, Y. Lin, and C. Xu (2002): Infrastructural analysis of geomagnetic field and earthquake prediction. Seismo Electromagnetics: Lithosphere-Atmosphere-Ionosphere Coupling, Hayakawa M. and O. A. Molchannov (Eds.), TERRAPUB, Tokyo, 463-468.

Zhang, X., Zeren, Z., Parrot, M., Battiston, R., Qian, J., Shen, X., 2011. ULF/ELF ionospheric electric field and plasma perturbations related to Chile earthquakes. Adv. Space Res. 47 (6), 991–1000.

Zhao, B.Q., Wang, M., Yu, T., Wan, W.X., Lei, J.H., Liu, L.B., Ning, B.Q. (2008): Is an unusual

large enhancement of ionospheric electron density linked with the 2008 greatWenchuan earthquake?, J. Geophys. Res. 113, A11304, doi:10.1029/2008JA013613

Zhao, B., Wang, M., Yu, T., Xu, G., Wan, W., Liu, L. (2010): Ionospheric total electron content variations prior to the 2008 Wenchuan earthquake, Int. J. Remote Sens. 31, 3545–3557.

Zhou, Y.Y.,Wu, Y., Qiao, X.J., Zhang, X.X. (2009): Ionospheric anomalies detected by ground-based GPS before the Mw7.9 Wenchuan earthquake of May 12, 2008. Chin. J. Atm. Sol. Terr. Phys. 71, 959–966.

Zhu, F.Y., Wu, Y., Lin, J., Xiong, J., Yang, J. (2009): Anomalous response of ionospheric VTEC before the Wenchuan earthquake. Acta Seismol. Sin. 22(2), 180–187.

Zhu, F., Zhou, Y., Wu, Y. (2013a): Anomalous variation in GPS TEC prior to the 11 April 2012 Sumatra earthquake. Astrophys. Space Sci. 345, 231–237.

Zhu, F.,Wu, Y., Zhou, Y., Gao, Y. (2013b): Temporal and spatial distribution of GPS-TEC anomalies prior to the strong earthquakes. Astrophys. Space Sci. 345, 239–246.

Zhu, F., Zhou, Y., Lin, J., and F. Su (2014): A statistical study on the temporal distribution of ionospheric TEC anomalies prior to M7.0+ earthquakes during 2003-2012, Astrophys. Space Sci., 350, 449-457, doi:10.1007/s10509-014-1777-2